AMERICAN UNIVERSITY OF BEIRUT

HEMATITE AND TITANIA INVERSE OPALS AND INVERSE
PHOTONIC GLASS NANOSTRUCTURED FILMS FOR SOLAR
ENERGY CONVERSION AND WATER SPLITTING

by
REMI GHASSAN FAYAD

A thesis
submitted in partial fulfillment of the requirements
for the degree of Master of Science
to the Department of Chemistry
of the Faculty of Arts and Sciences
at the American University of Beirut

Beirut, Lebanon
September 2014

AMERICAN UNIVERSITY OF BEIRUT

HEMATITE AND TITANIA INVERSE OPALS AND INVERSE PHOTONIC GLASS NANOSTRUCTURED FILMS FOR SOLAR ENERGY CONVERSION AND WATER SPLITTING

by
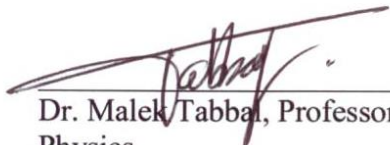## REMI GHASSAN FAYAD

Approved by:

_____

Dr. Lara Halaoui, Professor   Advisor
Chemistry

_____

Dr. Tarek Ghaddar, Associate Professor   Member of Committee
Chemistry

_____

Dr. Malek Tabbal, Professor   Member of Committee
Physics

Date of thesis defense: September 10, 2014

AMERICAN UNIVERSITY OF BEIRUT

THESIS, DISSERTATION, PROJECT RELEASE FORM

Student Name: __Fayad__   __Remi__   __Ghassan__

                     Last   First   Middle

● Master's Thesis   ○ Master's Project   ○ Doctoral Dissertation

[✓] I authorize the American University of Beirut to: (a) reproduce hard or electronic copies of my thesis, dissertation, or project; (b) include such copies in the archives and digital repositories of the University; and (c) make freely available such copies to third parties for research or educational purposes.

[ ] I authorize the American University of Beirut, **three years after the date of submitting my thesis, dissertation, or project,** to: (a) reproduce hard or electronic copies of it; (b) include such copies in the archives and digital repositories of the University; and (c) make freely available such copies to third parties for research or educational purposes.

_____

Signature _____   Date: September 18, 2014

ACKNOWLEDGMENTS

AN ABSTRACT OF THE THESIS OF

<u>Remi Fayad</u>   for   <u>Master of Science</u>
                                <u>Major</u>: Chemistry

Title: <u>Hematite and Titania Inverse Opals and Photonic Glass Nanostructured Films for Solar Energy Conversion and Water Splitting.</u>

This thesis consists of three different studies. In one study, the photoelectrochemical effects of order vs disorder was investigated at monodispersed disordered inverse opal and ordered inverse opals with and without coupling to nc-TiO$_2$ film under front wall and back wall illumination. While inverse opals (600-i-TiO$_2$-o) show only slight enhancement at the red edge of stop band (660-680 nm), inverse glass (i-TiO$_2$-g) when not coupled to nc-TiO$_2$ showed significant enhancement (compared to the conventional nc-TiO$_2$) in the entire spectrum. The observed enhancement was attributed to multiple internal scattering in the film that leads to longer light-matter interaction. The gain was similarly observed under front wall illumination and back wall illumination. Coupling nc-TiO$_2$ to i-TiO$_2$-g film on the other hand failed to enhance energy conversion as in the case of nc-TiO$_2$/600-i-TiO$_2$-o. Internal scattering and back scattering at nc-TiO$_2$/i-TiO$_2$-g hindered light from reaching the nc-TiO$_2$ layer where most of the dye is adsorbed and resulted in lower enhancements at the red edge of the stop band. Photonic effects due to the presence of order are causing localization of light within the nc-TiO$_2$ coupled to 600-i-TiO$_2$-o and that this effect does not persist in the presence of significant disorder.

In a second study, the effect of doping NiBi films with iron for catalyzing the oxygen evolution reaction was studied. Ni$_{40}$Fe$_{60}$Bi and Ni$_{60}$Fe$_{40}$Bi exhibited the highest turnover frequencies at high overpotentials whether anodized or non-anodized and hence had the highest catalytic activity, while the slightly doped Ni$_{90}$Fe$_{10}$Bi films had similar catalytic activity as NiBi films. To further confirm the catalytic effect of iron in Ni$_{1-x}$Fe$_x$Bi films, Ni$_{40}$Fe$_{60}$Bi and Ni$_{60}$Fe$_{40}$Bi films were also compared with thin NiBi having similar amounts of Ni. The higher turnover frequencies calculated for Ni$_{40}$Fe$_{60}$Bi and Ni$_{60}$Fe$_{40}$Bi than the thin NiBi films (which had similar TOF as the thicker NiBi films) further proves that it is iron that is enhancing the catalytic activity of the Fe- doped NiBi films. The anodization procedure that activates the films and increases their catalytic activity cannot merely be a result of incorporating iron in the film as deliberately introducing iron in non-anodized films still led to lower activity for oxygen evolution as compared to anodized NiBi films.

Finally, we studied the photoelectrochemical behavior of hematite inverse opals as photoanodes for water splitting. Hematite inverse opals prepared from two different polystyrene sphere assemblies (190 and 417 nm) were compared to unstructured films. At high light intensity, i-Fe$_2$O$_3$-o (417) exhibited the highest photocurrents compared to the other studied films whether in the front wall or back wall illumination with currents

reaching 0.79 mA/cm^2 at 100 mW/cm^2. However, at lower light intensitiy (25 mW/cm^2), i-Fe$_2$O$_3$-o (190) and i-Fe$_2$O$_3$-o (417) showed similar photocurrents (0.16 mA/cm^2). The lower photocurrents measured at i-Fe$_2$O$_3$-o (190) at high light intensity was attributed to the high carrier concentration leading to increased rates of recombination at the film. i-Fe$_2$O$_3$-o (417) films were decorated with photodeposited NiBi and Ni$_{90}$Fe$_{10}$Bi catalysts which led to similar cathodic shifts of ~ 200 mV and resulted in a slower decay of the photogenerated currents indicative of decreased recombination rates.

CONTENTS

Chapter

3. EXPLORATION OF THE EFFECT OF ORDER VS. DISORDER IN INVERSE OPALS AND BILAYER ELECTRODES ON THE ENERGY CONVERSION IN DYE-SENSITIZED SOLAR CELLS

ILLUSTRATIONS

TABLES

CHAPTER 1
INTRODUCTION

1.1. Energy Conversion at Semiconductors:

Between 80% to 85% of our energy comes from fossil fuels, a product of ancient biomass stored beneath Earth's surface for up to 200 million years.[1] However, this natural reserve will be depleted shortly. Solar energy, being a decentralized and inexhaustible natural resource places solar energy conversion at the heart of extensive research. The magnitude of the available solar power striking the earth's surface at any one instant is equal to the energy supplied by 130 million 500 MW power plants.[2,3] Utilizing this huge amount of power efficiently will solve our energy problem on one hand and will decrease unwanted gas emissions and make Earth greener on the other hand. Access to economically viable renewable energy sources is essential for the development of a globally sustainable society.[4] The challenge lies in the need of finding new inexpensive ways for capturing sunlight, converting this light to electrical energy or chemical energy, then storing and delivering this energy in a low-cost effective way.[5] Based on Shockley and Queisser calculations in 1961, the maximum theoretical efficiency limit for a single p-n junction illuminated with unconcentrated sunlight is 31%.[6] However, this theoretical limit can be exceeded by violating any of the assumptions used in the calculation, which include single p-n junction, unconcentrated illumination, one electron-hole pair generation per each photon absorbed, and thermal relaxation of the electron-hole pair energy in excess of the band gap.[1, 5-7] Concentrating sunlight increases the limit to 41%, while employing infinite number of p-n junctions with different band gaps that match the solar spectrum boosts the efficiency to 66%.[1] The most promising and significant increase is through multiple exciton generation by one

photon.[1, 8] Quantum confinement leads to the production of hot carriers which generates multiple electron-hole pair per each photon absorbed. This is attributed to the fact that when the carriers in the semiconductor are confined by potential barriers to regions of space that are smaller than or comparable to their deBroglie wavelength or to the Bohr radius of excitons in the semiconductor bulk, hot carrier cooling rates are reduced.[8]

1.2. Photonic Cystals and Photonic Glass:

Photonic crystals (PCs) are 3D ordered and periodic dielectric structures with alternating refractive index regions.[9,10,11,12,13] PCs possess a photonic gap and its position depends on the size of the dielectric beads. These structures attracted attention because they selectively allow the passage of certain wavelengths of light and inhibit the propagation of others. Within the photonic gap, incident light rays cannot propagate and are therefore reflected.[9,10,11] In this way, PCs behavior to photons is the same as semiconductors to electrons. A complete photonic gap exists if incident light rays at any angle are reflected. For a PC to exhibit a complete photonic gap, it should have high refractive index contrast (exceeding 2.8) and the sphere size should be in the order of the wavelength of light[14]. PCs were first reported in 1987 by Yablonovitch[9] and John[10] separately. They paved the way towards new applications in electronics such as low threshold lasers[15,16], optical polarizers[17,18], waveguides[19], perfect dielectric mirrors[20], and light-emitting diodes[21].

In this work, polystyrene beads of refractive index 1.55 and of sphere sizes 190 nm, 305 nm, and 417 nm were used to prepare Fe_2O_3 inverse opals and TiO_2 inverse opals. Hematite and Titanium oxide both have high refractive indices of 2.8 and 2.55 respectively. After filling the

PC voids with material, PCs were calcined to remove the polystyrene. This results in an inverse opal having 26 % material and 74 % air voids. The position of the stop band maxima can be calculated using Bragg equation:

$$\lambda = 2 \times D \sqrt{(0.74 \times n_s^2) + (0.26 \times n_v^2)}$$

n_s and n_v are the refractive indices of the infiltrated material (Fe_2O_3 or TiO_2) and air voids respectively. D is 0.87 times the diameter of the polystyrene sphere used.

Photonic crystals have been also introduced to the solar cell technology. They were incorporated in the assembly of nanostructured solar cells to study the energy conversion efficiencies in these structures. The interest in this direction developed for 2 reasons. First, PCs as mentioned above possess a stop band where light propagation is completely forbidden within the stop band frequencies. Second, the group velocity of light near the band edges becomes very small.[19,22] The dispersion curve (energy E vs wavevector k) has a slope that is proportional to the group velocity. At wavelengths just before and after the stop band, dE/dk approaches zero.[19,22,23,24] Thus, the group velocity of light is greatly reduced near the band edges.[24,25] This would therefore allow for longer light-matter interactions at the band edges. Electromagnetic variational theorem predicts that light behaves as a standing wave at the band edges where light at the red edge is confined in the high refractive index medium whereas light at the blue edge is confined in the low refractive index medium.[20]

Owing the interesting optical properties, PCs were incorporated in solar cells to study their energy conversion efficiencies. Recently, Bayram and Halaoui studied the energy conversion efficiencies in Q-CdSe sensitized opal-based solar cells.[26] Significant amplification in

photon-to-current conversion efficiency was measured in Q-CdSe i-TiO$_2$-o films with Se^{2-} as an electrolyte. The authors reported a maximum average enhancement factor of 6.7 ± 1.6 at 640 nm, which lies 60 nm to the blue of the stop band center, relative to the nc-TiO$_2$ film with comparable CdSe amounts. The gain was ascribed to the increased light-matter interaction as a result of slow light effects near the band edge, in addition to some disorder in the PC as a result of staking faults, cracks, and defects. Significant enhancement in energy conversion in Q-CdS sensitized TiO$_2$ inverse opals was previously reported by El Harake et al.[13] An enhancement factor of 4.7 ± 2.6 was observed to the blue of the stop band positioned at 450 nm compared to nc-TiO$_2$ film when sensitized with Q-CdS having absorption edge at 410 nm. Energy conversion at polydispersed disordered films prepared by replicating polystyrene with different sizes was investigated by El Harake et al.[13] Due to their polydispersity, these films do not show a stop band in the absorption spectra. Enhancement factors of 4.8 ± 2.4 at 420 nm and 5.1 ± 2.5 at 440 nm relative to nc-TiO$_2$ were observed. The enhancement was attributed to multiple internal scattering of light which increase the free mean path of light. These values are comparable with those obtained in ordered media at the blue edge of the stop band.

Photonic glass (PG) are monodispersed disordered photonic crystals, meaning that the size of the spheres is the same for all the particles, but the addition of salt destroys the order of the assembled particles (figure 1.1). This is different from polydispersed disordered films where the disorder is induced by mixing different polystyrene sizes. Different phenomena have been studied in random disordered media including coherent backscattering enhancement[27], and Anderson localization of light[28,29,30]. While (ordered) periodic photonic media take advantage of the periodicity in the dielectric constant, disordered ones – with no positional order – can still strongly affect light transport.[31,32] A single dielectric microsphere with size comparable to the

wavelength of light (a Mie sphere), can sustain electromagnetic resonances.[31,33,34,35] If the film

have many spheres with different sizes, then these resonances are washed out. On the other hand,

when all the spheres are identical, these modes occur all at the same frequency.[31,35] Resonance

modes in light are observed when light of wavelengths comparable to the optical diameter of the

spheres is shone on the PG. Polydispersed disordered PCs were fabricated previously in our lab

by mixing different ratios of different polystyrene sizes (150 nm, 190 nm, and 243 nm) during

the assembly of PC layer.[13]
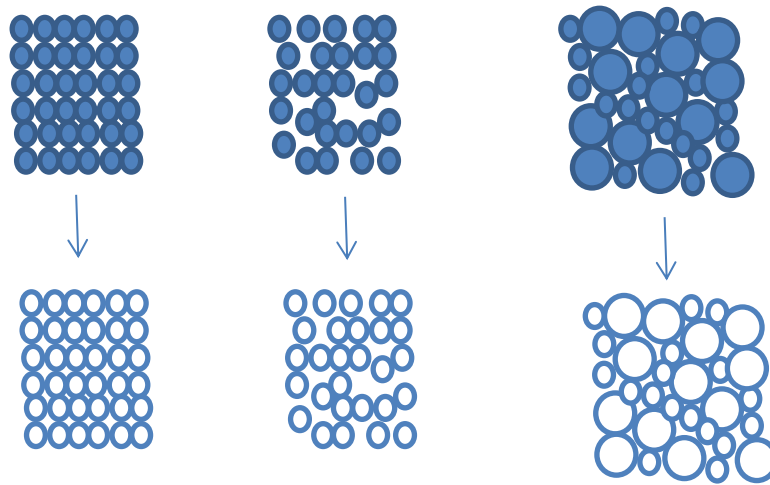
Figure 1.1: Photonic crystal (left), photonic glass (middle) and polydispersed disordered film
(right) and their respective inverse structures underneath.

1.3. Dye-Sensitized Solar Cells:

Dye sensitized solar cells (also known as Grätzel cell) which was developed in the early

1990's consists of a wide band gap semiconductor such as TiO_2 with a dye (usually ruthenium

based) adsorbed on it as the photoanode, iodide/triiodide redox couple as the electrolyte, and a

conductive substrate as the cathode (usually platinized).[36,37] Grätzel solar cells offer an

alternative to single-crystal solar cells for their low cost of fabrication, compact structure, and high power conversion efficiencies. The highest record for a liquid-based DSSC efficiency reached 13 % using cobalt(II/III) redox couple as an electrolyte.[38] DSSCs mimic natural photosynthesis and differ from conventional p–n junction devices because light collection and charge transport are separated in the cell.[39] Light is absorbed by the sensitizer while electron transfer occurs at the semiconductor surface. Upon illumination, a dye molecule gets excited and an electron is promoted from the HOMO to the LUMO, and is injected into the conduction band of the TiO_2. Through diffusion among the semiconductor particles, the electron reaches the conductive substrate, and moves through the external circuit. The photogenerated hole in the valence band of the dye is reduced by the (I^-/I_3^-) electrolyte.[36,40,41,42] (figure 1.2). The efficiency of a DSSC is calculated as the following:

$$\eta = \frac{J_{SC}V_{OC}FF}{P_{in}}$$

Where J_{SC} is the short circuit current density and is determined at V=0, the open circuit potential (V_{OC}) is determined at J=0, FF is the fill factor which describes the shape of the J-V curve and P_{in} is the power density of the incident light.[39] Alternatively, incident photon-to-current efficiency (% IPCE) allows us to study the spectral response of a particular DSSC at each wavelength. % IPCE can be calculated as follows:

$$\%IPCE = \frac{J_{@V}(A/cm^2)}{I_{@\lambda}(W/cm^2)} \times \frac{1240(eV.nm)}{\lambda(nm)} \times 100$$

Besides the desired electron transfer reaction that can be harvested to produce photocurrent, other recombination processes can occur in the cell. The photogenerated electrons located either

6

in band-gap traps or in the conduction band may recombine with the I_2 or I_3^- ions in the electrolyte or with the oxidized dye S^+.[43] These processes can either occur on the TiO_2 layer or on the conductive substrate.

Despite its attractive features, the DSSC suffers from several limitations whether at the level of the dye or at the level of the electrolyte, particularly light absorption limitation is of great importance. The widely used ruthenium dyes have very low or zero absorption in the longer wavelength region. Yet, over 60% of the AM 1.5 solar power spectrum comes from wavelength beyond 600 nm.[4] This presents a major obstacle in increasing the efficiency of a DSSC. On the other hand and despite the excellent results achieved using I^-/I_3^- redox couple, it presents some drawbacks such as evaporation, corrosion of several current collectors and partial absorption of visible light below 520 nm, resulting in a efficiency loss.[39,44]
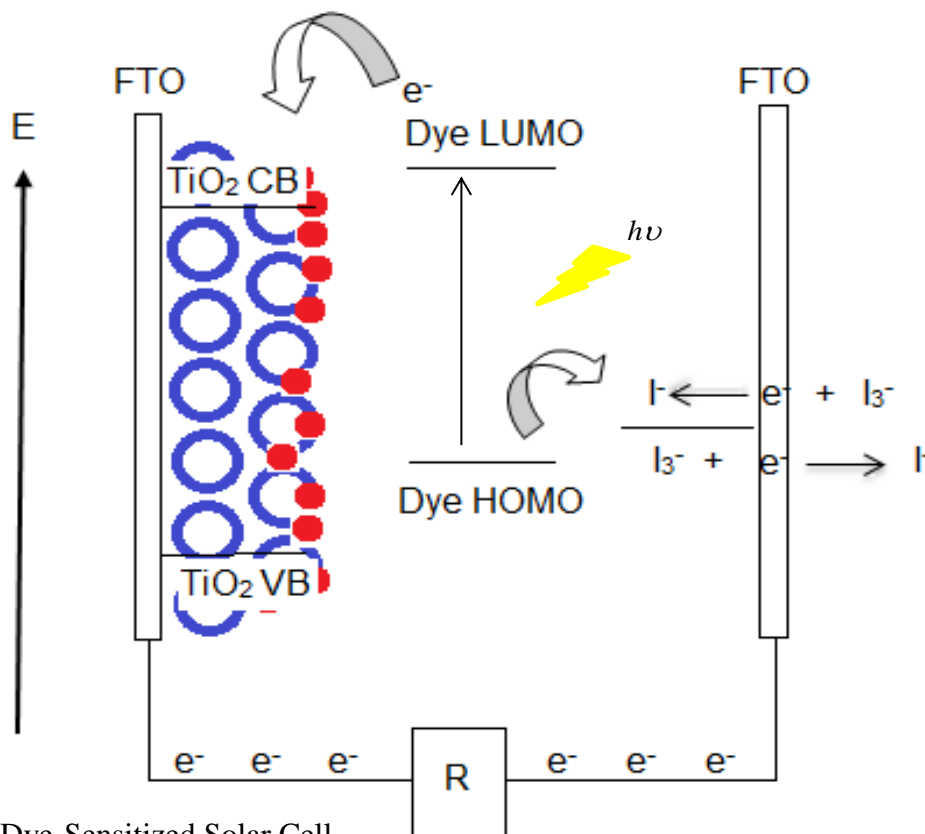
Figure 1.2: Dye-Sensitized Solar Cell.

Inverse opals are interesting material to be studied in a DSSC due to light localization effects that can be observed in desired regions of the solar spectrum. Titania inverse opals photoanodes consist of titania nanoparticles of sizes between 10 nm to 30 nm surrounded by air voids in the nanometer to micrometer range. Mallouk and coworkers and Halaoui et al investigated the effect of coupling of photonic crystals (PC) to nanocrystalline titanium dioxide (nc-TiO$_2$) on the optical absorption of DSSCs[23, 45, 46] and observed a 30 % overall gain in the short circuit photocurrent.[23] The significant enhancement in the % IPCE in the red region of the spectrum when a PC$_{327}$ layer was coupled to nc-TiO$_2$ film was attributed to localization of heavy photons near the edges of the photonic band gap, defect scattering in the inherent disorder regions in the PC layer, and Bragg diffraction in the periodic lattice.[45] Later, Mihi and Miguez attributed the light localization in these architectures to the appearance of multiple resonant modes resulting from the presence of an interface between photonic crystals and nc-TiO$_2$ and to longer light-matter interaction.[47] The lower efficiencies reported for a split-layer configuration of the bilayer electrode proved that optical coupling necessitates the intimate physical contact between the photonic crystal and nc-TiO$_2$ layers.[46] The effect of disorder in the inverse opals was studied in DSSCs and QD-sensitized solar cells. [13, 45] Halaoui et al observed an enhancement factor of 1.5 at 680 nm compared to nc-TiO$_2$ film for the disordered films prepared by mixing polystyrene of sizes 243 nm and 150 nm in 2:1 ratio. El Harake et al studied the behavior of disordered inverse opals in QD-sensitized solar cell in films prepared by mixing polystyrene spheres of sizes 150 nm, 190 nm and 243 nm. The enhancement factors for the disordered films reached 4.8 ($\pm$2.4) at 420 nm and 5.1 ($\pm$2.5) at 440 nm compared to nc-TiO$_2$ with comparable thickness. The high efficiencies reported for these disordered films were attributed to multiple internal scattering of light.[13,45] On the other hand, monodispersed

disordered photonic crystals (termed photonic glass) with sphere size comparable to the wavelength of light can sustain electromagnetic resonances, called Mie modes.[33] To the best of our knowledge, monodispersed disordered inverse photonic glass has not been fabricated yet. In this work, we report the fabrication, characterization and Photoelectrochemical behavior of inverse photonic glass films incorporated in Dye Sensitized Solar cells. These films were prepared in order to decouple light localization effects from nanostructuring, and to assess the roles of light localization and light scattering on enhancing light absorption in the different studied films.

Besides nanostructuring and the different architectures used to enhance light absorption in low energy spectrum, various attempts are being directed toward synthesizing new dyes that can absorb at long wavelengths, and at the same time can compete with N719; the dye should be stable, have a LUMO higher than the conduction band of TiO_2. It should have some linkages that would allow for its adsorption on the TiO_2 , as well as high extinction coefficient and high efficiency.[4, 37] For regeneration purposes, the dye should have an oxidized state level that is more positive than the redox potential of the electrolyte.[4] Until now, synthesis of such a dye was not achieved yet. Alternatively, co-sensitization of multiple dyes was employed. Noda and co-workers co-sensitized DSSC with a mixture of Ru complex (the black dye) and an organic sensitizer (D131).[37,48] Palomares et al employed CdS quantum dots in addition to the dye in the sensitization for extended light absorption.[49] Another interesting approach is to incorporate metal nanoparticles that exhibit plasmonic resonances such Au and Ag. [50,51]

In this respect, we studied the spectral response of inverse opal based DSSC sensitized by T118. T118 was synthesized by Professor Tarek Ghaddar at AUB. This dye exhibits an absorption peak at around 720 nm, in addition to the peaks at 520 nm and 430 nm. We aim at

investigating the light absorption enhancement in i-TiO$_2$-o and nc-TiO$_2$ sensitized with T118. These films were compared with cells sensitized with the conventional dye N719.

1.4. Watersplitting:

Plants use water splitting for solar energy conversion and storage. The process occurs in photosystem II in the cell membrane which upon excitation releases electrons.[52] The holes generated lead to the oxidation of the oxygen evolving complex (OEC), which comprises a cube on 4 manganese atoms and 1 calcium atom, in a process known as the KOK cycle which splits water into O$_2$ and H$^+$. In the KOK cycle, cells use proton-coupled electron transfer to produce 1 O$_2$ molecule, 4 electrons and 4 protons at the end of the cycle.[52] The photogenerated electrons are transferred to the Photosystem I through a series of cofactors and reduce protons by the action of ferrodoxin-NADP$^+$ reductase to from NADPH which in later steps is used to fix CO$_2$ in the form of carbohydrates.

Since solar energy is an infinite energy source, it can easily provide enough power for all of our energy needs if it can be efficiently harvested.[53] Because solar energy is diurnal, energy harvested from the sun needs to be efficiently converted into chemical fuel that can be stored, transported, and used upon demands in a similar manner as plant carry on photosynthesis.[54] Direct conversion of sunlight into fuels, often termed solar fuels, involves converting solar energy into energy stored in chemical bonds with the aid of an artificial photocatalyst.[55].Solar water splitting is a hot area of research because if it is accomplished efficiently it will provide sustainable and clean source of energy.

Efficiently splitting water into usable hydrogen could become a new industrial photosynthesis that would provide clean fuel whose only waste product upon utilization is

water.[2] Since the pioneering work of Honda and Fujishima[56], research has been directed towards finding and modifying materials with suitable band potentials that would be able to split water requiring minimal overpotential, and of relatively low cost. Water splitting involves two half reactions: the hydrogen evolution reaction (HER) and Oxygen evolution reaction (OER).

$$H_2O + 2h^+ \rightarrow 2H^+ + \frac{1}{2}O_2 \qquad\qquad \text{OER}$$

$$2H^+ + 2\bar{e} \rightarrow 2H_2 \qquad\qquad \text{HER}$$

$$H_2O \rightarrow H_2 + \frac{1}{2}O_2 \qquad\qquad \Delta E^o = 1.23 \text{ eV}, \Delta G^o = 237.2 \text{ KJ/mol}$$
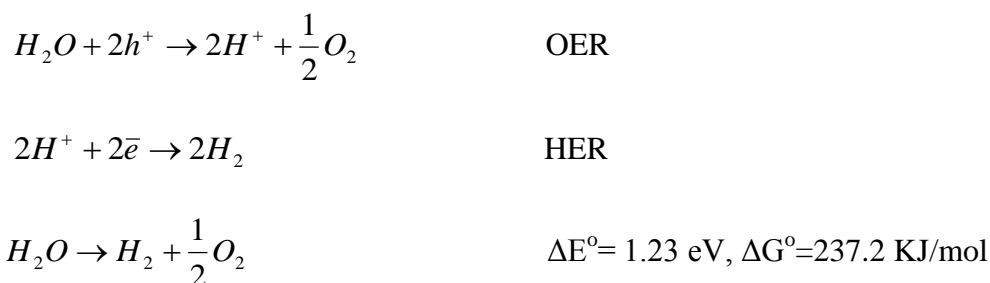
At normal conditions, only one electron/hole pair can be produced per each photon absorbed. The standard Gibbs free energy for the reaction is 273.2 kJ/mol which corresponds to $\Delta E^\circ = 1.23 \text{eV}$ per each photon absorbed. So this process requires 2 electron-hole pairs (with E=2.46 eV) per 1 molecule of H_2 or 4 electron-hole pairs (with E=4.92 eV) per 1 molecule of O_2.[2] The photons in the solar spectrum provide sufficient energy to drive this reaction, but the efficiency of the reaction depends upon how the reaction is carried out.[57] Since water molecules do not absorb appreciable radiation from the solar spectrum, one or more light/absorbing materials must be used to transduce the radiant energy to chemical or electrical energy.[57] However, even high absorbing materials need larger energy to carry out the reaction at a significant rate. This is because electron-transfer processes at semiconductor/liquid junctions produce losses due to the concentration and kinetic overpotentials needed to drive the HER and the OER.[2] To split a pair of water molecules into H_2 and O_2 at a reasonable rate, four photons of average energy 1.83 eV would be needed assuming no kinetic overpotential losses.[58]

Discovery of semiconductors that have appropriate light absorption characteristics and are stable in aqueous solutions is a key issue.[3] Water splitting cells require semiconductor

materials that are able to support rapid charge transfer at a semiconductor/aqueous interface, that exhibit long-term stability, and that can efficiently harvest a large portion of the solar spectrum.[2] In addition, bands potential is the most important issue that need to be addressed while choosing the appropriate semiconductor. As discussed earlier, the minimum energy required to split water is between 1.6 eV and 2.4 eV, therefore the semiconductor should have a band gap in this range or higher. Of the 51% of the total solar radiation that is absorbed by Earth, 95% of this radiation extends beyond 400 nm. If solar energy is to be used for water splitting, the semiconductor's band gap should not be wider than 3.1 eV. Moreover, to be able to split water, the conduction band of the semiconductor should be more negative than the reduction potential of H_2 and the valence band need to be more positive than the reduction potential of O_2.[59]
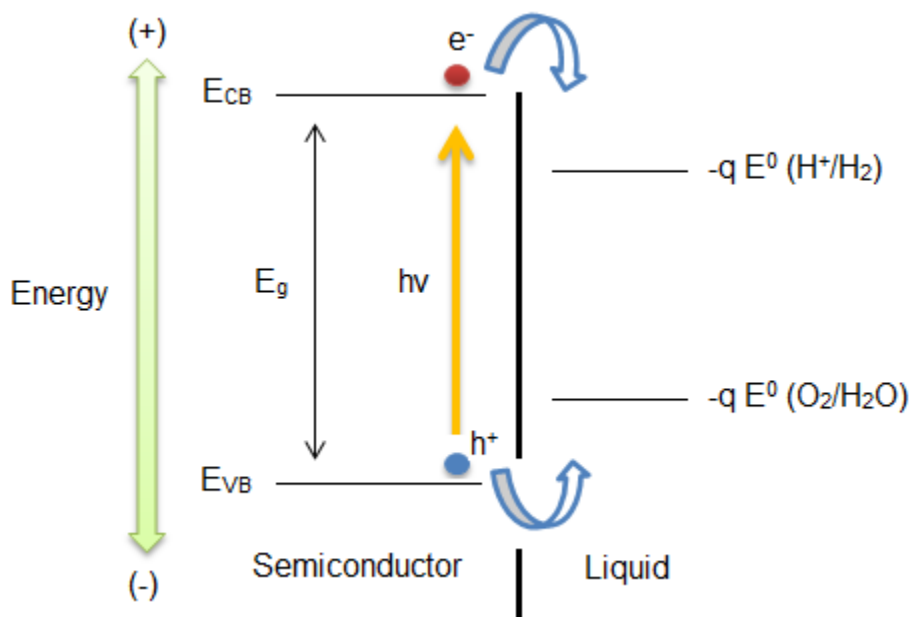
Figure 1.3: Oxygen evolution reaction (OER) and hydrogen evolution reaction (HER) for overall water splitting.

Unfortunately, it is nearly impossible to find a semiconductor that satisfies all the requirements for water splitting. Figure 1.4 shows the band potentials and gap for some widely used semiconductors.[2]
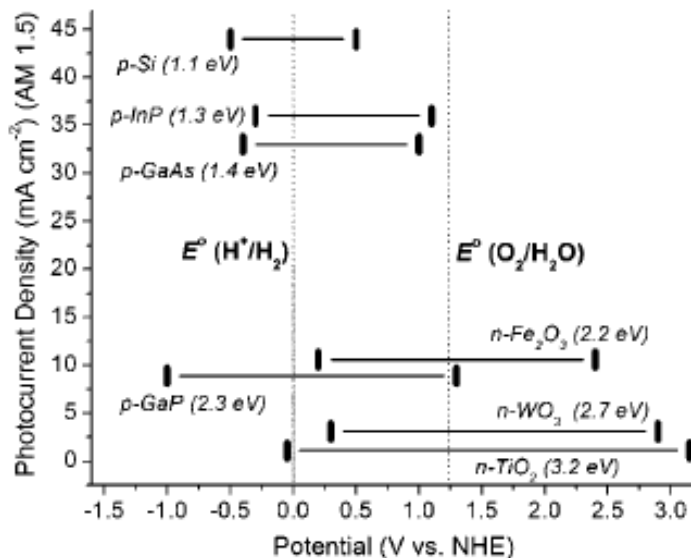
Figure 3.4: Conduction band (left bar) and valence band (right bar) positions vs NHE of common semiconductors used in photoelectrolysis cell. Adopted from reference 2.

Up-to-date, no single semiconductor satisfies all the requirements for water splitting. Alternatively, different configurations can be employed in which two or more materials are assembled in one cell whereby a specific material is selected for each of the half reactions. This could be a solution for 1) mismatch in the band potentials or 2) poor absorption characteristics for a particular semiconductor. In the first case, a semiconductor having a valence band more positive than the reduction potential of O_2 (i.e., suitable for water oxidation) and another semiconductor with a conduction band more negative than the reduction potential of H_2 (suitable

for water reduction) are connected in tandem (figure 1.3) For the second case, 2 semiconductors

with complementary band gaps, i.e. one with wide band gap capable of absorbing the high

energy photons and one with narrow band that would absorb the low energy photons are

assembled side by side. This configuration makes use of an appreciable fraction of the solar

spectrum.
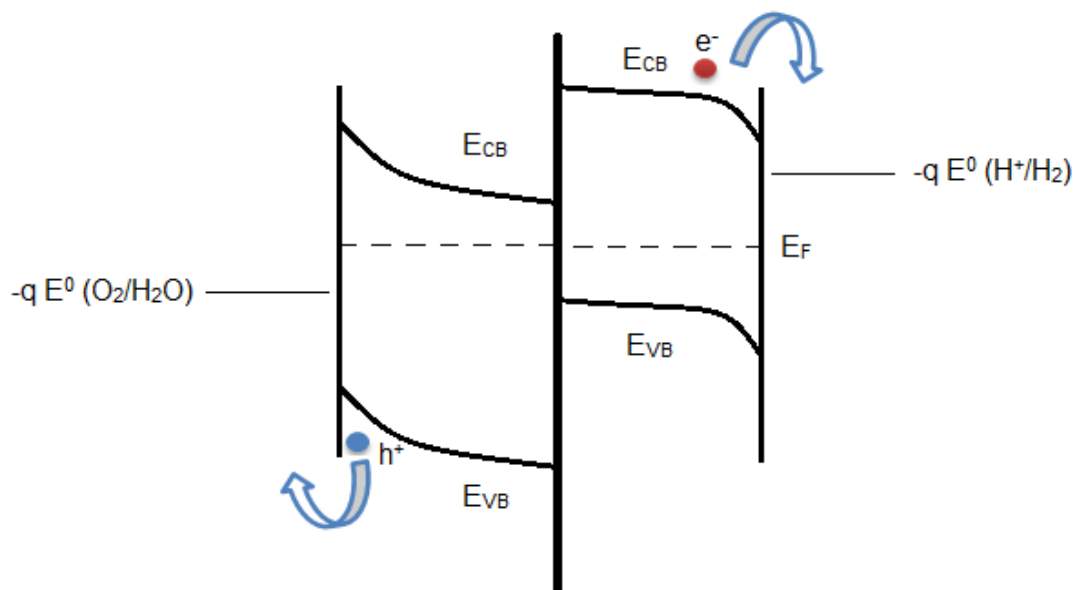
Figure 1.5: Energy diagram for a dual band gap p/n-PEC configuration with n-type and p-type
photoelectrodes electrically connected in series.

OER is a hard, 4-electron, 4 H^+ process and is governed by sluggish kinetics. Among the

different photoanode materials that have been investigated, hematite (Fe_2O_3) is of particular

interest. Hematite has emerged as a strong candidate in the photoassisted water oxidation

reaction because it is stable, prepared from cheap and abundant elements, and possesses a band

gap that permits the absorption of visible light ($E_g=2.1$ eV).[60] The valence band potential of

hematite is at 2.5 eV vs. NHE thus making it suitable for water oxidation. Despite these

attractive characteristics, hematite is not yet an effective material for photoanode conversion of

water to solar fuel.[61] Its performance as a photoanode for water oxidation has been crucially

limited by poor optoelectronic properties that lead to both low light harvesting efficiencies and a

large overpotential for photoassisted water oxidation.[53] Hematite has relatively low absorption

coefficient requiring thick films (400-500 nm) for complete light absorption[53,62,63]. It has an

indirect band gap and absorbs weakly in the long wavelength range.[61] This absorption is assigned

to Laporte-forbidden d-d transitions.[64,58] At shorter wavelengths, the absorption is due to oxo-

iron transitions which corresponds to the ligand to metal charge transfer (LMCT).[61] This is

manifested in the broad absorption bands in range of 400-600 nm.[65] It also exhibits short

minority carrier diffusion length (2-4 nm)[66] as a result of short exciton lifetime (~ 10 ps)[67,68] and

poor minority carrier mobility (0.2 $cm^2V^{-1}cm^{-1}$)[53,69]. The practical consequence of the short

transport length is that only those holes that are generated with a few to several nanometers of

the semiconductor/solution interface can reach the interface and can be used for water oxidation,

with the rest recombining with electrons and generating heat.[58] In addition, hematite suffers

from poor majority carrier conductivity.[58,69] Doping hematite with atoms with higher valency

such as tin, titanium, silicon, etc has proven to enhance its conductivity simply by adding more

majority carriers and therefore creating steeper voltage gradients.[58]

Attempts to circumvent the issue of bulk recombination in hematite are being directed

towards nanostructuring these hematite films in order to decrease the distance the hole must

travel to reach the interface. To this end, several approaches have been proposed. These include

nanoparticles, nanorods, or nanowires. Recent work on nanorods, synthesized with the aid of

anodic aluminum oxide, showed photocurrent densities of about 8 mA/cm^2 at 0.6 V vs Ag/AgCl

(sat KCl) in 1 M NaOH.[70] Nanoporous and nanotubular hematite which were prepared by Misra

et al with a wall thicknss of 5-6 nm produced 1 mA/cm^2 at 1.23V$_{RHE}$.[71] Duret et al recently

reported the synthesis of hematite leaflet structure consisting of 100 nm-sized platelets of 5–10 nm thickness bundled into 50 nm sheets oriented perpendicular to the FTO support by ultrasonic spray pyrolysis. The authors reported a photocurrent of 1.3 mA/cm^2 at 1.23 V$_{RHE}$ in 1 M NaOH and 16 % IPCE at 370 nm and 1.2 V$_{RHE}$.[72] Cauliflower nanostructures which were fabricated by Kay et al using atmospheric pressure chemical vapor deposition (APCVD) and silicon (IV) doping produced a photocurrent equals to 1.8 mA/cm^2 at 1.23 V$_{RHE}$ in 1 M NaOH.[72,73]. The cauliflower structures feature fine dendrites that facilitate electron transport.

In this work, our group among the first groups that reports the fabrication of hematite inverse opals that can be used as photoanodes for solar water splitting. The structure morphology of inverse opals is advantageous in this respect because it provides short distances for the minority carriers to reach the electrode/electrolyte interface. Our inverse opal films were investigated in terms of nanostructuring only; light localization effects were not investigated in this study because our films did not show the bragg diffraction peak in the UV-vis spectroscopy. However, the inverse opal structure was confirmed using scanning electron microscopy (SEM). Up to date, no one confirmed the presence of a stop band peak for hematite inverse opal. A possible explanation is that the high annealing temperature (550 ^{o}C), that is required for ensuring the electronic properties of hematite, is inducing a significant disorder in the structure, and thus preventing the peak from showing up. Park and coworkers synthesized hematite inverse opals from a 250 nm, 500 nm and 900 nm polystyrene templates and observed the best performance for the 250 nm size which produced 3.1 mA/cm^2 at 0.5 V vs Ag/AgCl in 1 M NaOH.[74] Other groups used hematite to coat the surface of SiO$_2$[75] and SnO$_2$[76] inverse opals. Depositing 15 nm of Fe$_2$O$_3$ and 8 nm thick ITO on top of SiO$_2$ inverse opal film showed a photocurrent density equals to 1.6 mA/cm^2 at 1.53 vs RHE in 1 M NaOH. [75]

1.5. Kinetics of Oxygen Evolution:

Apart from the large thermodynamic requirement to carry the oxygen evolution reaction, this reaction is also goverened by sluggish kinetics which is reflected in the high-surface-mediated charge recombination processes, especially that hematite is known to have poor OER catalytic activity.[73,77,78] Attempts to improve the interfacial kinetics of OER mainly focused on attaching materials capable of transferring the photogenerated holes to the surface at a higher rate and minimizing surface recombination on the semiconductor surface. Among the studied cocatalysts, cobalt, iridium oxide, and nickel have shown effective results. Upon doping Co^{2+} ions to the hematite cauliflower structure developed by Kay et al, the authors reported a 65% increase in the photocurrent (2.2 mA/cm^2) and 80 mV cathodic shift.[73] Tilley and coworkers observed a 200 mV shift in the onset potential upon decorating hematite cauliflower with Ir_2O_3 nanoparticles. An increase in the plateau current of 0.3 mA/cm^2 was also observed, which according to the authors suggests that surface recombination exists even at high overpotentials.[77] Nocera's research group has explored a very stable Nickel borate catalyst which can be deposited under mild conditions in the presence of borate.[79] To enhance the catalytic activity of NiBi catalyst, films were anodized for 2 hr after which the catalyst produced 1 mA/cm^2 at an overpotential of 425 mV at near-neutral conditions.[79] Anodization is thought to induce structural changes in the NiBi film and change the oxidation state of Ni atoms to Ni (IV).[80] Using nickel in the presence of potassium borate as an electrolyte for catalyzing oxygen evolution proved that the reaction is governed by proton coupled electron transfer (PCET). PCET reactions are of significant importance because plants use this type of reactions in order to generate energy and carry on the basic functions of cells.[81,82]

Several reports showed that in fact incorporating iron into nickel oxide electrocatalyst could enhance its OER performance. In his early report in 1987, Corrigan investigated the effect of iron coprecipitation into nickel oxide on OER.[83] A decrease of 100 mV in the overpontential was observed with 10% coprecipitated iron and tafel slopes decreased from 70 mV/decade in the absence of iron to 25 mV/decade.[83] Corrigan proposed that there must be a synergistic effect of mixing iron with nickel which poorly understood, which either involves a change in the rate determining step or increases the conductivity of the resistive quandrivalent NiO.[83] McFarland et al electrodeposited binary Ni-Fe complex on Ti-doped hematite films from equimolar solution of nickel sulfate and iron sulfate and showed that a 200 mV shift was observed for NiFe complex compared to 50 mV shift for Ni electrodeposited on Ti-doped hematite in 1 M NaOH.[84] Electrodeposited $Ni_{12.85}Fe_{5.15}$ from sulfate precursors has demonstrated the best catalytic activity for OER among the studied binary mixed-metal complexes having the smallest electron-transfer coefficient ($\alpha=0.0008$) and greatest exchange current density ($J_o=9.04\mu A/cm^2$) in 1 M KOH.[85] Landon et al synthesized different compositions of mixed NiFe oxide via evaporation induced self-assembly and showed that the highest catalytic activity was for NiFe (90:10) having the smallest tafel slope of 40 mV/decade.[78] Louie and coworkers examined the catalytic effect of iron (II) incorporation in nickel oxide films prepared from their sulfate precursors and showed that $Ni_{60}Fe_{40}$ shows the best catalytic performance and attributed the discrepancy in the optimal iron content between 10% and 50 % found in the literature to the similar specific current densities and overpotential values obtained within this Fe composition range.[86] The authors further showed using in situ Raman spectroscopy that aging of Ni films and Fe incorporation induce similar structural effects on Ni films which was further supported by tafel slope measurements.[86] Smith et al showed that although NiO and CoO have demonstrated good OER

catalytic activity, mixed Ni-Co oxide did not reveal better performance, while iron oxide that is known to have low OER catalytic ativity, modest amounts of 20-40 % iron significantly improved tafel slopes for mixed-metal oxide films with $Ni_{60}Fe_{40}$ prepared via photochemical metal-organic deposition showing the smallest slope of 34 mV/decade.[87] Gong and coworkers prepared $Ni_{80}Fe_{20}$ layered double hydroxide on multiwalled carbon nanotubes (NiFe-LHD/CNT) from nickel acetate and iron nitrate precursors and showed that NiFe-LHD/CNT outperformed the commercial iridium catalyst in terms of electrocatalytic activity and stability with tafel slope reaching 31 mV/decade in 1 M KOH compared to 40 mV/decade for the Ir catalyst.[88]

To the best of our knowledge, doping NiBi with iron has not been reported yet. In this work, we investigated the effect of incorporating different amounts of Fe into NiBi films. Thin films were electrodeposited on FTO from nickel nitrate and iron nitrate precursors. The amount of $Ni_{1-x}Fe_xBi$ electrodeposited was limited to the passage of 1 mC/cm^2. Films were anodized and tested for their OER electrocatalytic activity using cyclic voltammetry and tafel slope measurements and compared with NiBi films.

CHAPTER 2

EXPERIMENTAL SECTION

2.1. Materials:

The following were used in this study: suspensions of monodisperse carboxylate modified polystyrene particles of 305 nm and 417 nm sphere diameters ($\sigma \leq 3$ %), 10 % w/v in water, as determined by the manufacturer stored at 4 ^{o}C (Seradyn Co, Indianapolis); cis-bis(isothiocyanato)bis(2,2'-bipyridy-4,4'-dicarboxylato)ruthenium(II) bis(tetrabutylammonium) ($RuL_2(NCS)_2$-2TBA also known as Ruthenium 535 bis-TBA, or N719, Solaronix); polyoxy-ethylene(5)nonyl phenyl ether surfactant, Igepal (Aldrich); boric acid, H_3BO_3 (99.5%, Aldrich); ammonium hexafluorotitanate, $(NH_4)_2TiF_6$ (99.99 %, Aldrich); titanium isopropoxide, $Ti(OCH(CH_3)_2)_4$ (98 %, Aldrich); ferric nitrate nanohydrate $Fe(NO_3)_3$. $9H_2O$ (98%, Aldrich); nickel nitrate hydrate $Ni(NO_3)_2$ (99.999%, Aldrich); potassium hydroxide (Aldrich), nanocrystalline titanium dioxide, nc-TiO_2 (<d> = 13nm, Solaronix, Switzerland); nitric acid HNO_3 (65 %, Acros); absolute ethanol (99.8 %, Aldrich) , isopropanol (99 %, Acros); sodium hydroxide (Aldrich); potassium chloride (99 %, Riedel-de Haër); The redox couple/electrolyte solution consisted of iodide/ triiodide solution (Iodolyte TG-50, Solaronix). Double distilled water was used for cleaning. Deionized water (18$\mu\Omega$-cm, Nanopure Diamond, CRSL, AUB) was used for solution preparations.

2.2. Preparation of Substrates:

The working electrodes were fluorine-doped tin oxide coated glass substrates (FTO, SOLARONIX R=15 Ω/sq). FTO substrates were first cleaned with detergent and water, cleaned

by ultrasonication in isopropanol for 30 minutes, and then rinsed thoroughly with water. Substrates were then ultrasonicated in water for 10 minutes followed by drying in air.

2.3. Experimental Section for the preparation of inverse opals, inverse glass and nanocrystalline TiO$_2$ as electrodes for DSSC:

2.3.1. Fabrication of nanocrystalline TiO$_2$ films:

Nanocrystalline TiO$_2$ films were prepared using Squeegee method. A slurry of nc-TiO2 particles (13 nm diameter, anatase, Eg=3.2 eV; Seradyn) was applied on the FTO substrate and spread on the surface with the aid of a round glass rod (using pasteur pipet). Scotch-tape was used to control the thickness of the film. Two scotch-tape layers resulted in 5 to 7 microns thickness as measured by Ambios X2 Profilometer. The solvent was evaporated at 80 ^{o}C on a hot plate for around 10 seconds, and the films were sintered at 400 ^{o}C for an hour.

2.3.2. Preparation of Photonic Crystals for DSSC:

Polystyrene colloidal crystal templates were assembled on clean FTO substrates from solutions of polystyrene spheres (PS) by evaporation-induced self-assembly. Photonic crystals (PC) were assembled from a suspension of 0.05 % wt PS solution of 305 nm diameter prepared by weighing 0.373 g of 10 % PS spheres and suspending the particles in 75 ml of deionized water. 0.331 g of 0.5 % (wt/v) aqueous solution of igepal (CO–520) was added to minimize agglomeration and to better create a meniscus at the air-solution interface. Disordered photonic crystals (termed photonic glass, PG) were assembled from suspensions in 1 mM aqueous solution of sodium chloride instead of water by adding 0.00439 g NaCl salt 75 ml deionized water. Solutions were ultrasonicated for 40 min in an ultrasonic bath to disperse the polystyrene particles in solution then transferred to wide shallow containers. FTO substrates were totally

dipped in solution with their conductive side exposed to the solution. Water was then evaporated from the solution to allow the polystyrene particles to self-assemble on the substrates by placing the containers in a furnace oven at 55 ^{o}C for 48 hours. The resulting photonic crystal 305 nm and photonic glass templates had a thickness of 5-7 μm.

2.3.3. *Preparation of titanium dioxide inverse opals by Liquid phase deposition method (LPD):*

TiO_2 inverse opals were prepared by replicating the PS photonic crystals using a reported liquid- phase deposition (LPD) followed by burning of the spheres.[13,45,23,46,26] A seeding layer is required prior to LPD. In the seeding process, the synthetic opals were immersed vertically in a solution of 1.2 % (w/v) of titanium isopropoxide and 0.12 % (w/v) HNO_3 in ethanol for 5 minutes. This solution was prepared by dissolving 0.84 g of titanium isopropoxide and 0.084 g HNO_3 in 75 ml of ethanol. Seeding was followed by a hydrolysis step where the samples were kept in air for at least one hour to form a titania surface seed layer.

$$Ti(OCH(CH_3)_2)_4 + 4\ H_2O/H^+ \longrightarrow Ti(OH)_4 \longrightarrow TiO_2 + 2H_2O$$
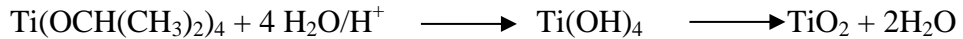
Opals were then dipped in a 75 ml aqueous solution of 0.2 M $(NH_4)2TiF_6$ and 0.25 M H_3BO_3 for 30 min. The solution was prepared by mixing 35 ml of an aqueous solution containing 2.769 g of $(NH_4)2TiF_6$ with a 35 ml of an aqueous solution containing 1.082 g of H_3BO_3 after heating each to 50 ^{o}C. The two solutions were mixed and their pH was adjusted to 2.9 with 1 M HCl and then heated till 50 ^{o}C again before immersing the substrates. The temperature was maintained at 50 ± 2 ^{o}C by a temperature controller unit (Corning) attached to a hot plate. After 30 min in this solution, the substrates were dipped in water for 1 minute and kept to dry in air at room temperature.

$$2\ TiF_6{}^{2-} + 3\ BO_3{}^{3-} + 10\ H^+ \longrightarrow 3\ BF_4\text{-} + 2\ TiO_2 + 5\ H_2O$$
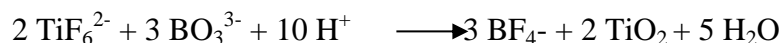
In order to remove the polystyrene spheres, FTO substrates were calcined in a programmable furnace oven (Barnstead thermolyne, 48000) at 400 ^{o}C; the temperature was raised from room temperature to 110 ^{o}C with a ramp of 3 ^{o}C/min, and kept at 110 ^{o}C for an hour. It was then raised to 400 ^{o}C at a rate of 5°C/min where it dwelled for 8 hours, followed by returning to 25 ^{o}C at a rate of 10 ^{o}C/min. FTO substrates were placed on an indium tin oxide coated glass sheet (ITO, Delta technologies) with their conductive side facing the ITO sheet. This results in the formation of TiO$_2$ inverse opal. Films were characterized using SEM, TESCAN MIRA 3 and UV-vis Spectrophotometer (JASCO, V-570 UV/VIS/NIR).
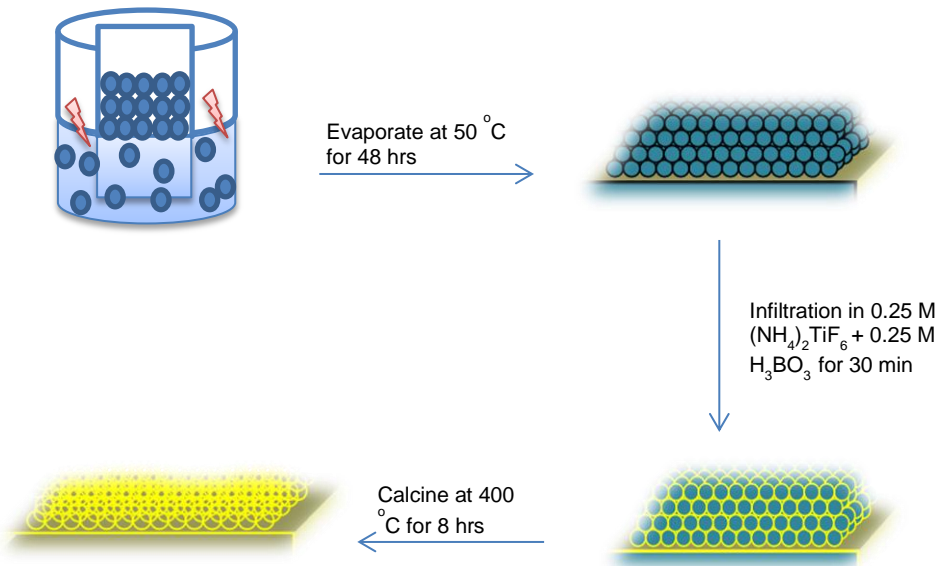
Figure 2.1: Scheme illustrating the preparation of the hematite inverse opals.

2.3.4. *Preparation of Bilayer Structure:*

Coupling of i-TiO$_2$-o and i-TiO$_2$-g to conventional nc-TiO$_2$ film was achieved by applying a slurry of nc-TiO$_2$ nanoparticles ($<d> = 13$nm) over the inverse opal by a squeegee method to give a total film thickness (of inverse opal and nc-TiO$_2$) of 8-11 μm using a double

scotch tape as spacer. The bilayer was dried over a hotplate after setting its temperature at 80 ℃

for 10 seconds, then placed face-down on an ITO sheet in a furnace oven at 400 ℃ for 1 hour.

2.3.5. Ru-N719 dye sensitization:

0.3 mM solution of N719 dye (Mwt = 1188.5 g/mol) was prepared by dissolving

0.0107 g in 30 ml of absolute ethanol. The dye solution was stored in the dark.   All samples (i-

TiO_2-o, i-TiO_2-d, nc-TiO_2/i-TiO_2-o, nc-TiO_2/i-TiO_2-d and nc-TiO_2) were dehydrated in the oven

at 120 ℃ for an hour prior to their dipping in the dye solution. The amount of the dye that was

adsorbed on the surface was determined by UV-vis spectroscopy after desorption in 3 ml 3.8 M

NaOH. Measurements were taken at fixed wavelength that corresponds to λ_{max} at 520 nm.

Calibration curve was drawn from the absorbance of 4 standards of concentrations 0.0075 mM,

0.015 mM, 0.03 mM, and 0.06 mM prepared from the original dye solution and diluted by 3.8 M

NaOH. The concentration of dye adsorbed on a sample was determined from the calibration

curve. Multiplying the concentration by the volume used to desorb the sample (3 ml) gave the

number of moles adsorbed, which was divided by the geometric area of the sample to get the

amount/area reported in ηmol/cm^2. Desorption and amount determination of T118 dye was

different from N719 dye. Films were desorbed in 3 ml 3.8 M NaOH in H_2O: Ethanol (50:50)

solution. The amount of dye adsorbed was calculated using Beer-Lambert law (A=εbc); the

measured absorbance was multiplied by the path length (1 cm) and the extinction coefficient of

the dye at 520 nm (16633.2 $Lmol^{-1}$ cm^{-1}). The obtained concentration was multiplied by the

volume used to desorb the film to calculate the number of moles of dye adsorbed.

2.3.6.   *Photoelectrochemistry of DSSC:*

2.4.6.1.   <u>Photoelectrochemical setup:</u>

Photoelectrochemical measurements were collected in a 3-electrode quartz cell using a CHI Model 630A electrochemical workstation. Home-made silver/silver chloride electrode (in saturated KCl) was used as a reference electrode. The working electrode was FTO/nc-TiO$_2$/Ru-N719 dye, FTO/i-TiO$_2$-o/Ru-N719 dye, FTO/i-TiO$_2$-o/nc-TiO$_2$/Ru-N719 dye, FTO/i-TiO$_2$-g/Ru-N719 dye, or FTO/i-TiO$_2$-g /nc-TiO$_2$/Ru-N719 dye. A clean FTO was used as a counter electrode. The light source used was a 300 W xenon lamp (Model 66901 lamp housing, Oriel instruments) that operated at 300 W. A ¼ m grating monochromator (Oriel Instruments, Model 77200) was used to disperse the light for monochromatic measurements. A 20 micrometer thick spacer (Solaronix) was sandwiched between the dye-sensitized photoelectrode and the FTO counter electrode in the cell assembly. The working and the counter electrodes were pressed by a binder clip and placed in quartz cell containing few drops of the   I⁻/I$_3^-$ iodolyte electrolyte. The reference electrode was a home-made Ag/AgCl (saturated KCl).

Photocurrent measurement at the dye sensitized photoelectrode was carried using linear sweep voltammetry by scanning the potential between -5 mV and 5 mV at a scan rate of 1 mV/sec. The photocurrent measured at 0 V was used to compute the % IPCE under monochromatic light illumination at 20 nm intervals from 400 nm to 720 nm. Two modes of illumination were used in the photoelectrochemical experiment: front-mode and back-mode. In the front wall illumination, light passes from the counter electrode to the working electrode passing through the electrolyte, while in the back-wall illumination light passes by the working electrode first and then to the electrolyte and then to the counter electrode.

The same experimental setup was used for experiments on comparing T118 dye to N719 dye except that 2-electrode system was used, the working electrode being the i-TiO$_2$-o or nc-TiO$_2$ and the counter electrode was a platinized FTO which was prepared by dropping 20 μl platinic acid on an FTO followed by sintering at 400 ^{o}C for 30 min.

2.4.6.2.   <u>Incident photon to current conversion efficiency (% IPCE) at a fixed voltage:</u>

Monochromatic incident-photon-to-current-conversion-efficiency (% IPCE) at a fixed voltage was calculated according to the following equation:

$$\% IPCE(atV) = \frac{J_{@V}(A/cm^2)}{I_{@\lambda}(W/cm^2)} \times \frac{1240(eV.nm)}{\lambda(nm)} \times 100$$

J represents the photocurrent density calculated by dividing the monochromatic photocurrent measured at a wavelength λ by the illuminated area of the sample at an applied potential V, and I is the light intensity at the wavelength λ. Linear Sweep Voltammetry was used to measure the photocurrents generated at a potential of 0 V vs. Ag/AgCl. Photocurrent densities were calculated by dividing the photocurrent by the geometric area of the sample after dark current subtraction. A thermopile light detector and power meter (Model 70260, Oriel Instruments) was used to measure the power of light at each wavelength at the approximated position of the electrode with 10 sec average light measurement. To calculate the power density, the power was divided by the area of the light. Normalized % IPCE was calculated to compare between different samples with different amounts of dye adsorbed. It was calculated by dividing the % IPCE by the amount of the dye adsorbed on the sample per area (ηmol/cm^2).
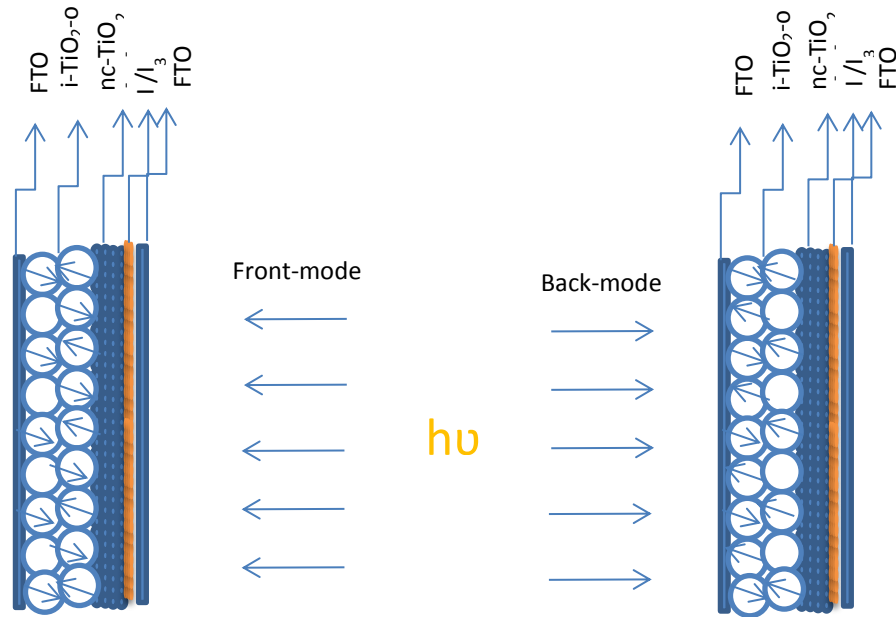
Figure 2.2: A scheme showing the bilayer architecture under front-wall and back-wall illumination.

2.4. Experimental Section for the Preparation of Hematite Photoanodes:

2.4.1. Fabrication of Photonic Crystals for Hematite Photoanodes:

Polystyrene colloidal crystal templates were assembled on clean FTO substrates from solutions of polystyrene spheres (PS) by evaporation-induced self -assembly. Thin films are required for the photoanodes in order to minimize recombination processes. PC 190 nm and 417 nm were assembled from a solution of 0.025% wt containing 0.1863 g of 10 % PS spheres and 0.1656 g of 0.5 % (w/v) aqueous solution of igepal in 75 ml of deionized water. Igepal (CO–520) was added to minimize agglomeration and to better create a meniscus at the air-solution interface. Solutions were ultrasonicated for 40 min in an ultrasonic bath to disperse the polystyrene particles in solution then transferred to wide shallow containers. FTO substrates were totally dipped in solution with their conductive side exposed to the solution. Water was

27

then evaporated from the solution to allow the polystyrene particles to self-assemble on the subtrates by placing the containers in a furnace oven at 55 ^{o}C for 48 hours.

2.4.2. *Preparation of Hematite Inverse Opals:*

Photonic crystals were placed on a flat tile, 60 µl of 0.025 M solution of iron (III) nitrate solution in ethanol were dropped on 3 cm^2 sample. This solution was prepared by dissolving 0.101 g of iron (III) nitrate in 10 ml of ethanol. The area of the photonic crystal was defined by the use of a scotch tape, to ensure that the solution was actually being adsorbed on the sample and not running off the sample. The samples were air dried for 15 min, then dried in the oven at 70 ^{o}C for 10 min. The deposited $Fe(NO_3)_3$ were thus hydrolyzed to $Fe_2O_3.xH_2O$.[89] This process was repeated 6-7 times. The samples were then calcined to burn the polystyrene spheres. Calcination was performed at 550 ^{o}C using a programmable furnace oven (Barnstead thermolyne, 48000); temperature was raised from room temperature to 550 ^{o}C at a ramp of 1°C/min, dwelled for 2 hours at 550 ^{o}C and then ramped down to room temperature at a rate of 10°C/min. This resulted in hematite inverse opals with thicknesses ranging between 2-4 µm as measured by Ambios X2 Profilometer. Films were characterized using UV-vis Spectrophotmeter (JASCO, V-570 UV/VIS/NIR), SEM, TESCAN MIRA 3 and XRD (BRUKER D8 Discover X-ray diffractometer oopertating at 4 kV/40 mA using Cu-KR radiation with a scanning speed of 0.5 ^{o}C /min).

20 μl/cm^2 Fe(NO$_3$)$_3$ in EtOH

Air dry for 10 min

5-7 cycles

Anneal at 800 ^{o}C for 20 min

Anneal at 550 ^{o}C for 2 hrs

Dry in oven for 10 min at 70 ^{o}C
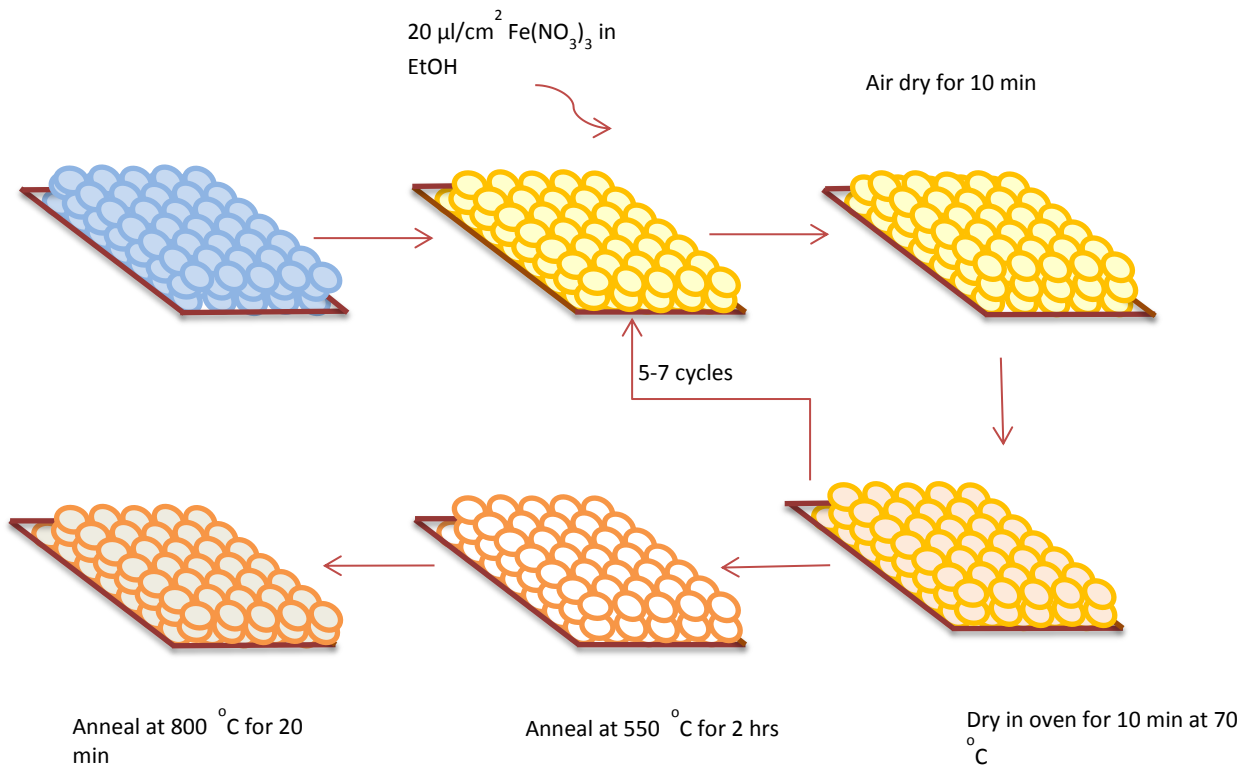
Figure 2.3: Scheme showing the preparation of hematite inverse opals from synthetic opals.

2.4.3. *Prepation of NaOH and KBi electrolytes:*

1 M NaOH and 1 M KBi were used as electrolytes for cyclic voltammetry, and chronoamperometry while 0.1 M KBi was used for photodepositions and electrodepositions. 1 M NaOH was prepared by dissolving 40 g of NaOH in 1 L deionized water. The pH of the solution was 13.6. 1 M KBi was prepared by dissolving 61.83 g of boric acid in 1 L of deionized water on a magnetic stirrer and adding around 50 g KOH gradually to reach a pH of 9.1-9.2. 6.18 g of boric acid and around 5 g of potassium hydroxide were dissolved in 1 L deionized water to obtain 0.1 M KBi solute on with a pH of 9.1-9.2.

2.4.4. *Preparation of Ni-borate and NiFe-borate Oxygen Evolving Catalyst on FTO by Electrodeposition and on Hematite by Photodeposition:*

2.3.4.1.   Preparation of Ni-borate and NiFe-borate solutions:

Electrodeposition and photodeposition of Ni-Bi and NiFe-Bi were carried in 0.1 M KBi solution (pH~9.2). 0.4 M $Ni(NO_3)_3$ and 0.4 M $Fe(NO_3)_3$ solution were prepared by dissolving 2.33 g of $Ni(NO_3)_3.9H_2O$ and 3.23 g $Fe(NO_3)_3.5H_2O$, respectively, in 20 ml of deionized water. 0.4 M $Ni_{90}Fe_{10}(NO_3)_3$ was prepared by mixing 2.09 g $Ni(NO_3)_3.9H_2O$ and 0.32 g $Fe(NO_3)_3.5H_2O$ in 20 ml of deionized water. For $Ni_{60}Fe_{40}(NO_3)_3$, 1.40 g $Ni(NO_3)_3.9H_2O$ was mixed with 1.30 g $Fe(NO_3)_3.5H_2O$ in 20 ml of deionized water while $Ni_{40}Fe_{60}(NO_3)_3$ was prepared by mixing 0.93 g $Ni(NO_3)_3.9H_2O$ and 1.04g $Fe(NO_3)_3.5H_2O$. 0.4 mM $Ni(NO_3)_3$ and 0.4 mM $NiFe(NO_3)_3$ solutions were prepared by diluting their respective solutions 1000 times with KBi. This was done by adding 20 µl of each of the 0.4 M solutions to 20 ml of 0.1 M KBi. These solutions were prepared directly before the electrodeposition.

2.3.4.2.   Electrodeposition of NiBi and $Ni_{1-x}Fe_xBi$ on FTO:

FTO substrates were cleaned as explained in section 2.2. Electrodeposition was performed in a electrochemical cell containing 0.4 mM solution of $Ni(NO_3)_3$/0.1 M KBi or $NiFe(NO_3)_3$/0.1 M KBi. It was carried out using amperometry (i-t) using a 3-electrode configuration with Ag/AgCl (in saturated KCl) as a reference electrode and 2 mm diameter Pt wire as the counter electrode at a potential of 0.953 V vs. Ag/AgCl. The amount of Ni and NiFe deposited was controlled by halting the experiment when the charge reaches 1 mC/cm^2. Alternatively, Ni and NiFe can be deposited by cyclic voltammetry. The potential was scanned between -0.6 V and 1.4 V vs Ag/AgCl at a scan rate of 100 mV/sec. The deposition by 5 CVs is equivalent to the deposition of 1mC/cm^2 as determined from integrating the Ni cathodic wave (at ~0.85 V vs Ag/AgCl). Films were anodized in 1 M KBi by holding the potential at 0.903 V for 2-3 hours with stirring.

2.3.4.3.   Photodeposition of NiBi and NiFeBi on Hematite Inverse Opals:

Photodeposition was carried out by dipping i-Fe_2O_3-o sample in a quartz cell containing 20 ml of 0.4 mM Ni-Bi or NiFe-Bi and exposing it to light of intensity equals to 100 mW/cm^2. The light source was a 300 W xenon lamp (Model 66901 lamp housing, Oriel instruments) without filter. Each photodeposition was carried for 10 minutes, and was repeated twice.

2.4.5. *Photoelectrochemistry on i-Fe$_2$O$_3$-o:*

2.4.5.1. Cyclic Voltammetry Measurements:

Photoelectrochemical measurements were collected in 3-electrode quartz cell using a CHI Model 630A electrochemical workstation. Photocurrents were measured using cylic voltammetry in a 3-electrode configuration with i-Fe_2O_3-o or FTO as working electodes, Ag/AgCl (saturated KCl) as a reference electrode and 2 mm diameter Pt wire as a counter electrode. CV's acquired in two electrolytes: in 1 M NaOH (pH 13.6), and 1 M KBi (pH 9.2). The potential was scanned between -0.6 V and 1.5 V vs. Ag/AgCl under light and dark conditions at 5 different scan rates: 10, 20, 50, 100, 200 mV/sec. The cell was subjected to white light from an Xe lamp with a power of 25, 50, 100, and 200 mW/cm^2 measured using a thermopile light detector and power meter (Model 70260, Oriel Instruments) in front-mode and back-mode illumination. In the front-mode, light is absorbed by the hematite film first then the FTO substrate, while in the back-mode light reaches the hematite from the FTO back contact. Cyclic voltamograms were collected before and after NiBi and NiFeBi photodeposition at scan rates of 10, 20, 50, 100, and 200 mV/sec in front-mode and back-mode illumination as well as in the dark.

2.3.5.2 <u>Amperometric Measurements:</u>

 I-t curves for the hematite samples were collected under chopped light illumination in both electrolyte solutions using the same 3-electrode setup. I-t curves were collected for 60 sec at different potentials ranging from the potential yielding the saturation photocurrent to the onset potential. The potentials in KBi ranged from 1.2 mV to -0.2 mV while in NaOH from 0.8 mV to -0.4 mV vs. Ag/AgCl.

2.3.5.3 <u>Incident Photon to Current Conversion Efficiency (% IPCE):</u>

 The photocurrents were measured in a 3-electrode configuration electrochemical cell at 0.6 V (vs Ag/AgCl) at i-Fe_2O_3-o (417), i-Fe_2O_3-o (190), and unstructured films using amperometric i-t technique between 380 nm and 600 nm. Photocurrent densities were calculated by dividing the photocurrent by the active geometric area of the sample after dark current subtraction. The lamp power spectrum and light intensity were measured using a thermopile light detector and power meter (Model 70260, Oriel Instruments) with 10 sec average light measurement.

2.3.5.4 <u>Tafel plots:</u>

 Current-Potential data were obtained by carrying controlled potential electrolysis in a solution of 1 M KBi electrolyte at pH 9.2. Prior to data collection, the open circuit potential and the resistance of the solution were measured using iR test function to correct for ohmic potential losses. Steady-state currents were measured at different applied potentials using amperometry (i-t curves) while the solution was stirred (at 600 rpm). Films required 400 to 600 sec to reach steady state. Currents were collected at potentials ranging between 1.12 V to 0.84 V vs Ag/AgCl (in sat. KCl) at 20 mV increments in descending fashion.

CHAPTER 3

EXPLORATION OF THE PHOTOELECTROCHEMICAL EFFECTS OF ORDER AND DISORDER IN DYE-SENSITIZED SOLAR CELLS

Dye-sensitized solar cells (DSSCs) are a promising alternative to conventional photovoltaic devices based on amorphous silicon p-n junctions.[90,91] DSSCs, based on highly porous nanocrystalline films of titanium dioxide, are of considerable technological interest because of their appreciable power conversion efficiency (7-13% at AM 1.5), potential low cost, and high semiconductor stability.[42] Notably, DSSCs performance is insensitive to temperature change. Raising the temperature from 20 to 60°C has practically no effect on the power conversion efficiency,[92] whereas conventional silicon cells exhibit a drastic decrease in the performance reaching ca. 20% within the same temperature range.[91] In addition, DSSCs exhibit lower sensitivity to light incident angle and shorter energy payback time.[91]

DSSCs, however, exhibit lower energy conversion efficiencies than single-crystal photovoltaic devices. One of the major challenges facing the progress in this technology is the poor light absorption of the best dyes in the longer wavelength region. Yet, more than 60% of the AM 1.5 solar power intensity corresponds to wavelengths beyond 600 nm.[4] The efficiencies of DSSCs will be significantly enhanced if the absorbance of the dyes is increased in the lower energy region without affecting the charge carrier transfer dynamics. Multiple attempts to increase the light absorption in this region focused mainly on synthesizing photosensitizers that show enhanced absorption in the red region of the visible spectrum (beyond 600 nm) and have high extinction coefficient.[4, 37] Lowering the HOMO-LUMO gap of the dye to shift its absorption to the red results in lowering the excited state free energy and thus lower rate for charge

33

injection.[37] N719 dye (di-tetrabutylammonium cis-bis(isothiocyanato)bis(2,2′-bipyridyl-4,4′-dicarboxylato)ruthenium(II)) remains the most suitable dye up to date; other dyes either suffered from low efficiency, weak anchoring ability, or poor stability.[93,94,95,40] Another approach to alter the absorption of dyes than chemical modification is the enhancement of light-dye interaction by modifying the optics in the dye medium. A prolonged light-matter contact can substantially increase the absorption events causing more excitation processes.

Tuning the propagation of light in nanostructured materials is possible via several mechanisms that greatly depend on the engineering of these structures in size, refractive indices, material composition, order, crystallinity, porosity and shape. One of the approaches is to use scattering nanolayers. An example is the addition of 300-nm titania spheres layers on top of nanocrystalline TiO_2,[96] or designing the TiO_2 layer in a certain architecture. TiO_2 inverse opals of different diameter cavities can be constructed by using polycrystalline or single crystalline polystyrene templates, infiltrating the voids with titania before calcination of the organic spheres.[23] Inverse opals are optically desired to attune the propagation of light because of their stop-bands, when light depending on its specific wavelength can be slowed or reflected.[19] Stop-bands arise as a result of refractive index modulation in the inverse opal chemical and void composition.[19,97] Their positions in the light spectrum are then dependent on the size of the cavities, the material filling the voids and the walls, as well as the percentage of each.[9,23,45] In 2003, Mallouk et al. successfully demonstrated the incorporation of inverse opals in DSSCs and showed that coupling the nc-TiO_2 photoelectrode to titania inverse opal enhances the photogenerated current.[23] They studied the effect of "heavy photons" on dye absorption and light to photocurrent conversion near the band edges of the stop band. The authors reported a pronounced red enhancement in the Ru- N719 dye absorbance relative to the conventional

photoelectrode. In the region between 540 nm and 750 nm, the short circuit photocurrent efficiency was increased by 30%, relative to an ordinary dye-sensitized nc-TiO$_2$ photoelectrode when an inverse opal with stop band positioned at 610 nm was coupled to a film of TiO$_2$ nanoparticles.[23] The mechanism of enhancement in the light harvesting efficiency was investigated by Halaoui et al by comparing the photoresponse of inverse opals with varying stop band positions to nc-TiO$_2$ and to the bilayer electrode (nc-TiO$_2$/486-i-TiO$_2$-o).[45] In the region extending from 580 nm to 800 nm, a substantial gain of 29% was observed for the nc-TiO$_2$/486-i-TiO$_2$-o bilayer. When the stop band position was shifted to 582 nm, the authors reported 38% gain.[45] The enhancement in the bilayer architecture was attributed to the enhanced beam intensity of light at the nc-TiO$_2$ layer in proximity to the PC layer where light scattering in disordered regions and Bragg reflection within stop band frequencies take place.[45,47,98] The authors reported higher % IPCE at the bilayer electrode (27 %) than the combined % IPCE of inverse opal (4 %) and nc-TiO$_2$ (7 %) suggesting a synergistic effect of 16 % at 680 nm. Mihi and Miguez used scalar wave approximation to study the optical response in inverse opal based DSSCs which showed that the enhancement is due to the presence of resonant modes at the interface between nc-TiO$_2$and the inverse opal film.[47,99,98] The effect of the inherent disorder in the PC layer on light enhancement was further studied by assembling a disordered PC film from a template of different polystyrene sizes (150 nm and 243 nm).[45] An enhancement factor of 1.5 was reported for the disordered film compared to the nc-TiO$_2$ with the same surface area. The enhancement was attributed to multiple internal scattering in the disordered film.[45]

Recently, Lopez et al were successful in inducing disorder to photonic crystals assembled from monodispersed polystyrene spheres by changing the ionic strength of the PS colloids assembly medium.[34,35,31] These newly disordered assemblies were termed photonic glass.

Monodispersity in disordered structures can ideally exhibit interesting phenomena such as coherent backscattering enhancement, Anderson localization, and random lasing which potentially makes use of photonic glass in various fields.[31,35] The ability of photonic glass to sustain resonance modes when their sphere size is comparable to the wavelength of light is a key feature in these structures.[34,35]

In this study, we aimed at 1) fabricating and characterizing inverse photonic glass (i-TiO_2-g) structure by infiltrating a polystyrene photonic glass with TiO_2 and burning out the polystyrene template, in a similar procedure to the preparation of inverse opals, 2) investigating the light conversion efficiency in i-TiO_2-g as well as in the bilayer inverse photonic glass (nc-TiO_2/i-TiO_2-g) architectures and systematically comparing it to that of inverse opals and bilayer inverse opal films to investigate the effects of order vs. disorder using the same polystyrene sphere size and by sensitizing by the same dye, 3) showing a preliminary study on inverse opals based DSSCs sensitized with T118 dye with absorption extending to the red of the solar spectrum to investigate enhancement in the long wavelength region of the visible spectrum. T118 dye was synthesized by Professor Tarek Ghaddar, and it shows an absorption shoulder at 710 nm in addition to the absorption peaks at 520 nm and 470 nm.

3.1 Characterization of the films using SEM and UV-Vis Spectroscopy:

The polystyrene opals used in this study were assembled from polystyrene colloidal solution with 305 nm sphere diameter (termed PC_{305}). Adding 4 mg NaCl salt (1mM ionic strength) to the colloidal solution resulted in monodispersed disordered photonic crystals (PG_{305}). Figure 3.1 shows the UV-Vis absorption spectra for PC_{305} (Fig 3.1 a) and PG_{305} (Fig 3.1 b)

acquired in air. PC$_{305}$ exhibits a stop band peak at 660 nm. Bragg equation relates the position of the stop band peak to the size of the polystyrene spheres based on face cubic centered (fcc) structure with 74 % polystyrene and 26 % air voids according to the following relation:

$$\lambda = 2 \times D \sqrt{(0.74n_s^2) + (0.26n_v^2)} \qquad (1)$$

where n$_s$ is the refractive index of the PS spheres (1.5), n$_v$ is the refractive index of the material filling the voids (air in this case, n=1), and D is 0.87 times the diameter of PS spheres. Using this relation, one finds a diameter equal to 273 nm indicating 10 % shrinkage for the PS$_{305}$ which is due to solvent evaporation. The presence of disorder in PG$_{305}$ is evidenced by the disappearance of the stop band peak at 660 nm.
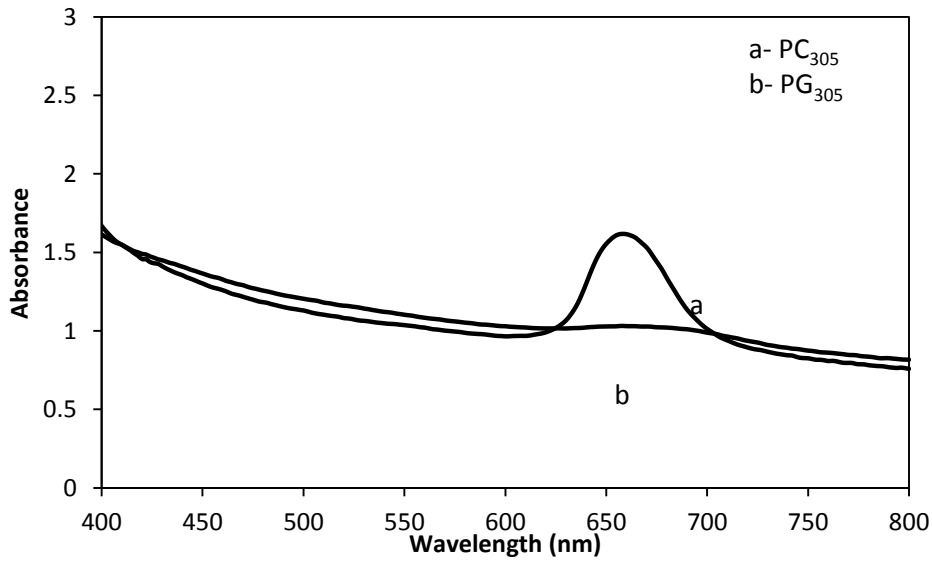
Figure 3.1: UV-Vis absorption spectra of photonic crystal PC$_{305}$ (a) and photonic glass PG$_{305}$ (b). The stop band peak of PC$_{305}$ is positioned at 660 nm, while PG$_{305}$ does not show any peak.

SEM images of the assembled crystals are shown in Fig 3.2. The SEM image for PC$_{305}$ shows that the latex particles are arranged in fcc lattice and exhibit a narrow size distribution of monodispersed spheres that are 275 ± 10 nm in diameter. This corresponds to a 9.8 % shrinkage which matches well with the calculated shrinkage based on the stop band peak.
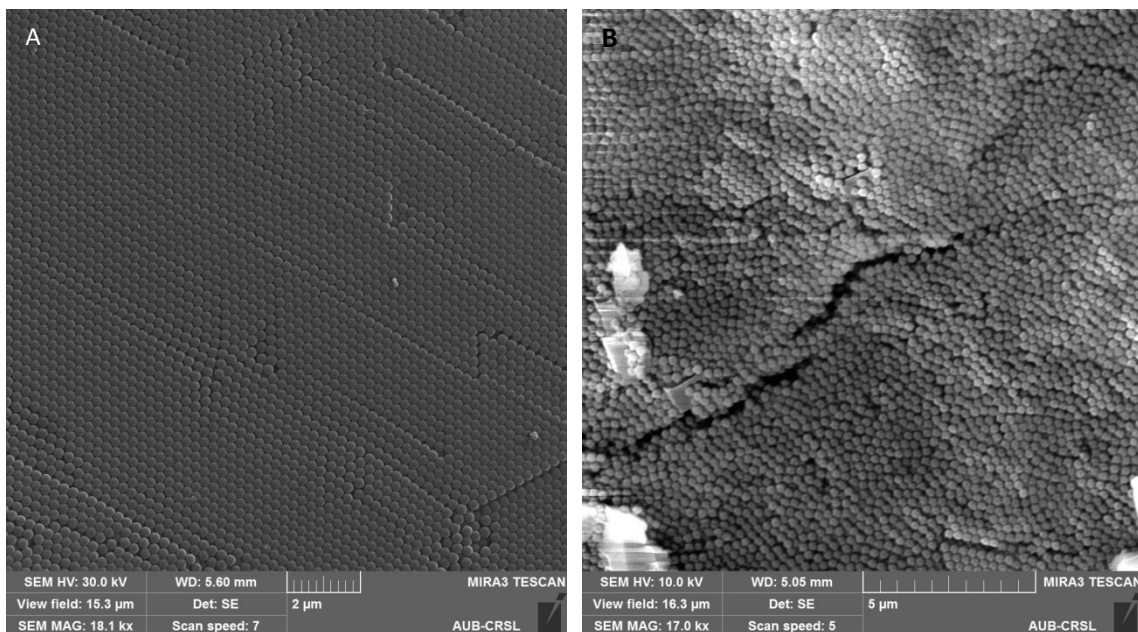
Figure 3.2: SEM images of photonic crystal PC$_{305}$ (A) and photonic glass PG$_{305}$ (B).

PC$_{305}$ and PG$_{305}$ were replicated with TiO$_2$ via liquid phase deposition and calcined at 400 $^{\circ}$C to result in the inverse opal (i-TiO$_2$-o) and inverse glass (i-TiO$_2$-g) structures. Figure 3.3 shows UV-Vis absorption spectra of obtained i-TiO$_2$-o and i-TiO$_2$-g acquired in ethanol (n=1.36) which has a similar refractive index to the iodide/triodide electrolyte (n=1.34) used in photoelectrochemical studies. i-TiO$_2$-o exhibits a stop band peak at 600 nm while i-TiO$_2$-g doesn't show any peak, yet they exhibit high background extinction that is indicative of scattering. i-TiO$_2$-o is now assumed to have 74 % air voids and 26 % TiO$_2$. When the air voids are filled with ethanol, the 600 nm stop band corresponds to a diameter equals to 199 nm

indicating 35 % shrinkage based on Bragg's equation. Fig 3.4 shows SEM images of i-TiO$_2$-o and i-TiO$_2$-g. Unlike the skeletal hexagonal closely packed order inherited from the ordered photonic spheres revealed in the i-TiO$_2$-o, the i-TiO$_2$-g shows random nanostructured TiO$_2$ walls that don't reveal any patterned arrays except small areas of ordered side-by-side TiO$_2$ walls. The calculated % shrinkage in the pore size was confirmed by SEM as it shows 195 ± 12 nm pore diameter corresponding to 36 % shrinkage. The observed shrinkage is due to infiltration and calcination steps.
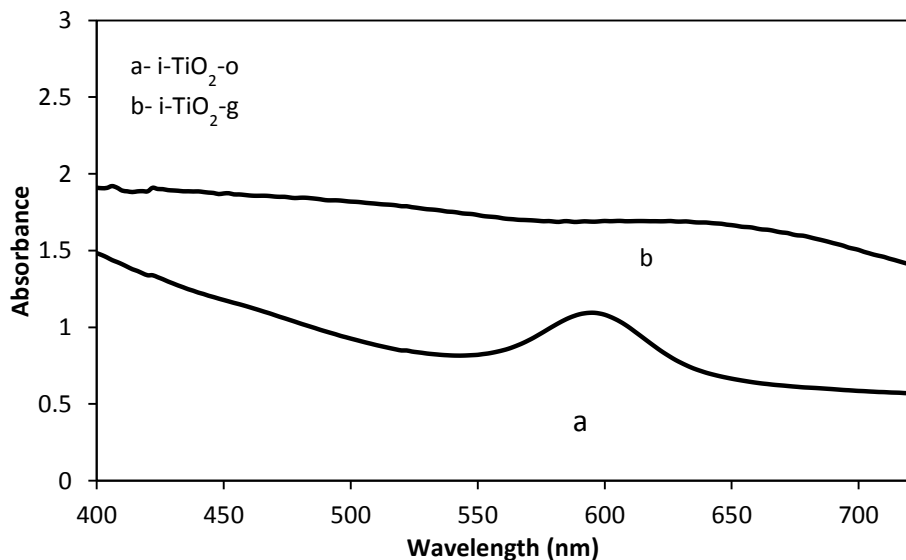
Figure 3.3: UV-vis absorption spectra of i-TiO$_2$-o showing the stop band maximum at 600 nm. i-TiO$_2$-g does not show any peak, yet it shows higher absorbance as compared to i-TiO$_2$-o. Plots were acquired in ethanol to provide a refractive index similar to the electrolyte used in the photoelectrochemical cell.
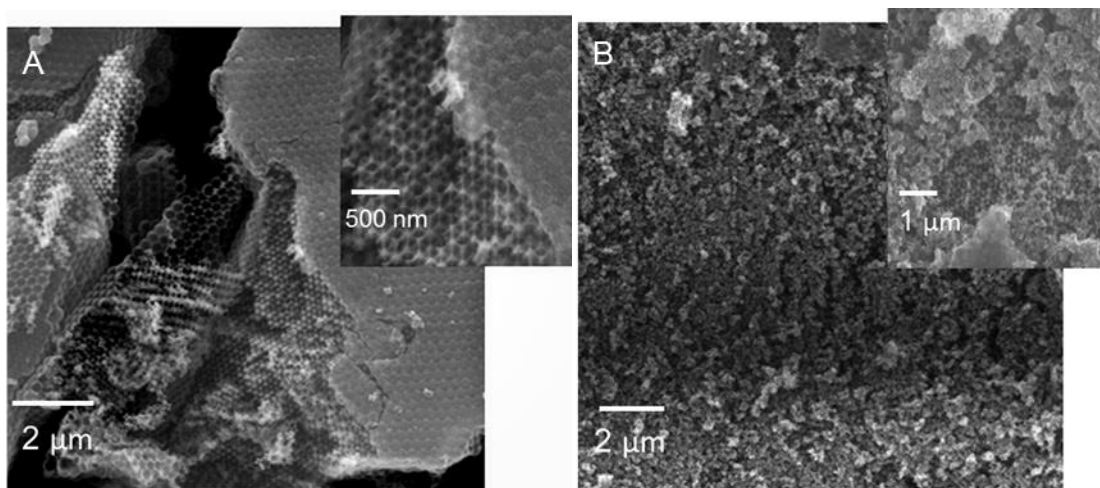
Figure 3.4: SEM images for (A) i-TiO$_2$-o and (B) i-TiO$_2$-g.

Figure 3.5 shows the UV-Vis spectra for 0.3 mM N719 Ru-dye solution in ethanol (Fig 3.5 A) and nc-TiO$_2$ before and after sensitization with the Ru-dye (Fig 3.5 B). The dye shows two absorption maxima at 375 nm and 530 nm in ethanol and on nc-TiO$_2$. The two absorption peaks correspond to the metal-to-ligand charge transfer (MLCT) transitions (4d – π*).[100] The dye easily loads the nc-TiO$_2$ films aided by the low surface tension of ethanol that allows for an almost complete percolation of the mesoporous film. Nanocrystalline anatase TiO$_2$ with a band gap 3.2 eV exhibits an absorption edge at 388 nm and significant absorbance below 360 nm. Usami predicted, based on Monte Carlo simulations for Maxwell equations, that about 99% of the incident light penetrates a TiO$_2$ film made up of 30-nm particles without scattering thus making nc-TiO$_2$ optically transparent.[101]
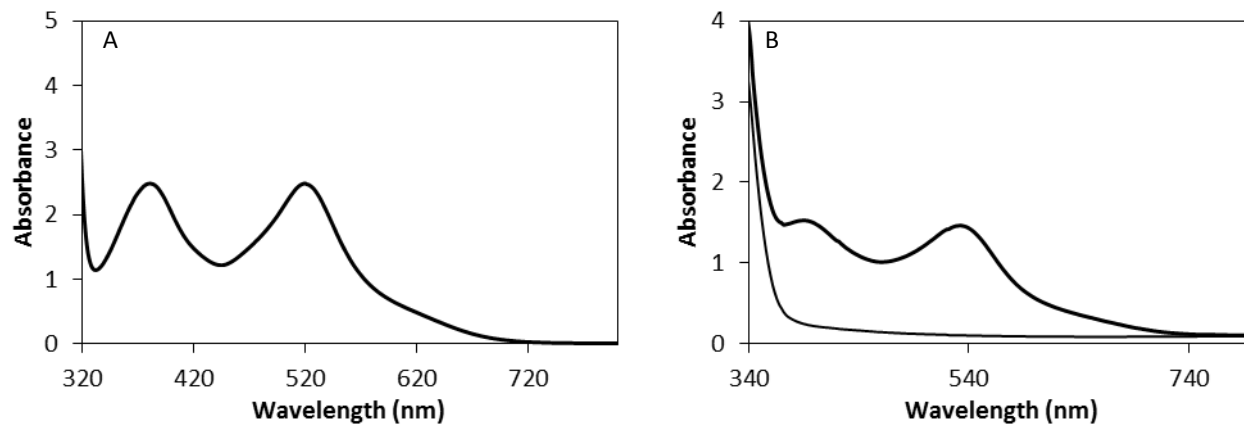
Figure 3.5: UV-Vis absorption spectra of 0.3 Mm Ru-N719 dye solution (A). It has two absorption maxima at 375 nm and 530 nm. Panel B shows the absorption spectra of nc-TiO$_2$ film before (thin line) and after sensitization (thick line).

Figure 3.6 shows the UV-Vis absorption spectrum of i-TiO$_2$-o before and after sensitization with N719 dye (Fig 3.6 A), the difference in absorbance between post-sensitization and pre-sensitization (Fig 3.6 B), the normalized absorbance difference (Fig 3.6 C) and the absorbance enhancement factor (EF) (Fig 3.6 D). The normalized absorbance was calculated by dividing the difference in absorbance by the amount adsorbed on each sample determined spectrophotometrically after desorbing the dye in NaOH. The absorbance enhancement factor was computed by dividing the normalized absorbance of i-TiO$_2$-o by the normalized absorbance of nc-TiO$_2$. The UV-Vis spectrum of N719/i-TiO$_2$-o exhibits a substantial enhancement in absorbance to the red of the stop band ($\sim$ 3 fold at 620 nm) (Fig 3.6 D).
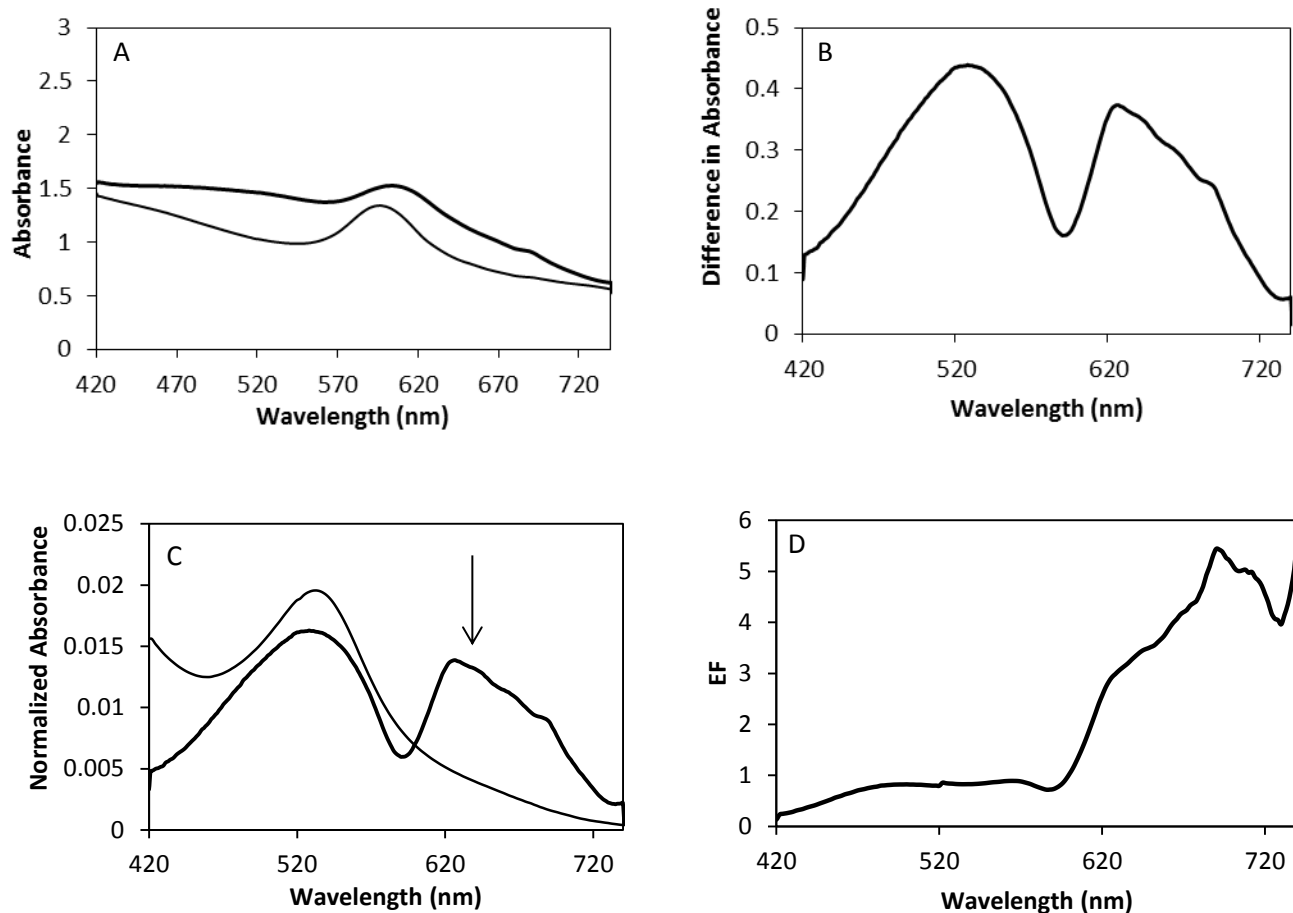
Figure 3.6: UV-Vis spectra showing A) inverse opal film before and after sensitization with 27 nmol/cm² N719 dye, B) difference in absorbance, C) normalized absorbance of inv-PC (thick line) and nc-TiO$_2$ (thin line). Higher normalized absorbance is observed to the red of the stop band. Panel D shows the calculated enhancement factor. EF values exceeding 1 are observed beyond 600 nm.

In the EF plots, values above unity signify enhanced absorbance in the i-TiO$_2$-o film compared to the nc-TiO$_2$ films. Beyond 600 nm, an EF of more than one is observed. This is attributed to the heavy photons at the red edge of the stop band which results in longer light-matter interaction as previously observed.[23] Figure 3.7 shows the UV-Vis absorption spectrum for a monodispersed disordered film before and after sensitization, difference in absorbance, normalized absorbance

and absorbance enhancement factor. i-TiO$_2$-g exhibits an enhanced absorbance in the low energy

region (i.e. beyond 600 nm) which is attributed to scattering. The films are highly scattering in

this spectral region as revealed by the absorption spectra of unsensitized films. However, the

absorbance enhancement alone does not necessarily lead to enhanced % IPCE as other factors

may interfere as will be discussed in the photoelectrochemical measurements section.
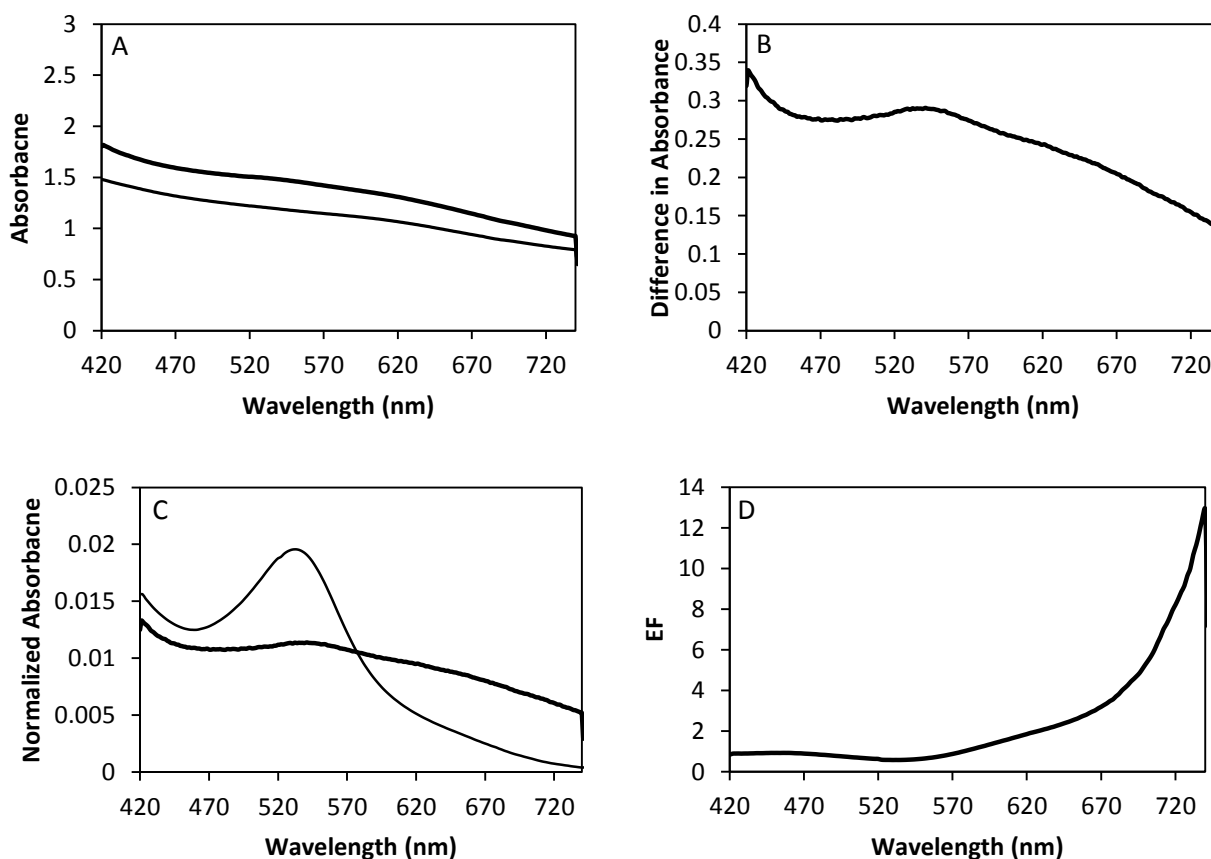
Figure 3.7: UV-Vis spectra showing A) i-TiO$_2$-g before and after sensitization with 26 nmol/cm^2 N719 dye, B) difference in absorbance, C) normalized absorbance of i-TiO$_2$-g (thick line) and nc-TiO$_2$ (thin line). Panel D shows the calculated enhancement factor. Values exceeding 1 are observed in the low energy region.

A bilayer electrode refers to an inverse opal film coupled to nc-TiO$_2$ overlayer. Figure 3.8 shows

UV-Vis spectra of nc-TiO$_2$/i-TiO$_2$-o (Fig 3.8 A) and nc-TiO$_2$ i-TiO$_2$-g (Fig 3.8 B). Due to the

transparency of the nc-TiO$_2$, the UV-Vis spectra acquired for the bilayer architectures (nc-TiO$_2$/i-TiO$_2$-o and nc-TiO$_2$/i-TiO$_2$-g) look similar to those of i-TiO$_2$-o andi-TiO$_2$-g, respectively.
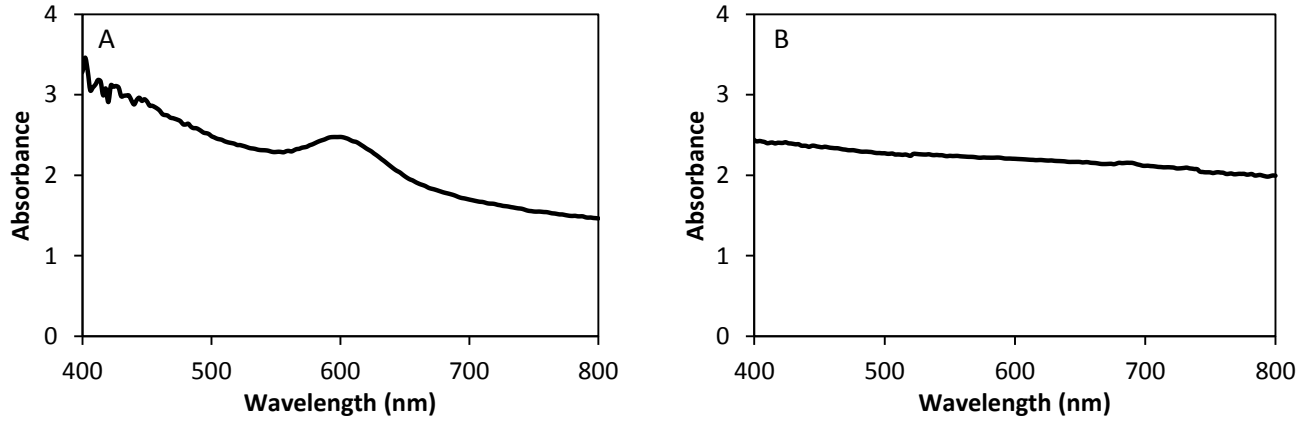
Figure 3.8: UV-Vis absorption spectra of A) nc-TiO$_2$/i-TiO$_2$-o and B) nc-TiO$_2$/i-TiO$_2$-g acquired in ethanol (n=1.36).

Figure 3.9 shows SEM images of the bilayer structures. The images clearly show the nanocrystalline layer and the underlying inverse opal/inverse glass. Due to their small size (~10 nm), nc-TiO$_2$ particles cannot be discerned under this SEM resolution. The film homogenous thickness and even elevation can be also noted in these images, which minimize scattering losses that might happen at rougher surface. A similar elevation of the nc-TiO$_2$ layer is noted on top of the i-TiO$_2$-g films. A scratch on the surface shows the underlying inverse opal architecture in both i-TiO$_2$-o and i-TiO$_2$-g.
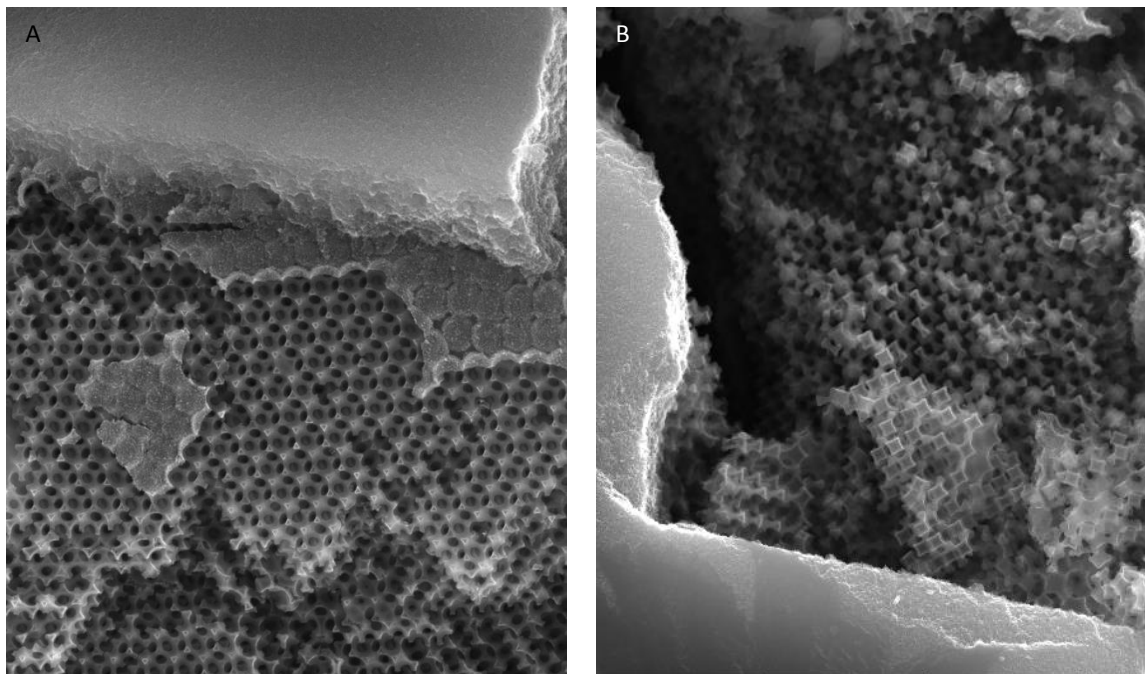
Figure 3.9: SEM images showing A) nc-TiO$_2$/i-TiO$_2$-o and B) nc-TiO$_2$/i-TiO$_2$-g.

3.2 Photoelectrochemical Studies:

3.2.1 Photoelectrochemical Measurements at Ru-N719/i-TiO$_2$-o, Ru-N719/i-TiO$_2$-g, Ru-N719/nc-TiO$_2$/i-TiO$_2$-o, Ru-N719/nc-TiO$_2$/i-TiO$_2$-g and Ru-N719/nc-TiO$_2$ photoelectrodes:

All electrochemical measurements were carried out in a 3-electrode configuration cell with home-made Ag/AgCl reference electrode, and a clean FTO as a counter electrode in iodide/triiodide electrolyte. The potential was scanned between -5 mV and +5 mV at a scan rate of 1 mV/s using linear sweep voltammetry. For % IPCE measurements, 3 scans were acquired at each wavelength, the photocurrent at 0 mV was averaged over the 3 scans after subtracting the dark current. The photocurrent density was computed by dividing the photocurrent by the active illuminated area of the photoelectrode. A thermopile light detector was used to measure the

power at each wavelength. The % IPCE was then plotted vs. wavelength according to the following formula:

$$\%IPCE(atV) = \frac{J_{@V}(A/cm^2)}{I_{@\lambda}(W/cm^2)} \times \frac{1240(eV.nm)}{\lambda(nm)} \times 100 \qquad (3.1)$$

Where J is the photocurrent density calculated by dividing the monochromatic photocurrent measured at a wavelength λ by the illuminated area of the sample at an applied potential V, and I is the light intensity at the wavelength λ.

Photocurrent measurements were carried with two illumination modes, front wall and back wall illumination. In the front wall illumination, the cell was illuminated from the counter electrode side (FTO); light passes through the FTO and electrolyte before reaching the photoanode. In the back wall illumination, the cell was illuminated from the photoanode side, thus light impinges on the working electrode before going through the electrolyte and counter electrode (Scheme 3.1). Back mode illumination is the commonly used illumination mode, however to be able to study light localization effects of the PC, front mode illumination was also studied.
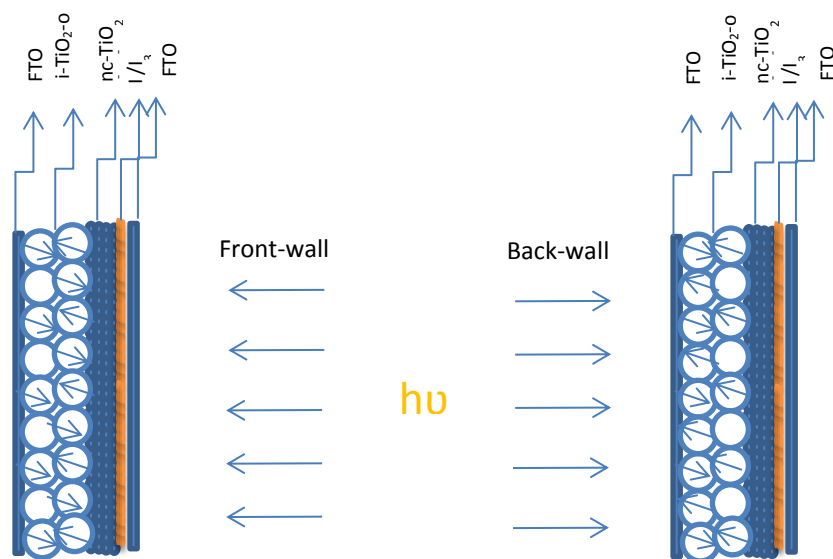
Scheme 3.1: Bilayer electrode under front wall and back wall illumination.

In the low absorbance region, absorbance is directly proportional to the amount of dye adsorbed and hence, power conversion efficiencies are also proportional to the amount of dye adsorbed on the film. % IPCE was normalized to the amount adsorbed to account for differences in surface area amongst the different studied films. The amount of dye adsorbed was determined using UV-Vis spectroscopy at the dye maximum absorbance (520 nm). The dye was desorbed from the titania films by immersing in 3 ml of 3.8 M NaOH solution for 3 min. A standard calibration curve was plotted by measuring the absorbance of standards of 0.00375 mM, 0.0075 mM, 0.015 mM, and 0.03mM in 3.8 M NaOH. Figure 3.10 shows a standard calibration curve obtained using the aforementioned standards. The amount of dye adsorbed on the samples was determined using the equation of the calibration curve.
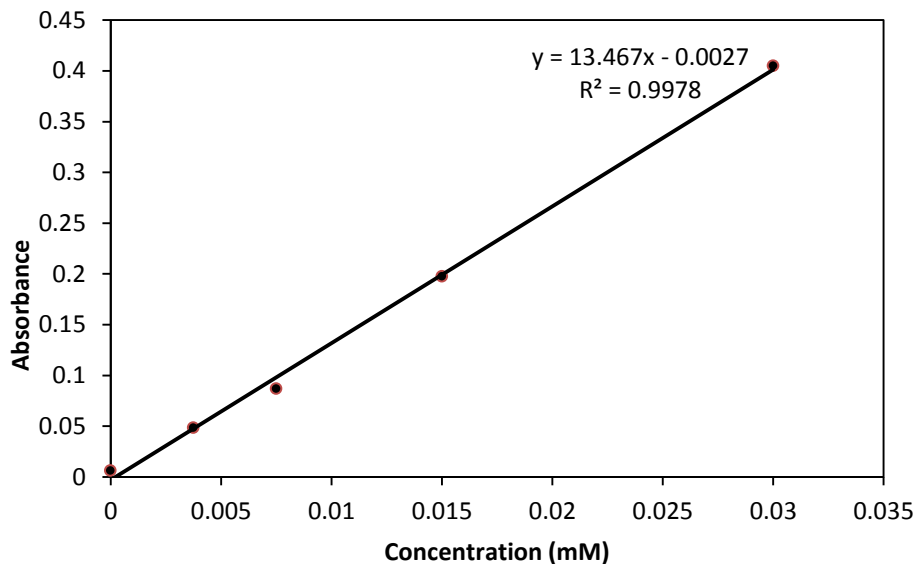
Figure 3.10: Dye calibration curve for the determination of the amount of Ru-N719 loading the titania films. Standards were prepared in 3.8 M NaOH and their visible absorbance was measured at 520 nm against a 3.8 M NaOH blank.

3.2.2 Investigation of the Energy Conversion at Ru-N719/i-TiO₂-o and Ru-N719/i-TiO₂ -g: order vs. disorder

Figure 3.11 represents a UV-Vis absorption spectrum that shows the relative position of the stop band with respect to the dye absorption peaks. The stop band peak of i-TiO$_2$-o (centered at 600 nm) lies to the red of the dye maximum absorption peak. The red edge of the stop band coincides with low absorbance of the dye. This is an essential requirement to investigate the effect of a stop band edge on an enhanced light-dye interaction since the absorbance is proportional to the dye amount only in the low energy region where the absorption is low. In other words, an inherent high absorption of the dye would override or mask any enhancement effect caused by slowing of light.
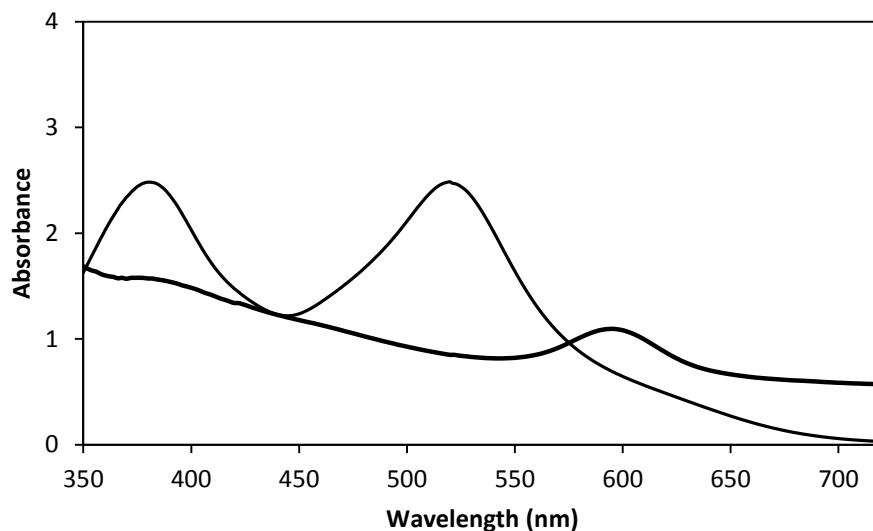
Figure 3.11: UV-vis spectra showing the relative position of the stop band with the dye absorption peaks.

Figure 3.12 A shows the plot of % IPCE vs. wavelength for nc-TiO$_2$ film under front wall and back wall illumination modes. The % IPCE of nc-TiO$_2$ under front wall illumination is suppressed below 520 nm. The UV absorption spectrum of I^-/I_3^- is shown in Figure 3.12 B. I^-/I_3^- exhibits a strong absorbance below 520 nm, which causes the observed suppression in the % IPCE at the nc-TiO$_2$ film. However, front wall illumination is useful for investigating light trapping effects at the bilayer electrodes as will be discussed later.
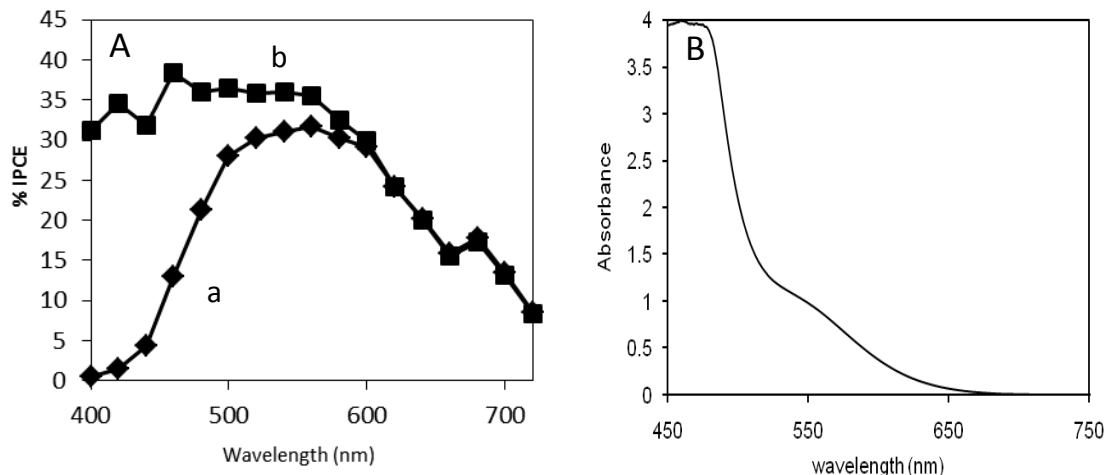
Figure 3.12: A) Plot of % IPCE vs wavelength at a nanocrystalline TiO_2 film with 134 nmol/cm^2 Ru dye in the front mode (a) and back mode (b) illumination I^-/I_3^- starts to absorb significantly below 520 nm and that was reflected in the decreased % IPCE in the front mode illumination. B) UV-Vis spectrum of iodide/triiodide electrolyte.

Table 3.1 shows the amount of dye adsorbed, thickness, % IPCE, and normalized % IPCE (in parentheses) upon front wall (in green) and back wall (in blue) illumination obtained at 4 i-TiO$_2$-o and 4 i-TiO$_2$-g. Figure 3.13 shows % IPCE (Fig 3.13- A) and normalized % IPCE (Fig 3.13- B) of the average of 4 i-TiO$_2$-o films and the average of 4 nc-TiO$_2$ films plotted against the wavelength. Since the amount of dye (determined spectrophotometrically) adsorbed on i-TiO$_2$-o (~26 nmol/cm^2) is much less that the amount adsorbed on nc-TiO$_2$ films (~ 120 nmol/cm^2), it can be inferred that the surface area of the inverse opal films is smaller than that of nc-TiO$_2$ films due to the relatively larger pore sizes and less TiO$_2$ material. As a result, the % IPCE values of Ru-N719/nc-TiO$_2$ are much higher than that of i-TiO$_2$-o and thus % IPCE cannot be compared to assess light localization effects. Instead, normalized % IPCE is used for comparing the photoelectrochemical behavior of the different films. Normalized % IPCE show similar values for nc-TiO$_2$ and i-TiO$_2$-o in the region of low dye absorbance. Panel C in Figure 3.13 represents the average enhancement factor (EF) of i-TiO$_2$-o. EF was calculated by dividing the normalized

% IPCE of each i-TiO$_2$-o film by the normalized % IPCE of each nc-TiO$_2$ film to result in 4

enhancement factors which were further averaged. The reported EF values at 660 nm and 680

nm are 1.1± 0.3 and 1.1 ± 0.4 respectively. This slight enhancement is attributed to localization

of heavy photons at the red edge of the stop band. Halaoui et al previously reported a similar

enhancement of 1.3 at 680 nm at 582-i-TiO$_2$-o film which was attributed to localization of heavy

photons possessing energies around 100 nm to the red of the 582 nm stop band and to multiple

internal scattering processes at disordered regions.[45] In the high absorbance region i.e. below 560

nm, the absorbance is not proportional to the amount of dye present due to the inner filter effect

which causes most of the incident light to be absorbed in top layers of the titania film. Therefore,

EF>1 at wavelengths shorter than 560 nm does not necessarily reveal enhancement in this

region. No enhancement was observed within the stop band frequencies (560 nm-640 nm) due to

Bragg reflection losses.
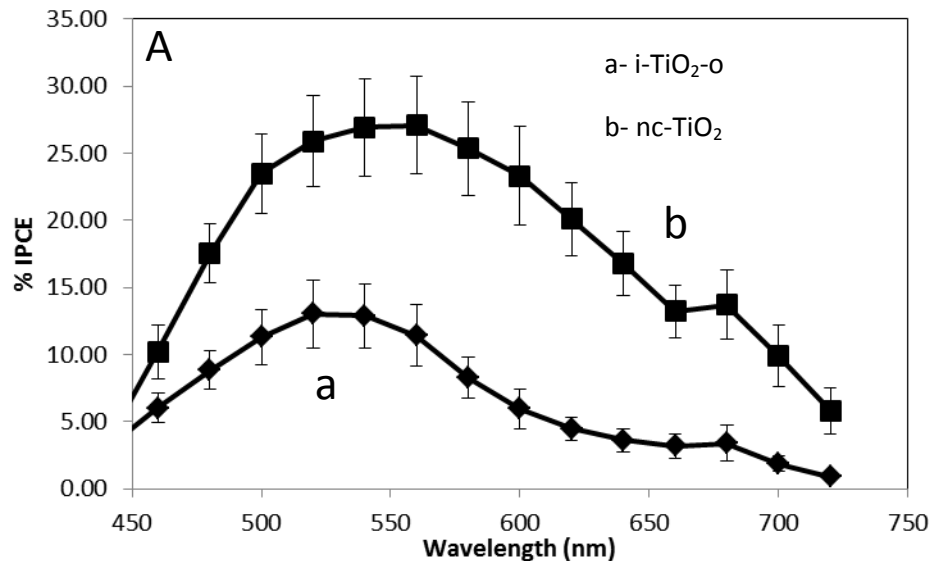
Figure 3.13: A) % IPCE and B) normalized % IPCE at a) 4 Ru-N719/i-TiO$_2$-o films and b) 4 nc-TiO$_2$ films upon front wall illumination. C) Enhancement factor calculated for the Ru-N719/ i-TiO$_2$-o films

Figure 3.14 shows % IPCE (fig 3.14 A) and normalized % IPCE (fig 3.14 B) of the average of 4 i-TiO$_2$-o films and the average of 4 nc-TiO$_2$ films in the back wall illumination. Similar photoelectrochemical behavior was observed in the back wall illumination. Slight enhancement

at the red edge of the stop band is observed due to the localization on heavy photons. An EF value of $1.2 \pm$ is observed at 660 nm.
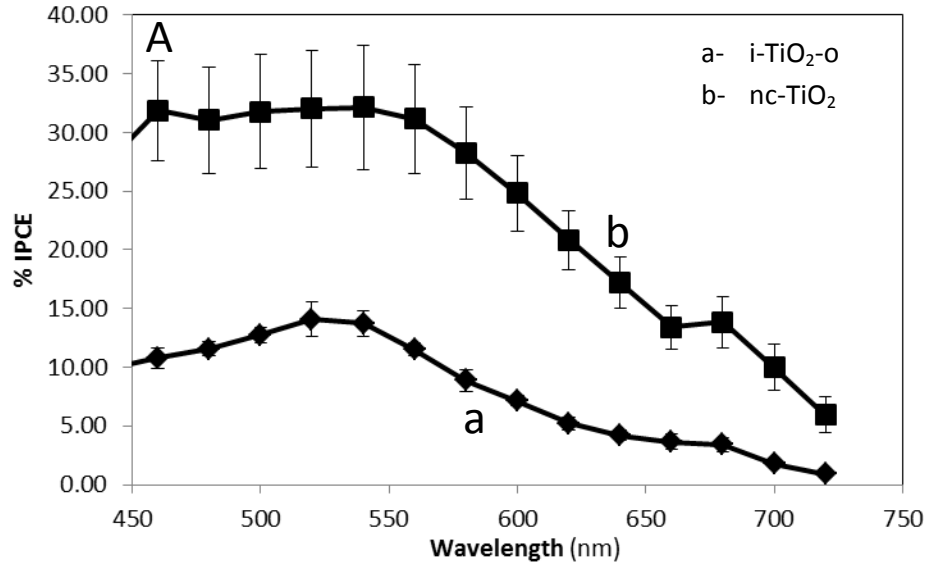
Figure 3.14: A) % IPCE and B) normalized % IPCE at a) 4 Ru-N719/i-TiO$_2$-o films and b) 4 nc-TiO$_2$ films upon back wall illumination. C) Enhancement factor calculated for the Ru-N719/ i-TiO$_2$-o films.

Table 3.1 shows the amount of dye adsorbed, thickness, % IPCE, and normalized % IPCE (in parentheses) upon front-mode (in green) and back-mode (in blue) illumination obtained at 4 i-TiO$_2$-g films. Figure 3.15 shows the plots of% IPCE, normalized % IPCE and enhancement factors obtained for the average i-TiO$_2$-g films. EF values of 2.01 ± 0.59 at 600 nm, 1.87 ± 0.58 at 620 nm, 1.86 ± 0.60 at 640 nm, 2.06 ± 0.67 at 660 nm, and 1.77 ± 0.66 at 680 nm were

measured. Multiple internal scattering at disordered regions increases the path length of light and

therefore increases the local transient time leading to a pronounced light-dye interaction.
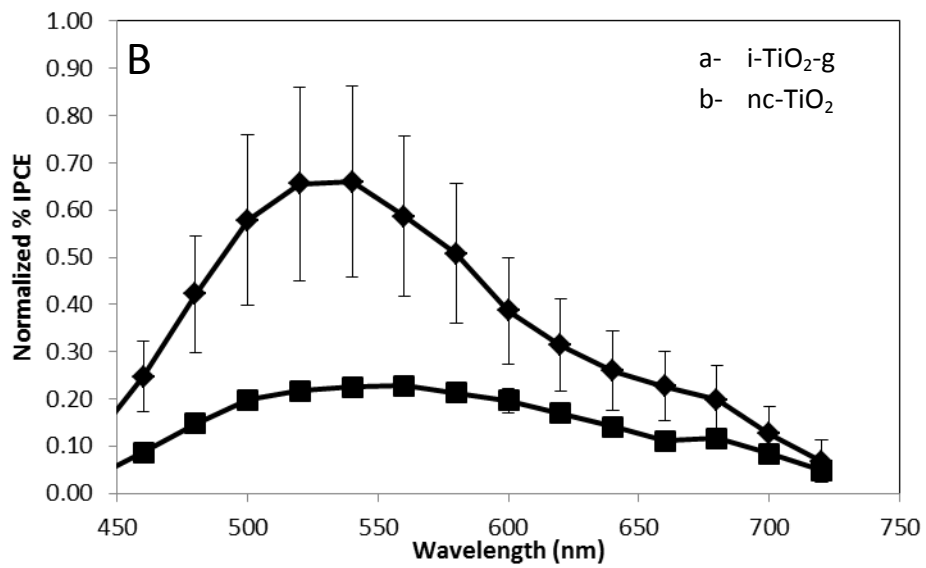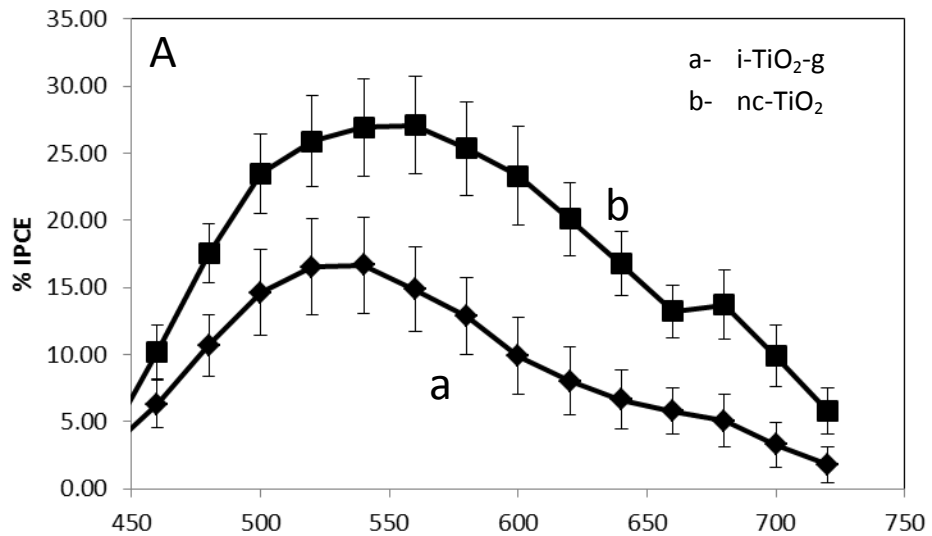
Figure 3.15: A) % IPCE and B) normalized % IPCE at a) 4 Ru-N719/i-TiO$_2$-g films and b) 4 nc-TiO$_2$ films upon front wall illumination. C) Enhancement factor calculated for Ru-N719/i-TiO$_2$-g films.

Similar EF values are observed in the back mode (1.91 $\pm$ 0.52 at 600 nm, 1.81 $\pm$ 0.49 at 620 nm, 1.84 $\pm$ 0.46 at 640 nm, 1.98 $\pm$ 0.47 at 660 nm, and 1.65 $\pm$ 0.51 at 680 nm). It is worth noting that i-TiO$_2$-g films, when not coupled to nc-TiO$_2$, behave similarly in the front wall and in the back wall illumination.
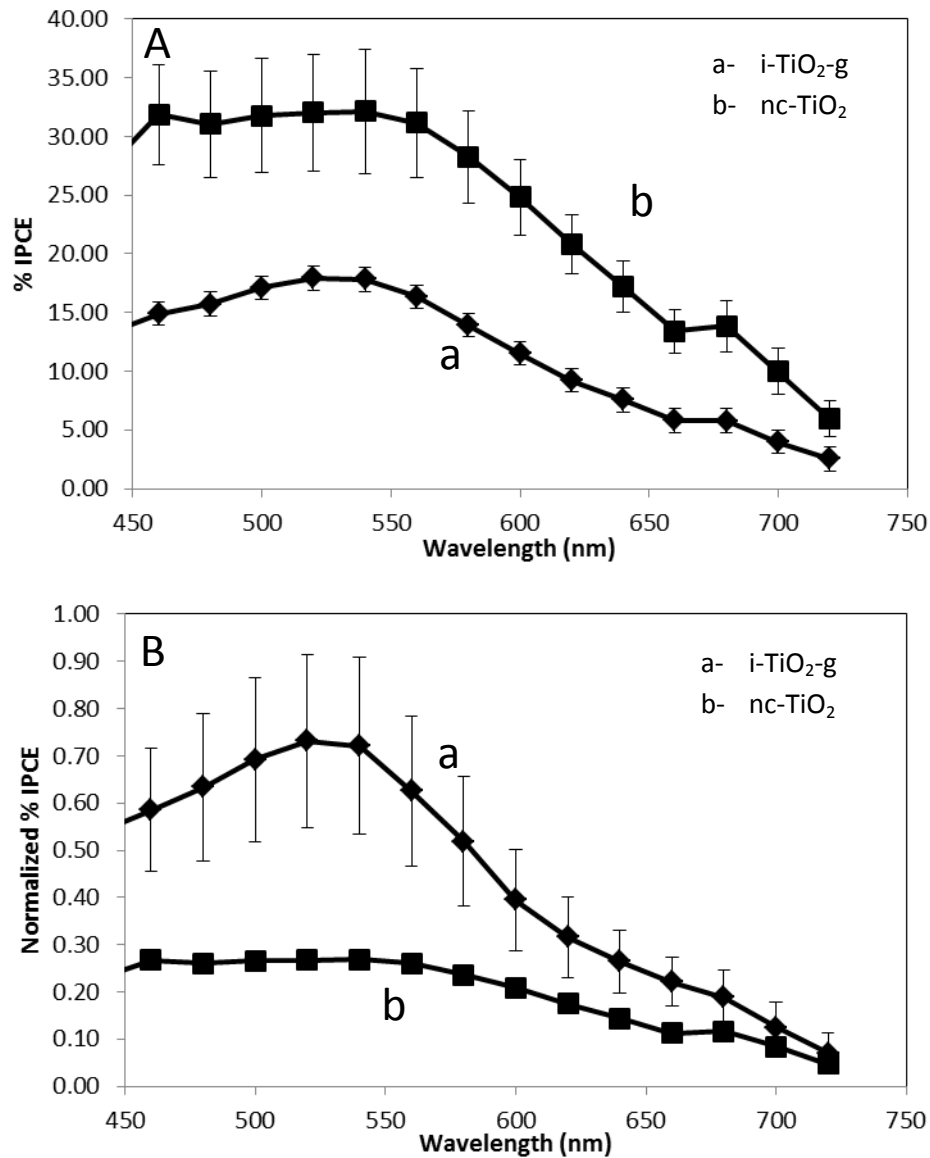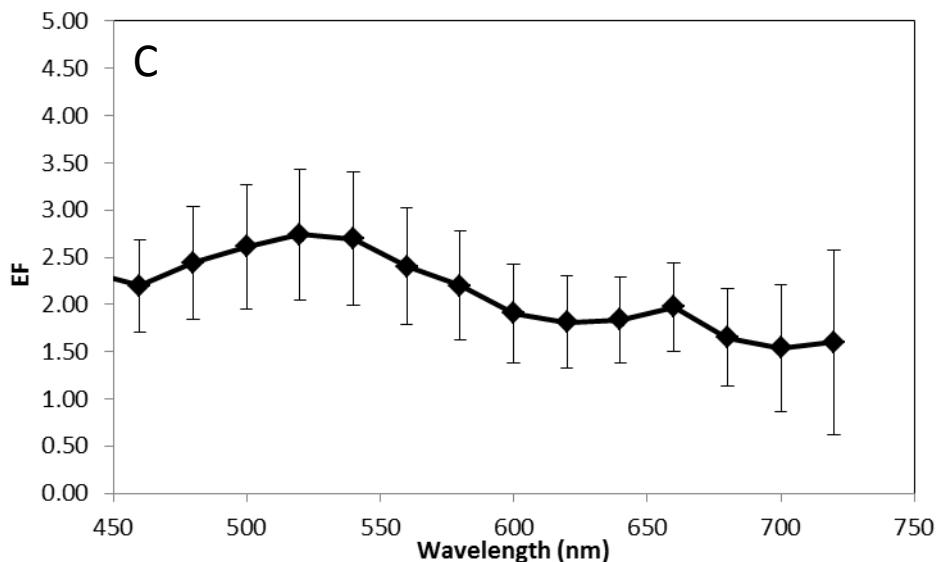
Figure 3.16: A) % IPCE and B) normalized % IPCE at a) 4 Ru-N719/i-TiO$_2$-g films and b) 4 nc-TiO$_2$ films upon back wall illumination. C) Enhancement factor calculated for the Ru/N719/i-TiO$_2$-g films.

Figure 3.17 shows the average enhancement factors of i-TiO$_2$-g and i-TiO$_2$-o in the front wall and back wall illumination. Inducing significant disorder in the photonic crystal architecture had led to substantial amplification in the whole visible region including within the stop band frequencies which is caused by multiple internal scattering events (although at short wavelengths, enhancements cannot be reliable). i-TiO$_2$-o on the other hand, shows only slight enhancement at the red-edge of the stop band that is the high refractive index medium comprising the Ru-adsorbed titania.
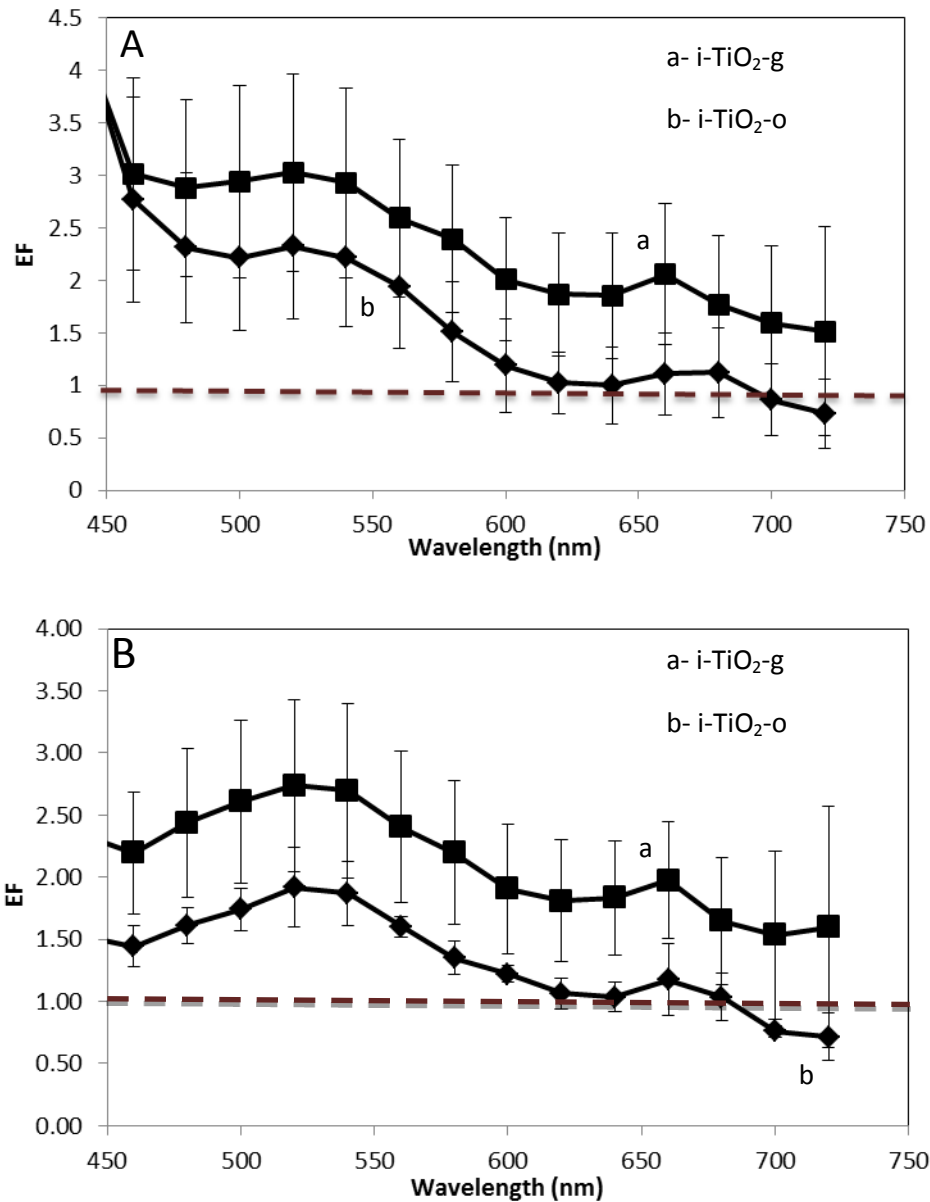
Figure 3.17: Enhancement factor for i-TiO$_2$-g (a) and i-TiO$_2$-o (b) in the front wall (A) and back wall (B) illumination. EF values of i-TiO$_2$-g are above 1.5 in entire region, while i-TiO$_2$-o shows only little enhancement at 660 and 680 nm in the low absorbance region.

3.2.3 Investigation of the energy conversion at Ru-N719/nc-TiO₂/i-TiO₂-o, and Ru-N719/nc-TiO₂/i-TiO₂-g films

Earlier reported results by Halaoui, Nishimura and coworkers showed that coupling of nanocrystalline TiO₂ layer to an inverse opal increased the efficiency of DSSC in 2 spectral regions, 1) within the stop band region under front mode illumination, 2) at the red edge of the stop band under both illumination modes.[23,45,46] Table 3.2 shows the amount of dye adsorbed, thickness, % IPCE, and normalized % IPCE (in parentheses) upon front wall (in green) and back wall (in blue) illumination obtained at 4 nc-TiO₂/i-TiO₂-o, nc-TiO₂/i-TiO₂-g while that of nc-TiO₂ films are shown table 3.3. % IPCE and normalized % IPCE for the average of the 4 nc-TiO₂/i-TiO₂-o and 4 nc-TiO₂ films plotted against wavelength upon front wall illumination are presented in Figure 3.18.The plot of enhancement factor vs wavelength is presented in panel C of figure 3.18.
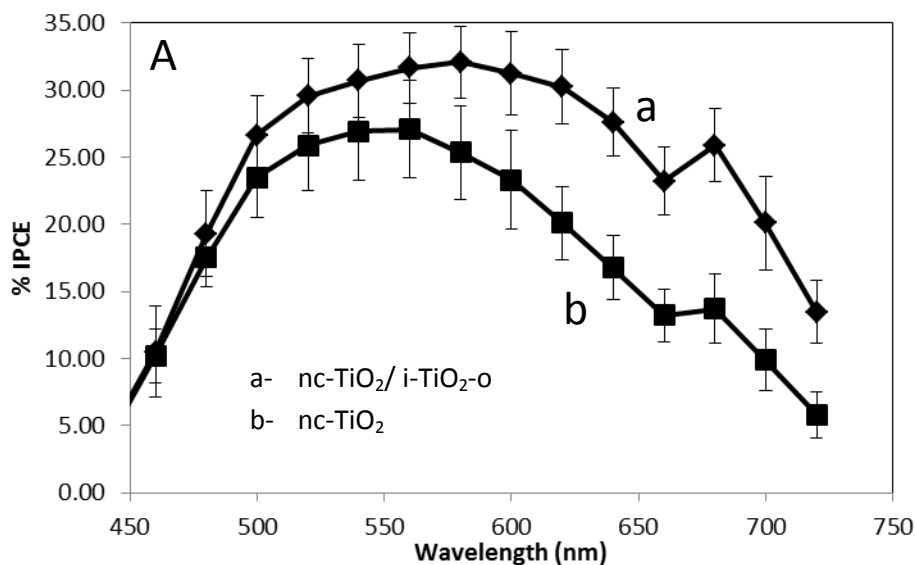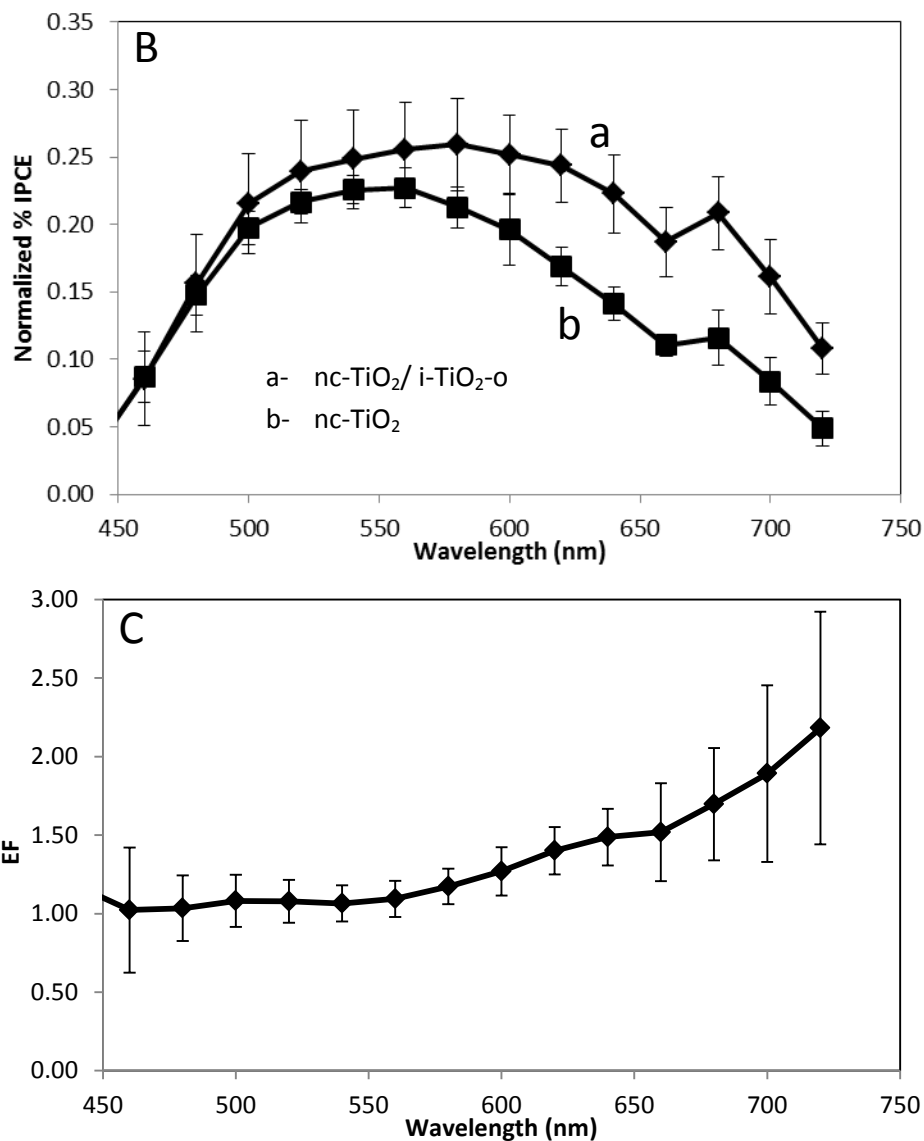
Figure 3.18: A) % IPCE and B) normalized % IPCE at a) 4 Ru-N719 nc-TiO$_2$/i-TiO$_2$-o films and b) 4 nc-TiO$_2$ films upon front wall illumination. C) Enhancement factor calculated for the Ru-N719 nc-TiO$_2$/i-TiO$_2$-o films

Within the stop-band region (560 nm-640 nm), the photonic crystal acts as a mirror reflecting light from the photonic crystal to the nc-TiO$_2$ layer where most of the dye is adsorbed. An enhancement factor of 1.3 ± 0.1 relative to the conventional nanocrystalline structure is observed in the front mode illumination due to Bragg reflection in the stop band of bilayer electrode

between 560 and 640 nm. The enhancement is attributed to the enhanced beam intensity at the nc-TiO$_2$ as a result of Bragg reflection of the photonic gap photons due to its interfacial position with the PC layer rather than the internal localization in the photonic crystal.[45] The photoaction spectra of Ru-N719/nc-TiO$_2$/i-TiO$_2$-o bilayer electrode upon back mode illumination are shown in Fig 3.19. In the back mode illumination, light of certain frequencies (within the stop band) is reflected before reaching the nc-TiO$_2$ film which is highly loaded with the dye. This explains the dip in the % IPCE and thus the lower EF value for the back-mode illumination within the stop band (EF of 1.1 ± 0.1 between 560 and 640 nm). The observed slight enhancement perhaps can be attributed to forward scattering at disordered regions. Mihi and Miguez investigated the optical response of DSSC incorporating an inverse opal (having a cavity diameter of 220 nm) using scalar wave approximation and deduced that the presence of a highly periodic photonic crystal interfaced with a nonperiodically structured material (nc-TiO$_2$) resulted in significant absorption amplification. This amplification was reported to be due to partial localization of light in the nc-TiO$_2$ layer due to multiple resonant modes within the stop band frequencies.
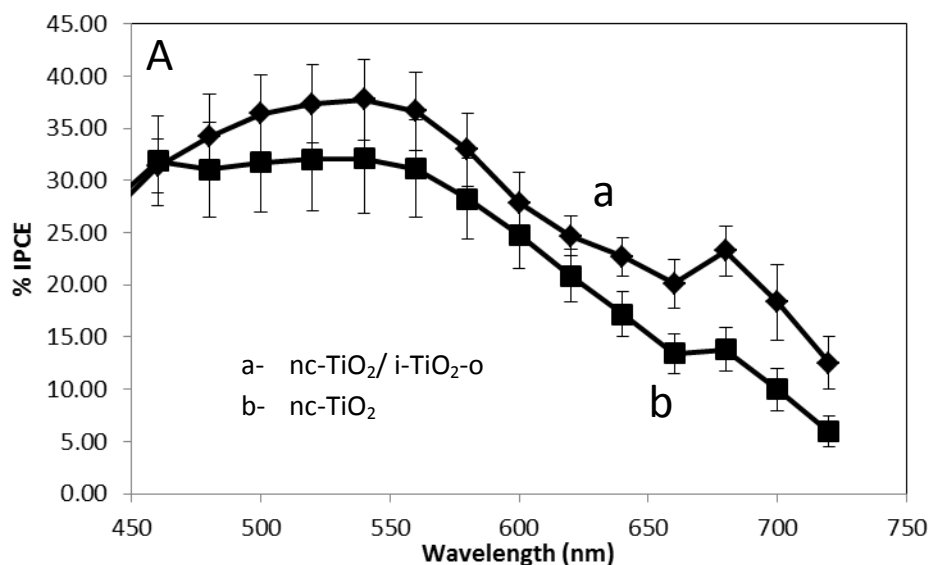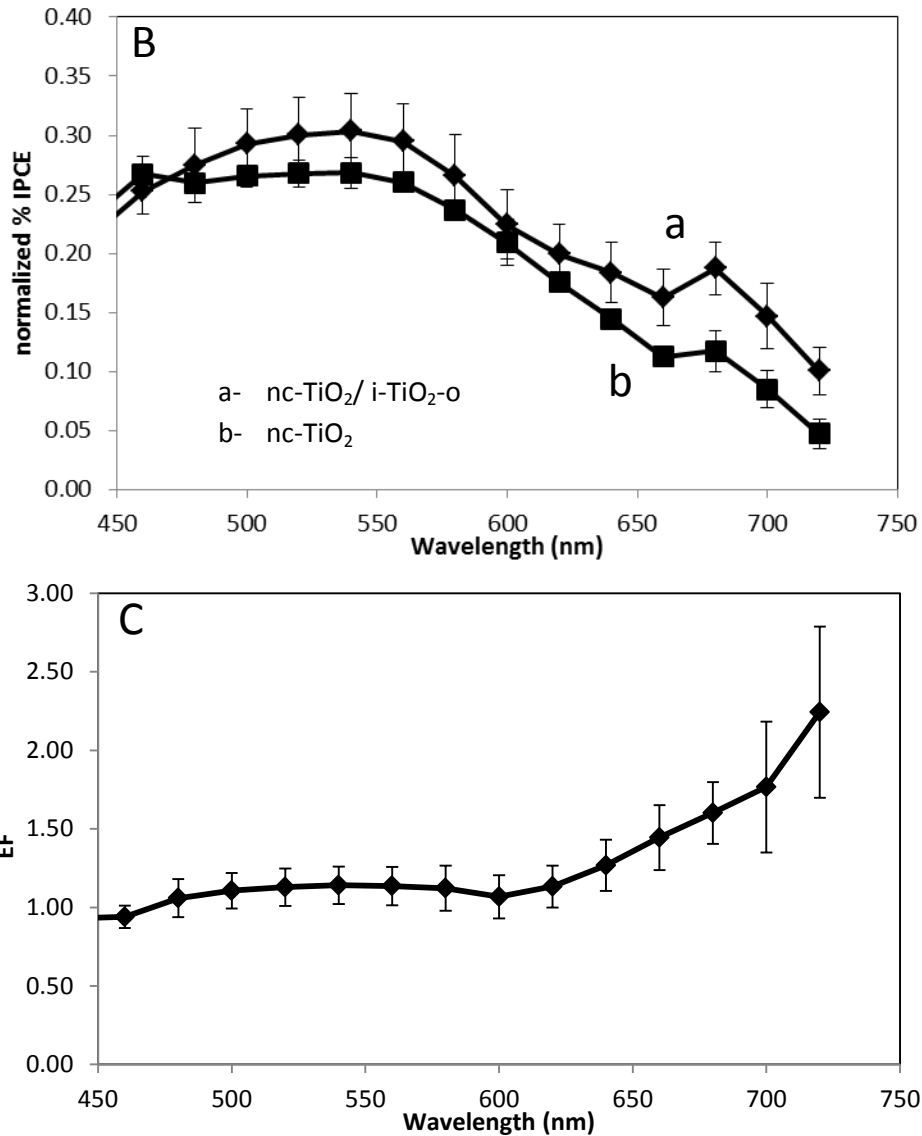
Figure 3.19: A) % IPCE and B) normalized % IPCE at a) 4 Ru-N719/nc-TiO$_2$/i-TiO$_2$-o films and b) 4 nc-TiO$_2$ films upon back wall illumination. C) Enhancement factor calculated for the Ru-N719/nc-TiO$_2$/i-TiO$_2$-o films.

On the red edge of the stop band, i.e. between 660 nm and 720 nm, an enhancement factor of 1.8 $\pm$ 0.2 is observed in the front wall illumination and 1.8 $\pm$ 0.30 in the back wall illumination. This

is attributed to the enhanced beam intensity at the nc-TiO_2 due to the presence of resonant modes at the interface rather than the internal localization in the photonic crystal as was previously reported by Mallouk et al[46] and explained by Mihi and Miguez[47]. The lower red enhancement observed at the i-TiO_2-o alone (not coupled to the nc-TiO_2 layer) further proves the presence of resonant modes at the interface between the PC layer and the nc-TiO_2 layer which in turn leads to better absorption of the incident photons.[45]

The study of nc-TiO_2/inverse opal was reported previously, but it was reproduced here to compare it to the monodispersed disordered opals assembled in the bilayer architecture. Disordered bilayer architecture was fabricated to decouple the effect of order vs disorder on light localization. Figure 3.20 shows the % IPCE, normalized % IPCE of nc-TiO_2/i-TiO_2-g and conventional nc-TiO_2 plotted against the wavelength. In the range between 560 nm and 640 nm where the stop band of the photonic crystal is positioned, the normalized % IPCE of the photonic glass and that of the nanocrystalline film are comparable (EF values of 1.09 and 0.99 for the front and back-mode respectively). This implies that the disordered bilayer electrode is converting light at the same efficiency as the nc-TiO_2 film, and hence regular scattering at disordered films does not yield the same effect as in the case for photonic crystal bilayers. Previous work was successful at confirming that the origin of light enhancement in the bilayer architecture is due to Bragg reflection by shifting the stop band position. The absence of the stop band in the disordered opals in the bilayer acts as a negative control to discuss the role of Bragg reflection in the noted EF within stop band frequencies. Herein, we further confirm that within the stop band frequencies, the observed enhancement (EF=1.3) is caused by the enhanced beam intensity due to Bragg reflection at the interface.
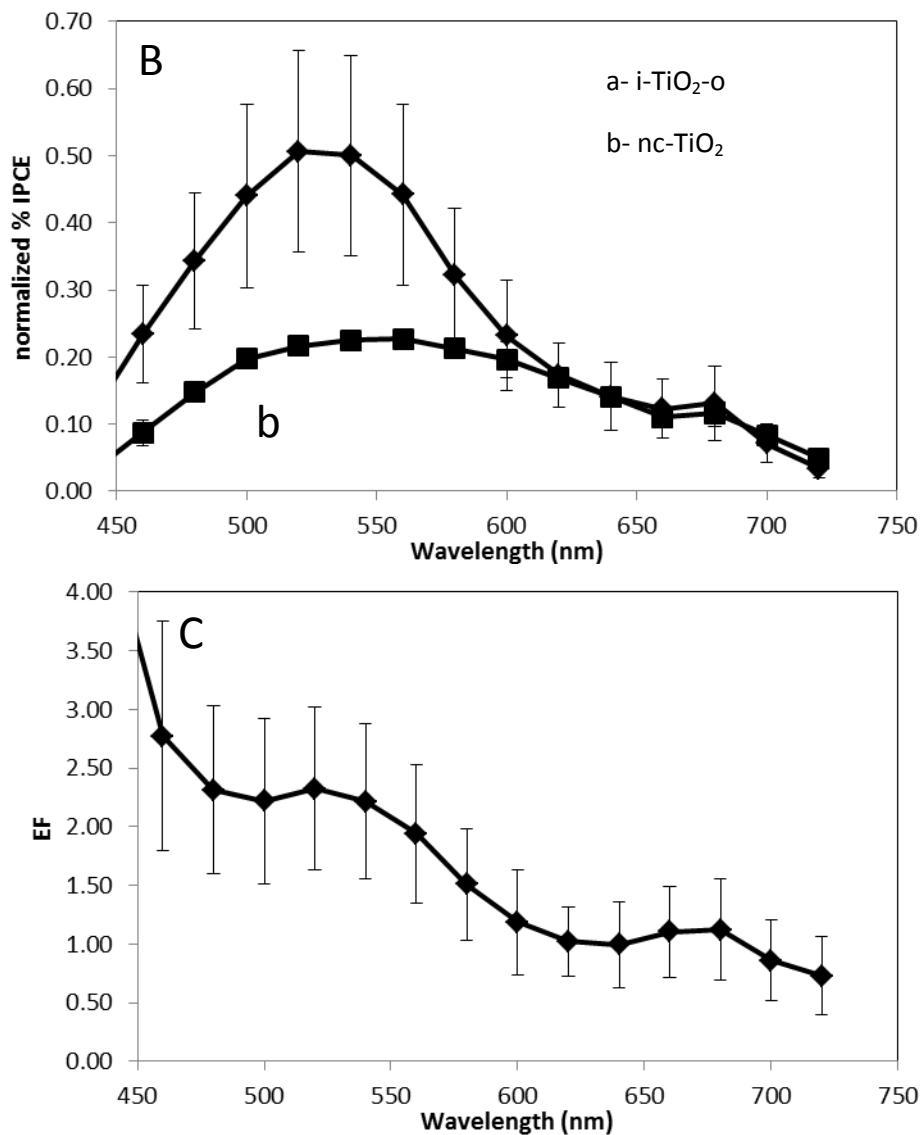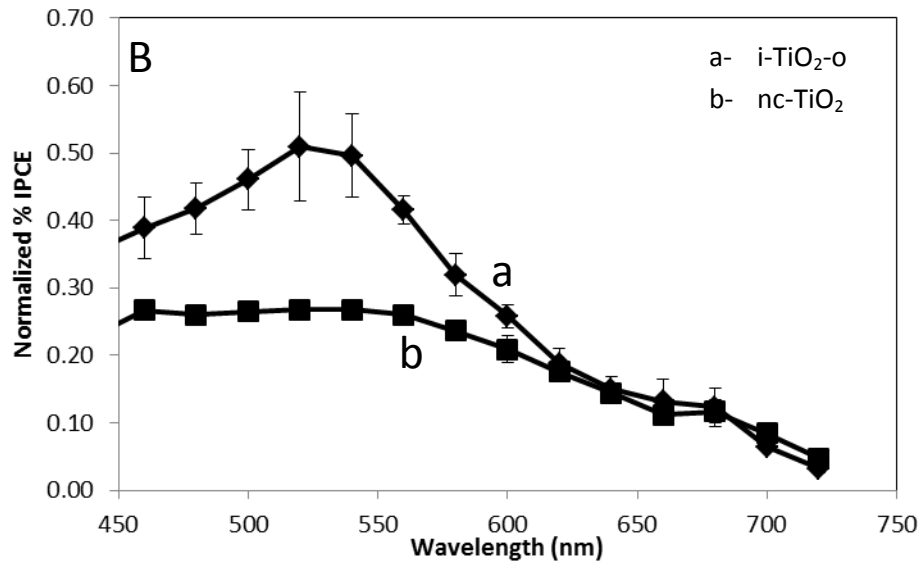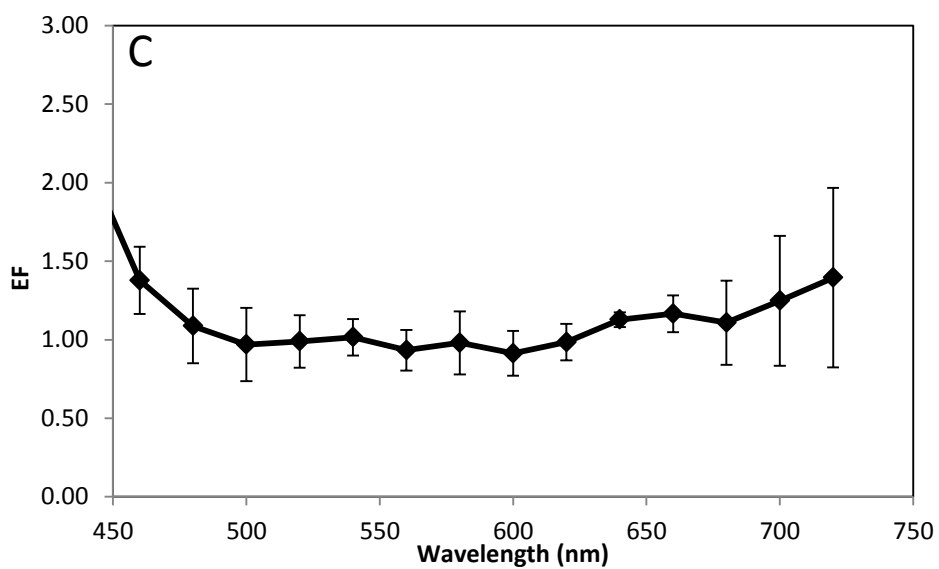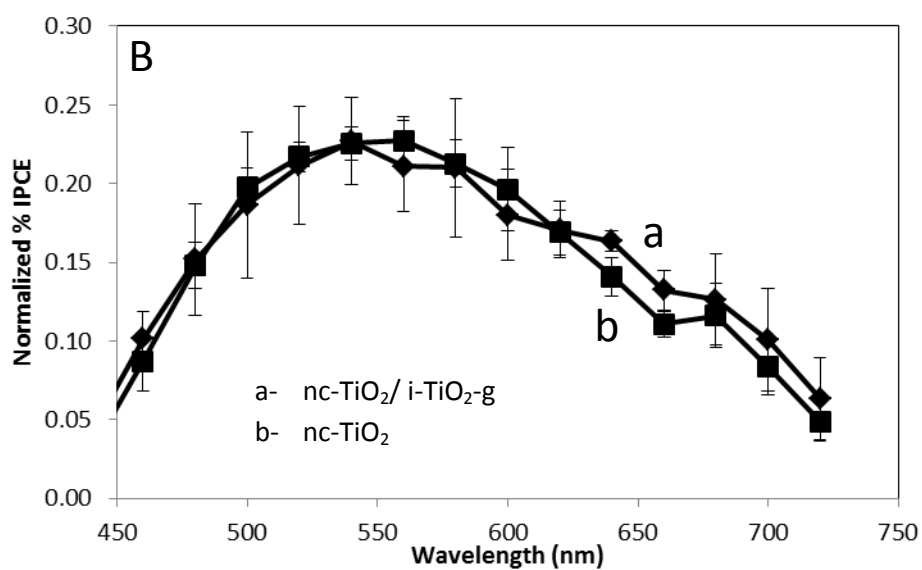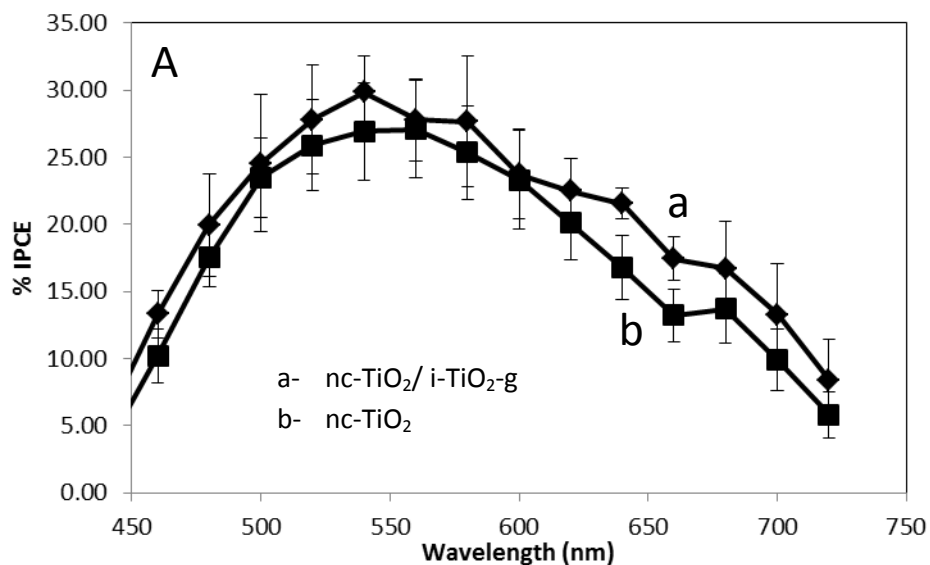
Figure 3.20: A) % IPCE and B) normalized % IPCE at a) 4 Ru-N719/nc-TiO$_2$/i-TiO$_2$-g films and b) 4 nc-TiO$_2$ films upon front wall illumination. C) Enhancement factor calculated for the Ru-N719/nc-TiO$_2$/i-TiO$_2$-g films.

Scattering is responsible for the enhancement in the region between 660 nm and 700 nm in the front-mode illumination. We observe an enhancement factor of 1.2 ± 0.1 at 660 nm, 1.1± 0.3 at 680 nm, 1.3 ± 0.4 at 700 nm. This enhancement might be due to the multiple internal scattering at the disordered regions of the photonic crystal; This consequently halts the propagation of light through the film and leads to its confinement within the nanostructure. The light localization within the film increases the exposure time of the dye to the excitation field. The low-energy photons can still excite the dye molecules if they correspond to the dye band gap energy. The higher collision frequency between photons and dyes due to prolonged exposure will augment the probability of generating photoelectrons. A suppressed enhancement is observed in the back mode illumination (0.9 ± 0.1 at 660 nm, 0.9 ± 0.2 at 680 nm and 0.9 ± 0.2 at 700 nm) which could be attributed to back scattering of light whereby light gets internally scattered inside i-TiO$_2$-g film without reaching the nanocrystalline layer where most of the dye is loaded. Hence light will not be harvested in the cell. Figure 3.21 shows the % IPCE, normalized % IPCE and enhancement factors of the back mode illumination of nc-TiO$_2$/i-TiO$_2$-g.
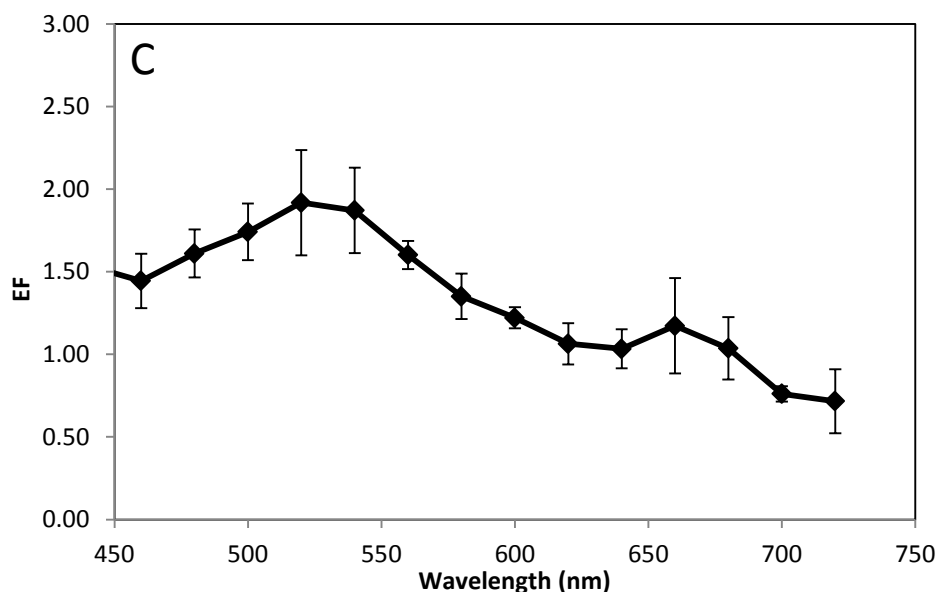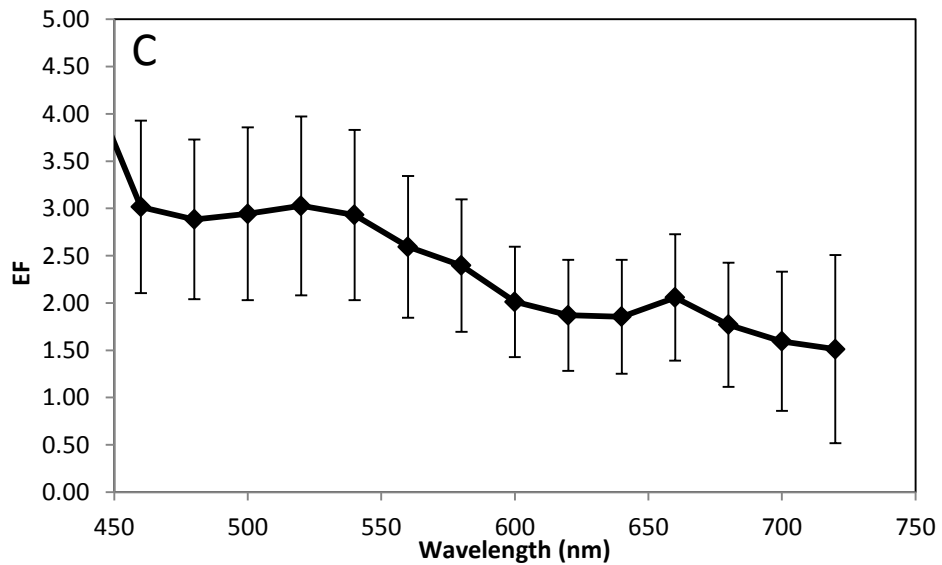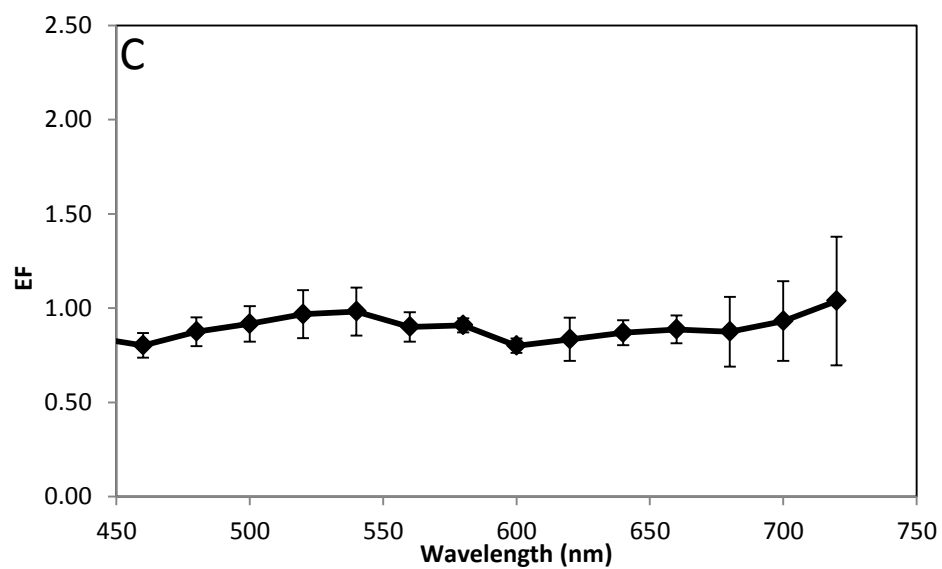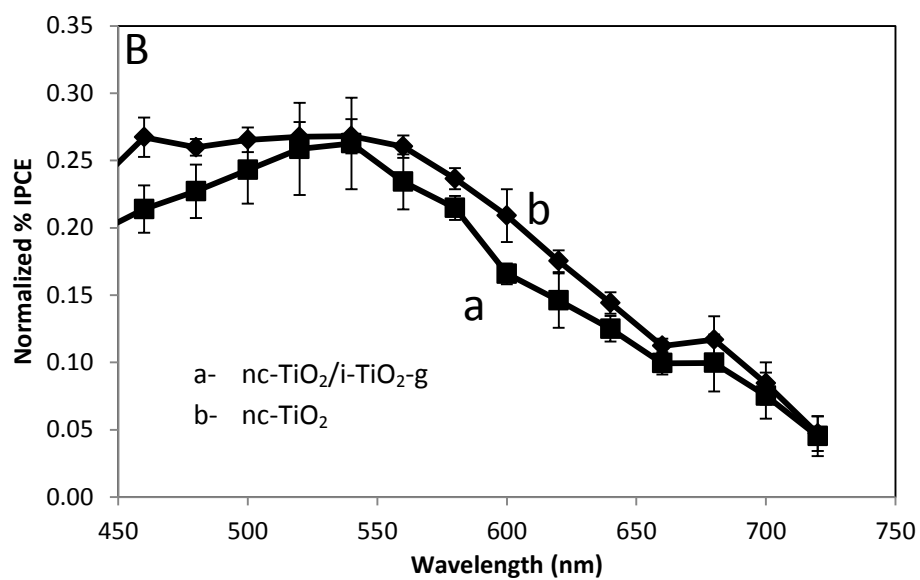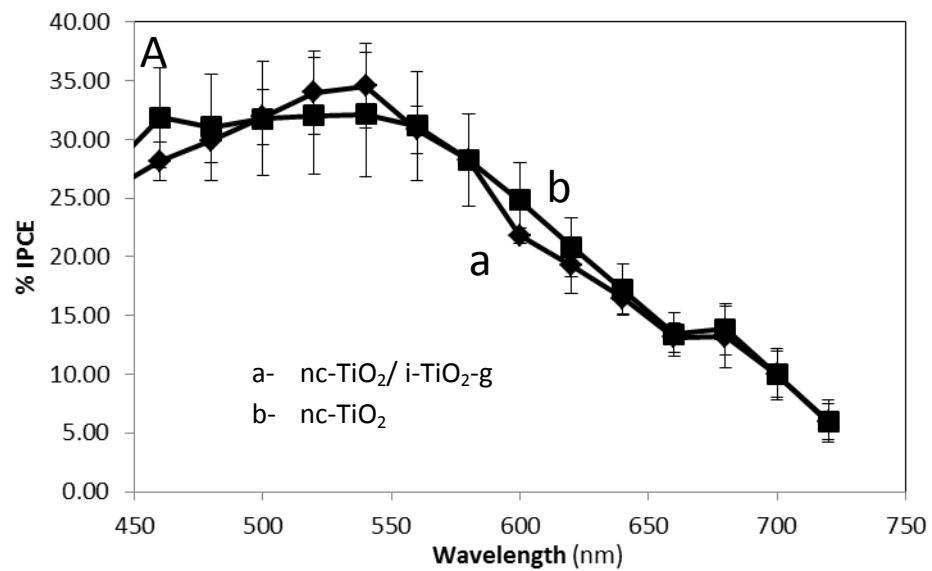
Figure 3.21: A) % IPCE and B) normalized % IPCE at a) 4 Ru-N719/nc-TiO$_2$/i-TiO$_2$-g films and b) 4 nc-TiO$_2$ films upon back wall illumination. C) Enhancement factor calculated for the Ru-N719/nc-TiO$_2$/i-TiO$_2$-g films. The plot does not show any potential enhancement in the whole region**.**

Coupling the photonic glass layer to nc-TiO$_2$ failed in enhancing light to current conversion. In the front mode, the nc-TiO$_2$/i-TiO$_2$-g films exhibited similar phototelectrochemical behavior to i-TiO$_2$-o films in the low energy region, i.e. between 660-700 nm showing 1.1-1.2 enhancement in the energy conversion relative to the conventional nc-TiO$_2$ films. This is attributed to the absence of resonant modes at the interface between the photonic glass and the nc-TiO$_2$ layers. Multiple internal scattering that leads to the enhancement in i-TiO$_2$-g not coupled to nc-TiO$_2$ layer, does not give the same result. This could be explained by the fact that scattering events are occurring inside the disordered film without being able to reach the nanocrystalline layer. But since the bulk of dye molecules get adsorbed on the nc-TiO$_2$ film, these scattering events are being lost without being actually harvested. Another possible explanation would be the occurrence of radiative or non-radiative decays of the photogenerated electrons before being collected by the electrode due to the longer transfer distances in the presence of the underlying disordered opal layer. This same effect was perhaps counteracted by the presence of resonance modes in the nc-TiO$_2$/i-TiO$_2$-o electrode.
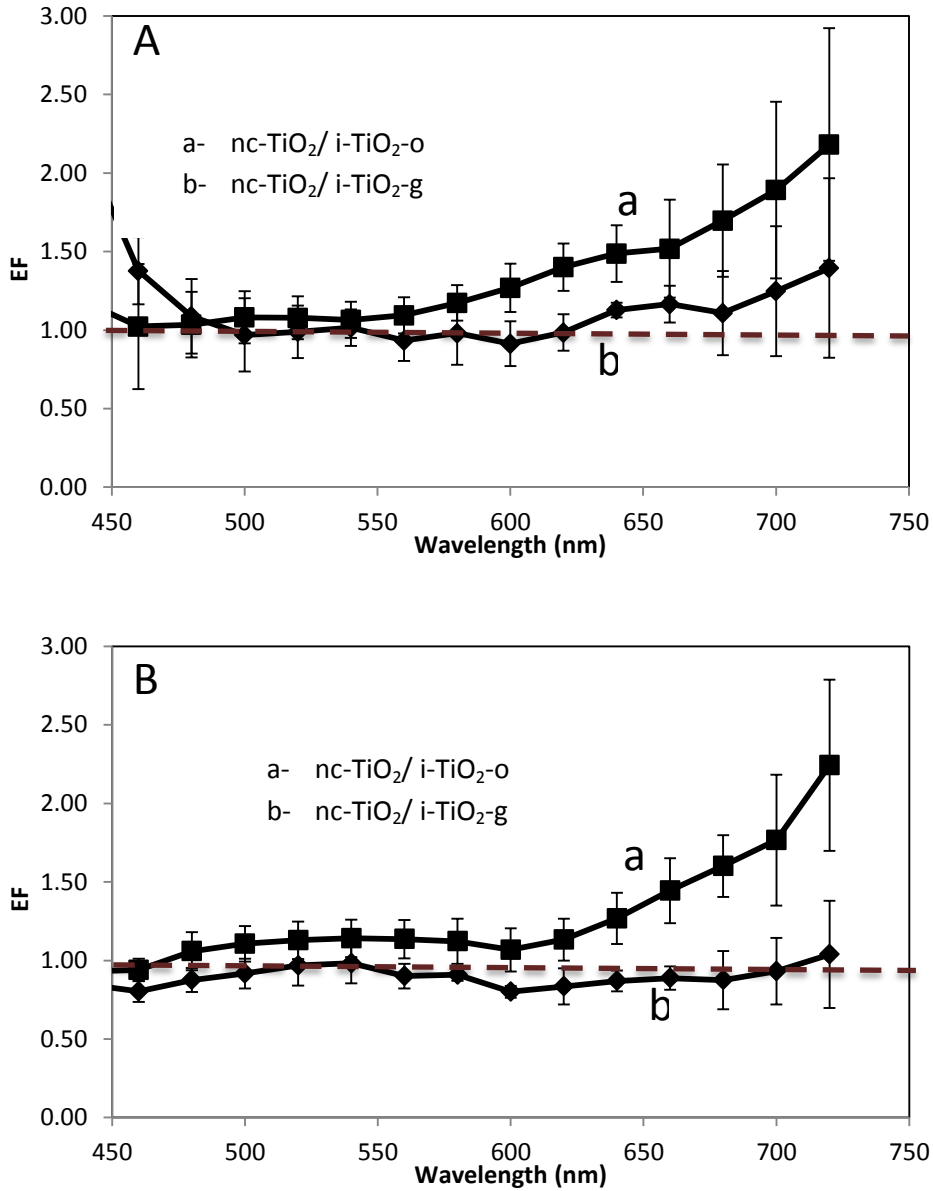
Figure 3.22: EF obtained for Ru-N719/nc-TiO$_2$/i-TiO$_2$-o (a) and Ru-N719/nc-TiO¬2/i-TiO$_2$-g (b) in the front wall illumination (A) and in the back wall illumination (B).

Inverse photonic glass showed the best performance among the different studied architectures

and gave the most potential enhancement reaching a 2-fold photoconversion amplification.

Multiple internal scattering at highly disordered films is more effective in light trapping than the

light localization in ordered systems. However, when coupled to nc-TiO$_2$, the disordered film does not lead to an enhancement in the back wall illumination since back-scattering does not allow light to reach the nc-TiO$_2$ layer. On the other hand, multiple internal scattering and back-scattering in front wall illumination had led to enhancement factor of 1.2 in the low energy region (660-700 nm).

	Amount of Ru-N719 (ηmol/cm²) (Thickness μm)	% IPCE (normalized % IPCE) at							
		560 nm	580 nm	600 nm	620 nm	640 nm	660 nm	680 nm	700 nm
i-TiO$_2$-o (1)	28 (6.9)	8.70 (0.313) 10.87 (0.392)	6.63 (0.239) 8.28 (0.299)	5.37 (0.193) 6.60 (0.238)	3.59 (0.130) 4.56 (0.164)	2.66 (0.096) 3.59 (0.129)	1.96 (0.071) 2.78 (0.100)	1.80 (0.065) 2.62 0.094	1.06 (0.038) 1.65 0.060
i-TiO$_2$-o (2)	22 (5.5)	13.54 (0.613) 14.86 (0.673)	10.28 (0.465) 11.30 (0.512)	7.66 (0.347) 8.90 (0.403)	5.25 (0.238) 6.52 (0.295)	4.72 (0.214) 5.48 (0.248)	3.63 (0.164) 3.98 (0.180)	3.57 (0.162) 3.84 (0.174)	2.28 (0.103) 2.46 (0.111)
i-TiO$_2$-o (3)	29 (5.5)	10.27 (0.358) 12.12 (0.423)	7.84 (0.273) 10.21 (0.356)	6.61 (0.231) 7.55 (0.264)	5.15 (0.180) 5.96 (0.208)	3.67 (0.128) 4.64 (0.162)	2.98 (0.104) 3.71 (0.129)	3.11 (0.109) 3.52 (0.123)	1.70 (0.059) 1.89 (0.066)
i-TiO$_2$-o (4)	29 (5.8)	13.02 (0.494) 11.59 (0.441)	8.33 (0.319) 8.16 (0.313)	4.22 (0.167) 7.31 (0.283)	3.90 (0.156) 5.11 (0.200)	3.37 (0.137) 4.25 (0.169)	4.10 (0.166) 4.48 (0.18)	5.08 (0.189) 4.09 (0.152)	2.23 (0.083) 1.89 (0.068)
Average normalized %IPCE		0.442 ± 0.135 0.480 ± 0.130	0.322 ± 0.100 0.368 ± 0.099	0.232 ± 0.082 0.294 ± 0.074	0.173 ± 0.048 0.214 ± 0.057	0.141 ± 0.051 0.174 ± 0.057	0.123 ± 0.044 0.144 ± 0.036	0.131 ± 0.055 0.136 ± 0.035	0.071 ± 0.028 0.076 ± 0.024
i-TiO$_2$-g(1)	28 (6.1)	15.28 (0.541) 16.50 (0.584)	13.71 (0.485) 14.43 (0.561)	12.93 (0.458) 12.99 (0.460)	10.84 (0.383) 10.59 (0.375)	9.11 (0.322) 8.80 (0.312)	7.38 (0.261) 7.02 (0.248)	7.53 (0.267) 7.44 (0.263)	5.70 (0.202) 5.73 (0.203)
i-TiO$_2$-g (2)	25 (6.4)	15.83 (0.644) (16.24)	13.47 (0.548) 13.42	9.87 (0.402) 10.00	7.98 (0.325) 7.81	6.46 (0.263) 6.31	4.74 (0.193) 4.57	4.32 (0.176) 4.13	2.35 (0.096) 2.21

		560 nm	580 nm	600 nm	620 nm	640 nm	660 nm	680 nm	700 nm
		0.661	(0.546)	(0.407)	(0.318)	(0.257)	(0.186)	(0.168)	(0.090)
i-TiO$_2$-g (3)	23 (6.0)	17.90 (0.644)	15.47 (0.548)	10.64 (0.402)	8.53 (0.325)	7.15 (0.263)	7.07 (0.193)	5.56 (0.243)	3.16 (0.138)
		18.74 (0.819)	15.46 (0.676)	10.80 (0.472)	8.64 (0.378)	7.19 (0.314)	6.43 (0.281)	4.48 (0.196)	2.76 (0.121)
i-TiO$_2$-g (4)	27 (5.8)	10.42 (0.782)	8.75 (0.676)	6.13 (0.465)	4.68 (0.373)	3.81 (0.313)	3.90 (0.309)	2.85 (0.104)	1.87 (0.068)
		11.98 (0.437)	9.43 (0.344)	6.55 (0.239)	5.35 (0.195)	4.76 (0.173)	4.65 (0.169)	3.42(0.125)	2.29 (0.084)
Average normalized %IPCE		0.587± 0.170	0.507 ± 0.148	0.387 ± 0.113	0.313 ± 0.098	0.259 ± 0.084	0.226 ± 0.074	0.197 ± 0.073	0.126± 0.058
		0.625± 0.159	0.519± 0.137	0.394 ± 0.107	0.316 ± 0.085	0.264± 0.066	0.221 ± 0.052	0.188± 0.058	0.124± 0.055

Table 3.1: Amount adsorbed, thickness (in parentheses), % IPCE, normalized % IPCE (in parentheses) of 4 i-TiO$_2$-o and 4 i-TiO$_2$-g films in front wall illumination (green) and back wall illumination (blue).

	Amount of Ru-N719 (ηmol/cm^2) (Thickness μm)	% IPCE (normalized % IPCE) at							
		560 nm	580 nm	600 nm	620 nm	640 nm	660 nm	680 nm	700 nm
Nc-TiO$_2$/ i-TiO$_2$-o (1)	130 (10.5)	30.48 (0.234)	32.30 (0.248)	29.86 (0.229)	(32.12) 0.247	(29.16) 0.224	(25.94) 0.199	24.22 (0.186)	19.52 (0.150)
		40.44 (0.310)	35.63 (0.274)	26.61 (0.204)	25.11 (0.193)	23.51 (0.180)	23.08 (0.177)	22.95 (0.146)	18.98 (0.098)
Nc-TiO$_2$/i-TiO$_2$-o (2)	127 (13.4)	35.01 (0.276)	(34.91) 0.275	(36.97) 0.228	(33.26) 0.262	29.77 (0.23)5	24.35 (0.192)	30.57 (0.241)	25.52 (0.201)
		40.14 (0.316)	36.18 (0.285)	32.92 (0.260)	26.58 (0.210)	23.54 (0.186)	20.56 (0.162)	27.29 (0.185)	23.52 (0.129)
Nc-TiO$_2$/i-TiO$_2$-o (3)	128 (11.7)	27.97 (0.219)	27.76 (0.217)	29.03 (0.227)	26.16 (0.205)	23.36 (0.183)	19.15 (0.150)	23.82 (0.186)	19.66 (0.154)
		31.70 (0.248)	27.46 (0.215)	25.05 (0.196)	21.50 (0.168)	19.54 (0.153)	16.49 (0.129)	21.01 (0.137)	17.47 (0.092)
Nc-TiO$_2$/i-TiO$_2$-o (4)	113 (11.8)	33.16 (0.294)	33.49 (0.297)	29.57 (0.262)	29.52 (0.262)	28.23 (0.250)	23.41 (0.208)	24.96 (0.221)	15.78 (0.140)
		34.04 (0.304)	32.57 (0.289)	28.81 (0.238)	25.65 (0.227)	24.29 (0.215)	20.43 (0.181)	21.85 (0.119)	13.45 (0.082)
Average normalized % IPCE		0.259 ± 0.035	0.252 ± 0.029	0.244 ± 0.027	0.236 ± 0.029	0.223 ± 0.029	0.187 ± 0.026	0.209 ± 0.027	0.161 ± 0.027
		0.295 ±	0.266 ±	0.224 ±	0.199 ±	0.184 ±	0.162 ±	0.187 ±	0.147 ±

		0.032	0.034	0.030	0.025	0.026	0.024	0.022	0.028
Nc-TiO$_2$/i-TiO$_2$-g (1)	136 (10.9)	27.83 (0.205)	26.08 (0.192)	23.38 (0.172)	24.55 (0.181)	21.33 (0.157)	17.64 (0.130)	20.09 (0.148)	15.44 (0.114)
		32.45 (0.239)	28.00 (0.206)	22.73 (0.167)	22.31 (0.164)	18.34 (0.135)	14.52 (0.107)	16.59 (0.122)	12.17 (0.090)
Nc-TiO$_2$/i-TiO$_2$-g (2)	128 (11.5)	23.09 (0.180)	20.43 (0.159)	18.36 (0.143)	18.44 (0.144)	20.47 (0.159)	18.69 (0.146)	18.99 (0.148)	16.76 (0.131)
		33.25 (0.259)	28.20 (0.220)	22.22 (0.173)	20.85 (0.162)	16.68 (0.130)	12.86 (0.100)	13.79 (0.107)	9.82 (0.076)
Nc-TiO$_2$/i-TiO$_2$-g (3)	127 (10.5)	31.78 (0.250)	32.94 (0.259)	26.66 (0.210)	23.12 (0.182)	20.94 (0.165)	14.69 (0.116)	11.04 (0.087)	6.93 (0.055)
		29.10 (0.229)	28.57 (0.225)	21.38 (0.168)	16.63 (0.131)	14.40 (0.113)	11.15 (0.088)	9.14 (0.072)	6.48 (0.051)
Nc-TiO$_2$/i-TiO$_2$-g (4)	136 (10.8)	28.43 (0.209)	31.22 (0.230)	26.58 (0.196)	23.96 (0.176)	23.44 (0.173)	18.74 (0.138)	16.64 (0.122)	14.01 (0.103)
		28.51 (0.210)	28.31 (0.208)	21.03 (0.155)	17.17 (0.126)	16.53 (0.122)	13.98 (0.103)	13.20 (0.097)	11.44 (0.084)
Average normalized % IPCE		0.211± 0.029	0.210± 0.044	0.180 ± 0.029	0.171 ± 0.018	0.163 ± 0.007	0.132 ± 0.013	0.126 ± 0.029	0.100 ± 0.033
		0.234 ± 0.020	0.215 ± 0.009	0.166± 0.008	0.146 ± 0.020	0.125 ± 0.010	0.099 ± 0.008	0.100 ± 0.021	0.075 ± 0.017

Table 3.2: Amount adsorbed, thickness (in parentheses), % IPCE, normalized % IPCE (in parentheses) of 4 i-TiO$_2$-o/nc-TiO$_2$-o and 4 i-TiO$_2$-o/nc-TiO$_2$-g films in front wall illumination (green) and back wall illumination (blue).

	Amount of Ru-N719 (ηmol/cm^2) (Thickness μm)	% IPCE (normalized % IPCE)							
		560 nm	580 nm	600 nm	620 nm	640 nm	660 nm	680 nm	700 nm
Nc-TiO$_2$ (1)	134 (6.9)	28.34 (0.210) 35.82 (0.266)	25.99 (0.193) 31.26 (0.232)	20.78 (0.154) 23.87 (0.177)	19.86 (0.147) 21.99 (0.163)	16.80 (0.125) 18.09 (0.134)	13.67 (0.101) 14.57 (0.108)	11.00 (0.082) 11.73 (0.087)	7.37 (0.055) 7.83 (0.058)
Nc-TiO$_2$ (2)	101 (5.5)	21.73 (0.216) 24.80 (0.246)	20.54 (0.204) 22.78 (0.226)	19.54 (0.194) 21.09 (0.209)	16.49 (0.164) 17.46 (0.173)	13.46 (0.134) 14.05 (0.139)	10.42 (0.103) 10.68 (0.106)	12.04 (0.119) 12.62 (0.125)	8.51 (0.084) 8.79 (0.087)
Nc-TiO$_2$ (3)	107 (6.2)	26.54 (0.247) 28.54 (0.266)	24.58 (0.229) 26.41 (0.246)	23.77 (0.221) 24.44 (0.228)	19.79 (0.184) 19.81 (0.185)	16.67 (0.155) 16.60 (0.155)	12.90 (0.120) 12.82 (0.119)	13.95 (0.130) 13.58 (0.127)	10.15 (0.095) 10.18 (0.095)
Nc-TiO$_2$ (4)	135 (5.8)	31.75 (0.236) 35.48 (0.263)	30.31 (0.225) 32.56 (0.242)	29.08 (0.216) 29.89 (0.222)	24.22 (0.180) 24.23 (0.180)	20.19 (0.150) 19.89 (0.148)	15.81 (0.117) 15.54 (0.115)	17.85 (0.133) 17.36 (0.129)	13.53 (0.100) 13.15 (0.098)
Average normalized %IPCE		0.227 ± 0.015 0.260 ± 0.008	0.213 ± 0.015 0.236 ± 0.008	0.196 ± 0.026 0.209 ± 0.020	0.169 ± 0.015 0.175 ± 0.008	0.141 ± 0.012 0.114 ± 0.008	0.111 ± 0.008 0.112 ± 0.005	0.116 ± 0.020 0.117 ± 0.017	0.084 ± 0.018 0.084 ± 0.016

Table 3.3: : Amount adsorbed, thickness (in parentheses), % IPCE, normalized % IPCE (in parentheses) of 4 nc-TiO$_2$ films in front wall illumination (green) and back wall illumination (blue).

3.3 Preliminary Study on the Photoelectrochemical behavior of inverse opals sensitized with T118

Another approach to increase the efficiency of DSSCs was studied in this work. Recently, Dr. Tarek Ghaddar synthesized a Ruthenium-based organic dye (T118) that shows interesting characteristics. The structure and UV-Vis absorption spectrum of 0.1 mM T118 dye solution in ethanol are shown in Figure 3.23. T118 exhibits an absorption peak in the low energy region of

the solar spectrum at 700 nm. T118 shows very comparable short circuit current density (J_{sc}) and open circuit potential (V_{oc}) values to N719. The J_{sc} and V_{oc} of DSSC sensitized by T118 are 12.3 mA/cm^2 and 0.67 V and that of N719 are 11.7 mA/cm^2 and 0.66 V, respectively in MPN 100 electrolyte.
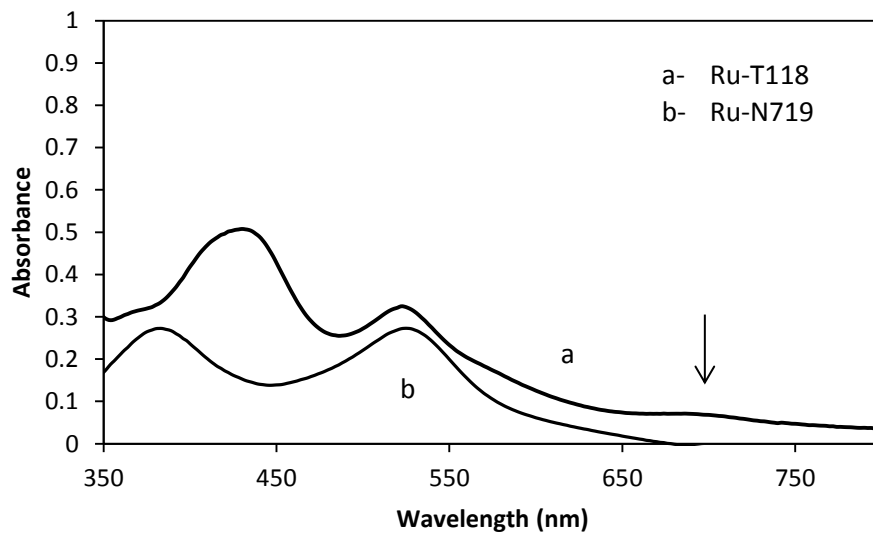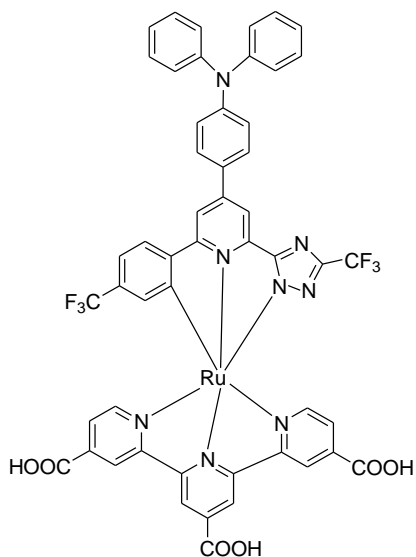
Figure 3.23: Structure of T118 and UV-Vis absorption spectrum of 0.1 mM T118 dye solution (a) and 0.1 mM N719 (b) in ethanol.

Herein, we report preliminary results of inverse opal-based DSSC sensitized with T118. The photocurrent measurements were acquired in 2-electrode configuration; Ru-N719/i-TiO$_2$-o, Ru-T118/i-TiO$_2$-o, Ru-N719/nc-TiO$_2$, or Ru-T118/nc-TiO$_2$ as the working electrode and platinized FTO as the counter electrode. The monochromatic photoaction spectra of nc-TiO$_2$ sensitized with either T118 or N719 are shown in figure 3.24. N719 still shows higher % IPCE values in the region of high dye absorption (~450-660 nm). However, the % IPCE becomes higher for the T118/nc-TiO$_2$ films beyond 670 nm. The % IPCE's are 190 % higher than N719/nc-TiO$_2$ films in the region extending from 680 nm-760 nm.
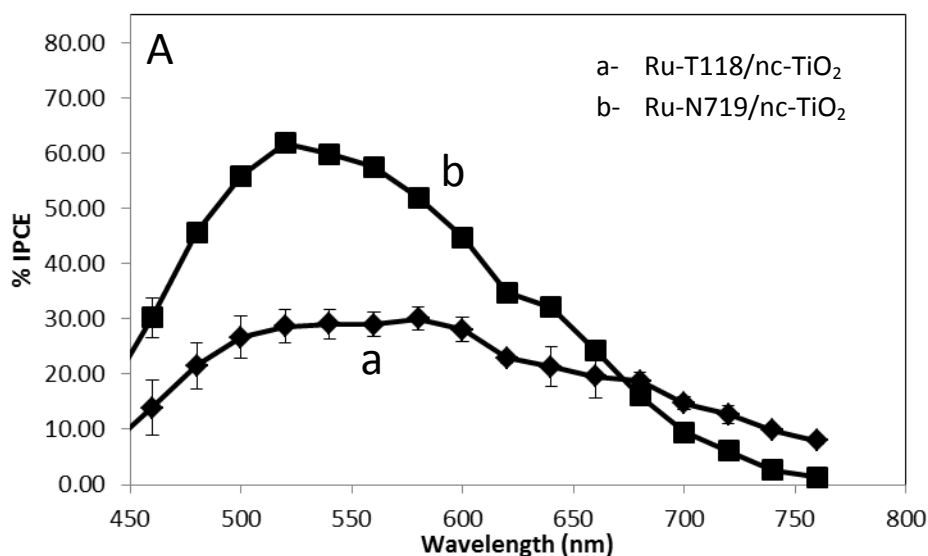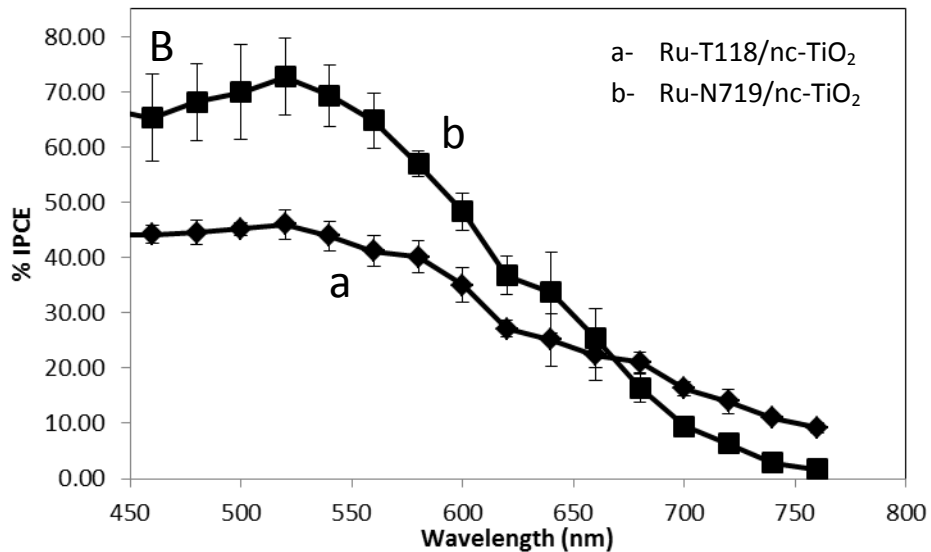
Figure 3.24: Plots of % IPCE of the average of 4 nc-TiO$_2$ films sensitized with T118 dye (a) and 4 nc-TiO$_2$ films sensitized with N719 dye in the front-mode (A) and back-mode (B) illumination.

The photoresponse of T118 on inverse opals has been studied using 2 polystyrene templates of particle sizes 305 nm and 417 nm. Figure 3.25 shows the UV-vis spectra of the photonic crystals and their respective i-TiO$_2$-o structures. PC$_{417}$ and PC$_{305}$ exhibited stop bands at 900 nm and 660 nm, and the stop bands of the resulting i-TiO$_2$-o structures are centered at 820 nm for 600 nm, respectively.
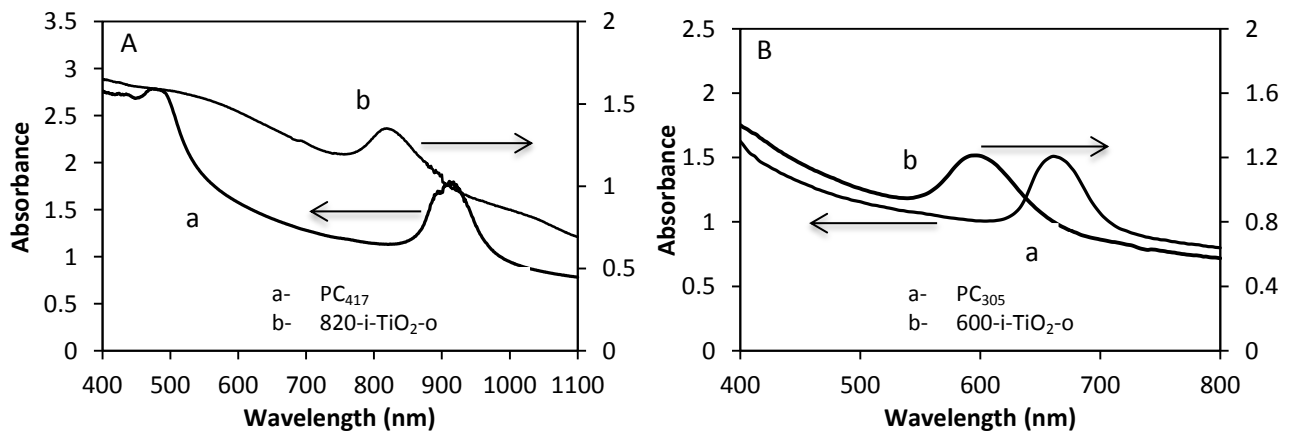
Figure 3.25: UV-Vis spectra of photonic crystal (a) and inverse opal (b) films. (A) PC_{417} and 820-i-TiO_2-o, (B) PC_{305} and 600-i-TiO_2-o. The stop bands of PC_{417} and PC_{305} are centered at 900 nm and 660 nm while those of i-TiO_2-o structures are at 820 nm and 600 nm respectively.

T118 absorption peak (at 710 nm) lies 100 nm to the red of the stop band of 600-i-TiO_2-o and 100 nm to the blue of 820-i-TiO_2-o. The % IPCE and normalized % IPCE of the average of 3 820-i-TiO_2-o (13.8 ± 1.9 nmol/cm^2, 4.5 ± 0.8 μm) and 3 600-i-TiO_2-o (15.2 ± 1.9 nmol/cm^2, 4.9 ± 0.4 μm) films are presented in figure 3.26. The plot of enhancement factor vs wavelength is presented in panel C of figure 3.26. In the low energy region (beyond 620 nm), 600-i-TiO_2-o shows similar normalized % IPCE to nc-TiO_2 electrode. An enhancement to the blue of the stop band was observed at 820-i-TiO_2-o. Bayram et al previously observed enhancements 100 nm to blue of the stop band at Q-CdSe/700-i-TiO_2-o.[26]
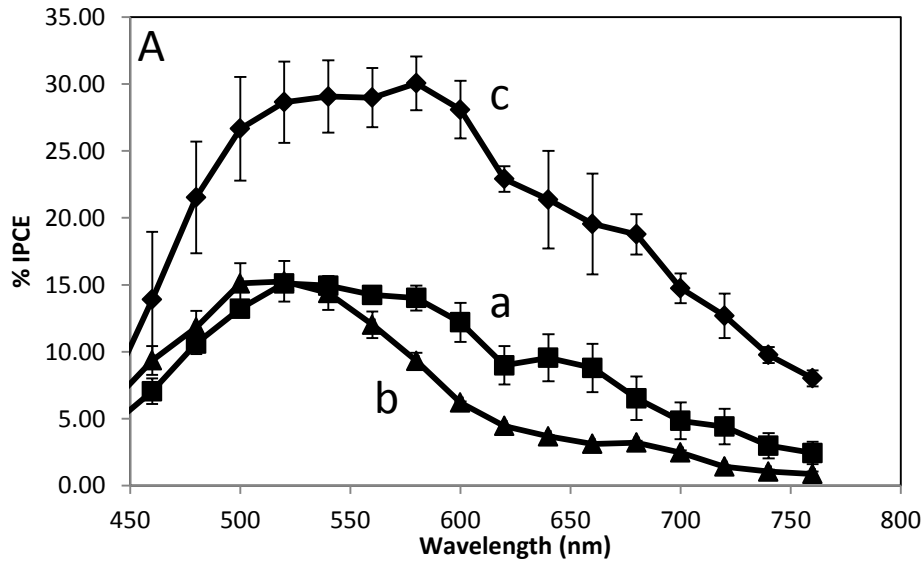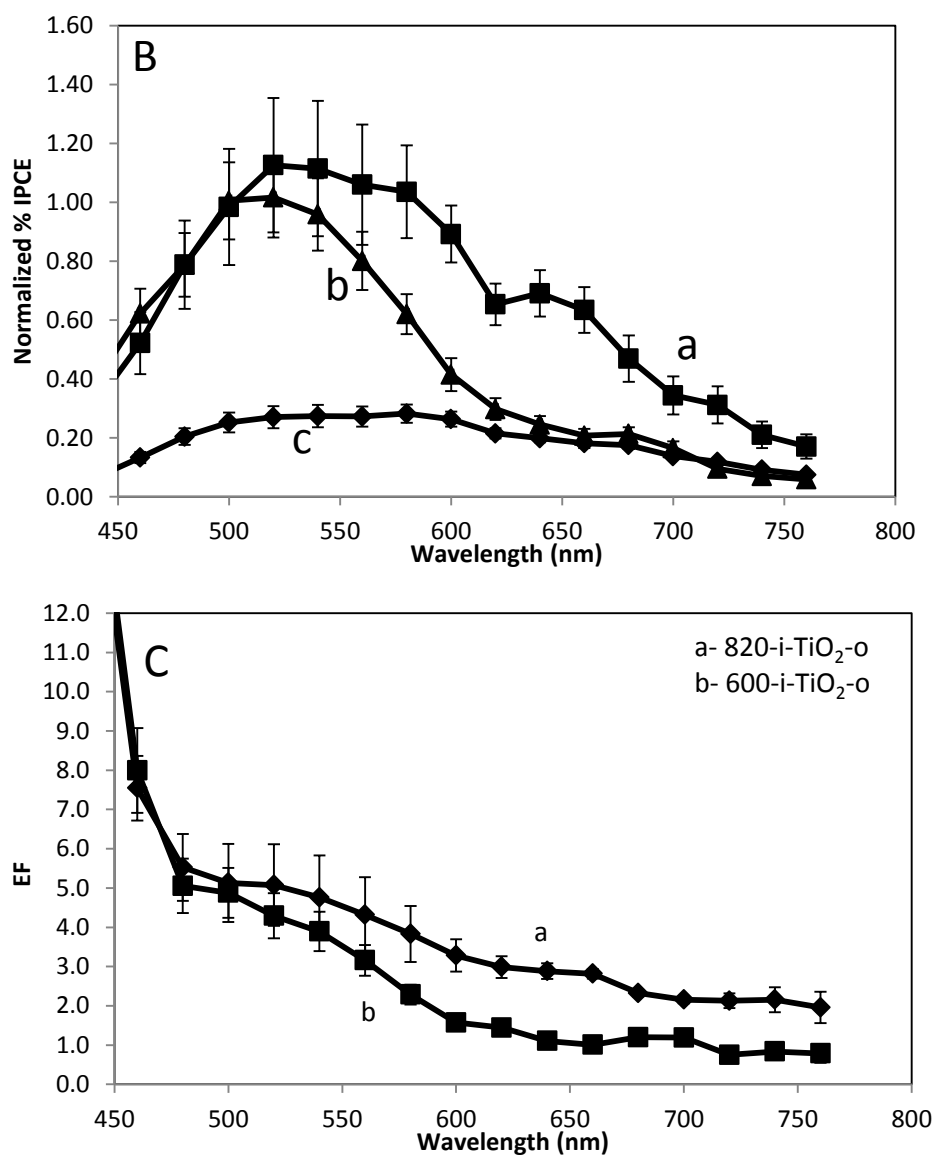
Figure 3.26: % IPCE (A) and normalized % IPCE (B) for the average of 3 820-i-TiO$_2$-o (a), 3 600-i-TiO$_2$-o (b) and 4 nc-TiO$_2$ films in the front mode illumination. Enhancement factor is presented in panel C.

Previous reports have showed that adding a 300 nm TiO$_2$ scattering layer increased the photoresponse on nanocrystalline TiO$_2$ films. Figure 3.27 shows the normalized % IPCE of

T118/inv-PC$_{417}$ with and without a scatter layer. Adding a scatter layer to the Ru-T118/i-TiO$_2$-o

electrode significantly increased the photoresponse uniformly all over the region.
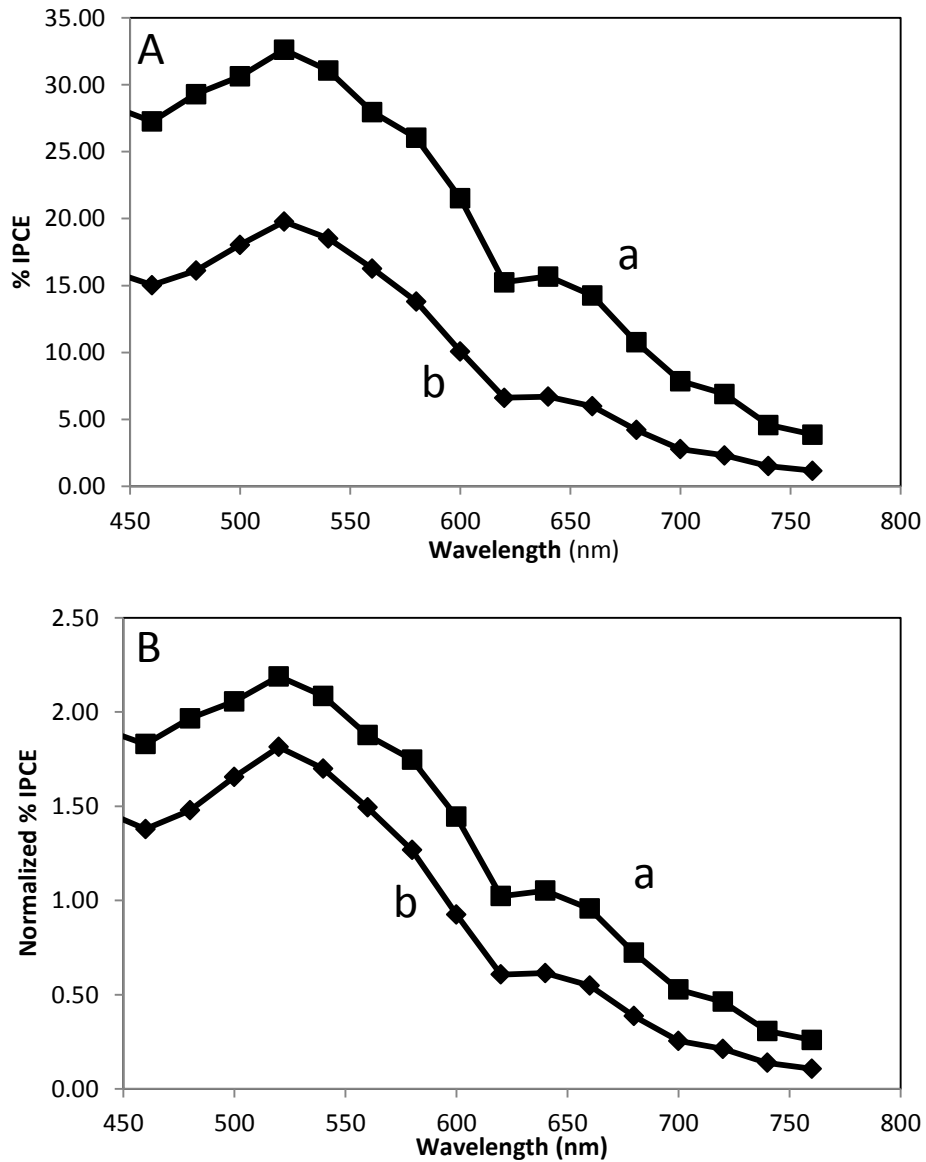
Figure 3.27: Plot of % IPCE and normalized % IPCE of 820-i-TiO$_2$-o with and without scatter layer.

We showed in this study that inducing significant disorder in the inverse opal film leads to

significant light absorption amplification caused by multiple internal scattering in the film and

that was manifested by the high absorbance and high light-to-photocurrent conversion efficiency reaching a 2-fold enhancement factor when compared to conventional nc-TiO$_2$ film with comparable thickness. However, assembling the disordered inverse opal film in bilayer architecture failed at enhancing light absorption. This demonstrates the importance of order in maintaining the resonance modes which are responsible for light enhancement in nc-TiO$_2$/i-TiO$_2$-o electrode. Sensitizing 820-i-TiO$_2$-o film with T118 showed an enhancement to the blue of the stop band. Future work will be directed to investigate the effect of light localization and the energy conversion efficiency at Ru-T118/nc-TiO$_2$/820-i-TiO$_2$-o and Ru-T118/nc-TiO$_2$/600-i-TiO$_2$-o bilayer architecture.

CHAPTER 4

INVESTIGATING THE EFFECT OF IRON DOPING IN NICKEL-BORATE CATALYST FILMS ON THE KINETICS OF OXYGEN EVOLUTION

Water splitting involves two half reactions, the oxygen evolution reaction (OER) and hydrogen evolution reaction (HER). Of the two half reactions, OER is the more demanding reaction as it is a 4 electron, 4 proton process to produce 1 molecule of O_2 from two water molecules. The naturally slow kinetics of the oxygen evolution reaction necessitates the use of a catalyst to stabilize the OER intermediates and increase the rate of the reaction and thus to lower the required overpotential on the electrode. Several oxygen evolution electrocatalysts have been studied including iridium oxide, cobalt, cobalt oxide and nickel oxide as well as other mixed metal complexes.[73,77,102,79,85] Thin Nickel oxo/hydroxo amorphous films prepared in borate (termed NiBi films) has been previously explored as an effective OER electrocatalyst, exhibiting low tafel slopes of 30 mV/decade following an electrochemical activation, and low overpotential (~425 mV) to evolve oxygen at an activity of 1 mA/cm^2.[103]

Nickel hydroxide can exist in 3 different polymorphs, α, β and γ.[104] Figure 4.1 represents the Bode diagram for the Ni(OH)$_2$. Until recently, β-NiOOH, having a valency of 3, has been historically known to be the most catalytically active form toward oxygen evolution reaction.[105,106] In a recent report, Bediako et al showed that perhaps the higher valency γ-NiOOH (with 3.6 oxidation state) is a more efficient OER electrocatalyst.[80] This will be discussed in more details later in the chapter. β- NiOOH and γ-NiOOH forms possess the same Ni-Ni distance, but γ-NiOOH exhibit an expanded crystal lattice such that the spacing between the

platelets are significantly greater than in the β- NiOOH phase (7 A^o for γ- NiOOH compared to 4.7 A^o for β- NiOOH).[107]
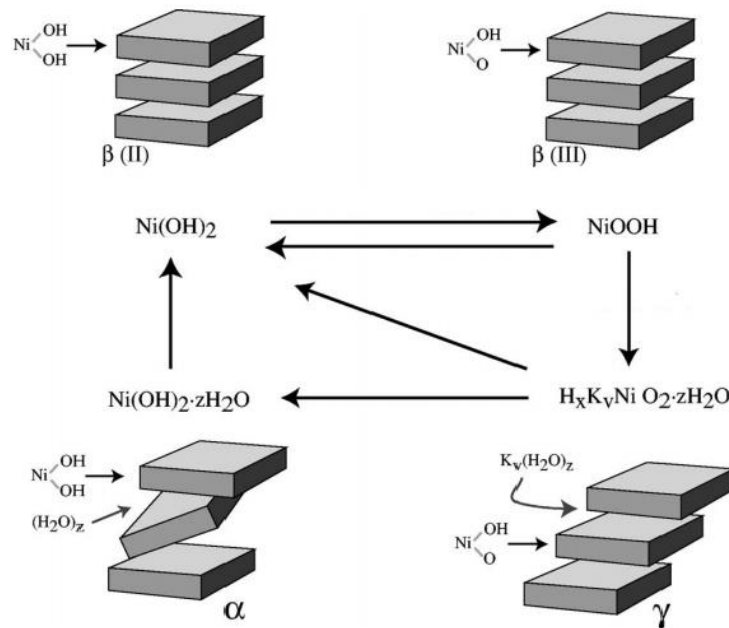
Figure 4.1: Bode diagram of Nickel hydroxide. Taken from reference 104.

Several studies reported that incorporating iron into nickel oxide electrocatalyst could enhance its OER performance.[79,108,109,110,111,85,83] In his early report in 1987, Corrigan investigated the effect of iron coprecipitation into amorphous nickel oxide on OER prepared by electrodeposition.[83] A decrease of 100 mV in the overpotential was observed with 10% coprecipitated iron while tafel slopes decreased from 70 to 25 mV/decade.[83] Electrodeposited Ni$_{12.85}$Fe$_{5.15}$ oxide from sulfate precursors has demonstrated the best catalytic activity for OER among the studied amorphous binary mixed-metal complexes having the smallest electron-transfer coefficient [109](α=0.008) in combination with relatively large exchange current density (J_o=9.04 μA/cm^2) in 1 M KOH, while amorphous Ni oxide exhibited an electron-transfer coefficient of 0.694 and J_o of 37.3 μA/cm^2 in 1 M KOH.[85] Landon et al reported high catalytic

activity at crystalline NiFe oxide (90:10), prepared via evaporation induced self-assembly followed by annealing at 300 $^{\circ}$C for 24 h, exhibiting 40 mV/decade tafel slope.[78] Louie and coworkers prepared amorphous mixed Ni-Fe oxide by electrodeposition from sulfate precursors, and showed that films with 40 % Fe had the lowest OER overpotential at 10 mA/cm^2.[86] The authors attributed the discrepancy in the optimal iron content between 10%[83,78,112] and 50%[113,86] found in the literature to the similar specific current densities and overpotential values obtained within this Fe composition range and showed using in situ Raman spectroscopy that aging of Ni films and Fe incorporation induce similar structural effects on Ni films which was further supported by tafel slope measurements.[86]

In this study, we aimed to investigate the effect of incorporating different amounts of iron in NiBi thin films prepared via electrodeposition. NiBi and mixed Ni$_{-x}$Fe$_x$Bi were studied electrochemically and kinetically using cyclic voltammetry and steady-state currents measurements. Turnover frequencies, tafel slopes, transfer coefficients, and exchange currents were extracted to assess the electrocatalytic behavior of the films and dependence on Fe content before and after electrochemical activation (anodization).

4.1 Cyclic Voltammetry Studies:

Ni oxo/hydroxo films were prepared on FTO by controlled potential electrolysis from a solution containing 0.4 mM Ni(NO$_3$)$_2$ in 0.1 M KBi pH 9.2. A total charge of 1 mC/cm^2 was passed during electrodeposition at a potential on 0.95 V vs Ag/AgCl. The depostion required a period of 40-60 seconds to be complete.
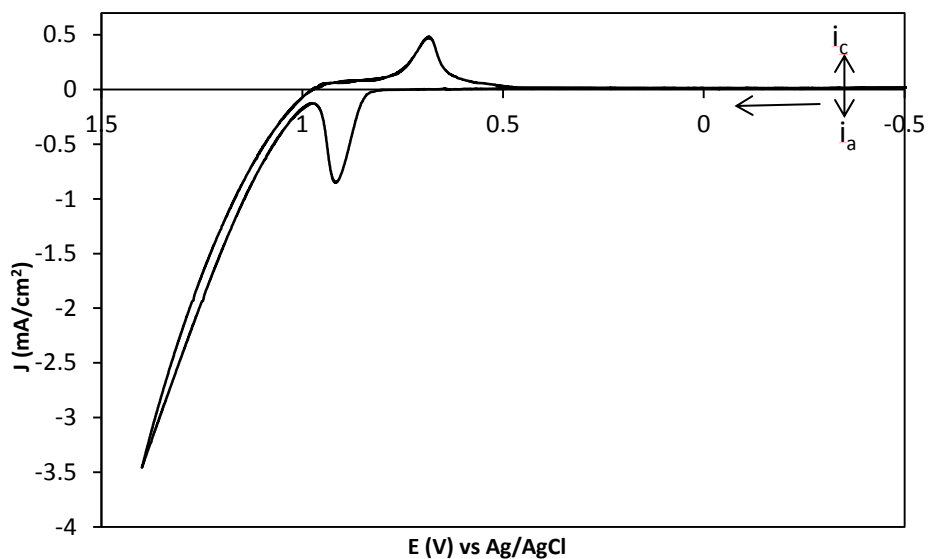
Figure 4.2: Cyclic voltammogram of NiBi film acquired in 1 M KBi electrolyte at pH 9.2. Scan rate is 100 mV/s.

Figure 4.2 presents the cyclic voltammogram of NiBi film acquired at 100 mV/s in 1 M KBi pH 9.2 scanned to the positive first then back to the negative potential. The plot displays a sharp anodic peak at 0.92 V vs Ag/AgCl corresponding to the oxidation of $Ni^{II}(OH)_2$ to $Ni^{III}O(OH)$. The return scan exhibits a cathodic peak at 0.69 V vs Ag/AgCl corresponding to the reduction of the surface adsorbed species formed from the oxidation in the initial scan.

The amount of charge passed during electrodeposition cannot be used to measure the amount of nickel in the film since oxygen evolution can occur with Ni electrodeposition and non-faradaic double-layer charging currents cannot be ignored for short deposition times.[80] Instead, the charge was calculated by intergrating the nickel cathodic peak ($NiO(OH) \rightarrow Ni(OH)_2$) from CV scanned at 10 mV/s and equaled to 0.4 mC/cm^2 on average. Bediako et al estimated the number of electrons transferred per Ni center by measuring the charge passed in the reduction of $Ni^{3.6+}$ to Ni^{2+} and subsequently digesting the film to determine Ni loading using ICP-MS which was

83

found to be 1.6 e$^-$/Ni center.[80] Knowing of the number of electrons transferred per nickel center and the charge under the cathodic peak, we calculated the number of moles of Ni centers by dividing the charge Q by Faraday's constant and the charge passed/Ni center. The integrated charge corresponded to 2-4 nmol Ni/cm^3 and the thickness of the film was approximated to be between 1-3 nm.[80] The obtained NiBi films had less Ni loading than the NiBi films reported by Bediako et al which had 7 nmol Ni/cm^2 (calculation is based on 1.6 e$^-$/Ni center) and were 8 nm thick.[114]
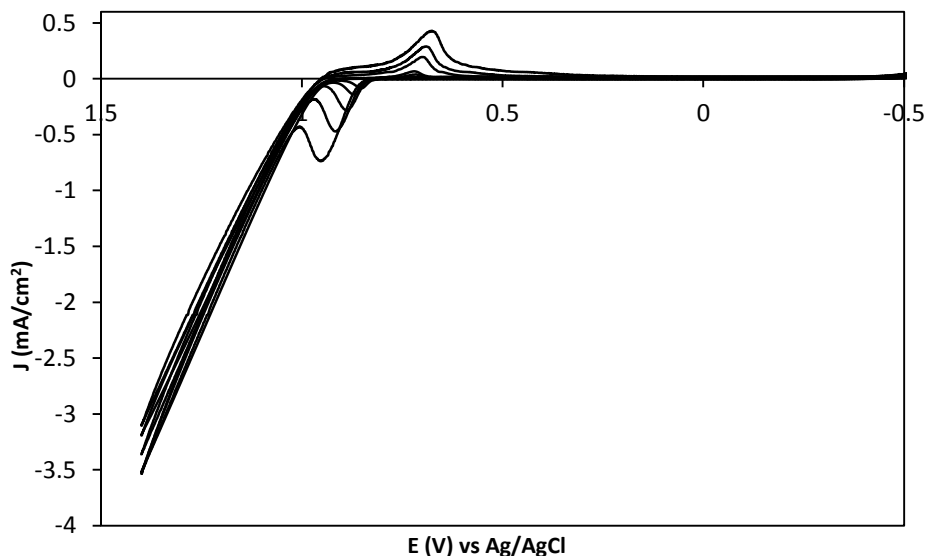
Figure 4.3: Cyclic voltammogram of NiBi film deposited on FTO in 1 M KBi at pH 9.2 at scan rate 10, 20, 50, 100, 200 mV/s, (charge passed during electrodeposition is equal to 1 mC/cm^2).

Figure 4.3 shows the cyclic voltammograms of NiBi film in 1 M KBi at pH 9.2 at different scan rates (10, 20, 50, 100, 200 mV/s). Note the catalytic activity of the film increases slightly with increasing the number of scans resulting from anodization of the film (discussed below). The peak currents corresponding to the oxidation and reduction of Nickel (Ni^{II}(OH)$_2$ $\leftrightarrow$ Ni^{III}O(OH)) increase with increasing scan rate. Figure 4.4 presents the plot of the cathodic peak current (i$_p$)

84

against the square root of the scan rate ($v^{1/2}$). One finds that i_p is linearly dependent on $v^{1/2}$ according to the following formula[115]:

$$i_p = (2.69 \times 10^5) n^{3/2} A D_0^{1/2} C_0 v^{1/2} \qquad (4.1)$$

Where A is the area, D_o is diffusion constant, C_o is the concentration and v is the scan rate.

NiBi films were expected to show a linear dependence of the peak current on the scan rate, since the reduction of Ni^{3+} is considered as an adsorption process on the surface of FTO, nonetheless a better fit was observed with the dependence of peak current on $v^{1/2}$. Since the process is a proton coupled electron transfer and the medium is basic (pH 9.2), the electron transfer could be limited by the diffusion of protons in the electrolyte which leads to the dependence of i_p on the $v^{1/2}$.
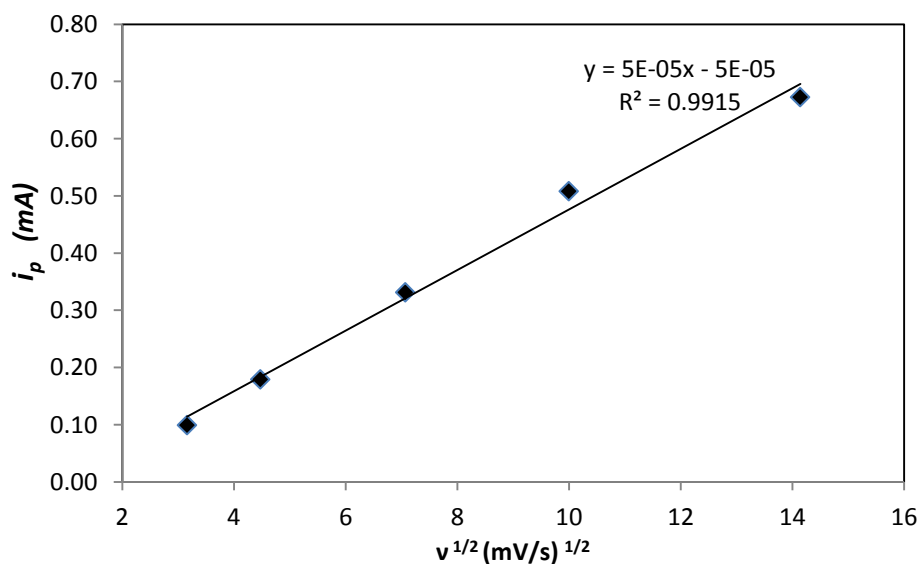
Figure 4.4: Plot of the peak current vs. the square root of the scan rate at NiBi film showing a linear dependence of i_p on $v^{1/2}$.

Mixed Ni/Fe oxo/hydroxo films (termed $Ni_{1-x}Fe_xBi$) were similarly prepared as NiBi films by controlled potential electrolysis at 0.95 V from a solution containing a mixture of

Ni(NO$_3$)$_2$/Fe(NO$_3$)$_3$ (0.4 mM total concentration) at the indicated ratio in 0.1 M KBi pH 9.2. NiBi

and Ni$_{1-x}$Fe$_x$Bi films can also be electrodeposited via cyclic voltammetry. Figure 4.5 shows the

cyclic voltammogram of 2 Ni$_{90}$Fe$_{10}$Bi films, one deposited by 5 CV scans (shown in red) and the

other by controlled potential electrolysis at 0.95 V vs Ag/AgCl and the passage of 1mC/cm^2

charge. From integrating the charge under the cathodic peak of Ni, the passage of 1 mC/cm^2 was

found to be equivalent to cycling the potential at 100 mV/s for 5 cycles.
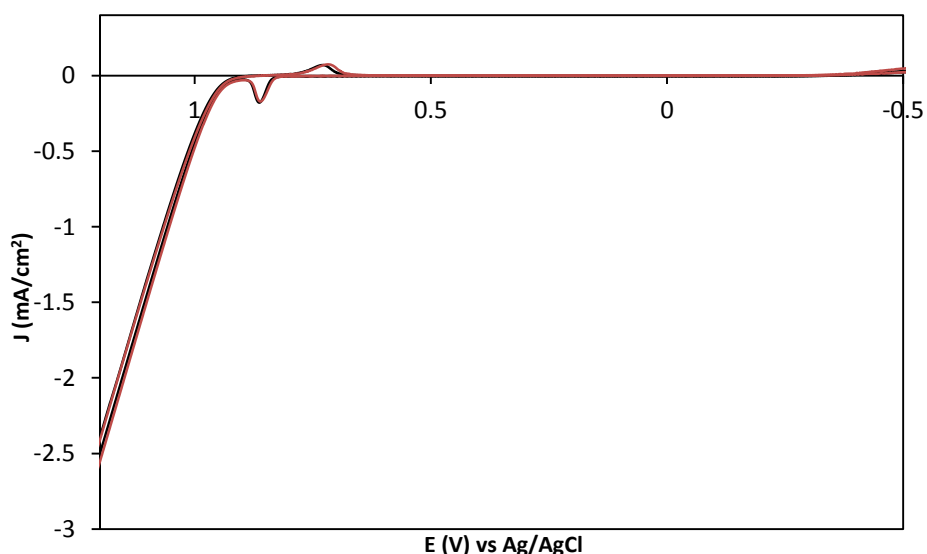
Figure 4.5: Cyclic voltammogram of Ni$_{90}$Fe$_{10}$Bi films deposited at 0.95 V vs Ag/AgCl set potential (black line) and by 5 CVs (red line) acquired in 1 M KBi (pH 9.2) and at 10 mV/s.

Thin NiBi films (termed NiBi$_{0.25}$) were similarly prepared by controlled potential electrolysis at

0.95 V vs Ag/AgCl from a solution containing 0.4 mM Ni(NO$_3$)$_2$ in 1 M KBi pH 9.2 but with the

passage of 0.25 mC/cm^2 instead of 1 mC/cm^2. NiBi$_{0.25}$ films had Ni loading (integrated charge)

in between Ni$_{60}$Fe$_{40}$Bi and Ni$_{40}$Fe$_{60}$Bi.

Figure 4.6 shows the cyclic voltammograms of the as-prepared NiBi, $Ni_{90}Fe_{10}Bi$, $Ni_{60}Fe_{40}Bi$, $Ni_{40}Fe_{60}Bi$, $NiBi_{0.25}$ and FeBi films in 1 M KBi at pH 9.2 at 10 mV/s. $Ni_{1-x}Fe_xBi$ films are termed in reference to the solution ratio, however this ratio does not necessarily indicate the ratio of Ni:Fe in the films. The inset shows that the anodic and cathodic peak currents corresponding to $Ni^{II}(OH)_2 \leftrightarrow Ni^{III}O(OH)$ are decreasing as the percentage composition of Fe is increasing in the deposition medium of $Ni_{1-x}Fe_xBi$ films. The graph shows that $Ni_{60}Fe_{40}Bi$ exhibits the highest catalytic activity followed by $Ni_{90}Fe_{10}Bi$, and then NiBi. The overpotential is calculated by subtracting the thermodynamic potential from the applied bias after compensating for ohmic resistance. The thermodynamic overpotential was calculated from Nernst equation as follows:

$$E(vsNHE) = 1.23V - 0.059pH + \frac{0.059}{4}\log 0.209 - 0.197V \qquad (4.2)$$

where 1.23 represents the standard potential for O_2/H_2O couple, 0.209 is the partial pressure of O_2 in the atmosphere at 293 K and 0.197 V is the standard redox potential of Ag/AgCl reference electrode to convert to NHE scale. At a current of 1 mA/cm^2, non-anodized catalyst films evolved O_2 with an overpotential of 679 ± 18 mV for NiBi (N=3), 674 ± 21 mV for $Ni_{90}Fe_{10}Bi$ (N=3), 637 ± 11 mV for $Ni_{60}Fe_{40}Bi$ (N=3), 691 ± 4 mV for $Ni_{40}Fe_{60}Bi$ (N=3) and 746 ± 35 mV for $NiBi_{0.25}$ (N=3) at near-neutral conditions of pH of 9.2 in 1 M KBi. At an activity of 1.5 mA/cm^2, non-anodized catalyst films evolved O_2 with an overpotential of 708 ± 18 mV for NiBi (N=3), 706 ± 20 mV for $Ni_{90}Fe_{10}Bi$ (N=3), 678 ± 19 mV for $Ni_{60}Fe_{40}Bi$ (N=3), 759 ± 4 mV for $Ni_{40}Fe_{60}Bi$ (N=3) and 797 ± 39 mV for $NiBi_{0.25}$ (N=3) in 1 M KBi pH 9.2 (see figure 4.7).
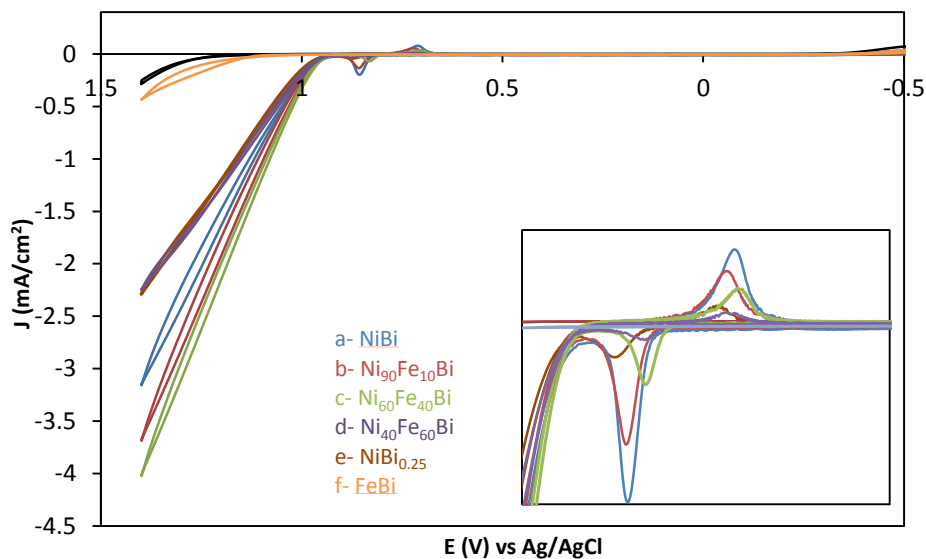
Figure 4.6: Cyclic voltammograms of the as-prepared NiBi, $Ni_{90}Fe_{10}Bi$, $Ni_{60}Fe_{40}Bi$, $Ni_{40}Fe_{60}Bi$, $NiBi_{0.25}$, and FeBi acquired at 10 mV/s in 1 M KBi pH 9.2. CV of bare FTO is shown in black. The inset shows the decrease in the nickel peaks with increasing Fe content in $Ni_{1-x}Fe_xBi$.
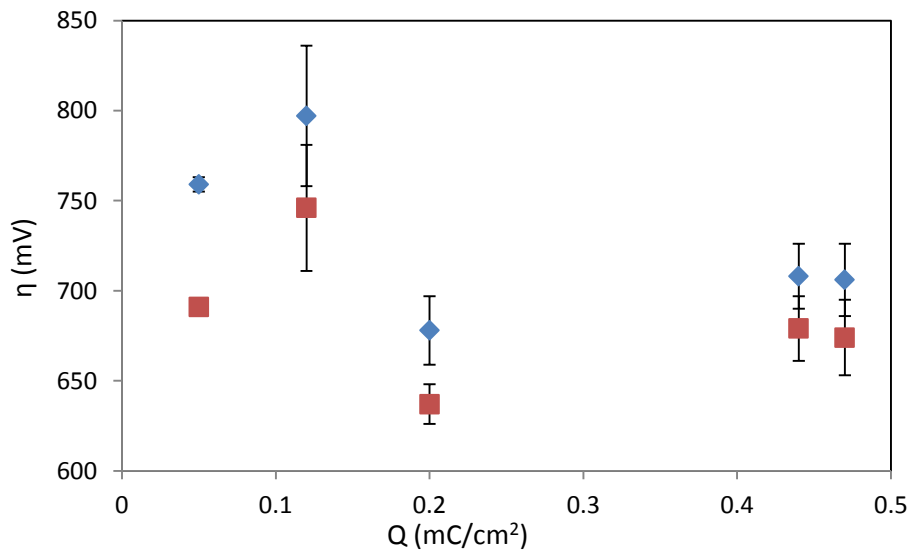
Figure 4.7: Overpotentials at 1 mA/cm^2 (red) and at 1.5 mA/cm^2 (blue) for as-prepared NiBi (0.44 mC/cm^2), $Ni_{90}Fe_{10}Bi$ (0.47 mA/cm^2), $Ni_{60}Fe_{40}Bi$ (0.20 mA/cm^2), $Ni_{40}Fe_{60}Bi$ (0.05 mA/cm^2), and $NiBi_{0.25}$ (0.12 mA/cm^2).

Previous reports showed that NiBi films require oxidative treatment (termed anodization) to attain a high OER catalytic activity.[80] Bediako et al studied the effect of anodization of NiBi films and showed that anodization induces significant structural changes and increases the population of Ni (IV) centers. The mean oxidation state was reported to increase from +3.16 to +3.6 during anodization.[80] The as-prepared NiBi film was found to be structurally analogous to β-NiOOH exhibiting Jahn-Teller distorted coordination geometry, while anodized NiBi films were similar to γ-NiOOH exhibiting edge-sharing NiO octahedra arranged into higher-order layers.[80]

Films were anodized following electrodeposition in stirred 1 M KBi solution by holding the potential at 0.9 V for 3 hours. Figure 4.8 presents an amperometric i-t plots that follows the anodization of NiBi and $Ni_{90}Fe_{10}Bi$ films. The current increased by an order of magntitude in the course of anodization with the steepest change observed during the first 20 min and almost a steady-state plateau after 3 hours.
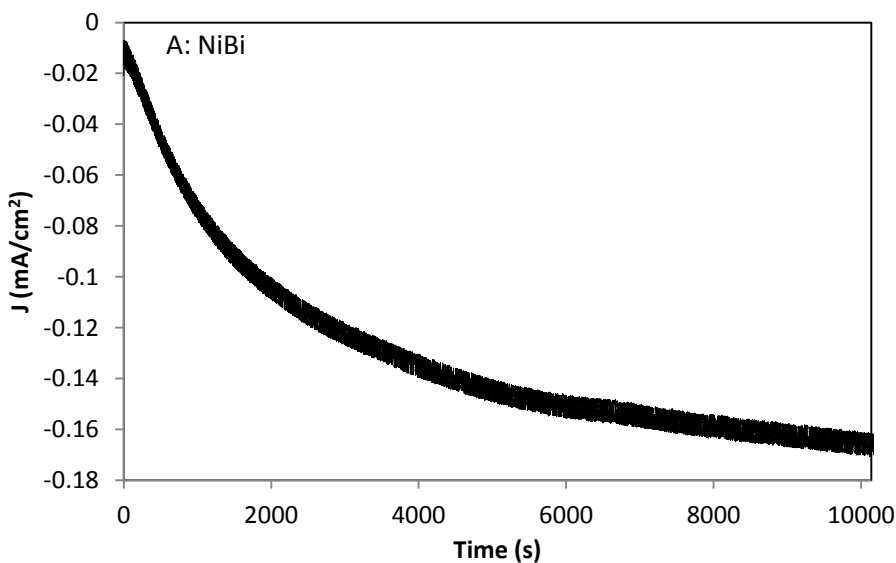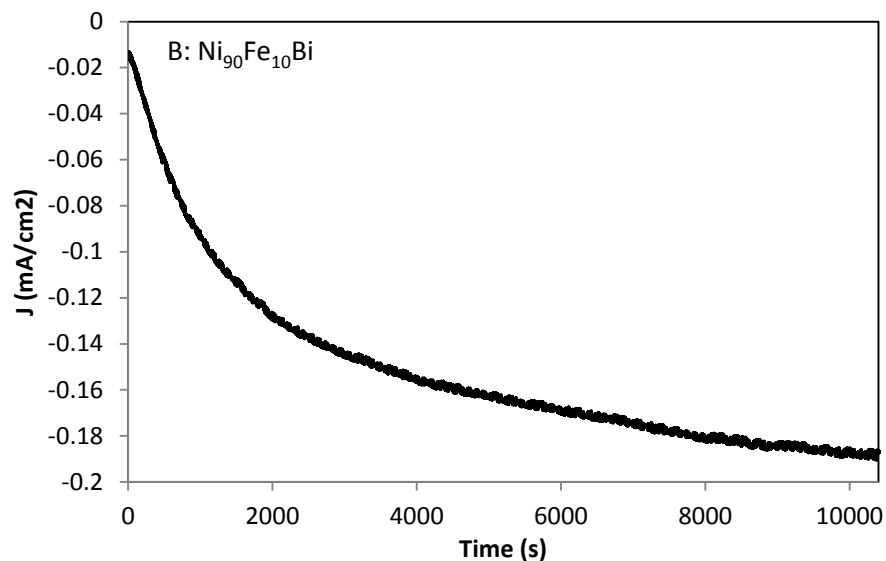
Figure 4.8: Amperiometric i-t plots showing the anodization of NiBi (A) and $Ni_{90}Fe_{10}Bi$ (B) films which was carried for 3 hours by setting the potential at 0.9 V vs Ag/AgCl. The current increased by an order of magnitude after anodization.

Figure 4.9 shows cyclic voltammograms of the as-prepared and anodized films. During anodization, the efficiency of the films towards enhancing OER activity increases drastically; at an overpotential of 500 mV, the currents obtained are one to several orders of magnitude higher after anodization. NiBi and $Ni_{90}Fe_{10}Bi$ exhibited greater anodic and cathodic Ni-oxo/hydroxo peak currents after anodization, however $Ni_{60}Fe_{40}Bi$ and $Ni_{40}Fe_{60}Bi$ exhibited decreased anodic and cathodic Ni-oxo/hydroxo peak currents after anodization. Note the Ni-oxo/hydroxo peak current for $NiBi_{0.25}$ increased after anodization which is consistent with the thicker NiBi films.
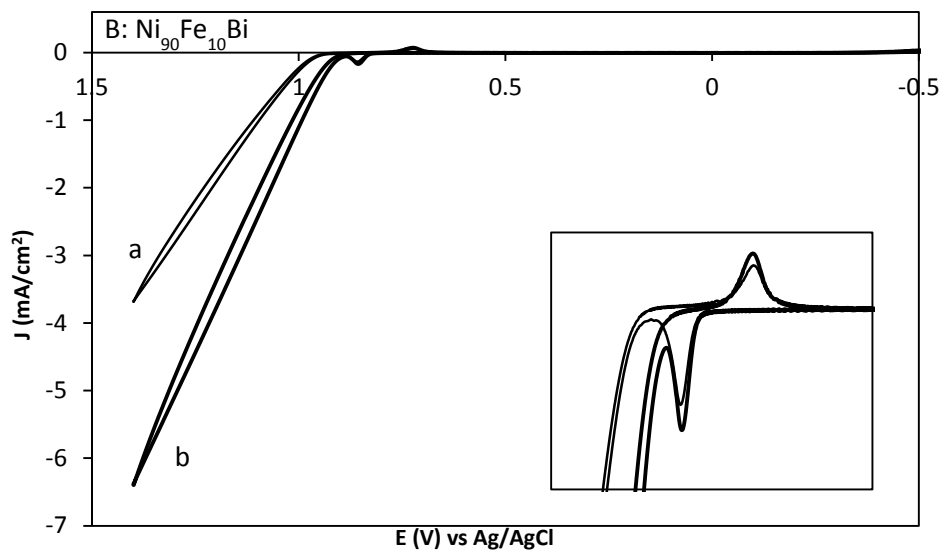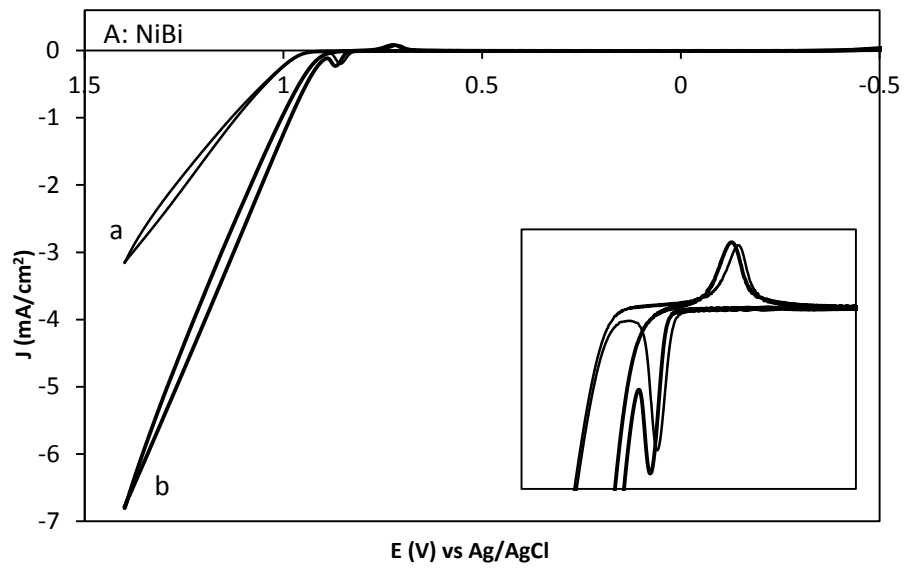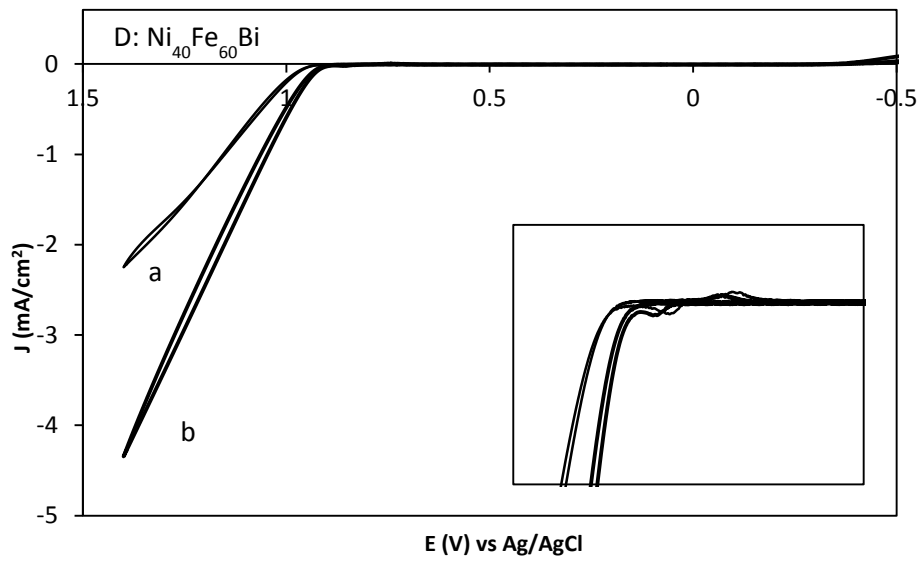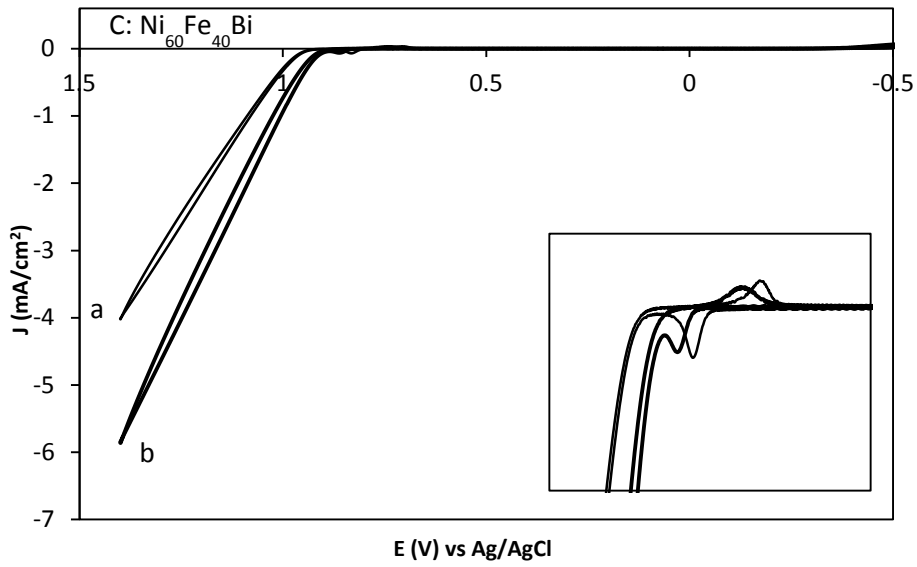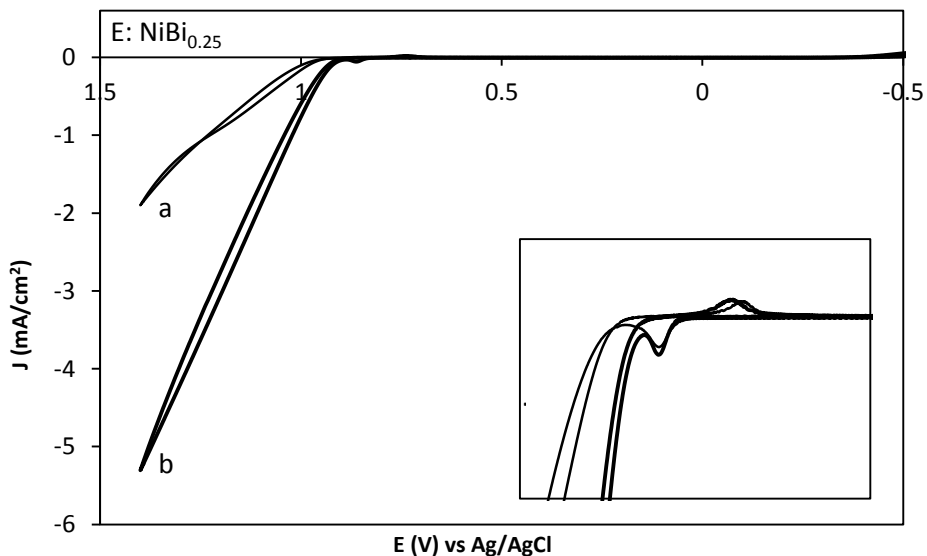
Figure 4.9: Cyclic voltammograms of NiBi (A), $Ni_{90}Fe_{10}Bi$ (B), $Ni_{60}Fe_{40}Bi$ (C), $Ni_{40}Fe_{60}Bi$ (D) and $NiBi_{0.25}$ (E) before (a) and after anodization (b) acquired at 10 mV/s in 1 M KBi pH 9.2.

Cyclic voltammograms of the anodized NiBi, $Ni_{90}Fe_{10}Bi$, $Ni_{60}Fe_{40}Bi$, and $Ni_{40}Fe_{60}Bi$ films are presented in figure 4.10. Anodized NiBi and $Ni_{90}Fe_{10}Bi$ show similar catalytic activity requiring 452 ± 10 mV (N=3) and 448 ± 15 mV (N=3) to evolve O_2 at 1 mA/cm^2. Slightly greater overpotential was required at $Ni_{60}Fe_{40}Bi$ and $Ni_{40}Fe_{60}Bi$ equaling 459 ± 9 mV (N=3) and 478 ± 12 mV (N=3) to maintain an activity of 1 mA/cm^2, respectively. This corresponds to a decrease by 227 mV, 219 mV, 177 mV and 212 mV for anodized NiBi, $Ni_{90}Fe_{10}Bi$, and $Ni_{60}Fe_{40}Bi$ films, respectively. $Ni_{60}Fe_{40}Bi$ and $Ni_{40}Fe_{60}Bi$ required higher overpotential than NiBi films and $Ni_{90}Fe_{10}Bi$ but when compared to the thin NiBi films ($NiBi_{0.25}$) which required 504 ± 27 mV, the mixed NiFe catalyst required less overpotential and thus exhibited higher activity. The overpotential required by the films to produce a current of 1.5 mA/cm^2 in 1 M KBi pH 9.2 was as follows: 461 ± 13 mV for NiBi, 457 ± 21 mV for $Ni_{90}Fe_{10}Bi$, 469 ± 11 mV for $Ni_{60}Fe_{40}Bi$, 490 ± 4 mV for $Ni_{40}Fe_{60}Bi$, and 523 ± 35 mV for $NiBi_{0.25}$ (see figure 4.11). The lower

93

overpotential required by NiBi than $NiBi_{0.25}$ is attributed to the greater number of active Ni centers in NiBi films. The lower overpotential required by $Ni_{60}Fe_{40}Bi$ and $Ni_{40}Fe_{60}Bi$ compared to $NiBi_{0.25}$ could be indicative of higher OER catalytic activity due to the presence of iron.
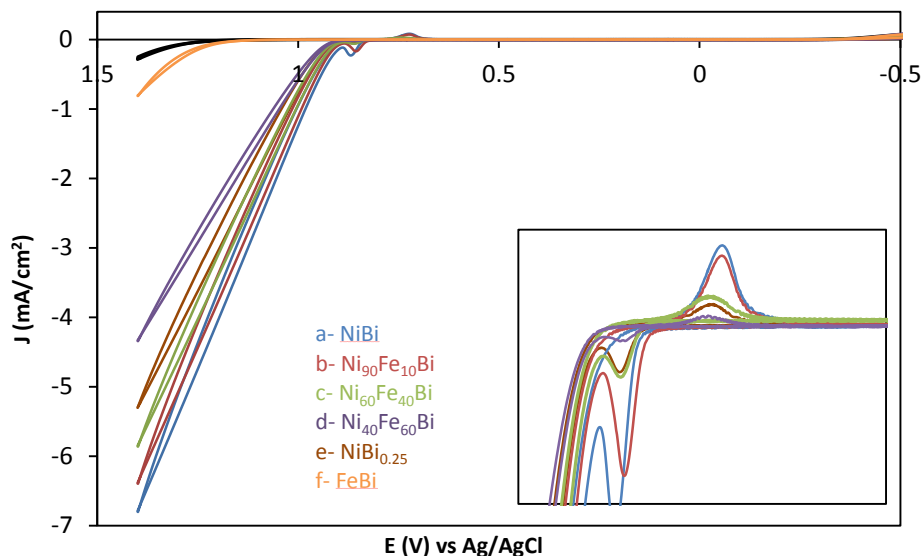
Figure 4.10: Cyclic voltammograms of anodized NiBi, $Ni_{90}Fe_{10}Bi$, $Ni_{60}Fe_{40}Bi$, $Ni_{40}Fe_{60}Bi$, $NiBi_{0.25}$, and FeBi acquired at 10 mV/s in 1 M KBi pH 9.2. CV of bare FTO is shown in black. The inset shows a close up on the Ni oxo/hydroxo peaks.
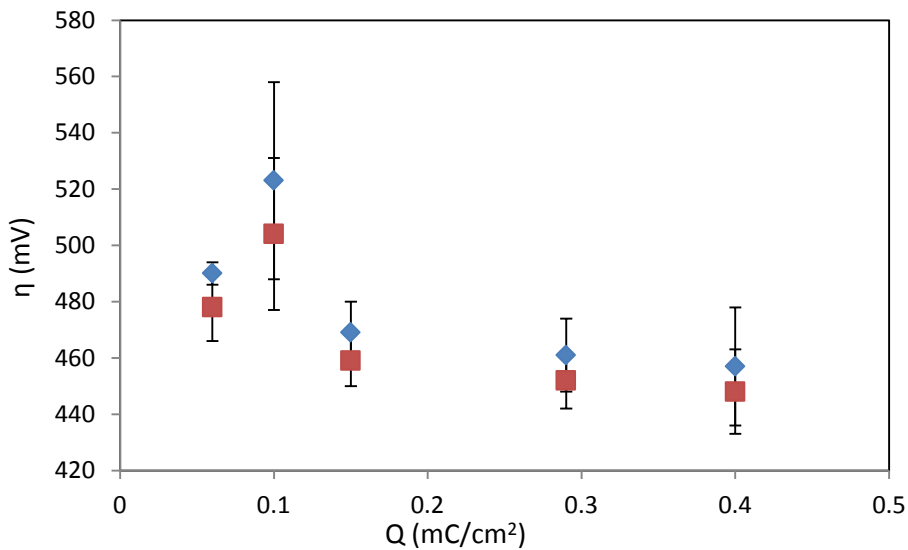
Figure 4.11: Overpotentials at 1 mA/cm^2 (red) and at 1.5 mA/cm^2 (blue) for anodized NiBi (0.29 mC/cm^2), Ni$_{90}$Fe$_{10}$Bi (0.40 mA/cm^2), Ni$_{60}$Fe$_{40}$Bi (0.15 mA/cm^2), Ni$_{40}$Fe$_{60}$Bi (0.06 mA/cm^2), and NiBi$_{0.25}$ (0.10 mA/cm^2).

As a control experiment, we prepared NiBi film by passing 1mC/cm^2 charge in an electrodeposition bath containing 0.16 mM Ni(NO$_3$)$_2$ in 0.1 M KBi solution, which has the same concentration of Ni(NO$_3$)$_2$ present in solutions used to prepare Ni$_{40}$Fe$_{60}$Bi films. Figure 4.12 shows the cyclic voltammogram for the film prepared in the diluted Ni(NO$_3$)$_2$ electrodeposition bath which looks very similar to NiBi film prepared from 0.4 mM Ni(NO$_3$)$_2$ solution. The as-prepared film exhibited similar charge (0.31 mC/cm^2) as NiBi films prepared from 0.4 mM Ni(NO$_3$)$_2$ indicating that the same amount of Ni deposit irrespective of initial concentration of the Ni(NO$_3$)$_2$ (in the absence of iron).
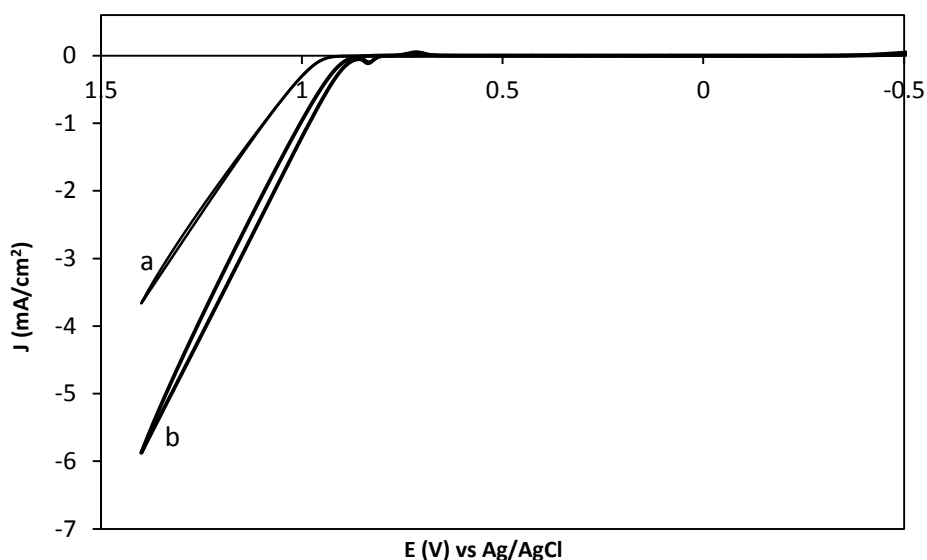
Figure 4.12: Cyclic voltammogram of NiBi film prepared by passing 1 mC/cm^2 charge in an electrodeposition bath containing 0.16 mM Ni^{2+} in 0.1 M KBi pH 9.2, before (a) and after anodization (b) acquired at 10 mV/s in 1 M KBi pH 9.2.

To asses the effect of iron if we assume that the Ni centers are the active sites, currents were normalized to the amount of Ni in each film. Figure 4.13 displays the normalized current (I/Q) of

NiBi (0.55 mC/cm^2), Ni$_{90}$Fe$_{10}$Bi (0.39 mC/cm^2), Ni$_{60}$Fe$_{40}$Bi (0.21 mC/cm^2), Ni$_{40}$Fe$_{60}$Bi (0.07 mC/cm^2), and NiBi$_{0.25}$ (0.14 mC/cm^2) before and after anodization. As-prepared and anodized NiBi and Ni$_{90}$Fe$_{10}$Bi exhibited the smallest normalized currents. Ni$_{40}$Fe$_{60}$Bi exhibited the highest normalized currents (i.e. current per active Ni site) before or after anodization although the cyclic voltammograms showed that such films exhibited the smallest current density. The normalized current for the as-prepared Ni$_{60}$Fe$_{40}$Bi were slightly higher than the thin as-prepared NiBi$_{0.25}$ film. On the other hand, the anodized NiBi$_{0.25}$ films exhibited slightly higher normalized currents than the anodized Ni$_{60}$Fe$_{40}$Bi at high overpotential. If Fe had no effect on enhancing the catalytic activity of NiBi films, then the normalized activity should be proportional to charge of Ni thus NiBi$_{0.25}$ (0.14 mC/cm^2) should exhibit normalized currents just halfway between the normalized currents of Ni$_{60}$Fe$_{40}$Bi (0.21 mC/cm^2) and Ni$_{40}$Fe$_{60}$Bi (0.07 mC/cm^2). Since this was not the case (before anodization, I/Q$_{NiBi0.25}$ was lower than those of Ni$_{60}$Fe$_{40}$Bi and Ni$_{40}$Fe$_{60}$Bi, and after anodization I/Q$_{NiBi0.25}$ was comparable to that of Ni$_{60}$Fe$_{40}$Bi), one can conclude that Fe is enhancing the activity of Ni$_{1-x}$Fe$_x$Bi.
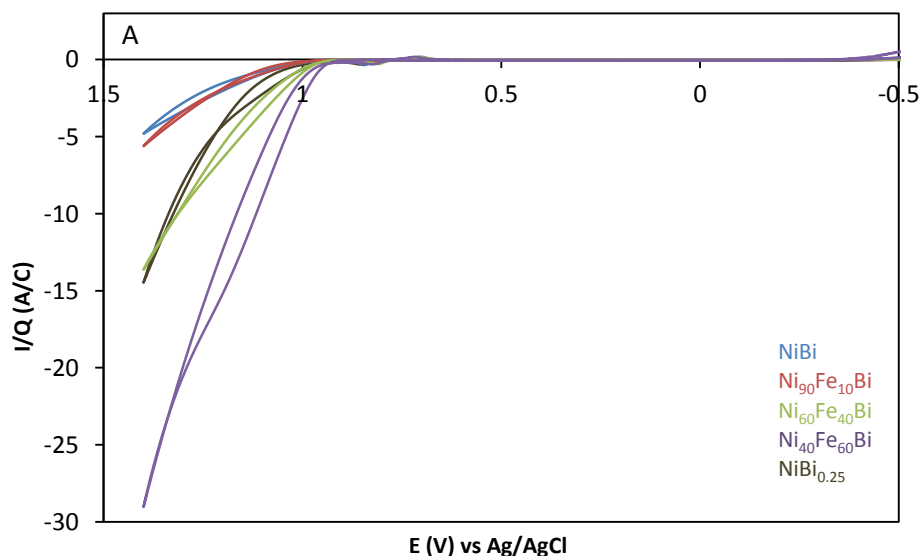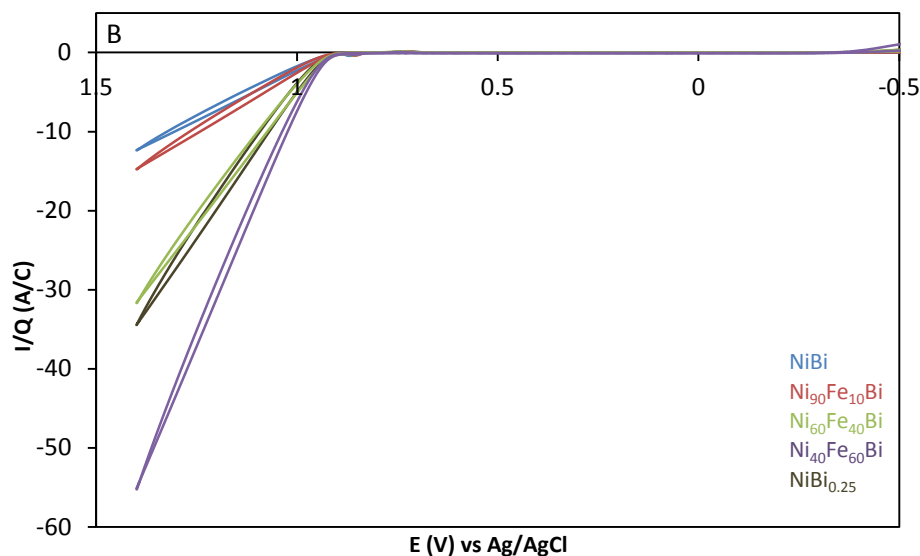
Figure 4.13: Normalized currents (I/Q) plotted against the potential of NiBi, $Ni_{90}Fe_{10}Bi$, $Ni_{60}Fe_{40}Bi$, $Ni_{40}Fe_{60}Bi$, and $NiBi_{0.25}$ before (A) and after anodization (B).

4.2 Turnover Frequency Calculations:

The turnover frequency is defined as the number of times per second a single active site (a metal center) evolves an oxygen molecule by accepting 4 electrons from water.[108] Since the TOF depends on the current and the current produced depends on the applied potential (and hence the overpotential) in accordance with butler-voltmer kinetics model[115], the overpotential at which the TOF values are calculated should be reported. To calculate TOF in this study, the following assumptions were made: 1) all the nickel centers that are electrochemically active (in the Ni cathodic peak) are catalytically active for oxygen evolution, 2) the charge passed during oxidation and reduction of the film is governed by the transfer of 1.6 electrons per nickel center as was established by Bediako et al[80], and it is independent of the iron atoms present, 3) catalytically active sites are assumed to be the nickel centers only (iron centers are not involved in the calculation). TOF was calculated from the following relation:

$$TOF = \frac{JA}{Fn} \qquad (4.3)$$

Where η is the overpotential which was calculated by subtracting the equilibrium potential (E^o) from the applied bias after compensating for ohmic resistance. The equilibrium potential was calculated from Nernst equation (as discussed in equation 2).

In equation 4.3, J represents the current density at an overpotential of 400 mV which was extracted from cyclic voltammograms of the films at a scan rate of 10 mV/s, A is the area of the electrodeposited film, F is Faraday's constant which is equal to 96485 C mol^{-1}, and n is the number of moles of Ni centers in each film. The currents were extracted from CV (rather than from steady state) to compare TOF before and after anodization since measuring steady state currents for the as-prepared films can lead to anodization. It is worth noting that the TOF for anodized films do not differ if the current was extracted from CV or from steady state. The number of moles of the electrodeposited Ni was estimated by intergrating the charge under the cathodic peak and dividing it by Faraday's constant and 1.6 (which corresponds the electron transfer per Ni center).

 Table 4.1 shows the charges on the 3 as-prepared films each of NiBi, $Ni_{90}Fe_{10}Bi$, $Ni_{60}Fe_{40}Bi$, $Ni_{40}Fe_{60}Bi$, and $NiBi_{0.25}$ which was obtained from the integrated Ni^{III}/Ni^{II} cathodic peak, the geometric area of the film which was measured, the number of moles of Ni present calculated from Faraday's law, the current density produced at each film at overpotentials of 400 mV and 500 mV obtained from CVs at 10 mV/s, and the calculated turnover frequencies at 400 mV and 500 mV.

Sample	Q (C)	A (cm²)	Q/A (C /cm²)	n (nmol)	J (mA/cm²) at 400 mV	J (mA/cm²) at 500 mV	TOF at 400 mV (s⁻¹)	TOF at 500 mV (s⁻¹)
NiBi (1)	3.42E-04	1.1	3.11E-04	2.01	2.79E-05	4.79E-05	0.04	0.07
NiBi (2)	6.05E-04	1.2	5.04E-04	3.27	2.02E-05	2.94E-05	0.02	0.03
NiBi (3)	5.46E-04	1.1	4.96E-04	3.22	2.66E-05	8.15E-05	0.02	0.07
NiBi				**2.83 ± 0.58**			**0.03 ± 0.01**	**0.06 ± 0.02**
$Ni_{90}Fe_{10}Bi$ (1)	3.90E-04	1.1	3.55E-04	2.30	3.53E-05	3.65E-05	0.04	0.05
$Ni_{90}Fe_{10}Bi$ (2)	4.60E-04	1.32	3.48E-04	2.26	2.84E-05	6.56E-05	0.04	0.10
$Ni_{90}Fe_{10}Bi$ (3)	6.88E-04	0.99	6.95E-04	4.50	3.13E-05	5.94E-05	0.02	0.03
$Ni_{90}Fe_{10}Bi$				**3.02 ± 1.02**			**0.04 ± 0.01**	**0.06 ± 0.03**
$Ni_{60}Fe_{40}Bi$ (1)	1.96E-04	1.2	1.63E-04	1.06	2.05E-05	1.24E-04	0.06	0.37
$Ni_{60}Fe_{40}Bi$ (2)	2.08E-04	1.2	1.73E-04	1.12	1.66E-05	9.83E-05	0.05	0.27
$Ni_{60}Fe_{40}Bi$ (3)	2.72E-04	1.1	2.47E-04	1.60	2.18E-05	9.01E-05	0.04	0.16
$Ni_{60}Fe_{40}Bi$				**1.26 ± 0.24**			**0.05 ± 0.01**	**0.27 ± 0.08**
$Ni_{40}Fe_{60}Bi$ (1)	6.76E-05	1.32	5.12E-05	0.33	1.09E-05	5.50E-05	0.11	0.57
$Ni_{40}Fe_{60}Bi$ (2)	5.72E-05	1.2	4.77E-05	0.31	1.21E-05	7.69E-05	0.12	0.77
$Ni_{40}Fe_{60}Bi$ (3)	7.02E-05	1.1	6.38E-05	0.41	1.87E-05	6.02E-05	0.13	0.42
$Ni_{40}Fe_{60}Bi$				**0.35 ± 0.05**			**0.12 ± 0.01**	**0.59 ± 0.15**
$NiBi_{0.25}$ (1)	1.37E-04	1.54	8.88E-05	0.58	2.40E-05	3.21E-05	0.17	0.22
$NiBi_{0.25}$ (2)	1.89E-04	1.32	1.43E-04	0.93	2.83E-05	3.80E-05	0.10	0.14
$NiBi_{0.25}$ (3)	1.59E-04	1.21	1.32E-04	0.85	3.00E-05	2.47E-05	0.11	0.09
$NiBi_{0.25}$				**0.79 ± 0.15**			**0.12 ± 0.03**	**0.15 ± 0.05**

Table 4.1: Table showing the integrated charge, number of moles, current density, TOF and the overpotential required to evolve O_2 at 1 mC /cm² for the different studied NiBi, $Ni_{90}Fe_{10}Bi$, $Ni_{60}Fe_{40}Bi$, $Ni_{40}Fe_{60}Bi$, $NiBi_{0.25}$ films prior to anodization. The calculated average and standard deviation are shown in bold.

TOF's calculated for the as-prepared non-anodized NiBi, $Ni_{90}Fe_{10}Bi$, $Ni_{60}Fe_{40}Bi$, $Ni_{40}Fe_{60}Bi$, and

$NiBi_{0.25}$ films at an overpotential of 500 mV were 0.06 (±0.02) s⁻¹, 0.06 (±0.03) s⁻¹, 0.27 (±0.08)

s⁻¹, 0.59 (±0.15) s⁻¹, and 0.15 (±0.05) s⁻¹, respectively. At lower overpotential (400 mV), lower

TOF were calculated for all the films. TOF's for the non-anodized films at 400 mV were as

follows: 0.03 ($\pm$0.01) s^{-1} for NiBi, 0.04 ($\pm$0.01) s^{-1} for $Ni_{90}Fe_{10}Bi$, 0.05 ($\pm$0.01) s^{-1} for $Ni_{60}Fe_{40}Bi$, 0.12 ($\pm$0.01) s^{-1} for $Ni_{40}Fe_{60}Bi$, and 0.12 ($\pm$0.03) s^{-1} for $NiBi_{0.25}$. $Ni_{40}Fe_{60}Bi$ exhibited the highest TOF at both overpotentials compared to films prepared at 1 mC/cm^2 implying that it is the most catalytic film under non-anodization regime, while trace amount of iron deliberately introduced in solution as in the case of $Ni_{90}Fe_{10}Bi$ did not have an effect on enhancing the TOF; NiBi and $Ni_{90}Fe_{10}Bi$ had comparable TOFs. When compared to NiBi, $NiBi_{0.25}$ (having 3.6 times less charge) had 4.1 times higher TOF at the low overpotential and 2.7 times higher TOF at the high overpotential. While $NiBi_{0.25}$ and $Ni_{40}Fe_{60}Bi$ had comparable TOFs at 400 mV overpotential, at the higher overpotential (500 mV) $Ni_{40}Fe_{60}Bi$ exhibited more than 5 times higher TOF than $NiBi_{0.25}$. This indicates that the decreased integrated charge and presence of iron are both leading to higher TOF and that the effect of iron is more apparent at higher overpotentials (and hence higher currents). NiBi prepared in 0.16 mM $Ni(NO_3)_2$ electrodeposition bath exhibited a similar TOF of 0.027 s^{-1} at η = 400 mV to the NiBi films prepared from 0.4 mM $Ni(NO_3)_2$.

Table 4.2 shows the charges of the same NiBi, $Ni_{90}Fe_{10}Bi$, $Ni_{60}Fe_{40}Bi$, $Ni_{40}Fe_{60}Bi$, and $NiBi_{0.25}$ studied above but after their anodization, the geometric area of the films, the number of moles of Ni present, the current density produced at each film at overpotentials of 400 mV and 500 mV, and the calculated turnover frequencies at 400 mV and 500 mV.

Sample	Q (C)	A (cm²)	Q/A (C /cm²)	n (nmol)	J (mA/cm²) at 400 mV	J (mA/cm²) at 500 mV	TOF at 400 mV (s⁻¹)	TOF at 500 mV (s⁻¹)
NiBi (1)	1.78E-04	1.1	1.61E-04	1.05	5.94E-05	2.32E-03	0.16	6.32
NiBi (2)	3.90E-04	1.2	3.25E-04	2.11	1.27E-04	6.15E-03	0.19	9.08
NiBi (3)	4.34E-04	1.1	3.95E-04	2.56	1.16E-04	5.04E-03	0.13	5.62
NiBi				**1.90 ± 0.63**			**0.16 ± 0.02**	**7.01 ± 1.49**
$Ni_{90}Fe_{10}Bi$ (1)	3.80E-04	1.1	3.45E-04	2.24	5.73E-05	4.97E-03	0.07	6.33

Ni$_{90}$Fe$_{10}$Bi (2)	3.82E-04	1.32	2.89E-04	1.87	6.44E-05	1.97E-03	0.12	3.59
Ni$_{90}$Fe$_{10}$Bi (3)	5.60E-04	0.99	5.66E-04	3.66	1.32E-04	5.57E-03	0.09	3.90
Ni$_{90}$Fe$_{10}$Bi				**2.59 ± 0.77**			**0.09 ± 0.02**	**4.61 ± 1.22**
Ni$_{60}$Fe$_{40}$Bi (1)	1.14E-04	1.2	9.50E-05	0.62	3.39E-05	2.44E-03	0.17	12.33
Ni$_{60}$Fe$_{40}$Bi (2)	1.26E-04	1.2	1.05E-04	0.68	3.88E-05	3.01E-03	0.18	13.76
Ni$_{60}$Fe$_{40}$Bi (3)	2.78E-04	1.1	2.53E-04	1.64	5.20E-05	2.94E-03	0.09	5.12
Ni$_{60}$Fe$_{40}$Bi				**0.98 ± 0.47**			**0.15 ± 0.04**	**10.40 ± 3.78**
Ni$_{40}$Fe$_{60}$Bi (1)	6.96E-05	1.32	5.27E-05	0.34	1.74E-05	1.84E-03	0.17	18.43
Ni$_{40}$Fe$_{60}$Bi (2)	6.40E-05	1.2	5.33E-05	0.35	1.70E-05	1.78E-03	0.15	16.02
Ni$_{40}$Fe$_{60}$Bi (3)	7.76E-05	1.1	7.05E-05	0.46	2.20E-05	2.20E-03	0.14	13.72
Ni$_{40}$Fe$_{60}$Bi				**0.38 ± 0.05**			**0.16 ± 0.02**	**16.06 ± 1.92**
NiBi$_{0.25}$ (1)	1.78E-04	1.54	1.15E-04	0.75	3.00E-05	1.34E-03	0.16	7.16
NiBi$_{0.25}$ (2)	1.16E-04	1.32	8.76E-05	0.57	4.54E-05	9.58E-04	0.27	5.78
NiBi$_{0.25}$ (3)	1.23E-04	1.21	1.02E-04	0.66	3.75E-05	4.74E-04	0.18	2.25
NiBi$_{0.25}$				**0.66 ± 0.07**			**0.20 ± 0.05**	**5.06 ± 2.07**

Table 4.2: Table showing the integrated charge, number of moles, current density, TOF and the overpotential required to evolve O_2 at 1 mC /cm^2 for the different studied NiBi, Ni$_{90}$Fe$_{10}$Bi, Ni$_{60}$Fe$_{40}$Bi, Ni$_{40}$Fe$_{60}$Bi, NiBi$_{0.25}$ films following their anodization. The calculated average and standard deviation are shown in bold.

The decreased Ni-oxo/hydroxo integrated charge after anodization in some films could be indicative of loss of active Ni centers in the film. Yet, the current densities for oxygen evolution in all the films increased after anodization with the highest increase observed for NiBi films. Anodization has caused significant enhancement in the OER activity especially for NiBi films where TOFs have increased from 0.03 (± 0.01) to 0.16 (± 0.02) s^{-1} corresponding to more than 5 times increase at 400 mV overpotential. Trotochaud et al obtained the same TOF values for NiO$_x$ but at higher pH in 1 M KOH and at an overpotential of 300 mV (considering a 1 e$^-$ transfer). TOF values reported by Bediako et al for 7 nmol/cm^2 anodized NiBi films were 0.9 s^{-1} at 400 mV overpotential in 1 M KBi and 1.7 s^{-1} in 1 M KOH at 325 mV (assuming the process involves 1.6

e$^-$ transfer). NiBi$_{0.25}$ still showed the highest TOF (0.20 ± 0.05 s^{-1}) at 400 mV overpotential after anodization. Lower TOF was calculated for the anodized Ni$_{1-x}$Fe$_x$Bi films at 400 mV overpotential with the lowest value for Ni$_{90}$Fe$_{10}$Bi (0.09 ± 0.02 s^{-1}). In a recent study, Trotochaud et al proposed that perhaps iron traces present in reagent grade salts and electrolytes are getting incorporated into the NiOOH structure during the course of anodization since earlier reports showed that the ordered β-NiOOH is more catalytically active than the disordered γ-NiOOH formed during anodization.[108] Non-anodized Ni$_{90}$Fe$_{10}$Bi exhibited much lower TOF than anodized NiBi which could mean that Fe does not play a role in enhancing the OER activity during the course of anodization and it is only the Ni which is undergoing structural changes, responsible for the increased OER performance. TOF calculated at higher overpotential (500 mV) showed that anodized Ni$_{40}$Fe$_{60}$Bi exhibit the highest TOF of 16.06 (± 1.92) s^{-1}, followed by Ni$_{60}$Fe$_{40}$Bi (10.40 ± 3.78 s^{-1}), while NiBi and Ni$_{90}$Fe$_{10}$Bi exhibited lower TOF of 7.01 ± 1.49 s^{-1} and 4.61 ± 1.22 s^{-1}, respectively. TOF calculated at 500 mV for NiBi$_{0.25}$ (5.06 ± 2.07 s^{-1}) were lower than Ni$_{60}$Fe$_{40}$Bi and Ni$_{40}$Fe$_{60}$Bi which further confirm that the presence of iron in the film is enhancing the catalytic activity of the films. It is worth noting that all the films exhibited higher TOF following their anodization. Since anodized NiBi films exhibited higher TOF than non-anodized Ni$_{60}$Fe$_{40}$Bi and Ni$_{40}$Fe$_{60}$Bi films and since NiBi exhibited the largest change after anodization, one can infer that 1) anodization causes structural change different from Fe incorporation and that 2) Fe incorporation possibly causes different structure which also becomes more OER catalytically active upon anodization.

At low overpotential, incorporating iron in the films did not result in increased TOF (and hence OER activity) in both anodized and non-anodized films. Although non-anodized Ni$_{60}$Fe$_{40}$Bi and non-anodized Ni$_{40}$Fe$_{60}$Bi film had higher TOF than non-anodized NiBi films, TOF for the thin

non-anodized $NiBi_{0.25}$ films were comparable to TOF for non-anodized $Ni_{40}Fe_{60}Bi$. Incorporating Fe in the films had a drastic effect on increasing the OER catalytics activity of the film at high overpotentials. At 500 mV overpotential, non-anodized $Ni_{40}Fe_{60}Bi$ had the highest TOF which is more than 10 times greater than non-anodized NiBi films and more than 5 times greater than non-anodized $NiBi_{0.25}$ films. Anodized $Ni_{40}Fe_{60}Bi$ films exhibited the highest OER catalytic activity at 500 mV overpotential, and had TOF that is more than 2 times higher than those of NiBi and $NiBi_{0.25}$ films.

4.3 Tafel Plots:

The kinetics of oxygen evolution can be studied precisely using Butler-Volmer kinetics model given in the equation below,

$$J = J_O \exp \frac{\alpha n F(E - E^o)}{RT} \tag{4.4}$$

Where J_o represents the exchange current density, α is the electron-transfer coefficient, E is the applied potential and E^o is the equilibrium potential. Rearranging the above equation results in the so-called tafel plot of η vs log i that is frequently used to extract the kinetic parameters for a certain system, namely α and J_o.

$$\eta = \frac{2.3RT}{\alpha F} \log j_o - \frac{2.3RT}{\alpha F} \log j \tag{4.5}$$

where η is the applied overpotential. α is the transfer coefficient. α (and hence the slope of the tafel plot) should have the lowest value possible for more active oxygen evolution catalyst since it measures how much J changes to applying overpotential. The exchange current density J_o is

proportional to the standard rate constant k^o and is a measure of how fast the forward and backward reaction occur during dynamic equilibrium.[2] Ideally, J_o should have the highest value while α need to have the lowest value possible for optimum kinetic performance.

The steady-state current density (J) for oxygen evolution was determined as a function of the overpotential η in stirred 1 M KBi electrolyte solution at pH 9.2 for NiBi and $Ni_{1-x}Fe_xBi$ films. The applied potential was subtracted from the thermodynamic potential E^o after compensating for ohmic losses. Figure 4.14 shows the plots obtained for representative anodized NiBi, $Ni_{90}Fe_{10}Bi$, $Ni_{60}Fe_{40}Bi$, and $Ni_{60}Fe_{40}Bi$ films. NiBi and $Ni_{90}Fe_{10}Bi$ films exhibited similar slopes of 37.2 (±1.6) and 36.7 (±1.8) mV/decade respectively, while $Ni_{60}Fe_{40}Bi$, $Ni_{40}Fe_{60}Bi$ films had higher slope of 43.6 (±0.7) mV/decade and 46.0 (±1.2) mV/decade, respectively. The obtained tafel slopes for NiBi films are comparable to the slopes obtained by Bediako et al under supporting electrolyte-free conditions.[103] NiBi prepared from 0.16 mM electrodeposition bath exhibited a tafel slope 36.8 mV/decade, which is comparable to tafel slopes obtained for films prepared in 0.4 mM $Ni(NO_3)_2$ solution, while $NiBi_{0.25}$ exhibited a tafel slope of 50.8 (±5.0) mV/decade.
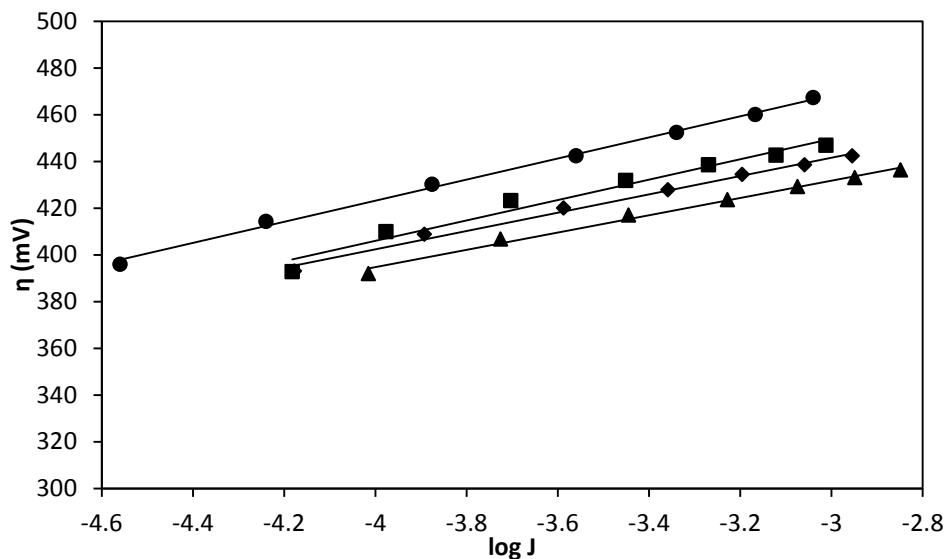
Figure 4.14: Tafel plots obtained for anodized NiBi (▲), $Ni_{90}Fe_{10}Bi$ (◆), and $Ni_{60}Fe_{40}Bi$ (●), $Ni_{40}Fe_{60}Bi$ (■) $\eta=E_{App}-E^o-iR$ of the catalyst films operated in 1 M KBi, pH 9.2 where iR accounts for the uncompensated solution resistance, and E^o is the thermodynamic potential of water. The slopes calculated by regression of NiBi, $Ni_{90}Fe_{10}Bi$, $Ni_{60}Fe_{40}Bi$, $Ni_{40}Fe_{60}Bi$ were 37, 39.2, 43.6 and 47.8 mV/decade, respectively.

Anodized $Ni_{40}Fe_{60}Bi$ and $Ni_{60}Fe_{40}Bi$ exhibited the highest exchange current density with more than an order of magnitude higher than NiBi and $Ni_{90}Fe_{10}Bi$. The exchange current density J_o which was extracted from the intercept of the tafel plots was $(6.8\pm4.3)\times10^{-14}$ A/cm^2 for $Ni_{40}Fe_{60}Bi$ (N=3), $(4.1\pm1.1)\times10^{-14}$ A/cm^2 for $Ni_{60}Fe_{40}Bi$ films (N=3), $(2.17\pm2.3)\times10^{-15}$ A/cm^2 for $Ni_{90}Fe_{10}Bi$ films (N=3), and $(2.22\pm1.6)\times10^{-15}$ A/cm^2 for NiBi films (N=3). J_o is the intrinsic activity of the electrode at the thermodynamic potential and is independent of the applied overpotential and thus can give an idea about the kinetics of the system. The higher J_o obtained for $Ni_{40}Fe_{60}Bi$ and $Ni_{60}Fe_{40}Bi$ could be due to the presence of highly active Ni centers neighboring Fe atoms. A summary on the kinetic values for the different studied films is shown in Table 4.3.

Sample	Tafel slope	Tafel intercept	J_O (mA/cm^2)
NiBi (1)	35.4	0.55	2.87E-16
NiBi (2)	39.2	0.563	4.24E-15
NiBi (3)	37	0.543	2.12E-15
NiBi	**37.2 ± 1.6**		**(2.22 ± 1.6) E-15**
$Ni_{90}Fe_{10}Bi$ (1)	39.2	0.559	5.46E-15
$Ni_{90}Fe_{10}Bi$ (2)	35.6	0.55	3.51E-16
$Ni_{90}Fe_{10}Bi$ (3)	35.3	0.535	6.99E-16
$Ni_{90}Fe_{10}Bi$	**36.7 ± 1.7**		**(2.2 ± 2.3) E-15**
$Ni_{60}Fe_{40}Bi$ (1)	44.5	0.593	4.80E-14
$Ni_{60}Fe_{40}Bi$ (2)	43.6	0.58	4.88E-14
$Ni_{60}Fe_{40}Bi$ (3)	42.7	0.58	2.60E-14
$Ni_{60}Fe_{40}Bi$	**43.6 ± 0.7**		**(4.1 ± 1.1)E-14**
$Ni_{40}Fe_{60}Bi$ (1)	47.8	0.6162	1.28E-13
$Ni_{40}Fe_{60}Bi$ (2)	45.1	0.6086	3.20E-14
$Ni_{40}Fe_{60}Bi$ (3)	45.2	0.604	4.34E-14
$Ni_{40}Fe_{60}Bi$	**46.0 ± 1.2**		**(6.8 ± 4.3) E-14**
$NiBi_{0.25}$ (1)	57.4	0.6452	5.75E-12
$NiBi_{0.25}$ (2)	45.2	0.6242	1.55E-14
$NiBi_{0.25}$ (3)	49.7	0.6471	9.55E-14
$NiBi_{0.25}$	**50.8 ± 5.0**		**(2.0 ± 2.7)E-14**

Table 4.3: Tafel data extracted from tafel plots of the studied NiBi, $Ni_{90}Fe_{10}Bi$, $Ni_{60}Fe_{40}Bi$, $Ni_{40}Fe_{60}Bi$, $NiBi_{0.25}$ films: tafel slopes, tafel intercept and the exchange current density. Average values and standard deviation are shown in bold.

Driven by the fact that non-anodized $Ni_{60}Fe_{40}Bi$ films exhibited higher catalytic activity in the

cyclic voltammetry study and TOF calculations, we sought at determining the tafel behavior of

non-anodized NiBi, $Ni_{90}Fe_{10}Bi$, $Ni_{60}Fe_{40}Bi$ and $Ni_{40}Fe_{60}Bi$ films and investigate whether Fe has

an effect in decreasing the tafel slopes of the films. Bell et al recently studied the electrochemical

oxygen evolution on Ni and mixed Ni-Fe film, with varying Fe percentage, electrodeposited

from their sulfate precursors on gold substrates.[86] The authors showed that aging of Ni films

enhances the OER activity by modifying the redox and Raman characteristics of Ni in a manner

similar to that observed for Fe incorporation in mixed Ni-Fe films and reported similar tafel

slopes for aged Ni films and mixed Ni-Fe films (40 % in iron) of 40 mV/decade.[86] Current

densities for tafel plots in this study were extracted from cyclic voltammograms acquired at 10

mV/s since measuring steady-state currents leads to partial anodization of the films. η values vs

log J were plotted to extract the tafel slope values. Table 4.4 shows the tafel data for the same

$NiBi$, $Ni_{90}Fe_{10}Bi$, $Ni_{60}Fe_{40}Bi$, $Ni_{40}Fe_{60}Bi$ and $NiBi_{0.25}$ films prior to anodization. Non-anodized

NiBi films exhibited an average tafel slope of 129 ± 7 mV/decade which is similar the tafel slope

for non-anodized NiBi films (100 mV/decade) reported by Bediako et al.[103] Non-anodized

$Ni_{90}Fe_{10}Bi$, $Ni_{60}Fe_{40}Bi$, $Ni_{40}Fe_{60}Bi$ films exhibited tafel slopes of 121 ± 5, 133 ± 12 and 143 ±

10, respectively. It was noticed that J_o was about 6 orders of magnitude higher in the as-prepared

films than in anodized films. Incorporation of Fe therefore did not result in similar tafel slopes to

anodized NiBi films. It is noted, however, that the values of J_o were higher at films containing

iron with the highest J_o at $Ni_{60}Fe_{40}Bi$ which is consistent with what was observed in the CV of

the as-prepared films (refer to figure 4.6).

Sample	Tafel slope	Tafel intercept	J_O (mA/cm^2)
NiBi (1)	136.9	1.05	2.14-08
NiBi (2)	120	1.05	1.78E-09
NiBi (3)	131	1.03	1.37E-08
NiBi	**129.3 ± 7.0**		**(1.2 ± 0.8) E-9**
$Ni_{90}Fe_{10}Bi$ (1)	126.6	1.06	4.24E-09
$Ni_{90}Fe_{10}Bi$ (2)	123.6	1	8.12E-09
$Ni_{90}Fe_{10}Bi$ (3)	115.3	0.99	2.60E-09
$Ni_{90}Fe_{10}Bi$	**121.8 ± 4.8**		**(5.0 ± 0.2) E-9**
$Ni_{60}Fe_{40}Bi$ (1)	149.8	1.07	7.20E-08
$Ni_{60}Fe_{40}Bi$ (2)	124.5	0.99	1.12E-08
$Ni_{60}Fe_{40}Bi$ (3)	125.7	0.99	1.33E-08
$Ni_{60}Fe_{40}Bi$	**133.3± 11.7**		**(3.2 ± 2.8) E-8**
$Ni_{40}Fe_{60}Bi$ (1)	143	1.08	2.80E-08
$Ni_{40}Fe_{60}Bi$ (2)	129.9	1.04	9.86E-09
$Ni_{40}Fe_{60}Bi$ (3)	126.7	1.04	6.19E-09
$Ni_{40}Fe_{60}Bi$	**133.2 ± 7.1**		**(1.5 ± 0.9) E-8**
$NiBi_{0.25}$ (1)	157.8	1.21	2.15E-08
$NiBi_{0.25}$ (2)	134.4	1.06	1.30E-08
$NiBi_{0.25}$ (3)	140.5	1.14	7.70E-09
$NiBi_{0.25}$	**143.2 ± 9.9**		**(1.4 ± 0.5) E-9**

Table 4.4: Tafel data for non-anodized studied NiBi, $Ni_{90}Fe_{10}Bi$, $Ni_{60}Fe_{40}Bi$, $Ni_{40}Fe_{60}Bi$, $NiBi_{0.25}$ films: tafel slopes, tafel intercept, and the exchange current density. Average values and standard deviation are shown in bold.

In this study, we incorporated Fe into NiBi at different percentages. The presence of Fe in the films was studied by comparing to two types of films: films prepared by passing the same amount of charge (1 mC/cm^2) as NiBi films but using a lower concentration of Ni in electrodeposition bath, and films prepared by limiting the amount of charge passing while keeping the concentration of Ni in the electrodeposition bath the same as that used to prepare

NiBi films. Non-anodized $Ni_{40}Fe_{60}Bi$ and $Ni_{60}Fe_{40}Bi$ showed better OER catalytic performance than non-anodized NiBi, $Ni_{90}Fe_{10}Bi$, and $NiBi_{0.25}$ films at moderate overpotentials, and to a higher extent at higher overpotential as apparent from TOF calculations and overpotential measurements (and tafel slopes when compared to $NiBi_{0.25}$). While at moderate overpotential, anodized $Ni_{40}Fe_{60}Bi$ and $Ni_{60}Fe_{40}Bi$ films exhibited comparable OER activity to NiBi films, $Ni_{40}Fe_{60}Bi$ and $Ni_{60}Fe_{40}Bi$ films were better than anodized NiBi and $Ni_{90}Fe_{10}Bi$ at high overpotential exhibiting more than 2-fold higher TOF of 16 ± 2 and 10 ± 3 s^{-1} at $\eta = 500$ mV respectively. This study shows an effect of Fe on enhancing the catalytic activity of amorphous thin Ni oxo/hydroxo films. The effect of anodization in inducing structural changes is not one caused directly by incorporating iron in the films as was proposed in more recent literature reports. The effect of Fe is to make the films more active initially, but the effect of anodization is more apparent with less iron content.

CHAPTER 5

PHOTOELECTROCHEMICAL STUDIES AT Fe_2O_3 INVERSE OPALS DECORATED WITH NiBi AND NiFeBi SURFACE CATALYSTS

Solar energy and water are the two most crucial and abundant essentials that maintain life on Earth. They have been used extensively by plants and cyanobacteria for carbon fixation as a mean to store energy for later use by the process of photosynthesis which serves as a water splitting machinery. Splitting water photoelectrochemically on a semiconductor is a promising solution for sustainable clean energy supply in the midst of the overgrowing energy demand and limited energy resources which dominantly come from fossil fuels (81% of total world's energy)[116] and allows the transformation of solar energy into chemical energy in the form of molecular hydrogen. Ideally, a semiconductor material that can be employed in a water splitting cell combines the following essential requirements: a small semiconductor band gap for ample solar light absorption, conduction and valence band energies that straddle the water oxidation and reduction potentials, facile kinetics and high conversion efficiency of photogenerated carriers to the water splitting products, durability in aqueous environments, and low cost.[53] Since such material has not been found, research has been directed towards assembling different materials each satisfying one or more conditions in one cell. Various materials have been investigated for water splitting including GaP, InP, and p-Si as photocathodes for hydrogen evolution[117,118,119] and Fe_2O_3, TiO_2, and WO_3 as photoanodes for oxygen evolution.[2, 53,77,73]

Hematite (α- Fe_2O_3) has been extensively researched over the past decades to serve as a photoanode for the oxygen evolution half-reaction.[58,53,120] Hematite (Fe_2O_3) has been an attractive photoanode material because it has a small band gap of 2.1 eV which permit visible

light absorption, has suitable band edges for oxidizing water, is stable, abundant and cheap. However, hematite photo-oxidizing water efficiency is limited due its low absorption in the visible region, a very short excited-state lifetime (10^{-12} s), a short hole diffusion length (2–4 nm) and slow kinetics of the oxygen evolution reaction.[55]

Structuring hematite in certain nanoscale architectures that facilitate hole transfer to the electrolyte solution by decreasing the distance the hole has to travel before reaching the interface, is thought to lead to improvements in the efficiency of water photooxidation. Hematite inverse opals, with large void structure and thin walls, provide an advantage of short distances for the hole to reach the electrolyte. Different methods have been devised to deposit hematite including thermal deposition of iron precursor such as $FeCl_3.6H_2O$,[89] pulsed laser deposition from hematite targets,[121] spray pyrolysis of $FeCl_3$,[120] evaporative deposition of Fe in oxygen onto a substrate,[122] electrodeposition from various Fe precursors,[74] chemical vapor deposition,[123] and dip coating.[124]

In this study, we aimed to fabricate hematite inverse opals (i-Fe_2O_3-o) from two different sphere sizes (190 and 417 nm) and to investigate their photoelectrochemical behavior in comparison with unstructured films similarly prepared in 1 M NaOH pH 13.6 and at benign pH using potassium borate buffer (KBi) pH 9.2. i-Fe_2O_3-o (417) were then surface decorated with NiBi and $Ni_{90}Fe_{10}Bi$ to investigate any differences caused by incorporating iron in the catalyst film on the photoelectrochemical behavior.

5.1 Characterization of hematite inverse opals and "unstructured" films using UV-vis spectroscopy, SEM and X-ray diffraction:

Photonic crystals were prepared from polystyrene colloidal solutions of sizes 190 nm and 417 nm via evaporation-induced self-assembly. UV-vis absorption spectra for the photonic crystals PC_{190} and PC_{417} acquired in air are shown in figure 5.1.
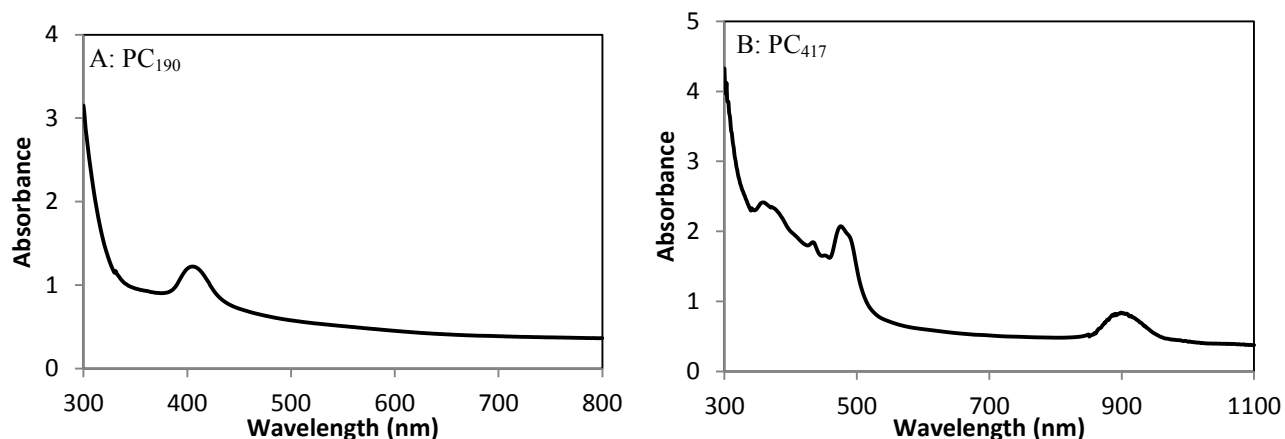
Figure 5.1: UV-vis absorption spectra showing the position of the stop band peaks of (A) PC_{190} and (B) PC_{417}.

PC_{190} exhibited a stop band peak at 400 nm and PC_{417} exhibited a stop band at 900 nm. SEM images for PC films are shown in fig 5.2. The two SEM images are acquired approximately under the same magnification. Using Bragg equation, one finds that a stop band at 400 nm in air corresponds to a sphere of diameter equal to 166 nm for the PC_{190} diameter indicating an 12.6 % shrinkage, and a stop band of 900 nm in air corresponds to a diameter equal to 373 nm for PC_{417} and hence a 10.6 % shrinkage. This shrinkage is confirmed in SEM images where diameters of 168 ± 8 nm (N=15) and 360 ± 10 nm (N=13) are measured corresponding to 11.5 % and 13.7 % shrinkage for PC_{190} and PC_{417}, respectively.

$$\lambda = 2d\sqrt{0.74n_s^2 + 0.26n_v^2}$$ (5.1)

Where d is the interlayer spacing and equal to 0.87 times the diameter of the polystyrene sphere, n_s and n_v are the refractive indices of polystyrene (n=1.5) and air (n=1), respectively.

Hematite inverse opal films were prepared by solvent casting $20\mu l/cm^2$ iron (III) nitrate solution in ethanol (25 mM) on top of the photonic crystal films in horizontal orientation. Films were air dried then placed in oven at 70° C for 10 min. This cycle was repeated 6 times. The samples were then calcined at 550° C to form iron oxide and burn the polystyrene spheres resulting in hematite inverse opal structure.
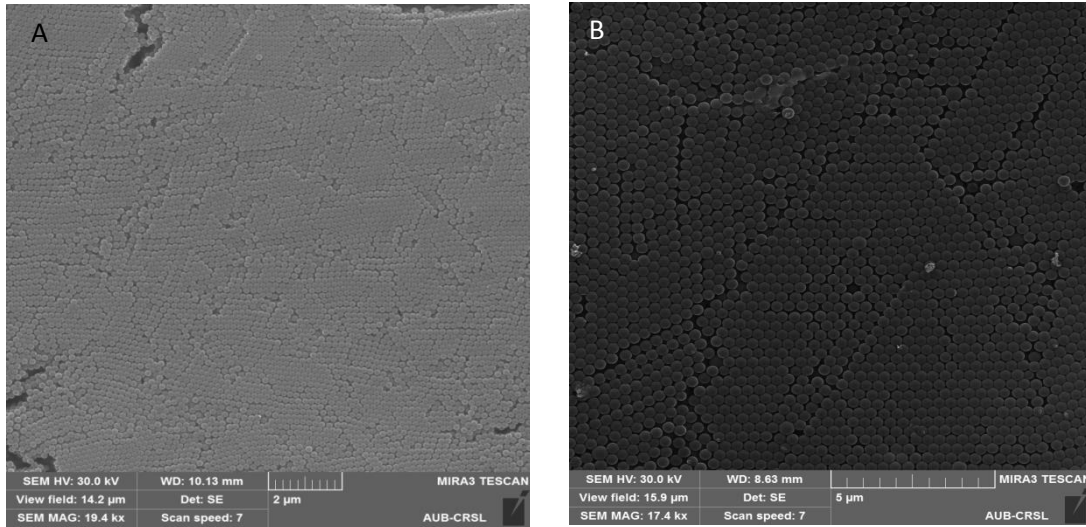
Figure 5.2: SEM images showing opals PC$_{190}$ (A) and PC$_{417}$ (B).

SEM images of resulting inverse opal films are shown in figure 5.3 and figure 5.4. According to SEM measurements, i-Fe$_2$O$_3$-o (417) and i-Fe$_2$O$_3$-o (190) exhibited pores with diameter of 312 ± 16 nm and 146 ± 7 nm, after the first annealing step corresponding to 25 % and 23 % shrinkage, respectively. Similar shrinkage of 26 % was observed in 450-i-TiO$_2$-o assembled from 243 nm polystyrene spheres.[13] The hematite inverse opal structure shrank further when subjected to a

second brief annealing at 800 ^{o}C and exhibiting pores of diameter 271 ± 19 nm corresponding to 35 % shrinkage in i-Fe$_2$O$_3$-o (417) and 103 ± 8 nm corresponding to 46 % shrinkage in i-Fe$_2$O$_3$-o (190). Figure 5.5 shows UV-vis absorption spectra of the films acquired with water filling the voids. The UV-vis spectra show broad absorption bands in the range of 400-600 nm that are due to oxo-iron transitions corresponding to the ligand to metal charge transfer (LMCT)[61,65], but do not show stop band peaks for the inverse opals. Based on the sphere size measured from SEM images, one can calculate the expected stop band positions of i-Fe$_2$O$_3$-o (417) and i-Fe$_2$O$_3$-o (190) from Bragg equation with n$_{water}$ = 1.33 and n$_{hematite}$=2.9[125]. The expected stop band peak for i-Fe$_2$O$_3$-o (417) shall be positioned at 1014 nm while that for i-Fe$_2$O$_3$-o (190) shall be centered at 475 nm after the first annealing. PS photonic crystals exhibited well-defined stop band peaks and SEM images confirmed the obtained inverse opal structure, however with significant long range disorder.
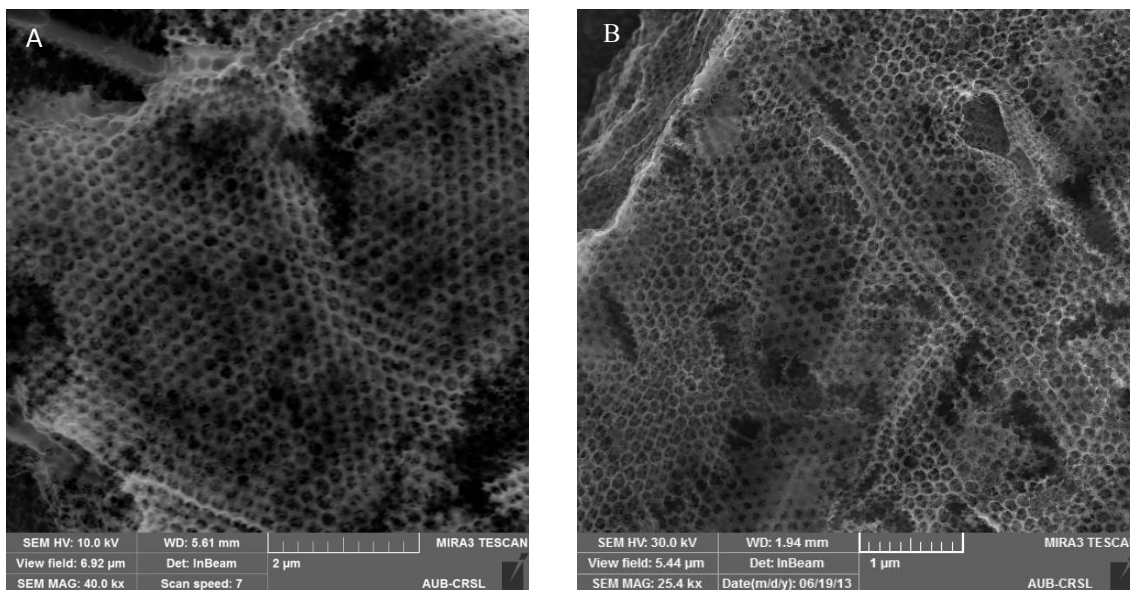
Figure 5.3: SEM images showing i-Fe$_2$O$_3$-o (190) after first annealing (A) and after second annealing (B).
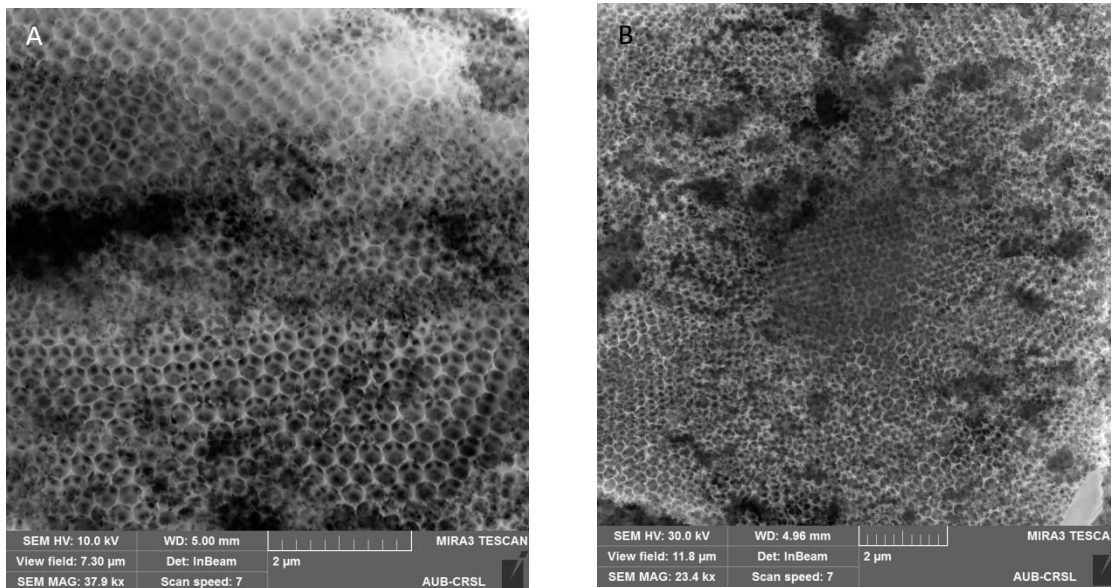
Figure 5.4: SEM images showing i-Fe$_2$O$_3$-o (417) after first annealing (A) and after second annealing (B).

This could be due to the significant disorder induced by the required high annealing temperatures to improve the electronic properties of hematite which is crucial for enhancing the photoelectrochemical properties of the films as photoanodes for water splitting. Films were subjected to a second annealing step at 800° C for 20 minutes, because photocurrents are low after the first annealing step. The second brief annealing step improves the film electronic properties.
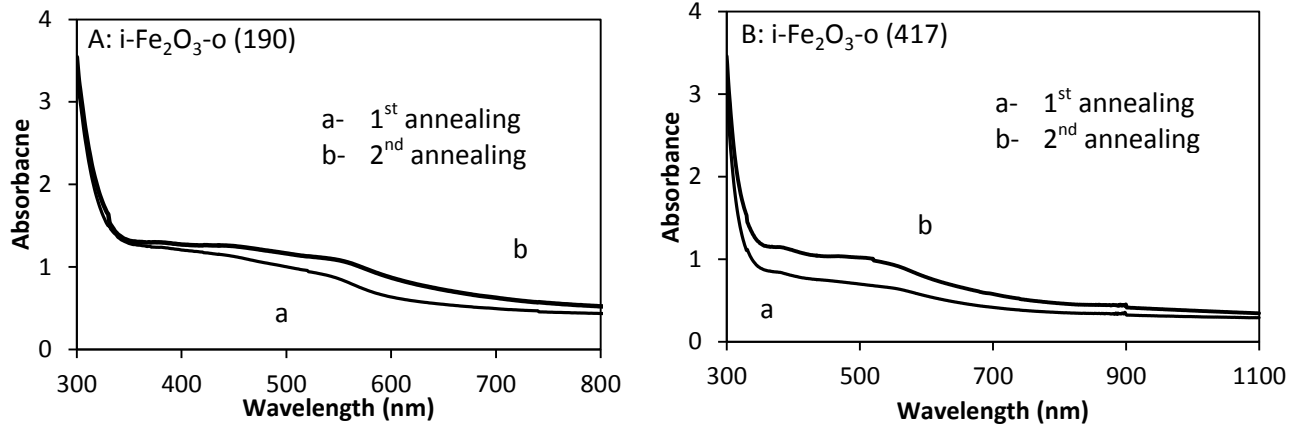
Figure 5.5: UV-vis absorption spectra for hematite after first annealing (a) and after second annealing (b) (A) i-Fe$_2$O$_3$-o (190) and (B) i-Fe$_2$O$_3$-o (417).

This step is believed to enhance the conductivity of hematite films possibly via the diffusion of Sn from the underlying SnO$_2$ electrode at the high temperature.[73] Note that the absorbance also increased after the annealing at 800 ^{o}C consistent with other reports.[120] The increase in absorbance is attributed to the decrease in band gap as the sintering temperature increase.[120,126,127]

Figure 5.6 shows the SEM image and UV-vis absorption spectrum of unstructured hematite film. Unstructured hematite films were prepared using the exact same procedure but on conducting glass electrode (FTO) in the absence of PC template for comparison. SEM images show that unstructured films consisted of nanorods horizontally oriented having dimensions of 160 ± 30 nm in length and 70 ± 9 nm in diameter (N=8) (fig. 5.6 A). The absorption spectrum of the unstructured films is very similar to that of the inverse opal samples (fig 5.6 B) exhibiting broad band hematite absorption peaks between 400 and 600 nm. Note that the absorbance of the unstructured hematite films also increased after being subjected to the 2nd annealing step.
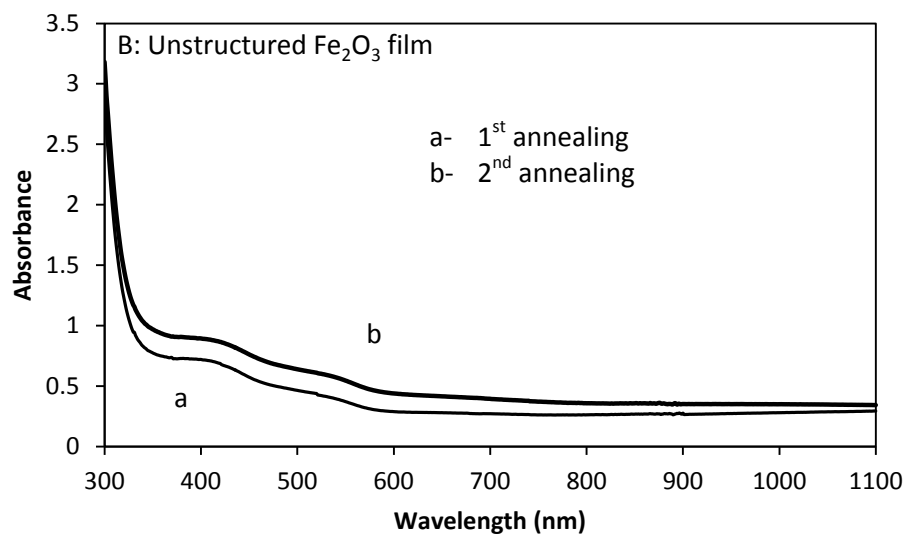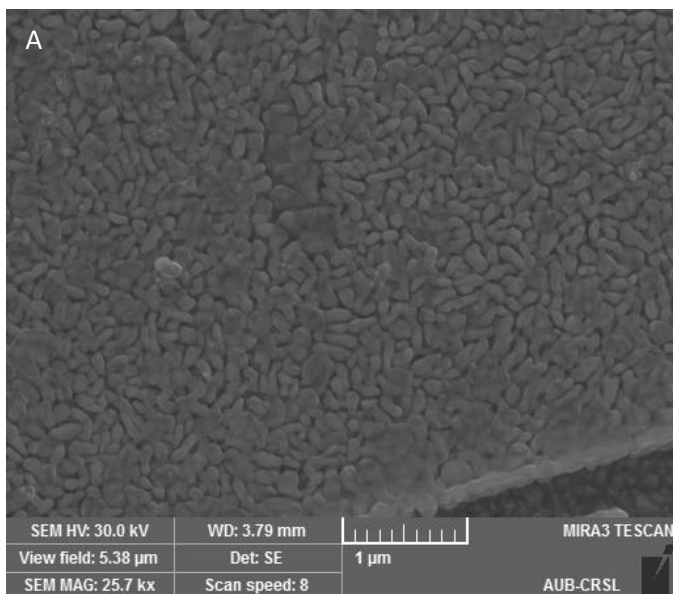
Figure 5.6: (A) SEM image of unstructured hematite film showing particles with nanometer dimensions, (B) UV-vis absorption spectra of the film.

X-ray diffraction pattern for an inv-PC$_{417}$ film is shown in figure 5.7. The plot shows several diffraction peaks, five peaks of which correspond to hematite. These are at 33.2°, 35.7°, 40.9°, 49.5°, and 54.1° which are consistent with the diffraction of the (104), (110), (113), (024), and

(116) planes of α-Fe$_2$O$_3$ respectively.[89] Note that all the other peaks correspond to FTO background on which the hematite film was deposited.
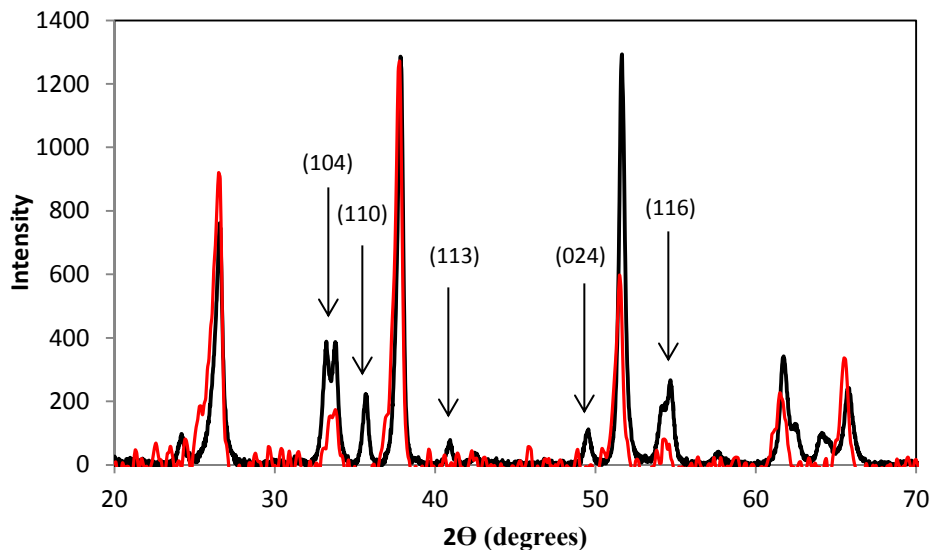
Figure 5.7: X-ray diffractograms of hematite inverse opal (i-Fe$_2$O$_3$-o(417)) confirming the structure of α-Fe$_2$O$_3$ shown in black while that of the FTO substrate is shown in in red. Peaks corresponding to hematite are labeled with an arrow.

5.2 Photoelectrochemical Studies:

5.2.1 *Photoelectrochemical Measurements:*

All electrochemical measurements were carried in a 3-electrode configuration cell with BASi Ag/AgCl reference electrode, and 2 mm platinum wire as a counter electrode in 25 mm quartz cell. Cyclic voltamograms were acquired by scanning the potential between -0.6 V and +1.5 V vs Ag/AgCl at 5 different scan rates of 10, 20, 50, 100, and 200 mV/s. CVs were acquired under white light illuminated from a 300 W Xe lamp at 100 mW/cm^2 at the electrode position as measured using a thermopile light detector. Two modes of illumination were employed, front wall and back wall illumination; In the front wall illumination, light impinges on the surface of hematite first from the electrolyte side while in the back wall illumination, light impinges on the

interface of FTO/hematite as presented in scheme 5.1. Cyclic voltammograms were acquired under 2 basic conditions: at pH 13.6 in 1 M NaOH, and at benign pH of 9.2 in 1 M potassium borate buffer (KBi).
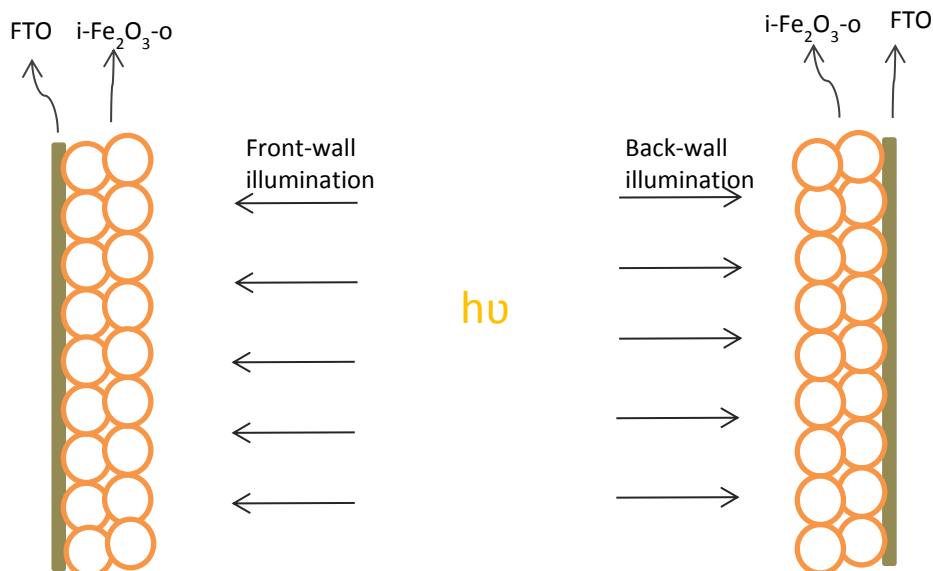
Scheme 5.1: Scheme showing the front-wall and back-wall illumination at i-Fe$_2$O$_3$-o.

5.2.2 *Photoelectrochemical Studies at Hematite Inverse Opals and Unstructured Films:*

Hematite inverse opals were assembled from polystyrene spheres of different sizes to compare the effect of pore size on the photoelectrochemical performance of the films as photoanodes for oxygen evolution. PS colloidal solutions of sizes 417 nm and 190 nm of the same concentration were self-assembled on FTO glass and then infiltrated by solvent casting method. Control unstructured film was similarly prepared on a clean FTO. The photoelectrochemical response of hematite films was studied under front wall and back illumination at 100 mW/cm^2 in 1 M NaOH pH 13.6 and 1 M KBi pH 9.2.

The average thickness of i-Fe$_2$O$_3$-o (190) films is 2.3 $\pm$ 0.2 μm (N=3), i-Fe$_2$O$_3$-o (417) films is 2.9 $\pm$ 0.5 μm (N=3) and unstructured ranged is 1.9 $\pm$ 0.2 μm (N=3). It is worth noting that since all the films were infiltrated with the same amount of iron nitrate solution, it is expected that the unstructured films will be the thinnest due to the lack of any polystyrene template, and that i-Fe$_2$O$_3$-o (417) films will be the thickest owing to their large pores in the structure. So this study aims at comparing i-Fe$_2$O$_3$-o (417) with i-Fe$_2$O$_3$-o (190) and unstructured films infiltrated with the same amount of hematite rather than comparing the films of same thickness. Figure 5.8 shows a plot of the photocurrent density versus voltage collected at i-Fe$_2$O$_3$-o (417) film under chopped illumination at 100 mW/cm^2. The maximum photocurrent is measured at 0.6 V vs Ag/AgCl.
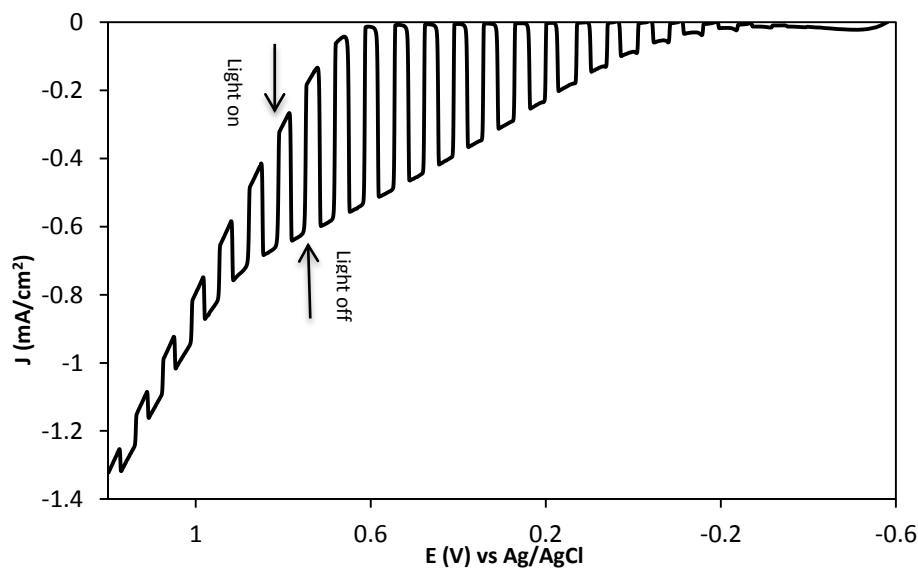
Figure 5.8: I-V curve under chopped illumination for i-Fe$_2$O$_3$-o (417) film in 1 M NaOH acquired at 50 mV/s.

Figure 5.9 shows representative I-V curves of i-Fe$_2$O$_3$-o (417), i-Fe$_2$O$_3$-o (190), and unstructured films under front wall illumination, back wall illumination and in the dark in 1 M NaOH at 50 mV/sec.
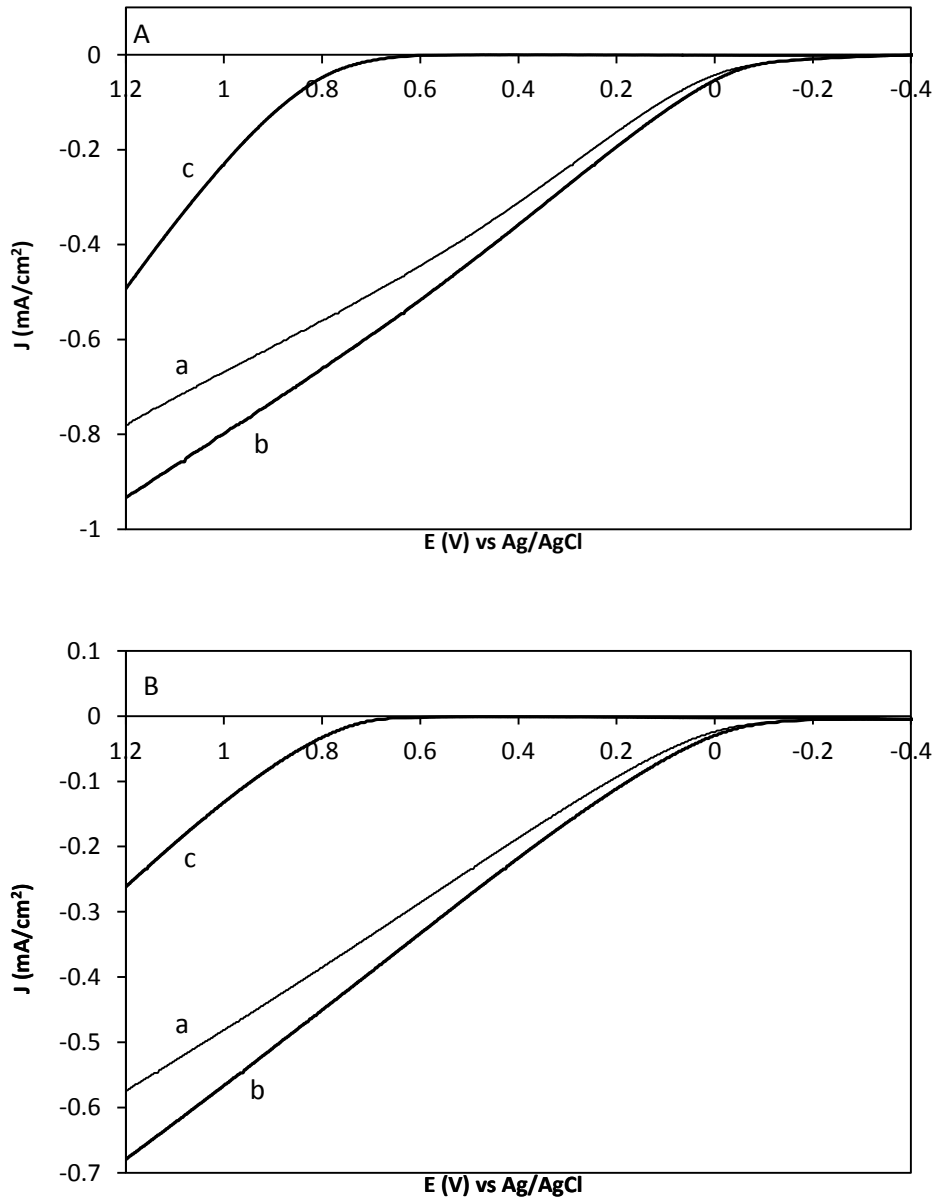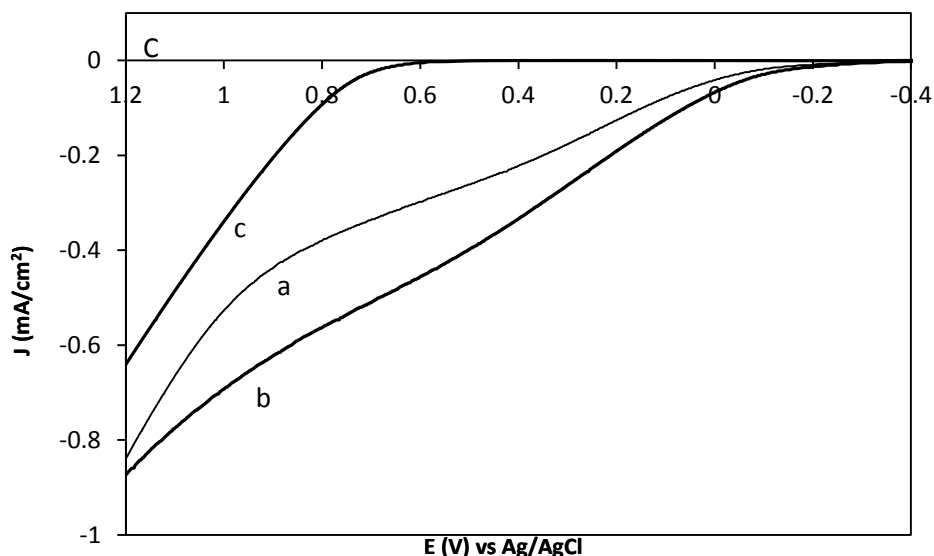
Figure 5.9: I-V curves of the different studied films: (A) i-Fe$_2$O$_3$-o (417) (3.2 µm) (B) i-Fe$_2$O$_3$-o (190) (2.3 µm), (C) unstructured film (1.7 µm) in front wall illumination (a) and back wall illumination (b) in 1 M NaOH and at a scan rate of 50 mV/s. I-V curves acquired in the dark are shown in plots C.

At 0.6 V vs Ag/AgCl and 100 mW/cm^2 illumination, i-Fe$_2$O$_3$-o (417) (3.2 µm thick) produced

0.45 mA/cm^2 and 0.52 mA/cm^2 in the front-wall and back-wall illumination, respectively. Lower

photocurrents were measured at i-Fe$_2$O$_3$-o (190) (2.3 µm thick) and unstructured film (1.7 µm).

At 0.6 V, 0.29 mA/cm^2 and 0.33 mA/cm^2 were measured at i-Fe$_2$O$_3$-o (190) and 0.30 mA/cm^2

and 0.46 mA/cm^2 were measured at the unstructured film in front wall and back wall

illumination, respectively.

I-V curves for the same samples acquired at 50 mV/s and 100 mW/cm^2 in 1 M KBi are presented

in Figure 5.10. Similar photocurrents were measured in 1 M KBi solution but at higher

overpotentials. At 1 V vs Ag/AgCl and 100 mW/cm^2 illumination, i-Fe$_2$O$_3$-o (417) produced

0.38 mA/cm^2 and 0.48 mA/cm^2 in the front-wall and back-wall illumination, respectively. Lower

photocurrents were measured at i-Fe$_2$O$_3$-o (190) and unstructured films; 0.33 mA/cm^2 and 0.36

mA/cm^2 were measured at i-Fe$_2$O$_3$-o (190) and 0.20 mA/cm^2 and 0.34 mA/cm^2 were measured at

the unstructured film in front wall and back wall illumination, respectively. The difference in

photocurrents between the front wall and back wall illumination was only negligible for the

inverse opal films compared to a more significant difference in photocurrents (more than 1.7

times difference) at the unstructured films even though they are the thinnest. The nanocrystalline

compact structure of unstructured films makes it more difficult for the photogenerated holes to

reach the electrolyte solution before recombination. Electron-hole pairs generated near the

interface therefore have the greatest probability of leading to photocurrent generation, while

electron-hole pairs generated away from the interface will recombine before. This results in

photocurrents being significantly greater in back wall illumination compared to front wall

illumination. This demonstrates the importance of the pores in the inverse opal architecture

which provide shorter distances for the photogenerated holes.
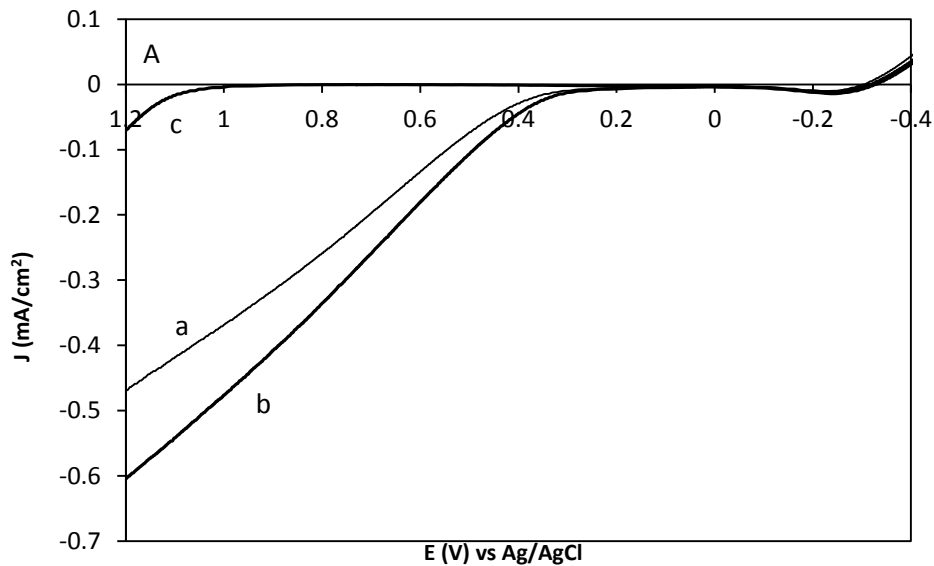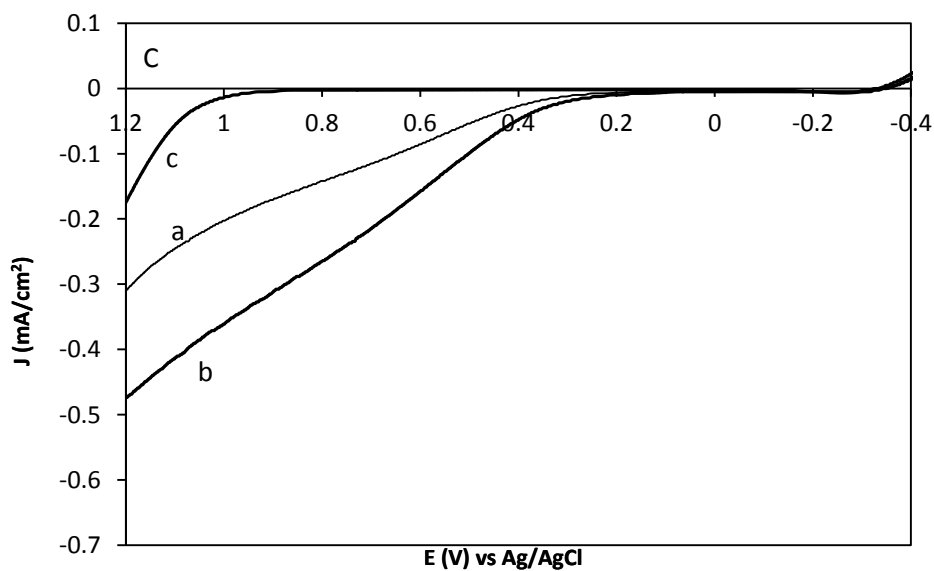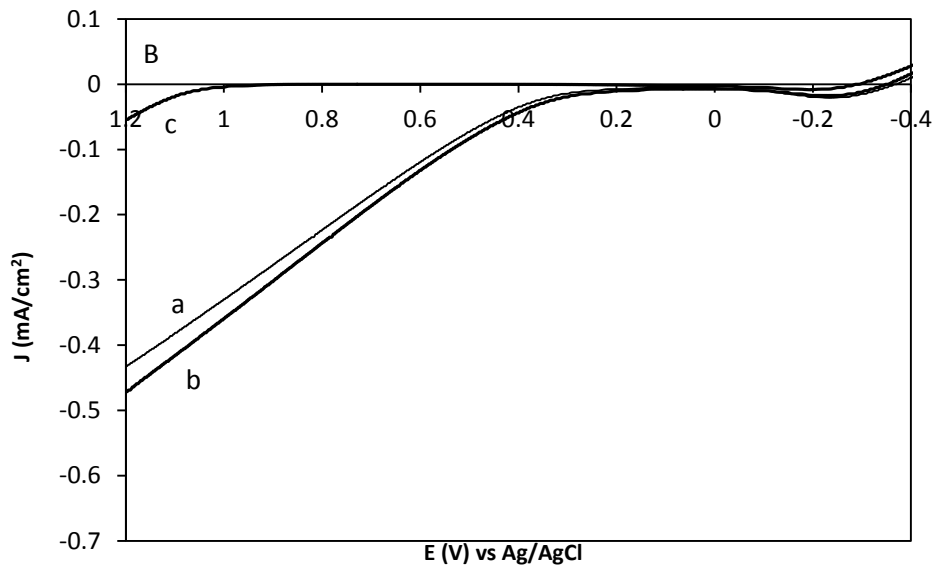
Figure 5.10: I-V curves of the different studied films: (A) i-Fe$_2$O$_3$-o (417) (3.2 µm) (B) i-Fe$_2$O$_3$-o (190) (2.3 µm), (C) unstructured film (1.7 µm) in front-mode (a) and back-mode (b) illumination in 1 M KBi and at a scan rate of 50 mV/s. I-V curves acquired in the dark are shown in plots C.

The overpotential for oxygen evolution is pH dependent and is governed by the following equations:

$$\eta = E_{app} - E^o + E_{ref} \tag{5.2}$$

Where E_{app} is the applied bias, E^o is the thermodynamic potential, and E_{ref} is the potential of the reference electrode (Ag/AgCl in this case). In turn, the thermodynamic E^o is governed by Nernst equation as such:[109]

$$E^o = E^{o'} - 0.059\, pH + \frac{0.059}{n} \log P_{O_2} \tag{5.3}$$

where $E^{o'}$ is the thermodynamic potential of O_2/H_2O and is equal to 1.23 V, n is the number of electrons transferred and is equal to 4. P_{O2} is the partial pressure of oxygen and is equal to 0.209 atm at 293 K.

Figure 5.11 shows cyclic voltammogram acquired at i-Fe_2O_3-o (417) in the dark in 1 M NaOH and 1 M KBi acquired at 10 mV/s. At 0.05 mA/cm^2, the water oxidation current is shifted by 370 mV more positive in KBi electrolyte, which corresponds to 84 mV/pH unit. Nocera reported similar shift (89 mV/pH unit) at NiBi films on FTO and suggested that the system is governed by proton-coupled electron transfer and that the observed shift corresponds to the transfer of 1.5 protons per each electron lost[79] which was also observed in the dimerization of Ir (IV) to form iridium oxide catalyst.[128] Similar shifts were observed at i-Fe_2O_3-o (190) and unstructured films exhibiting shifts of 350 and 345 mV corresponding to 79 and 78 mV/pH, respectively.
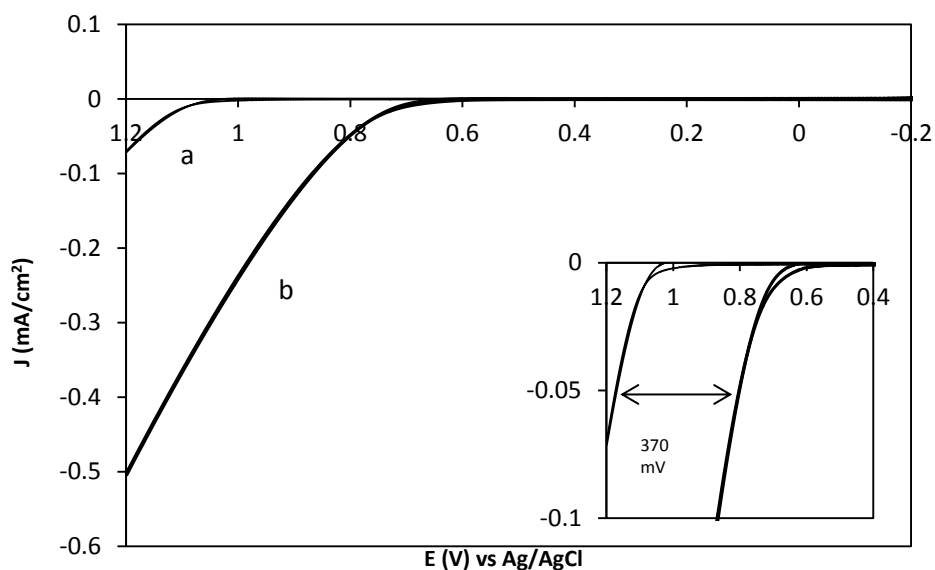
Figure 5.11: CV of i-Fe$_2$O$_3$-o (417) in the dark at 10 mV/s in 1 M KBi (a) and 1 M NaOH (b).

5.2.2.1 Photoaction Spectra and Dependence on Light Intensity:

The photoaction spectra of films were acquired in a 3-electrode electrochemical quartz cell with Pt electrode as auxiliary and Ag/AgCl as reference in 1 M NaOH electrolyte (pH 13.6). I-t curves were collected a 0.6 V by chopping the monochromatic light between 380 and 600 nm. This chosen voltage corresponds to the voltage at which the maximum photocurrent was measured (refer to figure 5.8). The monochromatic photocurrent density was measured by subtracting dark current from the light current and dividing by the geometric area of the films. The photocurrent density at each wavelength with the corresponding light power density were used to compute the % IPCE.

Figure 5.12 shows the % IPCE vs wavelength plots for i-Fe_2O_3-o (417), i-Fe_2O_3-o (190), and

unstructured films in the front wall and back wall illumination. Slightly greater % IPCE was

measured at i-Fe_2O_3-o (190) than at i-Fe_2O_3-o (417) in both front-wall and back-wall

illumination despite the smaller photocurrent measured under white light. At 400 nm, % IPCE

reached 2.4 % and 2.5 % in the front-wall illumination, and 8 % and 7.5 % in the back-wall

illumination for i-Fe_2O_3-o (190) and i-Fe_2O_3-o (417) films, respectively. On the other hand,

unstructured film exhibited much lower % IPCE in the entire range (380-600 nm) with a

maximum value of 0.7 % in the front wall illumination and 3.5 % in the back wall illumination at

400 nm. Photocurrent magnitudes became very low (< 1 $\mu A/cm^2$) for all the films at 600 nm. The

% IPCE values in the back-wall illumination were greater than front-wall illumination on all

hematite structures: 3.2 times higher at i-Fe_2O_3-o (417), 3.4 times higher at i-Fe_2O_3-o (190) and

3.9 times higher at unstructured films. The greater difference between front-wall illumination

and back-wall illumination for the unstructured films is consistent with the I-V curves but the

difference in % IPCE is greater than in I-V curves.
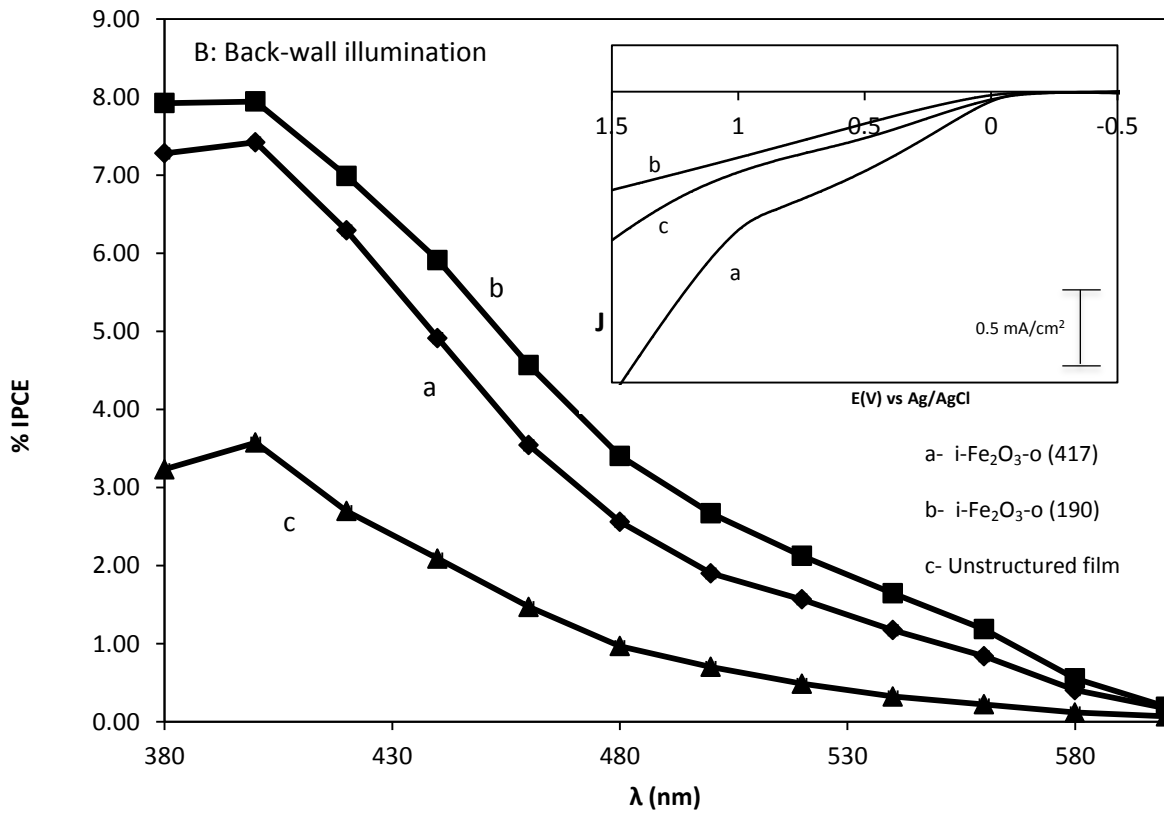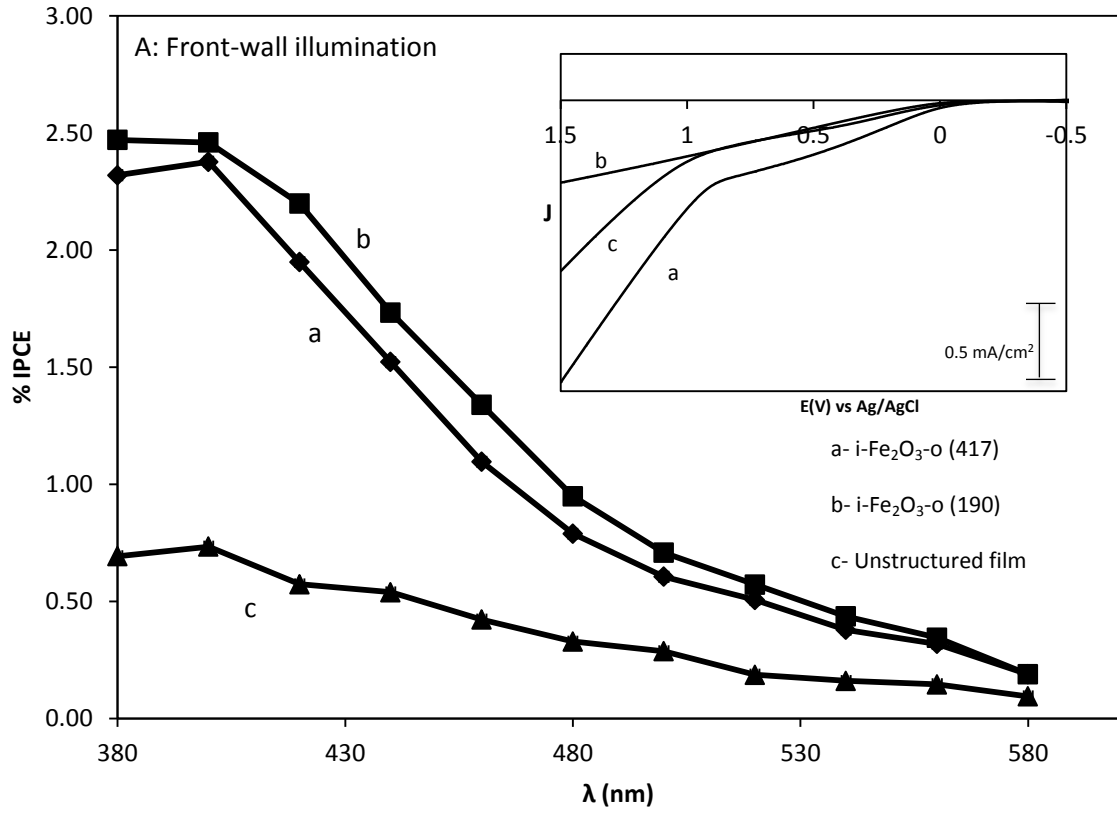
Figure 5.12: % IPCE plots vs wavelength of i-Fe$_2$O$_3$-o (417) (a), i-Fe$_2$O$_3$-o (190) (b) and unstructured film (c) under front wall illumination (A) and back wall illumination (B) in 1 M NaOH pH 13.6. I-V curves of films acquired at 50 mV/cm^2 in 1 M NaOH at 100 mW/cm^2 white light illumination are presented in the inset.

In accordance to the I-V measurements under 100 mW/cm^2 illumination, i-Fe$_2$O$_3$-o (417) was expected to exhibit the highest % IPCE and i-Fe$_2$O$_3$-o (190) was expected to have similar photoaction spectrum as the unstructured film. We sought to measure I-V curves at different light intensities to better understand this discrepancy between I-V curves and photoaction spectra. I-V curves at i-Fe$_2$O$_3$-o (417), i-Fe$_2$O$_3$-o (190), and unstructured films acquired at 25, 50, 100, and 200 mW/cm^2 in front-wall illumination and back-wall illumination are presented in Figure 5.13 and Figure 5.14, respectively.

B

J (mA/cm²)

E(V) vs Ag/AgCl

a- i-Fe$_2$O$_3$-o (417)
b- i-Fe$_2$O$_3$-o (190)
c- Unstructured film

C

J (mA/cm²)

E(V) vs Ag/AgCl

a- i-Fe$_2$O$_3$-o (417)
b- i-Fe$_2$O$_3$-o (190)
c- Unstructured film

130
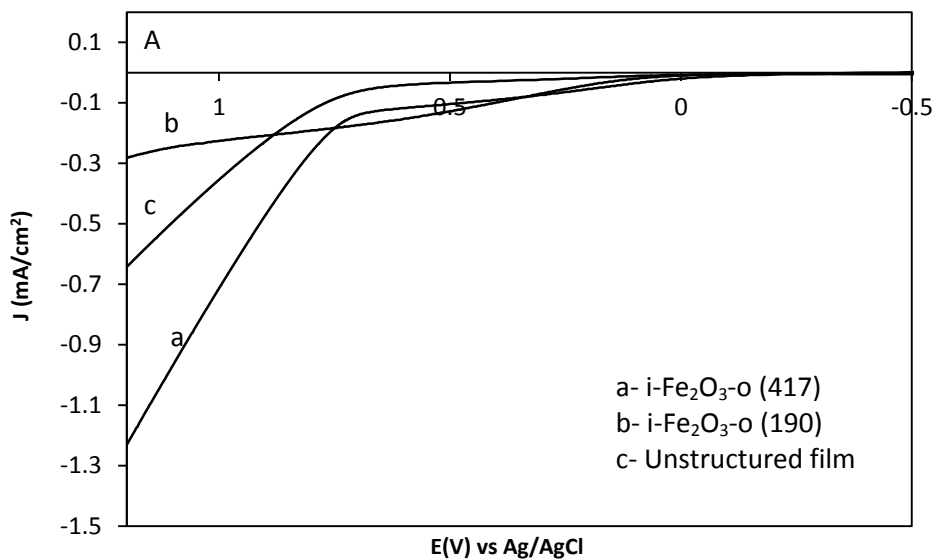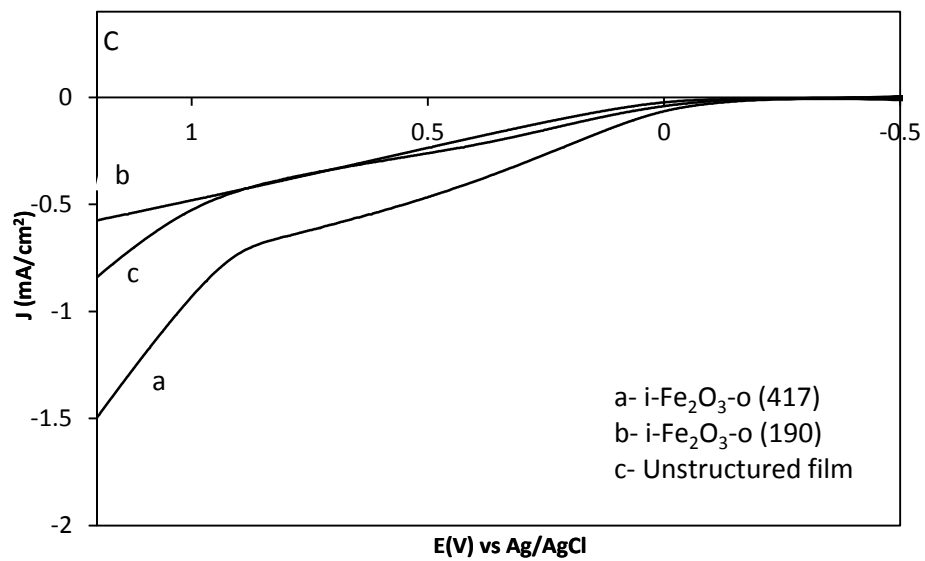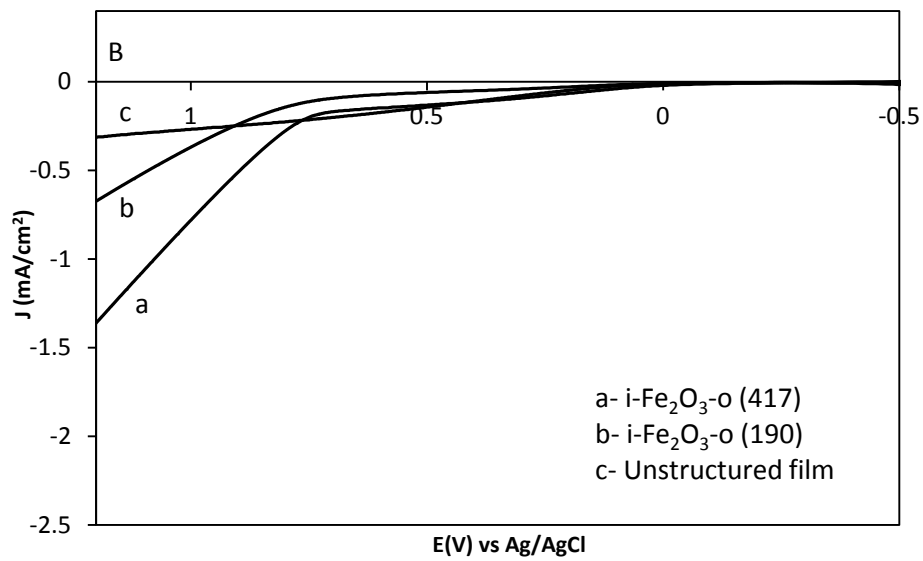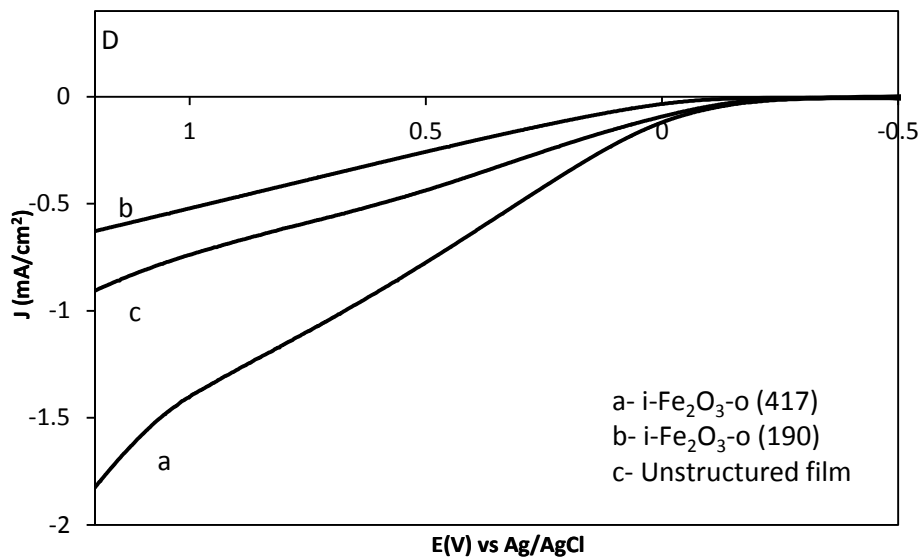
Figure 5.13: I-V curves at i-Fe$_2$O$_3$-o (417) (a), i-Fe$_2$O$_3$-o (190) (b), unstructured film (c) acquired at 50 mV/s in 1 M NaOH pH 13.6 in the front wall illumination at 25 mW/cm^2 (A), 50 mW/cm^2 (B), 100 mW/cm^2 (C), 200 mW/cm^2 (D). The insets in (A) and (B) show a close up on the measured maximum photocurrents.

B

a- i-Fe$_2$O$_3$-o (417)
b- i-Fe$_2$O$_3$-o (190)
c- Unstructured film

C

a- i-Fe$_2$O$_3$-o (417)
b- i-Fe$_2$O$_3$-o (190)
c- Unstructured film

132
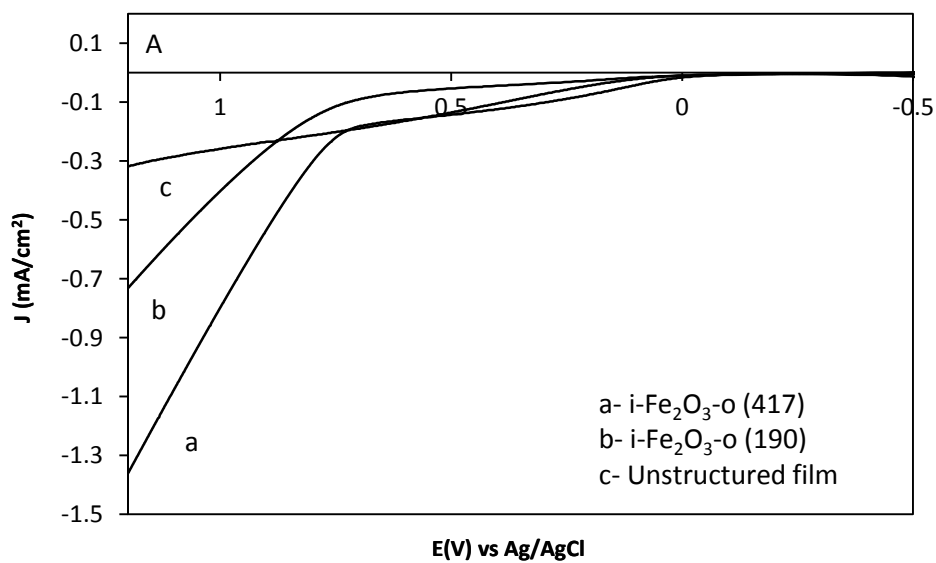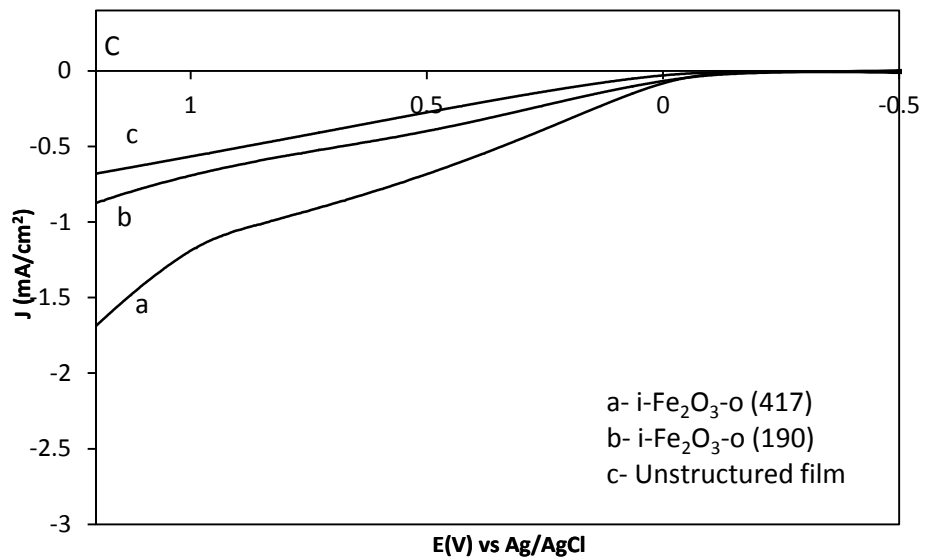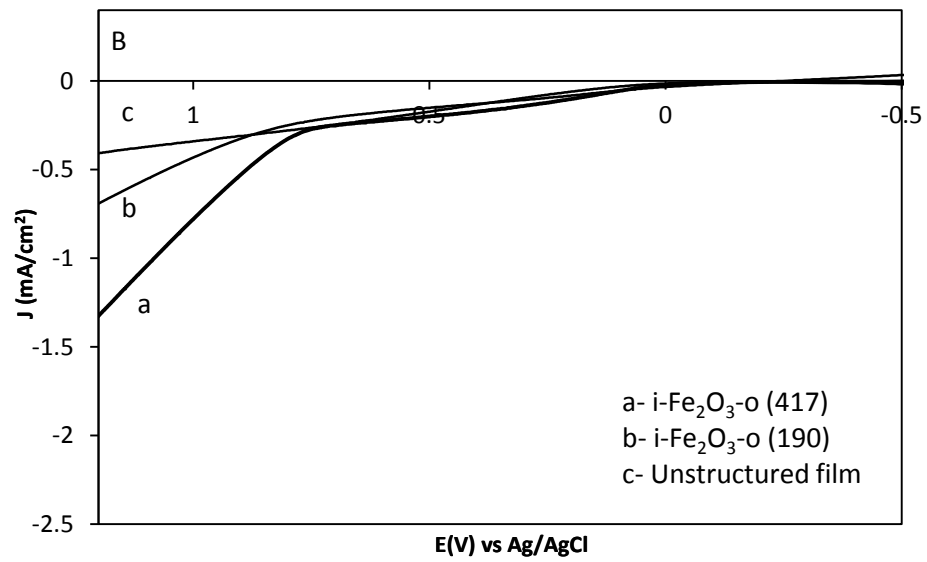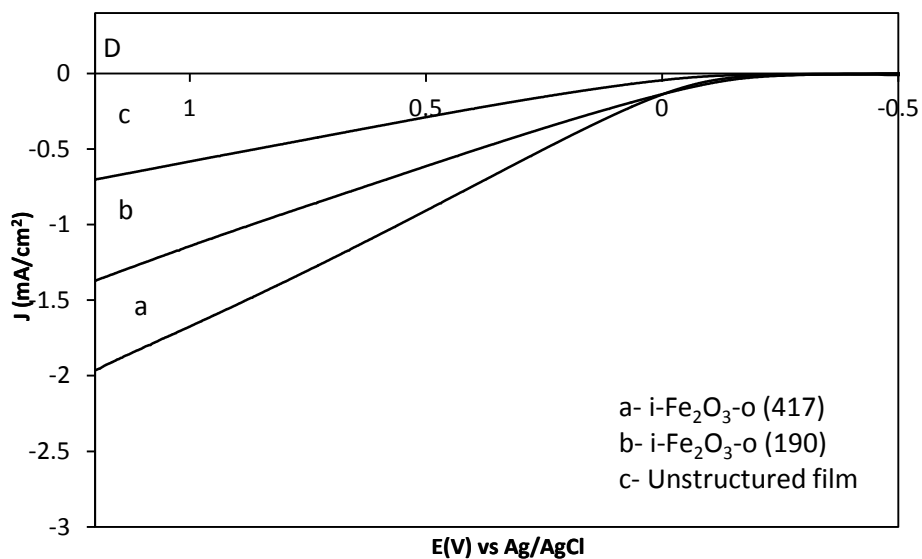
Figure 5.14: I-V curves at i-Fe$_2$O$_3$-o (417) (a), i-Fe$_2$O$_3$-o (190) (b), unstructured film (c) acquired at 50 mV/s in 1 M NaOH pH 13.6 in the back-wall illumination at 25 mW/cm^2 (A), 50 mW/cm^2 (B), 100 mW/cm^2 (C), 200 mW/cm^2 (D). The insets in (A) and (B) show a close up on the measured maximum photocurrents.

Photocurrents measured at 0.6 mV vs Ag/AgCl at different light intensities are presented in

Table 5.1 below.

	J (mA/cm^2)					
	i-Fe$_2$O$_3$-o (417)		i-Fe$_2$O$_3$-o (190)		Unstructured film	
I (mW/cm$^{2)}$	Front wall illumination	Back wall illumination	Front wall illumination	Back wall illumination	Front wall illumination	Back wall illumination
25	0.12	0.16	0.15	0.16	0.04	0.07
50	0.15	0.22	0.17	0.21	0.07	0.18
100	0.53	0.79	0.29	0.33	0.30	0.46
200	0.91	1.10	0.31	0.35	0.50	0.71

Table 5.1: photocurrents measured at i-Fe$_2$O$_3$-o (417), i-Fe$_2$O$_3$-o (190) and unstructured film at 0.6 V vs Ag/AgCl at 25, 50, 100, 200 mW/cm^2 in the front wall and back wall illumination.

At high light intensities (100 and 200 mW/cm^2), i-Fe$_2$O$_3$-o (417) exhibited the highest water photooxidation activity compared to i-Fe$_2$O$_3$-o (190) and unstructured films with photocurrent density reaching 0.91 mA/cm^2 in the front wall illumination and 1.10 mA/cm^2 in the back wall illumination at 200 mW/cm^2. On the other hand, at low light intensities (25 and 50 mW/cm^2), comparable photocurrents were measured at i-Fe$_2$O$_3$-o (417) and i-Fe$_2$O$_3$-o (190): 0.12 and 0.16 mA/cm^2 at i-Fe$_2$O$_3$-o (417) and 0.15 and 0.16 mA/cm^2 at i-Fe$_2$O$_3$-o (190) at 25 mW/cm^2 in the front wall and back wall illumination, respectively. Photocurrents measured at i-Fe$_2$O$_3$-o (417) and unstructured films are proportional within experimental error to the light intensity, but this is not the case for i-Fe$_2$O$_3$-o (190) which could indicate that the high carrier concentration in i-Fe$_2$O$_3$-o (190) at high light intensities is causing significant recombination in the film. At low light intensity, i-Fe$_2$O$_3$-o (417) and i-Fe$_2$O$_3$-o (190) exhibit similar behavior and are better than unstructured film; at 25 mW/cm^2 i-Fe$_2$O$_3$-o (417) and i-Fe$_2$O$_3$-o (190) films exhibited 4 times higher photocurrents in the front wall illumination and 2 times higher photocurrents in the back wall illumination when compared to the unstructured film. The smaller difference in photocurrents in back-wall illumination between i-Fe$_2$O$_3$-o (417) and i-Fe$_2$O$_3$-o (190) on one hand and the unstructured film on another can be attributed to the smaller amount of hematite contacting the interface for the inverse opals due to the porosity of the films. One can deduce from the study of the photoelectrochemical response at i-Fe$_2$O$_3$-o (417), i-Fe$_2$O$_3$-o (190), and unstructured films at different light intensity that i-Fe$_2$O$_3$-o (417) having the larger pore size can support greater carrier density which is consistent with the obtained I-V curves at 100 mW/cm^2 white light. However, at low light intensity, and with monochromatic light, i-Fe$_2$O$_3$-o (417) and

i-Fe$_2$O$_3$-o (190) exhibit similar photoelectrochemical behavior that is better than that of the unstructured film.

5.2.3 *Photoelectrochemical study of i-Fe$_2$O$_3$-o (417) decorated with NiBi and Ni$_{90}$Fe$_{10}$Bi:*

Earlier studies reported that Ni decreases the bias for oxygen evolution reaction and that incorporating iron in nickel oxide enhances the OER activity.[79,108,109,110,111] The photoelectrochemical response at i-Fe$_2$O$_3$-o (417) decorated with NiBi and Ni$_{90}$Fe$_{10}$Bi was investigated. NiBi and Ni$_{90}$Fe$_{10}$Bi were photodeposited from 0.4 mM solutions of Ni(NO$_3$)$_2$ and Ni(NO$_3$)$_2$/Fe(NO$_3$)$_3$ respectively by illuminating with 100 mW/cm^2 white light intensity for 10 min. Catalysts were photodeposited for additional 10 min (t$_{total}$=20 min) to increase the surface coverage on the hematite inverse opal film. Figure 5.15 shows the photoelectrochemical behavior of i-Fe$_2$O$_3$-o (417) before and after NiBi photodeposition. Cathodic shifts of 188 mV after 10 min photodeposition and 194 mV after 20 min photodeposition were measured at 3 μA/cm^2 for NiBi modified hematite inverse opal film in 1 M KBi. At 0.93 V vs Ag/AgCl, 0.45 mA/cm^2, 0.60 mA/cm^2, and 0.65 mA/cm^2 photocurrents were measured at the unmodified i-Fe$_2$O$_3$-o (417), i-Fe$_2$O$_3$-o (417)/NiBi-10 min, and i-Fe$_2$O$_3$-o (417)/NiBi-20 min, respectively.
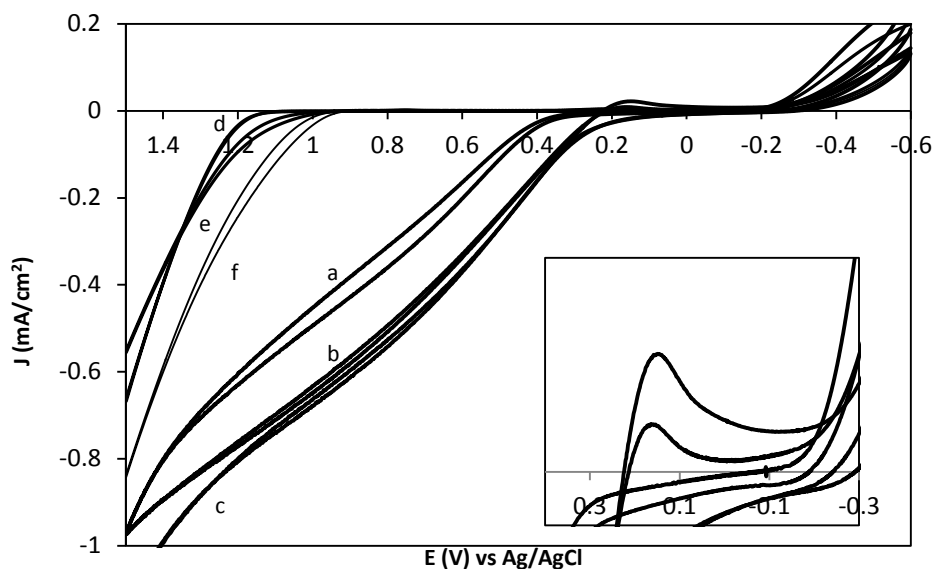
Figure 5.15: Cyclic voltammogram showing i-Fe$_2$O$_3$-o (417) (2.7 μm thick) before and after modification with NiBi acquired at 10 mV/s in 1 M KBi pH 9.2). Unmodified hematite film (a), i-Fe$_2$O$_3$-o/NiBi-10 min (b), i-Fe$_2$O$_3$-o/NiBi-20 min (c). Plots d, e and f represent the dark currents at i-Fe$_2$O$_3$-o, i-Fe$_2$O$_3$-o/NiBi-10 min, and i-Fe$_2$O$_3$-o/NiBi-20 min, respectively. The inset shows a close up on the photocurrent onset potentials.

Ni$_{90}$Fe$_{10}$Bi/hematite films were prepared in the same way as for NiBi/hematite films except that the solution contained 10 % (by atom) iron. Figure 5.16 shows cyclic voltammograms acquired at the Ni$_{90}$Fe$_{10}$Bi modified inverse opal film before and after photodeposition at 10 mV/s in 1 M KBi. A cathodic shift of 174 mV after 10 min photodeposition and 189 mV after 20 min after 20 min photodeposition were measured at 3 μA/cm^2 which is similar to the shift caused by NiBi film on the inverse opal. Under 100 mW/cm^2 and 0.93 V vs Ag/AgCl, a photocurrent of 0.38 mA/cm^2 at the unmodified inverse opal, 0.43 mA/cm^2 after 10 min Ni$_{90}$Fe$_{10}$Bi photodeposition and 0.50 mA/cm^2 after 20 min Ni$_{90}$Fe$_{10}$Bi photodeposition was measured. NiBi and Ni$_{90}$Fe$_{10}$Bi catalysts not only decreased the overpotential required for water oxidation but also increased the plateau photocurrents by ~0.1 mA/cm^2. This observation has been previously reported by Tilley

et al at iridium modified hematite cauliflower structure.[77] This may indicate a catalytic effect of the deposited complexes in this case since at large bias the hole is long-lived. The oxidation peak observed at ~0.15 mV in both NiBi and $Ni_{90}Fe_{10}Bi$ modified inverse opal hematite films (see inset of fig 5.14 and 5.15) was previously observed by Halaoui et al on hematite nanorods decorated with NiBi and is subject of a study to be published where the results are interpreted by the surface modification increasing the hole lifetime and thus allowing for longer time before recombination takes place for water oxidation to occur. Electrodepositon of NiBi and $Ni_{90}Fe_{10}Bi$ on bare FTO do not show the observed peak at 0.15 V vs Ag/AgCl (refer to fig 4.5).
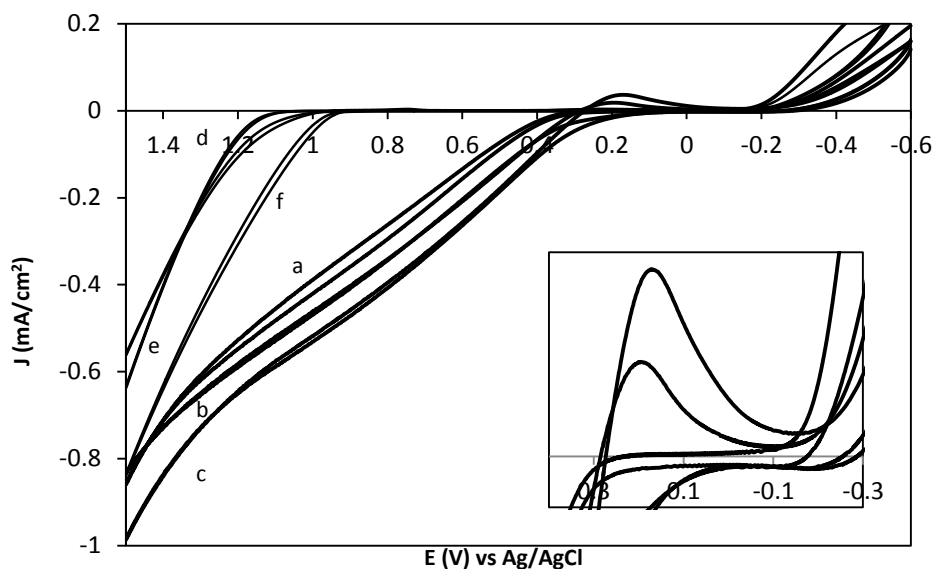
Figure 5.16: Cyclic voltammogram showing i-Fe_2O_3-o (417) (2.5 µm thick) before and after modification acquired at 10 mV/s in 1 M KBi pH 9.2. Unmodified hematite film (a), i-Fe_2O_3-o/NiFeBi-10 min (b), and i-Fe_2O_3-o/NiFeBi-20 min (c). Plots d, e and f represent the dark currents at i-Fe_2O_3-o, i-Fe_2O_3-o/NiFeBi-10 min, and i-Fe_2O_3-o/NiFeBi-20 min, respectively. The inset shows a close up on the photocurrent onset potentials.

Figure 5.17 shows the CV of i-Fe$_2$O$_3$-o/NiBi and i-Fe$_2$O$_3$-o/NiFeBi films in the dark at 10 mV/s in 1 M KBi. Upon surface modification with NiBi and NiFeBi, cathodic shifts were observed in the dark. 45 mV difference in the shift was observed between the 10 min photodeposition and 20 min photodeposition for i-Fe$_2$O$_3$-o/NiBi films. A similar increase in cathodic shift with increasing surface coverage was observed at i-Fe$_2$O$_3$-o/NiFeBi films. Although surface coverage did not significantly affect the cathodic shift under illumination, the dark cyclic voltammograms show a smaller overpotential at i-Fe$_2$O$_3$-o/NiBi-20 min for water oxidation compared to i-Fe$_2$O$_3$-o/NiBi-10 min. This can indicate that in the dark the OEC is catalyzing oxygen evolution.

138
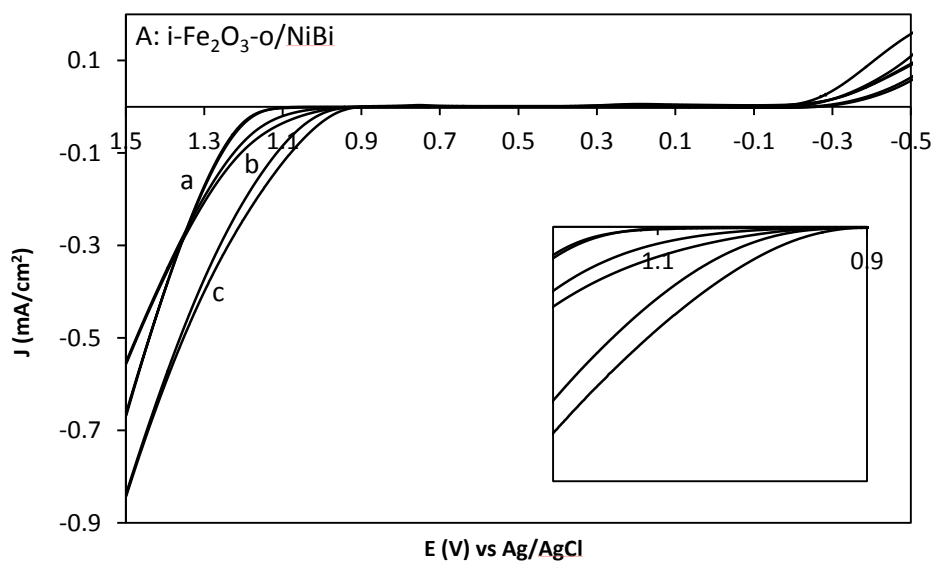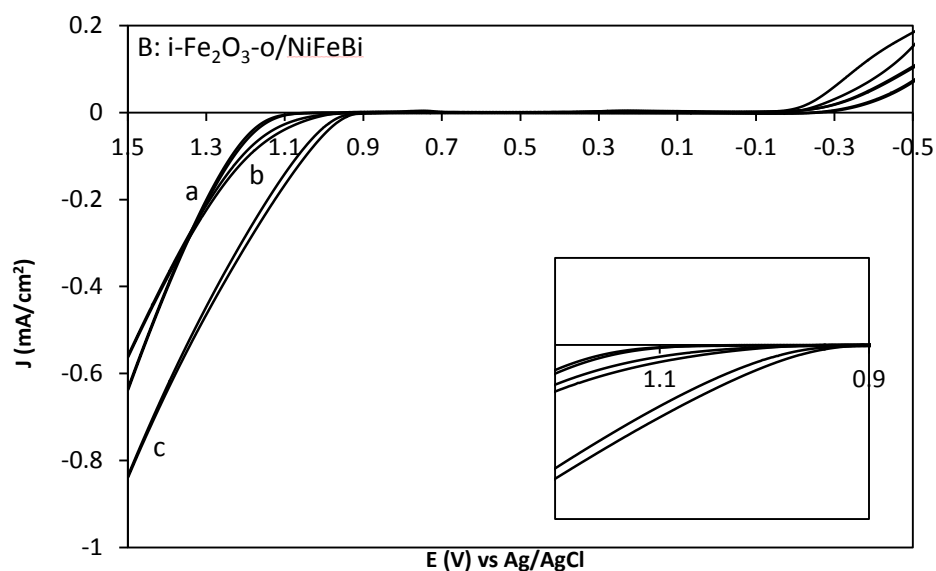
Figure 5.17: CV of i-Fe$_2$O$_3$-o/NiBi (A) and i-Fe$_2$O$_3$-o/NiFeBi (B) in the dark acquired at 10 mV/s in 1 M KBi before electrodeposition (a), with photodeposition for 10 min (b) and with photodeposition for 20 min (c).

5.2.3.1 Effect on Photocurrent Decay and Saturation Photocurrents:

Amperiometric I-t curves at hematite films were collected under chopped light illumination using 3-electrode setup in 1 M KBi. I-t curves were carried for 60 seconds for each scan and at different bias ranging from the potential leading to the saturation photocurrent to the onset potential.

Figure 4.18 and 4.19 shows i-t curves collected at the inverse opal films before and after modification with NiBi and Ni$_{90}$Fe$_{10}$Bi at 0.8 V, 0.4 V and 0.2 V vs Ag/AgCl in 1 M KBi, respectively. For smaller applied bias, the initial photocurrent decreases with time and its decay become steeper due to higher recombination. High overpotentials (at 0.8 V vs Ag/AgCl) on the other hand cause more bending and hence seperation of charges which decrease recombination. Attaching NiBi and Ni$_{90}$Fe$_{10}$Bi to the films increases the photocurrent and slows the decay

especially at low overpotentials (below 0.4 V vs Ag/AgCl). We observed that the slower decay

was not significantly affected significantly by increasing NiBi (or NiFeBi) surface coverage. The

results show that the surface modification causes two effects 1) a slower decay of photocurrent at

low bias indicating a longer hole lifetime and 2) a greater saturation photocurrent, this latter

possibly indicating a catalytic effect.
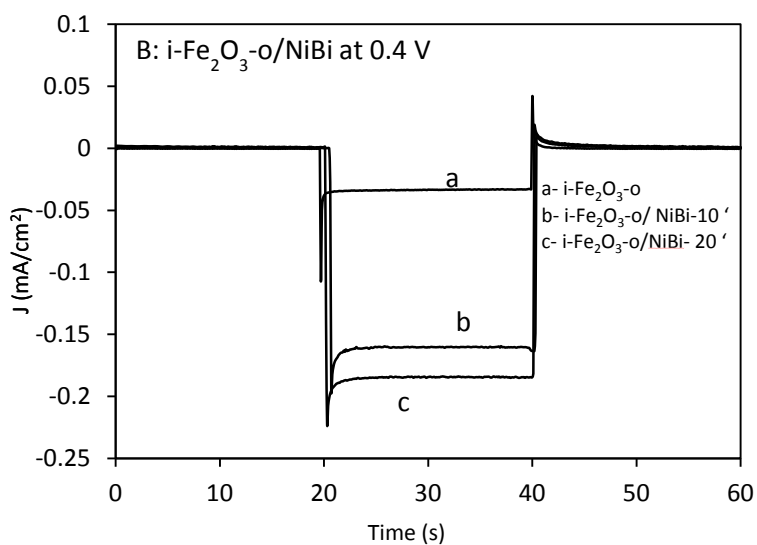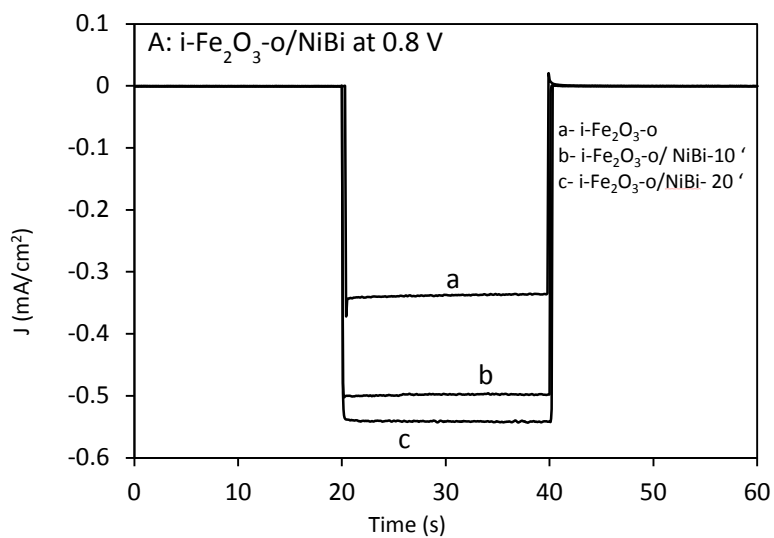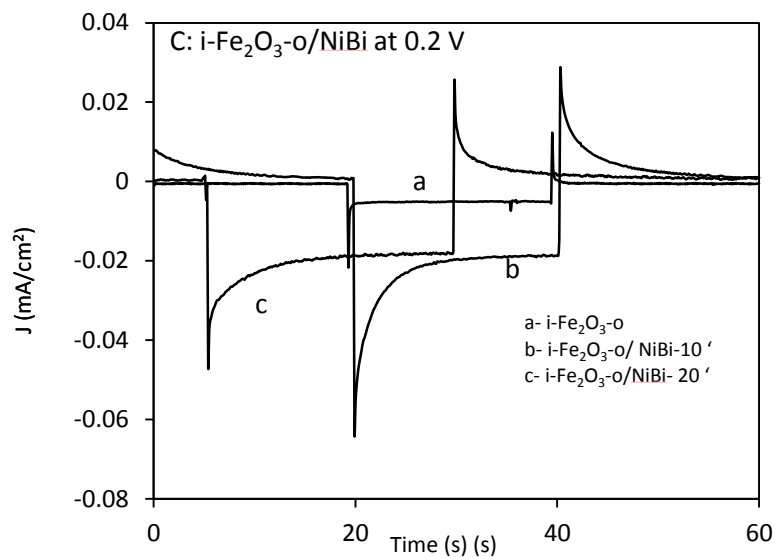
Figure 0.18: i-t amperometric curves for i-Fe$_2$O$_3$-o (a), i-Fe$_2$O$_3$-o/NiBi- 10 min (b), and i-Fe$_2$O$_3$-o/NiBi-20 min (c) at 0.8 V (A), 0.4 V (B) and 0.2 V (C) in 1 M KBi.
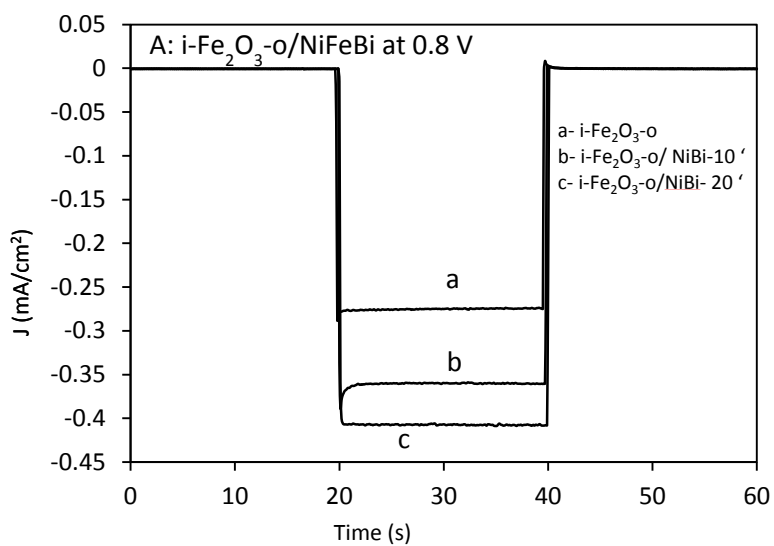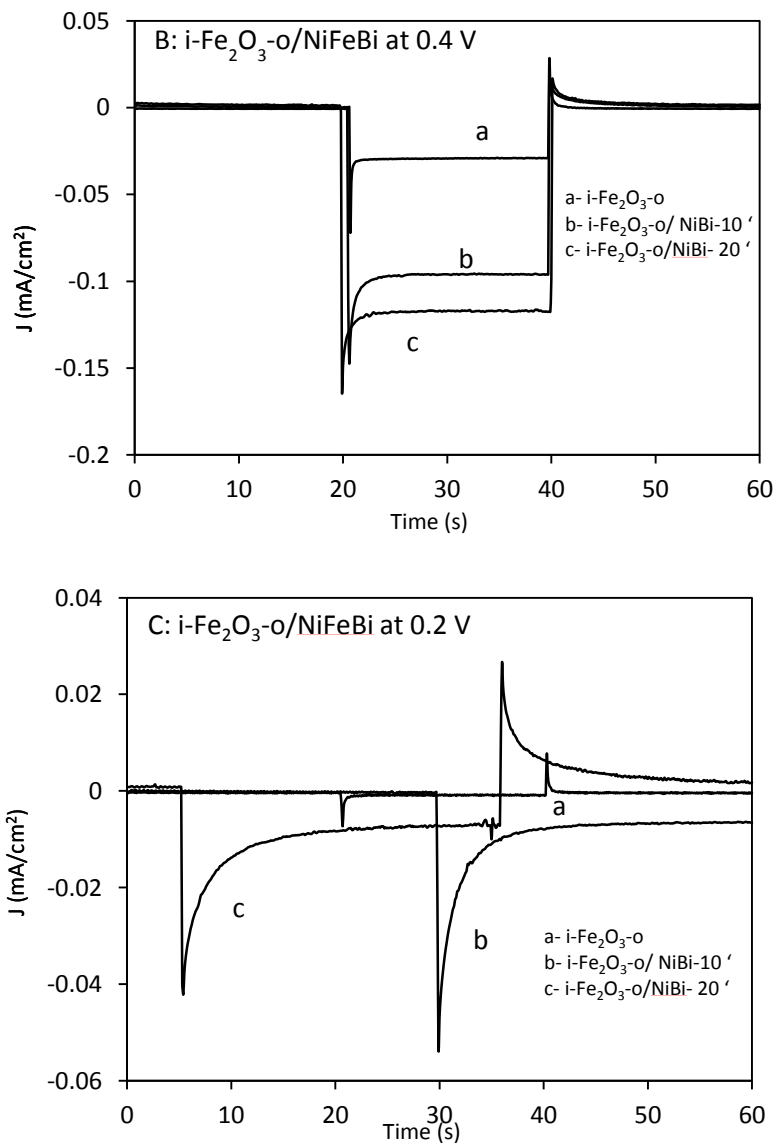
Figure 0.19: i-t amperometric curves for i-Fe$_2$O$_3$-o (a), i-Fe$_2$O$_3$-o/NiFeBi- 10 min (b), and i-Fe$_2$O$_3$-o/NiFeBi-20 min (c) at 0.8 V (A), 0.4 V (B) and 0.2 V (C) in 1 M KBi.

We showed in this study that i-Fe$_2$O$_3$-o (417) with their largest pore structure and hence greater interface with the solution, exhibited the best photoelectrochemical behavior towards water

142

oxidation producing photocurrents of 0.79 mA/cm^2 at 1 V vs Ag/AgCl in 1 M KBi pH 9.2 at 100 and 200 mW/cm^2. At low light intensities i-Fe$_2$O$_3$-o (417) and i-Fe$_2$O$_3$-o (190) exhibited similar photoelectrochemical behavior. Decorating i-Fe$_2$O$_3$-o (417) films with few monolayers of NiBi or Ni$_{90}$Fe$_{10}$Bi resulted in a comparable decrease in the onset potential by ~ 200 mV in 1 M KBi pH 9.2. NiBi and Ni$_{90}$Fe$_{10}$Bi surface catalysts resulted in a slower decay in the photocurrent at low potentials which resulted from a decrease in recombination processes, and had an effect also on increasing the photocurrent produced at high bias which might indicate a catalytic effect. Further research need to be directed towards fabricating photoelectrochemically efficient hematite inverse opals without detoriating its ordered architecture to be able to study light localization effects in these films.

CHAPTER 5
CONCLUSION

In one project, we investigated the role of order vs disorder at bilayer electrodes assembled from nc-TiO$_2$ coupled with photonic crystals and disordered photonic glass films. For this purpose we fabricated disordered films from an assembly of disordered polystyrene photonic glass from one sphere size by increasing the ionic strength. The photoelectrochemical behavior of the inverse opals, inverse glass and bilayer electrodes were investigated in front wall and back wall illumination. While i-TiO$_2$-o (with stop band at 600 nm) show only slight enhancement in energy conversion at the red edge of stop band (660-680 nm), disordered inverse glass (i-TiO$_2$-g) when not coupled to nc-TiO$_2$ showed a significant enhancement (compared to the conventional nc-TiO$_2$) in the entire spectrum which was attributed to multiple internal scattering in the film that causes longer light-matter interaction. The gain was similarly observed under front wall illumination and back wall illumination. Coupling nc-TiO$_2$ to i-TiO$_2$-d film on the other hand, did not result in prominent enhancement as in the case of nc-TiO$_2$/600-i-TiO$_2$-o which showed enhancement within the stop band region in the front wall illumination, and at red edge of the stop band extending to 720 nm for both illumination modes. Back scattering at nc-TiO$_2$/i-TiO$_2$-d hindered light from reaching the nc-TiO$_2$ layer where most of the dye is adsorbed in the back wall illumination. We concluded that photonic effects due to the presence of order are causing the localization of light within the nc-TiO$_2$ film coupled to inverse opal and that this effect does not persist in the presence of significant disorder.

In a second project, the effect of doping amorphous Ni-oxo/hydroxo films with iron for catalyzing the oxygen evolution reaction was studied. Ni$_{40}$Fe$_{60}$Bi and Ni$_{60}$Fe$_{40}$Bi exhibited

the highest turnover frequencies at high overpotentials whether anodized or non-anodized and hence had the highest catalytic activity. The films were also compared with thin NiBi having similar amounts of Ni. Thin NiBi films had similar TOF as the thicker NiBi films further proving that it is the effect of iron that is enhancing the catalytic activity of the Fe-doped NiBi films. We also showed in this study that the anodization procedure that activated the films and increases their catalytic activity cannot merely be a result of incorporating iron in the film, as deliberately introducing iron in anon-anodized films still led to lower activity for oxygen evolution when compared to anodized NiBi and anodized NiBi with iron in different proportions. Therefore, though it may be possible that Fe is being introduced in trace amounts from the electrolyte, it is evident that the anodization increases the activity because of possible structural changes (not merely incorporating Fe).

In a third project, we fabricated hematite inverse opals to be used as photoanodes for water splitting. Two sizes of polystyrene templates were used in this study, 417 nm and 190 nm and were compared to unstructured films. At high light intensity, i-Fe_2O_3-o (417) exhibited the highest photocurrents compared to unstructured hematite films and to hematite inverse opal films with the smaller pore size of 190 nm whether in the front wall or back wall illumination. However, at lower light intensity (25 mW/cm^2), i-Fe_2O_3-o (190) and i-Fe_2O_3-o (417) showed similar photocurrents. The lower photocurrens measured at i-Fe_2O_3-o (190) at high light intensity was attributed to the high carrier concentration leading to increased rates of recombination at the film. i-Fe_2O_3-o (417) was surface decorated with NiBi and $Ni_{90}Fe_{10}Bi$ catalysts which lead to similar cathodic shifts of ~ 200 mV and resulted in a slower decay of the photogenerated currents which is indicative of decreased recombination rates.

REFERENCES

1. Crabtree, G. W.; Lewis, N. S., Solar energy conversion. *Physics Today* **2007,** *60* (3), 37-41.

2. Walter, M. G.; Warren, E. L.; McKone, J. R.; Boettcher, S. W.; Mi, Q.; Santori, E. A.; Lewis, N. S., Solar Water Splitting Cells. *Chemical Reviews* **2010,** *110* (11), 6446-6473.

3. Lewis, N. S.; Crabtree, G.; Nozik, A. J.; Wasielewski, M. R.; Alivisatos, P.; Kung, H.; Tsao, J.; Chandler, E.; Walukiewicz, W.; Spitler, M.; Ellingson, R.; Overend, R.; Mazer, J.; Gress, M.; Horwitz, J.; Ashton, C.; Herndon, B.; Shapard, L.; Nault, R. M. *Basic Research Needs for Solar Energy Utilization. Report of the Basic Energy Sciences Workshop on Solar Energy Utilization, April 18-21, 2005*; 2005; p Medium: ED.

4. Hagfeldt, A.; Boschloo, G.; Sun, L.; Kloo, L.; Pettersson, H., Dye-sensitized solar cells. *Chemical Reviews* **2010,** *110* (11), 6595-6663.

5. Lewis, N. S., Toward Cost-Effective Solar Energy Use. *Science* **2007,** *315* (5813), 798-801.

6. Shockley, W.; Queisser, H. J., Detailed Balance Limit of Efficiency of p-n Junction Solar Cells. *Journal of Applied Physics* **1961,** *32* (3), 510-519.

7. Green, M. A., *Third generation photovoltaics: advanced solar energy conversion*. Springer: 2003.

8. Nozik, A. J., Quantum dot solar cells. *Physica E: Low-dimensional Systems and Nanostructures* **2002,** *14* (1–2), 115-120.

9. Yablonovitch, E., Inhibited Spontaneous Emission in Solid-State Physics and Electronics. *Physical Review Letters* **1987,** *58* (20), 2059-2062.

10. John, S., Strong localization of photons in certain disordered dielectric superlattices. *Physical Review Letters* **1987,** *58* (23), 2486-2489.

11. Carlson, R. J.; Asher, S. A., CHARACTERIZATION OF OPTICAL DIFFRACTION AND CRYSTAL-STRUCTURE IN MONODISPERSE POLYSTYRENE COLLOIDS. *Applied Spectroscopy* **1984,** *38* (3), 297-304.

12. Flaugh, P. L.; Odonnell, S. E.; Asher, S. A., DEVELOPMENT OF A NEW OPTICAL WAVELENGTH REJECTION FILTER - DEMONSTRATION OF ITS UTILITY IN RAMAN-SPECTROSCOPY. *Applied Spectroscopy* **1984,** *38* (6), 847-850.

13. El Harakeh, M.; Halaoui, L., Enhanced Conversion of Light at TiO2 Photonic Crystals to the Blue of a Stop Band and at TiO2 Random Films Sensitized with Q-CdS: Order and Disorder. *The Journal of Physical Chemistry C* **2010,** *114* (6), 2806-2813.

14. Muller, M.; Zentel, R.; Maka, T.; Romanov, S. G.; Torres, C. M. S., Photonic crystal films with high refractive index contrast. *Advanced Materials* **2000,** *12* (20), 1499-1503.

15. Yamamoto, Y.; Slusher, R. E., OPTICAL PROCESSES IN MICROCAVITIES. *Physics Today* **1993,** *46* (6), 66-73.

16. Loncar, M.; Yoshie, T.; Scherer, A.; Gogna, P.; Qiu, Y. M., Low-threshold photonic crystal laser. *Applied Physics Letters* **2002,** *81* (15), 2680-2682.

17. Ohtera, Y.; Sato, T.; Kawashima, T.; Tamamura, T.; Kawakami, S., Photonic crystal polarisation splitters. *Electronics Letters* **1999,** *35* (15), 1271-1272.

18. Tyan, R.-C.; Salvekar, A. A.; Chou, H.-P.; Cheng, C.-C.; Scherer, A.; Sun, P.-C.; Xu, F.; Fainman, Y., Design, fabrication, and characterization of form-birefringent multilayer polarizing beam splitter. *J. Opt. Soc. Am. A* **1997,** *14* (7), 1627-1636.

19. Mekis, A.; Chen, J. C.; Kurland, I.; Fan, S.; Villeneuve, P. R.; Joannopoulos, J. D., High Transmission through Sharp Bends in Photonic Crystal Waveguides. *Physical Review Letters* **1996,** *77* (18), 3787-3790.

20. Joannopoulos, J. D.; Meade, R. D.; Winn, J., *Photonic crystals: molding the flow of light*. Princeton University Press: Princeton, N.J, 1995.

21. Xu, Z.; Cao, L.; Tan, Q.; He, Q.; Jin, G., Enhancement of the light output of light-emitting diode with double photonic crystals. *Optics Communications* **2007,** *278* (1), 211-214.

22. Sakoda, K.; Sasada, M.; Fukushima, T.; Yamanaka, A.; Kawai, N.; Inoue, K., Detailed analysis of transmission spectra and Bragg-reflection spectra of a two-dimensional photonic crystal with a lattice constant of 1.15 µm. *J. Opt. Soc. Am. B* **1999,** *16* (3), 361-365.

23. Nishimura, S.; Abrams, N.; Lewis, B. A.; Halaoui, L. I.; Mallouk, T. E.; Benkstein, K. D.; van de Lagemaat, J.; Frank, A. J., Standing Wave Enhancement of Red Absorbance and Photocurrent in Dye-Sensitized Titanium Dioxide Photoelectrodes Coupled to Photonic Crystals. *Journal of the American Chemical Society* **2003,** *125* (20), 6306-6310.

24. Scalora, M.; Dowling, J. P.; Bowden, C. M.; Bloemer, M. J., Optical Limiting and Switching of Ultrashort Pulses in Nonlinear Photonic Band Gap Materials. *Physical Review Letters* **1994,** *73* (10), 1368-1371.

25. Vlasov, Y. A.; Petit, S.; Klein, G.; Hönerlage, B.; Hirlimann, C., Femtosecond measurements of the time of flight of photons in a three-dimensional photonic crystal. *Physical Review E* **1999,** *60* (1), 1030-1035.

26. Bayram, S.; Halaoui, L., Amplification of Solar Energy Conversion in Quantum-Confined CdSe-Sensitized TiO2 Photonic Crystals by Trapping Light. *Particle & Particle Systems Characterization* **2013,** *30* (8), 706-714.

27.   Albada, M. P. V.; Lagendijk, A., Observation of Weak Localization of Light in a Random Medium. *Physical Review Letters* **1985,** *55* (24), 2692-2695.

28.   Anderson, P. W., The question of classical localization A theory of white paint? *Philosophical Magazine Part B* **1985,** *52* (3), 505-509.

29.   Dalichaouch, R.; Armstrong, J. P.; Schultz, S.; Platzman, P. M.; McCall, S. L., MICROWAVE LOCALIZATION BY 2-DIMENSIONAL RANDOM SCATTERING. *Nature* **1991,** *354* (6348), 53-55.

30.   Genack, A. Z.; Garcia, N., Observation of photon localization in a three-dimensional disordered system. *Physical Review Letters* **1991,** *66* (16), 2064-2067.
31.   Garcia, P. D.; Sapienza, R.; Lopez, C., Photonic Glasses: A Step Beyond White Paint. *Advanced Materials* **2010,** *22* (1), 12-19.

32.   Sheng, P., 3 - Wave Scattering and the Effective Medium. In *Introduction to Wave Scattering, Localization, and Mesoscopic Phenomena*, Sheng, P., Ed. Academic Press: San Diego, 1995; pp 49-113.

33.   Mie, G., Beiträge zur Optik trüber Medien, speziell kolloidaler Metallösungen. *Annalen der Physik* **1908,** *330* (3), 377-445.

34.   Garcia, P. D.; Sapienza, R.; Blanco, A.; Lopez, C., Photonic glass: A novel random material for light. *Advanced Materials* **2007,** *19* (18), 2597-+.

35.   Garcia, P. D.; Sapienza, R.; Bertolotti, J.; Martin, M. D.; Blanco, A.; Altube, A.; Vina, L.; Wiersma, D. S.; Lopez, C., Resonant light transport through Mie modes in photonic glasses. *Physical Review A* **2008,** *78* (2).

36.   O'regan, B.; Grätzel, M., A low-cost, high-efficiency solar cell based on dye-sensitized. *Nature* **1991,** *353*, 24.

37.   Jena, A.; Mohanty, S. P.; Kumar, P.; Naduvath, J.; Gondane, V.; Lekha, P.; Das, J.; Narula, H. K.; Mallick, S.; Bhargava, P., Dye Sensitized Solar Cells: A Review. *Transactions of the Indian Ceramic Society* **2012,** *71* (1), 1-16.

38.   Mathew, S.; Yella, A.; Gao, P.; Humphry-Baker, R.; Curchod, B. F. E.; Ashari-Astani, N.; Tavernelli, I.; Rothlisberger, U.; Nazeeruddin, M. K.; Gratzel, M., Dye-sensitized solar cells with 13% efficiency achieved through the molecular engineering of porphyrin sensitizers. *Nature Chemistry* **2014,** *6* (3), 242-247.

39.   Maçaira, J.; Andrade, L.; Mendes, A., Review on nanostructured photoelectrodes for next generation dye-sensitized solar cells. *Renewable and Sustainable Energy Reviews* **2013,** *27* (0), 334-349.

40.   Nazeeruddin, M. K.; Kay, A.; Rodicio, I.; Humphry-Baker, R.; Mueller, E.; Liska, P.; Vlachopoulos, N.; Graetzel, M., Conversion of light to electricity by cis-X2bis(2,2'-bipyridyl-4,4'-dicarboxylate)ruthenium(II) charge-transfer sensitizers (X = Cl-, Br-, I-, CN-, and SCN-) on nanocrystalline titanium dioxide electrodes. *Journal of the American Chemical Society* **1993,** *115* (14), 6382-6390.

41.   Park, N. G.; van de Lagemaat, J.; Frank, A. J., Comparison of Dye-Sensitized Rutile- and Anatase-Based TiO2 Solar Cells. *The Journal of Physical Chemistry B* **2000,** *104* (38), 8989-8994.

42.   Huang, S. Y.; Schlichthörl, G.; Nozik, A. J.; Grätzel, M.; Frank, A. J., Charge Recombination in Dye-Sensitized Nanocrystalline TiO2 Solar Cells. *The Journal of Physical Chemistry B* **1997,** *101* (14), 2576-2582.

43.   Berginc, M.; Krašovec, U. O.; Topič, M., Evaluation of the recombination processes in DSSC by measuring the open circuit voltage over a wide illumination intensity range. *physica status solidi (a)* **2013,** *210* (9), 1750-1757.

44.   Martinson, A. B. F.; Hamann, T. W.; Pellin, M. J.; Hupp, J. T., New Architectures for Dye-Sensitized Solar Cells. *Chemistry – A European Journal* **2008,** *14* (15), 4458-4467.

45.   Halaoui, L. I.; Abrams, N. M.; Mallouk, T. E., Increasing the Conversion Efficiency of Dye-Sensitized TiO2 Photoelectrochemical Cells by Coupling to Photonic Crystals. *The Journal of Physical Chemistry B* **2005,** *109* (13), 6334-6342.

46.   Lee, S.-H. A.; Abrams, N. M.; Hoertz, P. G.; Barber, G. D.; Halaoui, L. I.; Mallouk, T. E., Coupling of Titania Inverse Opals to Nanocrystalline Titania Layers in Dye-Sensitized Solar Cells†. *The Journal of Physical Chemistry B* **2008,** *112* (46), 14415-14421.

47.   Mihi, A.; Míguez, H., Origin of Light-Harvesting Enhancement in Colloidal-Photonic-Crystal-Based Dye-Sensitized Solar Cells. *The Journal of Physical Chemistry B* **2005,** *109* (33), 15968-15976.

48.   Ogura, R. Y.; Nakane, S.; Morooka, M.; Orihashi, M.; Suzuki, Y.; Noda, K., High-performance dye-sensitized solar cell with a multiple dye system. *Applied Physics Letters* **2009,** *94* (7), 073308-073308-3.

49.   Shalom, M.; Albero, J.; Tachan, Z.; Martínez-Ferrero, E.; Zaban, A.; Palomares, E., Quantum Dot−Dye Bilayer-Sensitized Solar Cells: Breaking the Limits Imposed by the Low Absorbance of Dye Monolayers. *The Journal of Physical Chemistry Letters* **2010,** *1* (7), 1134-1138.

50.   Jeong, N. C.; Prasittichai, C.; Hupp, J. T., Photocurrent Enhancement by Surface Plasmon Resonance of Silver Nanoparticles in Highly Porous Dye-Sensitized Solar Cells. *Langmuir* **2011,** *27* (23), 14609-14614.

51.   Brown, M. D.; Suteewong, T.; Kumar, R. S. S.; D'Innocenzo, V.; Petrozza, A.; Lee, M. M.; Wiesner, U.; Snaith, H. J., Plasmonic Dye-Sensitized Solar Cells Using Core−Shell Metal−Insulator Nanoparticles. *Nano Letters* **2010,** *11* (2), 438-445.

52.   Nocera, D. G., The Artificial Leaf. *Accounts of Chemical Research* **2012,** *45* (5), 767-776.

53.   Sivula, K.; Le Formal, F.; Gratzel, M., Solar Water Splitting: Progress Using Hematite (alpha-Fe2O3) Photoelectrodes. *Chemsuschem* **2011,** *4* (4), 432-449.

54.   Walter, M. G.; Warren, E. L.; McKone, J. R.; Boettcher, S. W.; Mi, Q. X.; Santori, E. A.; Lewis, N. S., Solar Water Splitting Cells. *Chemical Reviews* **2010,** *110* (11), 6446-6473.

55.   Tran, P. D.; Wong, L. H.; Barber, J.; Loo, J. S. C., Recent advances in hybrid photocatalysts for solar fuel production. *Energy & Environmental Science* **2012,** *5* (3), 5902-5918.

56.   Fujishima, A.; Honda, K., ELECTROCHEMICAL PHOTOLYSIS OF WATER AT A SEMICONDUCTOR ELECTRODE. *Nature* **1972,** *238* (5358), 37-+.

57.   Bard, A. J.; Fox, M. A., Artificial Photosynthesis: Solar Splitting of Water to Hydrogen and Oxygen. *Accounts of Chemical Research* **1995,** *28* (3), 141-145.

58.   Katz, M. J.; Riha, S. C.; Jeong, N. C.; Martinson, A. B. F.; Farha, O. K.; Hupp, J. T., Toward solar fuels: Water splitting with sunlight and "rust"? *Coordination Chemistry Reviews* **2012,** *256* (21–22), 2521-2529.
59.   Dare-Edwards, M. P.; Goodenough, J. B.; Hamnett, A.; Trevellick, P. R., Electrochemistry and photoelectrochemistry of iron(III) oxide. *Journal of the Chemical Society, Faraday Transactions 1: Physical Chemistry in Condensed Phases* **1983,** *79* (9), 2027-2041.

60.   Kokorin, A. I.; Bahnemann, D. W., Chemical Physics of Nanostructured Semiconductors. VSP - An imprint of BRILL.

61.   Bora, D. K.; Braun, A.; Constable, E. C., "In rust we trust". Hematite - the prospective inorganic backbone for artificial photosynthesis. *Energy & Environmental Science* **2013,** *6* (2), 407-425.

62.   Itoh, K.; Bockris, J. O. M., Thin Film Photoelectrochemistry: Iron Oxide. *Journal of The Electrochemical Society* **1984,** *131* (6), 1266-1271.

63.   Itoh, K.; Bockris, J. O. M., Stacked thin-film photoelectrode using iron oxide. *Journal of Applied Physics* **1984,** *56* (3), 874-876.

64.   Kennedy, J. H.; Frese, K. W., Photooxidation of Water at α - Fe2 O 3 Electrodes. *Journal of The Electrochemical Society* **1978,** *125* (5), 709-714.

65.   He, Y. P.; Miao, Y. M.; Li, C. R.; Wang, S. Q.; Cao, L.; Xie, S. S.; Yang, G. Z.; Zou, B. S.; Burda, C., Size and structure effect on optical transitions of iron oxide nanocrystals. *Physical Review B* **2005,** *71* (12), 125411.

66.   Hardee, K. L.; Bard, A. J., Semiconductor Electrodes: V . The Application of Chemically Vapor Deposited Iron Oxide Films to Photosensitized Electrolysis. *Journal of The Electrochemical Society* **1976,** *123* (7), 1024-1026.

67.   Joly, A. G.; Williams, J. R.; Chambers, S. A.; Xiong, G.; Hess, W. P.; Laman, D. M., Carrier dynamics in α-Fe2O3 (0001) thin films and single crystals probed by femtosecond transient absorption and reflectivity. *Journal of Applied Physics* **2006,** *99* (5), -.

68.   Cherepy, N. J.; Liston, D. B.; Lovejoy, J. A.; Deng, H.; Zhang, J. Z., Ultrafast Studies of Photoexcited Electron Dynamics in γ- and α-Fe2O3 Semiconductor Nanoparticles. *The Journal of Physical Chemistry B* **1998,** *102* (5), 770-776.

69.   Townsend, T. K.; Sabio, E. M.; Browning, N. D.; Osterloh, F. E., Photocatalytic water oxidation with suspended alpha-Fe2O3 particles-effects of nanoscaling. *Energy & Environmental Science* **2011,** *4* (10), 4270-4275.

70.   Mao, A.; Han, G. Y.; Park, J. H., Synthesis and photoelectrochemical cell properties of vertically grown [small alpha]-Fe2O3 nanorod arrays on a gold nanorod substrate. *Journal of Materials Chemistry* **2010,** *20* (11), 2247-2250.

71.   Mohapatra, S. K.; John, S. E.; Banerjee, S.; Misra, M., Water Photooxidation by Smooth and Ultrathin α-Fe2O3 Nanotube Arrays. *Chemistry of Materials* **2009,** *21* (14), 3048-3055.

72.   Duret, A.; Grätzel, M., Visible Light-Induced Water Oxidation on Mesoscopic α-Fe2O3 Films Made by Ultrasonic Spray Pyrolysis. *The Journal of Physical Chemistry B* **2005,** *109* (36), 17184-17191.
73.   Kay, A.; Cesar, I.; Grätzel, M., New Benchmark for Water Photooxidation by Nanostructured α-Fe2O3 Films. *Journal of the American Chemical Society* **2006,** *128* (49), 15714-15721.

74.   Shi, X.; Zhang, K.; Shin, K.; Moon, J. H.; Lee, T. W.; Park, J. H., Constructing inverse opal structured hematite photoanodes via electrochemical process and their application to photoelectrochemical water splitting. *Physical Chemistry Chemical Physics* **2013,** *15* (28), 11717-11722.

75.   Riha, S. C.; Vermeer, M. J. D.; Pellin, M. J.; Hupp, J. T.; Martinson, A. B. F., Hematite-based Photo-oxidation of Water Using Transparent Distributed Current Collectors. *Acs Applied Materials & Interfaces* **2013,** *5* (2), 360-367.

76.   Moir, J.; Soheilnia, N.; O'Brien, P.; Jelle, A.; Grozea, C. M.; Faulkner, D.; Helander, M. G.; Ozin, G. A., Enhanced Hematite Water Electrolysis Using a 3D Antimony-Doped Tin Oxide Electrode. *ACS Nano* **2013,** *7* (5), 4261-4274.

77. Tilley, S. D.; Cornuz, M.; Sivula, K.; Grätzel, M., Light-Induced Water Splitting with Hematite: Improved Nanostructure and Iridium Oxide Catalysis. *Angewandte Chemie International Edition* **2010,** *49* (36), 6405-6408.

78. Landon, J.; Demeter, E.; Inoglu, N.; Keturakis, C.; Wachs, I. E.; Vasic, R.; Frenkel, A. I.; Kitchin, J. R., Spectroscopic Characterization of Mixed Fe-Ni Oxide Electrocatalysts for the Oxygen Evolution Reaction in Alkaline Electrolytes. *ACS Catalysis* **2012,** *2* (8), 1793-1801.

79. Dinca, M.; Surendranath, Y.; Nocera, D. G., Nickel-borate oxygen-evolving catalyst that functions under benign conditions. *Proceedings of the National Academy of Sciences of the United States of America* **2010,** *107* (23), 10337-10341.

80. Bediako, D. K.; Lassalle-Kaiser, B.; Surendranath, Y.; Yano, J.; Yachandra, V. K.; Nocera, D. G., Structure–Activity Correlations in a Nickel–Borate Oxygen Evolution Catalyst. *Journal of the American Chemical Society* **2012,** *134* (15), 6801-6809.

81. Cukier, R. I.; Nocera, D. G., Proton-coupled electron transfer. *Annual Review of Physical Chemistry* **1998,** *49*, 337-369.

82. Reece, S. Y.; Nocera, D. G., Proton-Coupled Electron Transfer in Biology: Results from Synergistic Studies in Natural and Model Systems. In *Annual Review of Biochemistry*, 2009; Vol. 78, pp 673-699.

83. Corrigan, D. A., The Catalysis of the Oxygen Evolution Reaction by Iron Impurities in Thin Film Nickel Oxide Electrodes. *Journal of The Electrochemical Society* **1987,** *134* (2), 377-384.

84. Kleiman-Shwarsctein, A.; Hu, Y.-S.; Stucky, G. D.; McFarland, E. W., NiFe-oxide electrocatalysts for the oxygen evolution reaction on Ti doped hematite photoelectrodes. *Electrochemistry Communications* **2009,** *11* (6), 1150-1153.

85. Merrill, M. D.; Dougherty, R. C., Metal Oxide Catalysts for the Evolution of O2 from H2O. *The Journal of Physical Chemistry C* **2008,** *112* (10), 3655-3666.

86. Louie, M. W.; Bell, A. T., An Investigation of Thin-Film Ni-Fe Oxide Catalysts for the Electrochemical Evolution of Oxygen. *Journal of the American Chemical Society* **2013,** *135* (33), 12329-12337.

87. Smith, R. D. L.; Prevot, M. S.; Fagan, R. D.; Trudel, S.; Berlinguette, C. P., Water Oxidation Catalysis: Electrocatalytic Response to Metal Stoichiometry in Amorphous Metal Oxide Films Containing Iron, Cobalt, and Nickel. *Journal of the American Chemical Society* **2013,** *135* (31), 11580-11586.

88. Gong, M.; Li, Y. G.; Wang, H. L.; Liang, Y. Y.; Wu, J. Z.; Zhou, J. G.; Wang, J.; Regier, T.; Wei, F.; Dai, H. J., An Advanced Ni-Fe Layered Double Hydroxide Electrocatalyst for Water Oxidation. *Journal of the American Chemical Society* **2013,** *135* (23), 8452-8455.

89.   Xie, H.; Li, Y.; Jin, S.; Han, J.; Zhao, X., Facile Fabrication of 3D-Ordered Macroporous Nanocrystalline Iron Oxide Films with Highly Efficient Visible Light Induced Photocatalytic Activity. *The Journal of Physical Chemistry C* **2010,** *114* (21), 9706-9712.

90.   Desilvestro, J.; Graetzel, M.; Kavan, L.; Moser, J.; Augustynski, J., Highly efficient sensitization of titanium dioxide. *Journal of the American Chemical Society* **1985,** *107* (10), 2988-2990.

91.   Grätzel, M., Conversion of sunlight to electric power by nanocrystalline dye-sensitized solar cells. *Journal of Photochemistry and Photobiology A: Chemistry* **2004,** *164* (1), 3-14.

92.   Cahen, D.; Grätzel, M.; Guillemoles, J. F.; Hodes, G., Dye-sensitized Solar Cells: Principles of Operation. In *Electrochemistry of Nanomaterials*, Wiley-VCH Verlag GmbH: 2007; pp 201-228.

93.   Yanagida, M.; Yamaguchi, T.; Kurashige, M.; Hara, K.; Katoh, R.; Sugihara, H.; Arakawa, H., Panchromatic Sensitization of Nanocrystalline TiO2 with cis-Bis(4-carboxy-2-[2'-(4'-carboxypyridyl)]quinoline)bis(thiocyanato-N)ruthenium(II). *Inorganic Chemistry* **2003,** *42* (24), 7921-7931.

94.   He, J.; Benkö, G.; Korodi, F.; Polívka, T.; Lomoth, R.; Åkermark, B.; Sun, L.; Hagfeldt, A.; Sundström, V., Modified Phthalocyanines for Efficient Near-IR Sensitization of Nanostructured TiO2 Electrode. *Journal of the American Chemical Society* **2002,** *124* (17), 4922-4932.

95.   Altobello, S.; Argazzi, R.; Caramori, S.; Contado, C.; Da Fré, S.; Rubino, P.; Choné, C.; Larramona, G.; Bignozzi, C. A., Sensitization of Nanocrystalline TiO2 with Black Absorbers Based on Os and Ru Polypyridine Complexes. *Journal of the American Chemical Society* **2005,** *127* (44), 15342-15343.

96.   Sauvage, F.; Chen, D.; Comte, P.; Huang, F.; Heiniger, L.-P.; Cheng, Y.-B.; Caruso, R. A.; Graetzel, M., Dye-Sensitized Solar Cells Employing a Single Film of Mesoporous TiO2 Beads Achieve Power Conversion Efficiencies Over 10%. *ACS Nano* **2010,** *4* (8), 4420-4425.

97.   Müller, M.; Zentel, R.; Maka, T.; Romanov, S. G.; Sotomayor Torres, C. M., Photonic Crystal Films with High Refractive Index Contrast. *Advanced Materials* **2000,** *12* (20), 1499-1503.

98.   Colodrero, S.; Mihi, A.; Anta, J. A.; Ocaña, M.; Míguez, H., Experimental Demonstration of the Mechanism of Light Harvesting Enhancement in Photonic-Crystal-Based Dye-Sensitized Solar Cells. *The Journal of Physical Chemistry C* **2009,** *113* (4), 1150-1154.
99.   Mihi, A.; López-Alcaraz, F. J.; Míguez, H., Full spectrum enhancement of the light harvesting efficiency of dye sensitized solar cells by including colloidal photonic crystal multilayers. *Applied Physics Letters* **2006,** *88* (19), -.

100.	Hirata, N.; Lagref, J.-J.; Palomares, E. J.; Durrant, J. R.; Nazeeruddin, M. K.; Gratzel, M.; Di Censo, D., Supramolecular Control of Charge-Transfer Dynamics on Dye-sensitized Nanocrystalline TiO2 Films. *Chemistry – A European Journal* **2004,** *10* (3), 595-602.

101.	Usami, A., Rigorous solutions of light scattering of neighboring TiO2 particles in nanocrystalline films. *Solar Energy Materials and Solar Cells* **1999,** *59* (3), 163-166.

102.	Young, E. R.; Costi, R.; Paydavosi, S.; Nocera, D. G.; Bulovic, V., Photo-assisted water oxidation with cobalt-based catalyst formed from thin-film cobalt metal on silicon photoanodes. *Energy & Environmental Science* **2011,** *4* (6), 2058-2061.

103.	Bediako, D. K.; Surendranath, Y.; Nocera, D. G., Mechanistic Studies of the Oxygen Evolution Reaction Mediated by a Nickel–Borate Thin Film Electrocatalyst. *Journal of the American Chemical Society* **2013,** *135* (9), 3662-3674.

104.	Van der Ven, A.; Morgan, D.; Meng, Y. S.; Ceder, G., Phase stability of nickel hydroxides and oxyhydroxides. *Journal of The Electrochemical Society* **2006,** *153* (2), A210-A215.

105.	Pletcher, D., Electrochemical oxygen technology : K. Kinoshita, The Electrochemical Society, Wiley, Chichester, 1992, ISBN 047 157 0435, xiv + 431 pp., £98. *Journal of Electroanalytical Chemistry* **1993,** *345* (1–2), 485-486.

106.	Lyons, M. E. G.; Brandon, M. P., The Oxygen Evolution Reaction on Passive Oxide Covered Transition Metal Electrodes in Aqueous Alkaline Solution. Part 1-Nickel. *International Journal of Electrochemical Science* **2008,** *3* (12), 1386-1424.

107.	Thaller, L. H.; Zimmerman, A. H., *Nickel-hydrogen Life Cycle Testing: Review and Analysis*. AIAA: 2003.

108.	Trotochaud, L.; Boettcher, S. W., Precise oxygen evolution catalysts: Status and opportunities. *Scripta Materialia* **2014,** *74*, 25-32.

109.	Trotochaud, L.; Ranney, J. K.; Williams, K. N.; Boettcher, S. W., Solution-Cast Metal Oxide Thin Film Electrocatalysts for Oxygen Evolution. *Journal of the American Chemical Society* **2012,** *134* (41), 17253-17261.

110.	He, C. Y.; Wu, X. L.; He, Z. Q., Amorphous Nickel-Based Thin Film As a Janus Electrocatalyst for Water Splitting. *Journal of Physical Chemistry C* **2014,** *118* (9), 4578-4584.

111.	Subbaraman, R.; Tripkovic, D.; Chang, K. C.; Strmcnik, D.; Paulikas, A. P.; Hirunsit, P.; Chan, M.; Greeley, J.; Stamenkovic, V.; Markovic, N. M., Trends in activity for the water electrolyser reactions on 3d M(Ni,Co,Fe,Mn) hydr(oxy)oxide catalysts. *Nature Materials* **2012,** *11* (6), 550-557.

112.   Li, X.; Walsh, F. C.; Pletcher, D., Nickel based electrocatalysts for oxygen evolution in high current density, alkaline water electrolysers. *Physical Chemistry Chemical Physics* **2011,** *13* (3), 1162-1167.

113.   Matsumoto, Y.; Sato, E., ELECTROCATALYTIC PROPERTIES OF TRANSITION-METAL OXIDES FOR OXYGEN EVOLUTION REACTION. *Mater. Chem. Phys.* **1986,** *14* (5), 397-426.

114.   Bediako, D. K. Structural and mechanistic studies of nickel-borate thin-film oxygen evolving electrocatalysts. MIT, 2013.

115.   Bard, A. J., Faulkner, Larry R., *Electrochemical methods : fundamentals and applications*. 2nd Edition ed.; Wiley: 2001.

116.   Brinkmann, B. The Carbon Reality. http://bobbrinkmann.blogspot.com/2013/07/the-carbon-reality.html (accessed may 20, 2014).

117.   Price, M. J.; Maldonado, S., Macroporous n-GaP in Nonaqueous Regenerative Photoelectrochemical Cells. *The Journal of Physical Chemistry C* **2009,** *113* (28), 11988-11994.

118.   Dominey, R. N.; Lewis, N. S.; Bruce, J. A.; Bookbinder, D. C.; Wrighton, M. S., Improvement of photoelectrochemical hydrogen generation by surface modification of p-type silicon semiconductor photocathodes. *Journal of the American Chemical Society* **1982,** *104* (2), 467-482.

119.   Nakato, Y.; Yano, H.; Nishiura, S.; Ueda, T.; Tsubomura, H., Hydrogen photoevolution at p-type silicon electrodes coated with discontinuous metal layers. *Journal of Electroanalytical Chemistry and Interfacial Electrochemistry* **1987,** *228* (1–2), 97-108.

120.   Sivula, K.; Zboril, R.; Le Formal, F.; Robert, R.; Weidenkaff, A.; Tucek, J.; Frydrych, J.; Grätzel, M., Photoelectrochemical Water Splitting with Mesoporous Hematite Prepared by a Solution-Based Colloidal Approach. *Journal of the American Chemical Society* **2010,** *132* (21), 7436-7444.

121.   Junyu, C.; Tetsuya, K.; Naoki, K.; Jinhua, Y., Photoanodic properties of pulsed-laser-deposited α-Fe 2 O 3 electrode. *Journal of Physics D: Applied Physics* **2010,** *43* (32), 325101.

122.   Hahn, N. T.; Ye, H.; Flaherty, D. W.; Bard, A. J.; Mullins, C. B., Reactive Ballistic Deposition of α-Fe2O3 Thin Films for Photoelectrochemical Water Oxidation. *ACS Nano* **2010,** *4* (4), 1977-1986.

123.   Tahir, A. A.; Wijayantha, K. G. U.; Saremi-Yarahmadi, S.; Mazhar, M.; McKee, V., Nanostructured α-Fe2O3 Thin Films for Photoelectrochemical Hydrogen Generation. *Chemistry of Materials* **2009,** *21* (16), 3763-3772.

124. Bora, D. K.; Braun, A.; Erat, S.; Ariffin, A. K.; Löhnert, R.; Sivula, K.; Töpfer, J. r.; Grätzel, M.; Manzke, R.; Graule, T.; Constable, E. C., Evolution of an Oxygen Near-Edge X-ray Absorption Fine Structure Transition in the Upper Hubbard Band in α-Fe2O3 upon Electrochemical Oxidation. *The Journal of Physical Chemistry C* **2011,** *115* (13), 5619-5625.

125. Al-Kuhaili, M. F.; Saleem, M.; Durrani, S. M. A., Optical properties of iron oxide (alpha-Fe2O3) thin films deposited by the reactive evaporation of iron. *Journal of Alloys and Compounds* **2012,** *521*, 178-182.

126. Morrish, R.; Rahman, M.; MacElroy, J. M. D.; Wolden, C. A., Activation of Hematite Nanorod Arrays for Photoelectrochemical Water Splitting. *Chemsuschem* **2011,** *4* (4), 474-479.

127. Kleiman-Shwarsctein, A.; Hu, Y.-S.; Forman, A. J.; Stucky, G. D.; McFarland, E. W., Electrodeposition of α-Fe2O3 Doped with Mo or Cr as Photoanodes for Photocatalytic Water Splitting. *The Journal of Physical Chemistry C* **2008,** *112* (40), 15900-15907.

128. Burke, L. D.; Whelan, D. P., A NEW INTERPRETATION OF THE CHARGE STORAGE AND ELECTRICAL-CONDUCTIVITY BEHAVIOR OF HYDROUS IRIDIUM OXIDE. *Journal of Electroanalytical Chemistry* **1981,** *124* (1-2), 333-337.